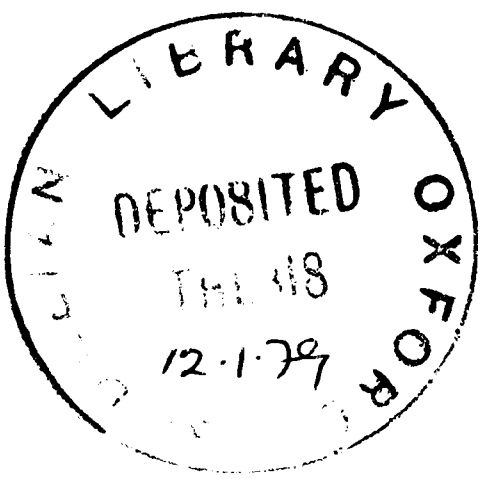
Photoelectron Spectroscopy of Metal Oxides

by

Neil Beatham

Wadham College

Oxford



A thesis submitted to the Board of the Faculty of Physical Sciences for the Degree of Doctor of Philosophy in the University of Oxford

September 1978

MS. D. Phil. d. 6464

N. BEATHAM D.Phil Thesis Sept. 78

ERRATA

page 3	line 23	for 'hv' read 'hν'
page 6	line 9	for 'K.E. energy' read 'K.E'
page 8	line 26	for 'measurments' read 'measurements'
page 16	ref.46	for 'Leisegang' read 'Liesegang'
page 16	ref.52	for '5(1974)' read '5(1974)259'
page 19	line 22	for 'wavefunction' read 'wavefunctions'
page 21	equation (2-9)	for '$M_{f\leftarrow i}^{2}$' read '$\|M_{f\leftarrow i}^{2}\|$'
page 23	line 21	for 'represents' read 'θ represents'
page 24	line 25	for '(h>1KeV)' read '(hν>1KeV)'
page 28	line 6	for '|n>' read '|n'>'
page 29	line 18	for '$P_{nm}(K)$' read '$P_{nm}(k)$'
page 31	line 6	for 'of the material scattering of' read 'of the material. Scattering of'
page 32	line 9	for 'PE spectrum' read 'X-PE spectrum'
page 40		the x-axis indicates electron kinetic energy
page 42	ref.18	for 'Beruind' read 'Berglund'
page 42	ref.33	for 'McCruire' read 'McGuire'
page 45	line 3	delete 'and $IrO_2.5H_2O$'
page 47	line.12	for 'stoichiometrics' read 'stoichiometries'
page 47	line 15	for 'Mn TiO_3,Fe TiO_3' read '$MnTiO_3$,$FeTiO_3$'
page 54	line 9	for 'shpae' read 'shape'
page 55	line 28	for 'as low as of' read 'as low as'
page 64	ref.22	for 'phosphorous' read 'phosphorus'
page 75	line 6	for 'Fig. 4 3' read 'Fig. 4.3'
page 76	line 15	for 'bais' read 'bias'
page 82	ref.1	for '490' read '137'
page 91	line 27	for 'engated' read 'engaged'

page 93 line 7	for 'concomittant' read 'concomitant'
page 93 line 11	for 'fo' read 'of'
page 105 lines 8&10	for 'C_H' read 'c_H'
page 105 line 13	for 'oribtals' read 'orbitals'
page 124 line 5	for '_____' read '$\longleftrightarrow$'
page 137 ref.23	for '490' read '137'
page 147 line 1	for '^{5}Eg' read '^5E_g'
page 161 eqn.(7-8)	for '$Q_{nk}(r)$' read '$iQ_{nk}(r)$'
page 162 eqn.(7-13)	One should also include the Darwin term, which is necessary to give the correct shift for s-states along with the p^4 term.
page 167 line 11	for 'explict' read 'explicit'
page 168	The last sentence in the first paragraph should read as follows - 'The weighted average of the $\bar{f}$ and f partial cross-sections realises the non-relativistic f electron photoionisation cross-section as $c \rightarrow \infty$.'
page 182 line 6	for '$\bar{s}$ ' read 's'
page 211 line 2	for 'non-relastivistic' read 'non-relativistic'
page 217 ref.10	for 'Moddenman' read "Moddeman'
page 224 line 23	for 'summetry' read 'symmetry'
page 228 line 16	for 'x → y → x → x' read 'x → y → z → x'
page 229 3rd eqn.	The equation should read as follows - $S_{xk,yk} = \left[(1 + \chi_{xk})(1 + \chi_{yk})\right]^{-\frac{1}{2}} 2\{S_\sigma + S_\pi\}\sin\phi_x \sin\phi_y$
page 229 line 18	for 'all' read 'cell'

ABSTRACT

PHOTOELECTRON SPECTROSCOPY OF METAL OXIDES. by N. Beatham, Wadham College, Oxford. Submitted for the degree of Doctor of Philosophy, Trinity Term. 1978.

The work described in the thesis divides essentially into two parts: (1) the experimental measurements of photoelectron spectra of a variety of solid metal oxides; and (2) the theoretical investigation of electronic structure problems concerning the final states of the photoionisation process (the states of the ionised system), much of which is directly relevant to the experimental studies.

The spectroscopic investigation concentrates upon transition-metal oxides (for example, the rutile series MO_2, various sesquioxides M_2O_3, and ternary systems such as ilmenites ($MTiO_3$). Such materials are of considerable general interest by virtue of their diverse electronic properties, and their technological importance. Photoelectron spectra were measured from polycrystalline samples, using both UV (He I and He II) and X-ray (Mg Kα) excitation. The sequential measurement of UV- and X-ray photoelectron spectra is an important element of this work. From the technical point of view another important feature of the experimental work is the attention given to preparation of clean sample surfaces.

The theoretical work concerns the 'fine structure' of photoelectron signals due to (1) electrostatic coupling effects and (2) electronic relaxation in the final state. The ionic approximation is invoked, all electronic structure calculations being performed on atomic species.

Both core electrons in general, and the outer-shell electrons of heavy atoms, are highly relativistic in nature, their description demanding the use of Dirac-Fock theory rather than the simple Hartree-Fock model. A major feature of the theoretical work described is the use, where appropriate, of Dirac-Fock theory to obtain required atomic wavefunctions and state energies. The use of a relativistic model proves essential in many cases.

ACKNOWLEDGEMENTS

I should particularly like to thank my supervisor, Tony Orchard, for his guidance and encouragement during the course of this work. Andrew Hamnett has also been of considerable influence and I am indebted to him for both his friendship and sound advice. I would also like to thank Ian Grant for his interest in the theoretical work and the position of research assistant which I have held since April 1978.

Lugciano Fragala, Nick Pyper, David Mayers, Russ Egdell, Tony Cox, Stephen Rose, Ian Nicol, Mike Gordon and Geoff Thornton have helped to contribute in a variety of ways and I would also like to thank the ICL technical staff, and in particular, Harry Davenport and Keith Mayo, for their assistance. The generous donation of compounds from Ghania Bindaar, Phil Dunn, John Birtill, Dave Palmer and Phil Wiseman is greatly appreciated and I am also grateful to Sally Price for typing my manuscript so skilfully.

Finally, I would like to thank my wife Helen for playing second fiddle to photoelectron spectroscopy for the last three years.

CONTENTS

		Page
Chapter 1	INTRODUCTION	1
1.1	Photoelectron spectroscopy	2
1.2	Survey of the various sources of ionising photons	3
1.3	Theoretical considerations regarding PES	5
1.4	Scope of the present work	7
Chapter 2	GENERAL PRINCIPLES OF PHOTOELECTRON SPECTROSCOPY	17
2.1	Fundamental aspects of photoionisation	18
2.2	Atomic photoionisation	20
2.3	Photoemission from solids	28
2.4	The fate of inner shell vacancies	32
2.5	Photoionisation from open shell systems	32
2.6	Calibration and charging effects	35
Chapter 3	INSTRUMENTAL AND EXPERIMENTAL PROCEDURES	44
3.1	Sample preparation and characterisation	45
3.2	The photoelectron spectrometer	48
3.3	The presentation of PE spectra	55
3.4	Computing facilities	58

Page

Chapter 4 GENERAL ASPECTS OF THE PHOTOELECTRON SPECTRA OF TRANSITION METAL OXIDES 65

4.1 The electronic structure of transition metal oxides 66

4.2 The effects of sample charging 72

4.3 Probe-biassing experiments 74

Chapter 5 PHOTOELECTRON SPECTRA OF BINARY OXIDES 83

5.1 Transition metal dioxides 84

5.2 The higher oxides of Nb, Mo and W 96

5.3 Transition metal sesquioxides 100

5.4 Transition metal monoxides 107

Chapter 6 PHOTOELECTRON SPECTRA OF TERNARY OXIDES 140

6.1 Introduction 141

6.2 Transition metal titanates 143

6.3 Transition metal perovskites 147

Chapter 7 APPLICATION OF MULTICONFIGURATIONAL DIRAC-FOCK THEORY TO PHOTOELECTRON SPECTROSCOPY 158

7.1 Dirac-Fock theory 159

7.2 Implementation of the MCDF method 163

7.3 Relativistic formulation of final state structure in PES 166

7.4 Ionisation of a 4f electron from lanthanoid compounds 171

7.5 Structure in the core-level X-PE spectra of lanthanoid and transition metal compounds 175

7.6 Valence electron structure in the UV-PE spectra of metal atom vapours 180

Page

Chapter 8 APPLICATION OF THE SUDDEN APPROXIMATION TO PHOTOELECTRON SPECTROSCOPY 194

8.1 Theoretical analysis of the sudden approximation 195

8.2 Core-electron ionisation from closed shell systems 201

8.3 Core-electron ionisation from open shell systems 204

Appendices 218

A.1 Conventions adopted in this thesis 219

A.2 Description of computer programmes used in this thesis 221

A.3 Description of the semi-empirical band structure calculations performed on a face-centred cubic oxide framework. 224

A.4 The special theory of relativity 230

CHAPTER ONE

INTRODUCTION

1.1 Photoelectron spectroscopy

1.2 Survey of the various sources of ionising photons

1.3 Theoretical considerations regarding PES

1.4 Scope of the present work

1.1 Photoelectron Spectroscopy

Photoelectron spectroscopy (PES) is concerned with the electron kinetic energy (KE) analysis when a sample is subjected to electromagnetic radiation of sufficient energy to cause photoionisation. Application of the principle of conservation of energy leads to the Einstein equation,[1]

$$T_i = h\nu - \Delta E_i - e\phi \qquad (1\text{-}1)$$

Here T_i is the kinetic energy of the electron; $h\nu$ is the incident photon energy, held constant during the experiment; ΔE_i, the energy difference between the initial and ionised states of the system; and $e\phi$ is the work function of the irradiated material (zero for a gas).

Photoionisation is intrinsically a one-photon one-electron ($h\nu$, e) process; as a consequence there should exist a simple correspondence between the observed PE spectrum and the orbital electronic structure of the irradiated sample.

The pioneering work in the field of PES was directed along two independent lines: (i) ultra-violet PES (UV-PES) on gases[2, 3] and (ii) X-ray PES (X-PES) on solids.[4, 5] Recent advances, however, have been towards integrating these two approaches.[6, 7] Indeed, much of this thesis is devoted to the application of UV-PES to solids.

There are, arguably, three main areas which are of special current interest as regards exploring the full potential of the technique. These are: (i) the changes that occur in a PE spectrum as a consequence of altering the photon energy of the ionising radiation;[8, 9] (ii) the development of a more comprehensive and workable theory of the many electron theory of photoionisation;[10-13] and (iii) angular distribution studies.[14-17]

This thesis is intimately concerned with the first two of these topics. However, before outlining the scope of the present work, it is necessary to provide a brief introduction to (i) the various sources of ionising photons that are currently available, and (ii) some of the theoretical concepts arising in PES.

1.2 Survey of the various sources of ionising photons

Both ultra-violet (UV) and X-radiation are routinely employed to excite PE spectra. In UV-PES the photon sources are commonly provided by passage of a direct-current (DC) or microwave discharge through a noble gas at a low pressure (< 1 torr).[18] In this work extensive use has been made of He-I and He-II radiation; occasionally it also proved profitable to employ Ne-I and Ne-II radiation. In a helium discharge the strongest emission line, the He-Iα line at 21.22eV, is associated with the $1s2p \longrightarrow 1s^2(^1P \longrightarrow {}^1S)$ transition in neutral helium. The other emission lines labelled β, γ etc. and deriving from the series $1snp \longrightarrow 1s^2$ ($n = 3$, 4 etc.) are rather weak because of internal de-activation of helium atoms in the higher excited configurations.[18] Under favourable conditions, ionised atoms can be produced in discharge lamps, and in the case of He are responsible for the He-II emission line ($np \longrightarrow 1s$ in He^+). The α line (40.81 eV) again dominates this series but the flux of the He-IIβ photons, with $h\nu = 48.37$eV may amount to ca. 10% of the total He-II output. Table 1.1 lists the predominant lines emitted by He and Ne discharge lamps. Discharges in other noble gases normally emit a wider range of lines, and thus tend to be less used as sources of ionising photons. Monochromatisation of the output from discharge lamps is

normally prohibitive in PES due to the severe attenuation of photon flux but recent advances have shown that it is possible in favourable circumstances.[19]

The simplest type of X-ray photon source is one which utilises the characteristic emission lines from a target (anode) bombarded by high energy electrons. In addition to these characteristic lines, a continuous spectrum, referred to as the Bremsstrahlung is also produced and this is dependent upon the primary electron energy. The most commonly used X-ray lines in X-PES are the $K\alpha_{1,\,2}$ emission lines of Al and Mg which have half-widths (FWHM) of 0.83eV and 0.68eV and energies of 1486.6 eV and 1253.6eV respectively.[20] The $K\alpha_{1,\,2}$ line in each case is an unresolved doublet resulting from $2p_{\frac{1}{2}} \longrightarrow 1s$ and $2p_{3/2} \longrightarrow 1s$ transitions but these are accompanied by "satellite" lines resulting from similar transitions within multiply ionised atoms (e.g. $K\alpha_{3,\,4}$) and from valence band to 1s transitions ($K\beta$). Details of the half-widths, positions and relative intensities of the various Mg and Al $K\alpha$ lines are presented in Tables 1-2 and 1-3 respectively.

The degree of resolution achievable in PES is a convolution of the intrinsic linewidth of the exciting radiation with an instrumental factor, which is dependent upon the resolving power, $R = E/\Delta E$, of the analyser system. The gas discharge emission lines used in UV-PES have linewidths of only a few meV (largely determined by Doppler effects in the discharge). Thus there is considerable difference in resolution between very slow UV-excited photoelectrons ($\leqslant 0.2$eV) and highly energetic photoelectrons ejected by X-radiation (ca. 1.5eV).

The line-width of the X-ray source can be reduced, and the troublesome satellite lines and Bremsstrahlung removed, by

recourse to monochromatisation.[21, 22] The customary method is to use crystal dispersion techniques resulting in a limiting half-width of 0.22eV.[21] Some other X-ray lines are beginning to emerge as useful photon sources for PES[23-27] and these are tabulated in Table 1-4. Finally, an electron storage ring (synchroton) is capable of providing a continuously tunable, polarised photon source.[28-30] Where the facility is available synchrotron radiation is being exploited to provide, after monochromatisation, photon sources in the energy range 50 to 1000eV.[30]

Almost all the X-PE spectra reported in this thesis were excited with achromatic Mg Kα radiation.

1.3 Theoretical considerations regarding PES

PES is concerned with transitions from a neutral system, which is almost invariably in its ground electronic state, to various states of the ionised system characterized by having one less bound electron. The main motivation for the development of PES has been that the observed PE spectrum should essentially reflect the ground electronic structure of the system. Thus the technique should be able to provide a means of studying the orbital electronic structure of molecules and atoms, and the band structure of continuous solids. This principle is embodied in the frequent application of Koopmans' theorem[31] to the interpretation of PE spectra.

Photoionisation can however be an extremely complex process and to appreciate all the subtle aspects of PES demands both rigorous and detailed knowledge of the electronic structure of the neutral and ionised system, together with an

adequate description of the continuum electron.

Additional complications arise when the sample is in the form of a solid, due to the fact that when electrons propagate through a medium, they have a high probability of suffering inelastic energy loss.[32, 33] Consequently the flux of photo-electrons emerging from the solid is much attenuated, with the implication that PES is a surface technique. Furthermore, all PE signals from solids display an enhancement in background intensity towards lower K.E. energy. The effects of inelastic scattering tend to be much more pronounced in UV-PES (where electrons have quite low K.E.) than in X-PES.[7]

However, despite the inherent complexity of the technique, much of PES can be satisfactorily explained within the frame-work of simple models involving various approximations.

In the one-electron model, which represents the simplest approach, both the neutral and ionised system are described by Hartree-Fock theory; the 'primary' features in the PE spectrum correspond to distinct electronic states of the ionised system obtained by ejection of a single electron from the neutral system. (Relativistic effects can be explicitly taken into account by recourse to Dirac-Fock theory).[34]

When dealing with closed-shell systems, Koopmans' theorem is frequently invoked. The theorem assumes that the ionisation energy I_K of an electron species K can be identified with the negative of its self-consistent field (SCF) orbital energy ϵ_K^{SCF}.

$$I_K = - \epsilon_K^{SCF} \qquad (1\text{-}2)$$

This imposes the additional constraint that it assumes all the electrons, bar the one that is photoejected, are

spatially invariant during photoemission (the frozen orbital approximation). Thus electronic relaxation in the ionised system is neglected.

In itself, the Hartree-Fock method treats electron-electron repulsion without explicitly introducing electron-electron coordinates into the self-consistent field equations and as such neglects electron correlation. Consequently, PE spectra often display features the origin of which lie in the many-electron nature of photoemission; these cannot be understood within a one-electron framework. Several mechanisms are frequently invoked which attempt to take account of the effects of electron relaxation and correlation. One important objective of this thesis is to explore more fully the applications and limitations of the two most important of these mechanisms, namely the sudden approximation[35-37] and configuration interaction,[11, 38, 39] and to discuss the inter-relation between the two.

Finally, turning to the problem of band intensities in PES, an understanding of photoionisation cross-sections and their dependence on incident photon energy requires a detailed description of the continuum electron. This aspect of PES remains, by far, the most difficult to predict theoretically and detailed quantitative agreement has only been obtained for atoms[12] and small molecules.[40]

1.4 Scope of the present work

The work described in this thesis has two separate themes: (i) the application of UV-PES to metal oxides; and (ii) theoretical investigations of the many-electron aspect of photoionisation, with particular emphasis on the effects of relativity.

The field of UV-PES as applied to solids is bedevilled by two major problems: (i) the difficulty of ensuring surface integrity (i.e. the same composition at the surface as in the bulk material); and (ii) the effects of sample charging. As a result, previous work on the subject has tended to concentrate on: (i) clean metal surfaces;[41-44] (ii) single crystals that may readily be cleaved (e.g. $MoTe_2$);[45] and (iii) easily sublimable inorganic materials which can be presented as films (e.g. NaCl).[46] Little work has been performed on involatile materials, where it is usually difficult to obtain single crystals (and crystals that readily permit cleavage).

In this laboratory, attempts have been made to obtain clean surfaces in bulk polycrystalline materials by *in situ* sample treatment; the particular method involves heating the sample in an appropriate atmosphere.[47] This technique has proved reasonably successful for securing good quality X-PE spectra and this thesis is concerned with the application and extension of the basic methodology to the field of UV-PES. We have concentrated on transition metal oxides for the following reasons:

(i) Most of them are stable at the temperatures necessary to out-gas typical surface contaminants such as CO_2 and H_2O.

(ii) They exhibit a wide range of physical properties, the transition metal dioxides being particularly intriguing from the electronic viewpoint. For instance, electrical conductivity measurments reveal that TiO_2 is an insulator, MoO_2 and RuO_2 are metals, while both VO_2 and NbO_2 exhibit temperature-dependent semi-conductor $\longleftrightarrow$ metal transitions.[48] Both X-ray and UV-PES can provide invaluable information regarding the valence electronic structure of these materials; the extra resolution in UV-PES is often a crucial advantage.

The relationship between structure and physical properties of oxides appears to be well understood, largely through the ideas of Goodenough.[49] The PE spectra should afford a stringent test of such phenomenological models. For many oxides, elaborate band structure calculations are also available. The recent trend[50, 51] in such calculations of partitioning the valence band density of states into the respective metal nd and oxygen 2p components is particularly welcome. This is because one particular motivation in developing UV-PES on oxides is to complement the X-ray technique and exploit more fully the different relative partial photoionisation cross-sections of the metal nd and oxygen 2p electrons to UV and X-ray photons.[8]

The metal core-electron PE spectra of transition metal (and lanthanoid) compounds exhibit extensive, and often detailed, many-electron structure.[52-54] Although it is clear that part of this structure derives from covalency effects, it is anticipated that much of it should be interpretable within a purely ionic framework.[55, 56] It should be possible to distinguish between two major 'sources' of such secondary structure, namely: (i) electronic relaxation; and (ii) multiplet splitting due to electrostatic coupling of the core hole with open-shell valence electrons. An attractive model for investigating the role of electronic relaxation is the sudden approximation.[35, 38] In order to analyse properly the effects of electrostatic coupling involving core holes it is essential to include relativistic effects. The recent development in this University, of a multiconfigurational Dirac-Fock SCF programme,[57] capable of open shell atomic calculations, now makes this possible, within the confines of the ionic model.

The availability of the SCF package has also stimulated theoretical work on two other aspects of PES where relativistic effects are of importance. The first concerns photoionisation from an open-shell of f electrons.[58] The second topic concerns the interpretation of the gas phase UV-PE spectra of metal vapours where the effects of electron correlation and relativity terms are intimately connected.[59-61]

Table 1.1

Line Emissions from He and Ne discharges

Line	Energy/eV	Relative Intensity*
He-Iα	21.22	100
He-Iβ	23.09	2
He-IIα	40.81	1
He-IIβ	48.37	0.1
Ne-I	16.67	15
	16.85	100
Ne-II	26.81	100
	26.91	100

* Intensities refer to a typical DC capillary discharge.

Table 1.2

Characteristics of the Energy Distribution of Al K_α Radiation (Each Line is assumed to have a Lorentzian Shape)[20]

Line	Position relative to the α_1 line (eV)	FWHM (eV)	Relative Integrated Intensity
α_2	-0.416	0.50 ± 0.02	50
α_1	0	0.50 ± 0.02	100
α_3	+9.65	0.83 ± 0.03	10.8 ± 0.2
α_4	+11.64	0.83 ± 0.03	5.4 ± 0.1

Table 1.3

Characteristics of the Energy Distribution of Mg Kα Radiation (Each Line is assumed to have a Lorentzian Shape).[20]

Line	Position relative to the α_1 line (eV)	FWHM (eV)	Relative Integrated Intensity
α_2	-0.33 ± 0.02	0.41 ± 0.03	50
α_1	0	0.41 ± 0.03	100
α_3	$+8.4\pm0.1$	0.70 ± 0.07	12.8 ± 0.3
α_4	$+10.15\pm0.1$	0.75 ± 0.07	6.9 ± 0.2

Table 1.4

Some X-Ray Lines of use in PES[23]

Line	Energy (eV)	FWHM (eV)
Y Mζ	132.3	0.47
Zr Mζ	151.4	0.77
F Kα	676.4	0.5
Mg Kα	1253.6	0.68
Al Kα	1486.6	0.83
Cr Kα	5417	2.1
Cu Kα	8048	2.6

REFERENCES FOR CHAPTER 1

1. A. Einstein, Ann. Physik. 17 (1905) 132.
2. D. W. Turner, M. I. Al-Jobury, J. Chem. Phys. 37 (1962) 3007.
3. D. W. Turner, C. Baker, A. D. Baker, C. R. Brundle, "Molecular Photoelectron Spectroscopy" (1970), Wiley Interscience, London.
4. K. Siegbahn, C. Nordling, A. Fahlman, R. Nordberg, K. Hamrin, J. Hedman, G. Johansson, T. Bergmark, S-E. Karlsson, I. Lindgren, B. Lindberg, "ESCA: Atomic, Molecular and Solid State Structure Studied by Means of Electron Spectroscopy", (1967) Nova Acta Reg. Sci. Upsatiensis, Ser. IV, Vol. 20.
5. K. Siegbahn, C. Nordling, A. Fahlman, J. Hedman, P. F. Heden, K. Hamrin, U. Crelius, T. Bergmark, L. O. Werne, R. Manne, Y. Baer, "ESCA Applied to Free Molecules" (1969) North Holland, Amsterdam.
6. U. Gelius, J. Elect. Spec. 5 (1974) 985.
7. P. M. Williams, p 313 in "Handbook of X-ray and ultraviolet Photoelectron Spectroscopy" ed D. Briggs (1977) Heyden.
8. D. E. Eastman, J. L. Freeouf, Phys. Rev. Lett. 34 (1975) 395.
9. R. G. Egdell, A. F. Orchard, D. R. Lloyd, N. V. Richardson, J. Elect. Spec. 12 (1977) 415.
10. R. L. Martin, D. A. Shirley, p 75 in "Electron Spectroscopy: Theory, Techniques and Applications Vol. 1" (1977) Academic Press.
11. S. T. Manson, J. Elect. Spec. 9 (1976) 21.

12. P. G. Burke, p 61 in "Photoelectron Emission: proceedings of the Daresbury Study Weekend, 6-7 March 1976" ed. I. H. Munro, G. V. Marr, (1976) Science Research Council Publication DL/SRF/R8.

13. P. G. Burke, W. D. Robb, Adv. Atom Mol. Phys. 11 (1975) 143.

14. G. V. Marr, p 81 in "Photoelectron Emission: proceedings of the Daresbury Study Weekend, 6-7 March, (1976) Science Research Council Publication DL/SRF/R8.

15. D. R. Lloyd, C. M. Quinn, N. V. Richardson, p 179 in "Surface and Defect Properties of Solids" Vol 6 ed. M. W. Roberts, J. M. Thomas (1977) Chemical Society Specialist Periodical Report.

16. C. S. Fadley, J. Elect. Spec. 5 (1974) 725.

17. C. S. Fadley, Prog. Solid State Chem. 11 (1976) 265.

18. J. A. R. Samson, "Techniques of Vacuum Ultraviolet Spectroscopy" (1967) John Wiley, New York.

19. J. A. R. Samson, G. N. Haddard, J. L. Gardener, J. Phys. B10 (1977) 1749.

20. N. Beatham, A. F. Orchard, J. Elect. Spec. 9 (1976) 129.

21. A. Barrie , N. E. Christensen, Phys. Rev. B14 (1976) 2442.

22. A. Barrie , p 79 in "Handbook of X-ray and Ultra Violet Photoelectron Spectroscopy" ed D. Briggs (1977) Heyden.

23. F. Wuilleumier, M. O. Krause, Phys. Rev. A10 (1974) 242.

24. R. G. Cavell, D. A. Allison, Chem. Phys. Lett. 36 (1975) 514.

25. M. S. Banna, D. A. Shirley, J. Elect. Spec. 8 (1976) 23.

26. R. Nilsson, R. Nyholm, A. Berndtsson, J. Hedman, C. Nordling, J. Elect. Spec. 9 (1976) 337.

27. A. Berndtsson, R. Nyholm, R. Nilsson, J. Hedman, C. Nordling, J. Elect. Spec. 13 (1978) 131.

28. M. L. Perlman, E. M. Rowe, R. E. Watson, Phys. Today 27 (1974) 30.

29. T. Ishii, S. Kono, S. Suzuki, I. Nagakura, T. Sagawa, R. Kato, M. Watanabe, S. Sato, Phys. Rev. B12 (1975) 4320.

30. P. Pianetta, I. Lindau, C. Garner, W. E. Spicer, Phys. Rev. Lett. 35 (1975) 1356.

31. T. Koopmans, Physica 1 (1934) 104.

32. J. Daniels, C. v. Festenberg, H. Raether, K. Zeppenfeld, p 77 in "Springer Tracts in Modern Physics" Vol. 54 (1970). Springer-Verlag.

33. N. Beatham, Chemistry Part II Thesis, Oxford (1975).

34. I. P. Grant, Adv. Physics 19 (1970) 747.

35. R. Manne, T. Åberg, Chem. Phys. Lett. 7 (1970) 282.

36. C. S. Fadley, J. Elect. Spec. 5 (1974) 895.

37. M. Mehta, C. S. Fadley, P. S. Bagus, Chem. Phys. Lett. 37 (1976) 454.

38. J. Berkowitz, J. L. Dehmer, Y.-K. Kim, J. P. Desclaux, J. Chem. Phys. 61 (1974) 2556.

39. J. E. Hansen, Phys. Rev. A15 (1977) 810.

40. T. N. Rescigno, C. F. Bender, B. V. McKoy, P. W. Langhoff, J. Chem. Phys. 68 (1978) 970.

41. E. W. Plummer, B. J. Waclawski, T. V. Vorburger, C. E. Kuyatt, Prog. Surf. Sci. 7 (1976) 149.

42. J. C. Fuggle, M. Steinkilberg, D. Menzel, Chem. Phys. 11 (1975) 307.

43. D. R. Lloyd, C. M. Quinn, N. V. Richardson, J. Chem. Soc., Faraday Trans. 72 (1976) 1036.

44. S. Evans, J. Peilaszek, J. M. Thomas, Surface Sci. 55 (1976) 644.

45. I. T. McGovern, R. H. Williams, J. Phys. C9 (1976) L337.

46. R. T. Poole, J. G. Jenkin, J. Leisegang, R. C. G. Leckey, Phys. Rev. B11 (1975) 5179.

47. G. Thornton, D. Phil. Thesis, Oxford (1976).

48. D. B. Rogers, R. D. Shannon, A. W. Sleight, J. L. Gillson, Inorg. Chem. 8 (1969) 841.

49. J. B. Goodenough, Prog. Solid State Chem. 5 (1971) 145.

50. L. F. Mattheiss, Phys. Rev. B13 (1976) 2433.

51. A. B. Kunz, G. T. Surratt, Solid State Commun. 25 (1978) 9.

52. B. Wallbank, I. G. Main, C. E. Johnson, J. Elect. Spec. 5 (1974)

53. N. Spector, C. Bonnelle, G. Dufour, C. K. Jørgensen, H. Berthou, Chem. Phys. Lett. 41 (1976) 199.

54. A. F. Orchard, G. Thornton, J. Elect. Spec. 13 (1978) 27.

55. R. P. Gupta, S. K. Sen, Phys. Rev. B10 (1974) 71.

56. R. P. Gupta, S. K. Sen, Phys. Rev. B12 (1975) 15.

57. I. P. Grant, D. F. Mayers, N. C. Pyper, J. Phys. B9 (1976) 2777.

58. P. A. Cox, Structure and Bonding 24 (1975) 56.

59. S. Süzer, M. S. Banna, D. A. Shirley, J. Chem. Phys. 63 (1975) 3473.

60. S. Süzer, S.-T. Lee, D. A. Shirley, Phys. Rev. A13 (1976) 1842.

61. N. S. Hush, S. Süzer, Chem. Phys. Lett. 46 (1977) 411.

CHAPTER TWO

GENERAL PRINCIPLES OF PHOTOELECTRON SPECTROSCOPY

2.1 Fundamental aspects of photoionisation

2.2 Atomic photoionisation

2.3 Photoemission from solids

2.4 The fate of inner shell vacancies

2.5 Photoionisation from open shell systems

2.6 Calibration and charging effects

2.1 Fundamental aspects of photoionisation

Photoionisation is one aspect of the interaction of matter with radiation. The radiation field can be described by a vector potential $\underline{A}$ and a scalar potential ϕ. These satisfy the wave-equation and in addition satisfy the subsidary condition

$$\nabla . \underline{A} + \frac{1}{c^2} \frac{\partial \phi}{\partial t} = 0 \qquad (2\text{-}1)$$

which is necessary in order to conserve the electron charge-current. The vector $-i\hbar\nabla$ is the sum of momentum operators for the individual particles; $\nabla = \sum_i \nabla_i$. A transformation on the potentials which preserves these relations and the values of the field strength is known as a gauge transformation. Within the Coulomb gauge ($\nabla . \underline{A} = 0$ and $\phi = 0$), the vector potential for radiation propagating in the form of a plane wave of wave-vector $\underline{q}$ and frequency ω can be written as

$$\underline{A} = \underline{u} A_0 \left[\exp(-i\underline{q}.\underline{r}) \exp(i\omega t) + \exp(i\underline{q}.\underline{r}) \exp(-i\omega t) \right] \qquad (2\text{-}2)$$

where $\underline{u}$ is the unit vector specifying the direction of the electric field vector and A_0 is the amplitude of the potential.

The interaction between the electrons of the system and the electromagnetic field (given by the operator - e $\underline{A}.\underline{p}$) is sufficiently small that it can be adequately handled using first-order perturbation theory, this provides the following expression for the differential photoionisation cross-section for ejection of an electron into a solid angle $d\Omega$, with respect to some axis e.g. that of the electric field vector.

$$\frac{d\sigma}{d\Omega} = \frac{4\pi^2\alpha}{\omega}\left|\underline{u}\langle\Psi_f|\exp(i\underline{q}\cdot\underline{r})\,\underline{\nabla}|\Psi_i\rangle\right|^2 \qquad (2\text{-}3)\ \text{a.u}$$

Here $|\Psi_f\rangle$ represents the final state of the ionised system plus continuum electron.

The exponential factor in the matrix element can be expanded in the series

$$\exp(i\underline{q}\cdot\underline{r}) = 1 + i\underline{q}\cdot\underline{r} + \tfrac{1}{2}(i\underline{q}\cdot\underline{r})^2 + \cdots \qquad (2.4)$$

Retention of only the first term results in the <u>electric dipole</u> approximation. This assumes that the wavelength of the photon is large compared with the linear dimensions of the atom. Equation (2-3) thus gives the differential cross-section in terms of the <u>dipole velocity</u> matrix element

$\langle\Psi_f|\nabla|\Psi_i\rangle$ in the long wavelength limit.

It is often convenient to transform this to

$$\frac{d\sigma}{d\Omega} = 4\pi^2\alpha\omega\left|\underline{u}\cdot\langle\Psi_f|\underline{r}|\Psi_i\rangle\right|^2 \qquad (2\text{-}5)\ \text{a.u.}$$

using the relation

$$[\underline{r}, H] = \underline{\nabla} \qquad (2\text{-}6)\ \text{a.u}$$

Here $\underline{r} = \sum_i \underline{r}_i$ Equation (2-5) can also be regarded as a gauge transformation on the potentials.[2]

It follows that these two expressions for $\frac{d\sigma}{d\Omega}$ can only be expected to give the same numerical values if $|\Psi_f\rangle$ and $|\Psi_i\rangle$ satisfy the charge-current continuity equation. In general this will not be true for approximate wavefunction and the discrepancy between the two provides one with a major difficulty in predicting absolute cross-sections.

2.2 Atomic Photoionisation

Tensor algebra provides a powerful technique for discussing atomic PE cross-sections and intensity distributions. We restrict ourselves initially to the case of photoionisation from a closed shell system.

The electric dipole operator is a tensor of rank one. The matrix element of the qth component of the electric dipole operator between an initial N-electron state defined by the quantum numbers $(\alpha LSM_L M_S)$ and a final state designated $(\alpha' L' S' M_L' M_S')$ is given by

$$M_{f \leftarrow i} = \langle l^{n-1}(\alpha'' L'' S''), l'; (\alpha' L' S' M_L' M_S') \left| \sum_{i=1}^{N} T_q^K(i) \right| l^n (\alpha L S M_L M_S) \rangle \qquad (2\text{-}7)$$

it being implicitly assumed that all electron orbitals are spatially invariant to photoabsorption (the one-electron approximation). All 'spectator' orbitals have been excluded from consideration. $T_q^K(i)$ is the q^{th} component of the tensor of rank K (here K = 1) which operates on the ith electron and is completely independent of spin. The orbital labelled l' belongs to a continuum channel and the quantum labels $(\alpha'' L'' S'' M_L'' M_S'')$ refer to the ionic state. Our assumption that the sub-shell l is initially closed implies that L = S = 0 and n = 4l + 2.

Application of the Wigner-Eckart theorem[3] results in

$$M_{f \leftarrow i} = \delta_{SS'} \delta_{M_S M_S'} (-1)^{2K} \langle L' M_L' | L k M_L q \rangle \times \langle l^{n-1}(\alpha'' L'' S''), l'; \alpha' L' S' \| \sum_{i=1}^{N} T^K(i) \| l^n (\alpha L S) \rangle$$

(2-8)

Selection rules connected with the conservation of angul-
momentum
ar/can be derived from the above relationship. The matrix element vanishes unless $M_L' = q + M_L$ and L', K and L satisfy triangle conditions.

Photoionisation cross-sections depend upon $\left|M_{f \leftarrow i}\right|^2$. In order to take account of all transitions between the states αLS and $\alpha' L' S'$, we must average over the initial magnetic quantum numbers and sum over the final magnetic quantum numbers. This provides

$$\phi_{L,L'} = \frac{1}{[S]}\frac{1}{[L]} \sum_{M_L M_S M_L' M_S'} M_{f \leftarrow i}^2 = \frac{\delta_{SS'}}{[L]} \sum_{M_L M_L'} \langle L' M_L' | L k M_L q \rangle^2$$

$$\times \left| \langle l^{n-1}(\alpha'' L'' S''), l'; (\alpha' L' S') \| \sum_{i=1}^{N} T_{(i)}^{k} \| l^n (\alpha L S) \rangle \right|^2$$

(2-9)

Here $[J] = 2J + 1$. The coupling coefficients have the following useful orthonormality property:

$$\sum_{M_L M_{L'}} \langle L' M_L' | L k M_L q \rangle \langle L' M_L' | L k' M_L q' \rangle = \delta_{kk'} \delta_{qq'} \frac{[L']}{[k]}$$

(2-10)

The summation over M_L and M_L' naturally implies a summation over q and thus we obtain

$$\phi_{L,L'} = \frac{\delta_{SS'}}{[K]}\frac{[L']}{[L]} \left| \langle l^{n-1}(\alpha'' L'' S''), l'; (\alpha' L' S') \| \sum_{i=1}^{N} T_{(i)}^{k} \| l^n (\alpha L S) \rangle \right|^2$$

(2-11)

It proves more convenient to rewrite this expression in terms of the reversed reduced matrix element.

$$\phi_{l',L'} = \frac{\delta_{SS'}}{[K]} \left| \langle l^n(\alpha L S) \| \sum_{i=1}^{N} T^K(i) \| l^{n-1}(\alpha'' L'' S''), l'; \alpha' L' S' \rangle \right|^2 \qquad (2\text{-}12)$$

In the closed-shell problem the N-electron reduced matrix element decomposes to provide

$$\phi_{l',L'} = \delta_{SS'} \frac{n}{[K]} \left| \langle l \| T^K \| l' \rangle \right|^2 \qquad (2\text{-}13)$$

For the one-electron reduced matrix to be non-zero, two conditions have to be fulfilled: (i) l, l' and K satisfy triangle conditions; and (ii) l + l' + K must be an even number. For the electric dipole operator (K = 1), these constraints afford the important selection rule $l' = l \pm 1$. This means that two channels are open to the continuum electron, save when an s electron is ionised. Furthermore, there are no restrictions as to the type of electron that can be ionised.

The two respective reduced matrix elements can be readily evaluated from standard formulae.[3] The relevant expressions are

$$\left| \langle l \| T^1 \| l+1 \rangle \right|^2 = \frac{l+1}{2l+1} R^2_{l+1} \qquad (2\text{-}14)$$

and

$$\left| \langle l \| T^1 \| l-1 \rangle \right|^2 = \frac{l}{2l+1} R^2_{l-1} \qquad (2\text{-}15)$$

The radial matrix elements are given by

$$R_{l\pm1} = \int_0^\infty P_l \, T \, P_{l\pm1} \, dr \qquad (2\text{-}16)$$

in the dipole-length form of the operator, and by

$$R_{l\pm1} = \int_0^\infty P_l \left(\frac{d}{dr} \pm \frac{2l+1\pm1}{2r} \right) P_{l\pm1}\, dr \qquad (2\text{-}17)$$

in the dipole-velocity form of the operator.

The total photoionisation cross-section for production of the ionic state (α"L"S") is obtained by summing over all values of l' and L'. For the closed-shell problem, L' can only take the value 1. Hence our expression is

$$\sigma_{tot} = n\bar{\sigma}_l \qquad (2\text{-}18)$$

where

$$\bar{\sigma}_l = \frac{4\pi^2\alpha C}{3}\left\{ |\langle l \| T^1 \| l-1 \rangle|^2 + |\langle l \| T^1 \| l+1 \rangle|^2 \right\} \qquad (2\text{-}19) \text{ a.u}$$

C = ω in the dipole-length approximation and C = ω^{-1} in the velocity approximation. $\bar{\sigma}_l$ is defined as the sub-shell photoionisation cross-section.

Our analysis has yielded the total photoionisation cross-section (this was because we averaged over all polarisations of the electric vector). It can be readily established, however, that the partial differential cross-section for a randomly orientated sample, subjected to unpolarised radiation, is given in the dipole approximation by[4]

$$\frac{d\sigma}{d\omega} = \frac{\sigma}{4\pi}\left[1 - \frac{\beta}{2}\left(\frac{3\cos^2\theta - 1}{2} \right) \right] \qquad (2\text{-}20)$$

represents the angle between the directions of photoelectron and incident photon propagation. β is the asymmetry parameter[5]; for single-channel photoionisation it is solely a function of l and l'. Intra-channel coupling,

however, has the effect of imposing a marked energy dependence on β.[5] The sub-shell photoionisation cross-section $\bar{\sigma}_l$ is invariant to channel mixing (a consequence of simple orthonormality rules).

The major difficulties encountered in theoretical studies on photoionisation are associated with the description of the radial part of the continuum wavefunction. The simplest but most drastic approximation is to assume that the continuum electron is unperturbed by the residual ion potential (the plane wave method). The radial wave-equation is then given by

$$P_{\epsilon l}(r) = kr\, j_l(kr) \qquad (2\text{-}21)$$

where k is the wave-vector of the electron and $j_l(kr)$ is a spherical Bessel function. The plane wave method appears to be fairly reasonable for fast electrons ($h > 1$ KeV) but has proved to be less than adequate for UV excited photons.

Within the Hartree-Fock framework the radial wave-equation is given by

$$\left[\frac{d^2}{dr^2} - \frac{l(l+1)}{r^2} - V(r) + k^2\right] P_{\epsilon l}(r) = -\sum_n \lambda_{\epsilon l, nl} P_{nl}(r) \qquad (2\text{-}22)\text{a.u}$$

where the function V (r) includes both the nuclear and electron exchange potentials; the Lagrange undetermined multipliers ensure that the continuum orbitals are orthogonal to bound orbitals with the same angular symmetry.

Although our discussion has been couched in terms of the LS coupling scheme, relativistic effects can be readily

included by recourse to Dirac-Fock theory.[6] (This topic is postponed until Chapter 7).

Moving outside the one-electron approximation, the wavefunctions for both the initial and final states can be systematically improved to include the effects of electron correlation by the technique of configuration interaction (CI). The exact wavefunction may be written as

$$|\Psi\rangle = \sum_k C_k |\phi_k\rangle$$

where the C_K are the expansion coefficients and $|\phi_K\rangle$ are anti-symmetrised N-electron wavefunctions, each specifying a distinct configuration. In principle, there is no restriction as to the types of wavefunction we can admix.

CI in the initial state (ISCI) is expected to be the prime contributor to the observed satellite peaks in the UV-PE spectra of Zn, Cd and Hg vapours.[7, 8] (See Chapter 7). CI in the final system (of ionic state plus continuum electron) is often referred to 'inter-channel coupling' (IC). Admixture of configurations to the final state in which all electrons are in bound orbitals (i.e. no continuum channels) gives rise to the phenomenon of autoionisation; this causes photoionisation cross-sections to be dominated at certain energies by resonances. Resonance structure however only tends to be important for $h\nu < 100eV$. Allowance in the final state wavefunction for configurations with two continuum electrons accounts for electron shake-off.

Another failing of the one-electron approximation is that it neglects electron relaxation; the one-electron orbitals have different spatial extensions in the initial

and final states of the system. The subsequent non-orthogonality of orbitals possessing the same value of l but having different primary quantum numbers presents severe technical problems in the computation of photoionisation matrix elements; it also implies that certain final states which are strictly inaccessible in the one-electron model may acquire considerable intensity.[9] No difficulties are encountered as far as energy separations are concerned; SCF calculations can be performed on both the initial and final ionic states of the system. It is customary to introduce the concept of "relaxation energy"; for a closed-shell system the relaxation energy for a particular sub-shell (ϵ^{i}_{relax}) is defined by

$$\epsilon^{i}_{relax} = (E^{T}_{init} - E^{T}_{ionic}) - \epsilon^{i} \qquad (2\text{-}23)$$

E^{T}_{init} and E^{T}_{ionic} are the total Dirac-Fock energies of the initial and final ionic states of the system respectively, and ϵ^{i} is the orbital energy of the ith subshell. The quantity in bracket is referred to as the "Δ SCF" energy.

The effects of electronic relaxation and correlation are intimately connected; indeed, many body perturbation theory (MBPT)[10, 11] does not distinguish between relaxation and CI as we have defined them here. With respect to theoretical calculations on PE cross-section profiles (that is, the cross-section plotted as a function of energy of the exciting radiation or of the kinetic energy of the photoelectron) and intensity distributions, it is customary to expand both initial and final states in terms of the same basis set in order to alleviate the non-orthogonality problem.

Within the HF approximation, this will result in only a slight loss of accuracy unless the electron being ionised derives from a tightly bound orbital (i.e. < 100eV). Even so, it is clear that HF calculations are not particularly reliable in providing detailed quantitative agreement with experimental PE cross-section profiles.[12] Better agreement is naturally afforded by enlargement of the basis set in order to allow for the effects of electron correlation; the R-matrix method[13, 14] represents such an approach. Although both CI methods and MBPT are capable of effecting detailed quantitative agreement with experimental data, they are usually expensive computationally and often permit little physical insight into the situation. The main drawback of CI methods is that they frequently employ "pseudo-orbitals" (orbitals introduced to expand the basis set and which have little physical significance); this situation is much aggravated if there is extensive electronic relaxation.

An approach which has attracted considerable attention for analysing relative PE intensity distributions arising from core-electron photoionisation (where the effects of electronic relaxation can be considerable) is the sudden approximation.[15-17] The ionisation process is considered to take place much more rapidly than the consequent relaxation of the electrons in the system and the dynamical interaction between the photoelectron and the residual ion is ignored. If $|\Psi_+\rangle$ is the (N-1) electron state of the unrelaxed ion, and differs from the ground state only by having an electron missing from a particular orbital, then it will not in general be an eigenstate of the Hamiltonian of the ion. If the proper eigenstates are labelled $|\Psi_1\rangle$, $|\Psi_2\rangle$ etc., then the state $|\Psi_+\rangle$ will relax

into $|\Psi_n\rangle$ with probability simply given by $|\langle\Psi_+|\Psi_n\rangle|^2$. For this probability to be non-zero, $|\Psi_+\rangle$ and $|\Psi_n\rangle$ must have the same symmetry (the monopole selection rule). Furthermore, application of the orbital approximation imposes the same selection rule on the shake-up from an occupied orbital $|m\rangle$ to an empty orbital $|n\rangle$; m and n' must possess the same azimuthal quantum number. The sudden approximation is discussed in more detail in Chapter 8.

2.3 Photoemission from Solids

Berglund and Spicer[18] have proposed the following three-step model for photoemission from solids.

Step 1: Excitation of an electron in some Bloch state $|\Psi_K^m\rangle$ with energy E_i, in the bulk of the solid, to the conduction band state $|\Psi_{K'}^n\rangle$ with energy $E_j = E_i + h\nu$ by absorption of a photon with energy $h\nu$. $\underline{K}$ and $\underline{K}'$ are the wavevectors of the bands n and m respectively. The velocity form of the matrix element for photoabsorption is given by[19,20]

$$\underline{P}(n,\underline{K}';m,\underline{K}) = \langle \Psi_{K'}^n | \exp(i\underline{q}\cdot\underline{r})\,\underline{\nabla}\,| \Psi_K^m\rangle \qquad (2\text{-}24)$$

The Bloch function Ψ_K^m is of the form

$$\Psi_K^m(\underline{r}) = N^{-1/2}\exp(i\underline{k}\cdot\underline{r})\,u_K^m(\underline{r}) \qquad (2\text{-}25)$$

N is the number of unit cells of volume Ω. Using the reduced zone scheme, equation (2-24) can be written

$$\underline{P}(n,\underline{K}';m,\underline{K}) = \delta_{K',K+q}\,N^{-1}\int_\Omega u_{K'}^{n*}\,\underline{\nabla}\,u_K^m\,d\tau \qquad (2\text{-}26)$$

which affords the important selection rule for a direct

transition:

$$\underline{K}' = \underline{K} + \underline{q} \qquad (2\text{-}27)$$

Again (see section 2.1) it is often safe to neglect $\underline{q}$, the wave-vector of the photon. It is also possible to have indirect transitions where $\underline{K}' \neq \underline{K} + \underline{q}$. In order that crystal momentum is conserved in an indirect transition, creation or annihilation of a phonon takes place. Only direct transitions tend to be important in PES.

The energy distribution (EDC) of primary photoemitted electrons (N_{int}) due to direct transitions can readily be established as[21]

$$N_{int}(E,h\nu) = C\sum_{n,m}\int_{BZ} |P_{nm}(\underline{k})|^2 \delta(E_j - E_i - h\nu)\delta(E-E_i)\, d^3\underline{k} \qquad (2\text{-}28)$$

C is a normalisation factor while BZ refers to the Brillouin zone. Hence N_{int} is proportional to the joint interband density of states (the convolution of the density of filled states (DOS) with the density of unoccupied conduction band states) modulated by the interband momentum matrix elements $P_{nm}(\underline{K})$. The summation over bands m and n is particularly important with respect to photoemission from the valence band where the DOS usually consists of several overlapping bands (partial density of states PDOS).

At photoelectron kinetic energies in excess of ca 30 eV, the conduction band is relatively unstructured.[21] As a consequence, N_{int} is simply given by the transition matrix modulated DOS. Below this energy, PE spectra will exhibit features characteristic of both the occupied and unoccupied DOS. The exact point at which the conduction

band becomes unstructured (E_{crit}) is particularly dependent on the actual compound and may in fact be less than 10 eV for oxides.

A more detailed analysis[21] of equation (2-28) indicates that providing the DOS is derived from only one type of atomic orbital, then for energies in excess of E_{crit}

$$N_{int} = C'p(E) \qquad (2\text{-}29)$$

that is the primary energy distribution (EDC) is directly proportional to the occupied density of states. This is substantiated by the often detailed agreement obtained between experimental valence region X-PE spectra from transition metals and the corresponding theoretical DOS curves.[22-24] In the case of transition metal oxides, the valence band consists of overlapping metal nd and oxygen 2p PDOS. The EDC is then expected to be given by[25]

$$N_{int} \simeq A\left[\rho_p(E)\sigma_p(h\nu) + \rho_d(E)\sigma_d(h\nu)\right] \qquad (2\text{-}30)$$

Here ρ_p and ρ_d are the photon-energy-independent oxygen 2p and metal nd PDOS respectively and σ_p and σ_d the corresponding $h\nu$ -dependent photoionisation cross-sections. Interference terms between the oxygen 2p and the metal nd orbitals are expected to be extremely small.[26] With X-ray excitation (e.g. Mg Kα, $h\nu$ = 1253.6eV), the metal nd photoionisation cross-section is considerably greater than the O 2p cross-section, with the result that the valence band PE spectra are dominated by the metal nd PDOS;[27] but the metal nd structure is much reduced in intensity, relative

to O 2p, in PE spectra excited with vacuum UV radiation (e.g. He-I, $h\nu$ = 21.2 eV). The intensity changes of the valence band PE spectra offer, in principle, a means of estimating the degree of covalency in the compound.

Step 2: Propagation of the excited electron to the surface of the material scattering of the electron may occur during transport as a result of electron-electron and electron-photon processes. For K.E in excess of 5 eV, the electron-electron interaction provides the dominant scattering mechanism. The photoelectron may suffer either elastic or inelastic collisions with an unexcited ground state electron in the valence band. The detection of elastically scattered (diffracted) electrons affords a novel method of surface structural analysis.[28] Inelastic scattering, on the other hand governs the mean escape depth of the photoelectron (i.e. the extent of attenuation). The mean escape depth is usually quite small, commonly less than 1 nm for UV excited photoelectrons but slightly greater (3 nm) for electrons with kinetic energies in excess of 1000 eV. Inelastic scattering produces an enhanced background intensity to lower K.E. This background represents a convolution of successive energy loss processes. For fast photoelectrons (E > 1000 eV), the Born approximation can be applied to the scattering event.[29] Subsequently it is possible to make a reasonable estimate of the secondary electron contribution to a PE spectrum and then remove it. The relevant procedure has been discussed in previous work.[29]

Step 3: Ejection from the solid into the vacuum. This involves surmounting the potential barrier at the surface; the main effect is to shift the spectrum uniformly towards lower K.E (see section 2.6).

Recently more rigorous theoretical approaches than the three-step model have been described,[30,31] but they do not drastically alter the physical description of the process as outlined above.

2.4 The fate of inner shell vacancies

Inner shell vacancies created via photoionisation can decay by either photon emission (X-ray fluorescence)[32] or secondary electron emission (the Auger effect).[33] Auger structure is invariably present in a PE spectrum (e.g. fig. 2-1 which shows a wide scan of $NiTiO_3$) but can be differentiated from genuine PE structure by the fact the K.E. of Auger electrons is independent of incident photon energy.

For light atoms, radiationless decay by the Auger process is usually more probable than X-ray emission, but the situation is reversed for heavier elements. The rate of deactivation of the core hole governs the natural line-width of an X-PE signal (the Uncertainty Principle). For light atoms, natural line-widths tend to be of the order of 0.1 to 0.2 eV, but for heavier elements they can be much larger.[21]

2.5 Photoionisation from Open-Shell Systems

(i) Atomic Systems

Even in the one-electron approximation, several ionic states may be accessible when an open shell system is photoionised. Let us consider initially the case of ionisation from a single open shell. If we return to equation (2-12) in section 2.2 we have

$$\sigma_{L',L'} = \delta_{SS'} \frac{4\pi^2 \alpha C}{3} \left| \langle l^n(\alpha LS) \| \sum_i^N T^1(i) \| l^{n-1}(\alpha'' L'' S''), l'; (\alpha' L' S') \rangle \right|^2$$

(2-31)a.u

where we retain the same definitions, except that the sub-shell l is now open. The total photoionisation cross-section for production of the ionic state ($\alpha''L''S''$) is obtained by summing over all values of l' and L'.

$$\sigma_{tot} = \sum_{l',L} \sigma_{l';L} \qquad (2\text{-}32)$$

Application of the standard techniques for evaluating matrix elements of one-particle operators yields[34,35]

$$\sigma_{tot} = \frac{4\pi^2 \alpha C}{3} n \left| \langle (\alpha L S) \{ (\alpha'' L'' S''), l \rangle \right|^2$$

$$\times \sum_{l',L} [l][L'] W^2(l' k L'' L; l L') \left| \langle l \| T^1 \| l' \rangle \right|^2 \qquad (2\text{-}33)a.u$$

The term $\langle (\alpha LS) \{ | (\alpha'' L'' S''), l \rangle$ represents the <u>coefficient of fractional parentage</u> (cfp). These coefficients have been conveniently tabulated for the most important atomic and molecular cases.[36, 37] The Racah coefficients have the useful orthonormality relationship

$$\sum_{L'} [l][L'] W^2(l' k L'' L; l L') = 1 \qquad (2\text{-}34)$$

Hence equation (2-33) now yields

$$\sigma_{tot} = \frac{4\pi^2 \alpha C}{3} n \left| \langle (\alpha L S) \{ | (\alpha'' L'' S''), l \rangle \right|^2$$

$$\times \left[\left| \langle l \| T^1 \| l+1 \rangle \right|^2 + \left| \langle l \| T^1 \| l-1 \rangle \right|^2 \right] \qquad (2\text{-}35)$$

The term in square brackets is the sub-shell photoionisation cross-section ($\bar{\sigma}_l$). Thus if we assume that the $\bar{\sigma}_l$ for

all ionic states ($\alpha''L''S''$) derived by ionisation from the initial state (αLS) is constant (this will hold when $h\nu$ is greatly in excess of the threshold ionisation energy) then this leads to the following rule: when an electron is removed from a unique open shell, final states appear with a probability proportional to the square of the respective coefficient of fractional parentage.

When the shell being ionised is but one of several open-shells in the system evaluation of the photoionisation cross-section is hampered by the increased complexity of the angular momentum recoupling coefficients. However, the case of two open shells is discussed in Chapter 7.

Finally, an important case frequently met in PES, is ionisation from a closed-shell of a system which has a single open shell. All possible states resulting from spin and orbital coupling of the hole with the open-shell are produced. The total intensity of ionised states with spin and orbital angular momenta (L_2S_2) is proportional to the spin-orbital degeneracy,[38]

$$\sum_{\alpha_2}(\alpha_2 L_2 S_2) = \frac{[S_2][L_2]}{[S_1][L_1]} \qquad (2\text{-}36)$$

where S_1 and L_1 refer to the angular momenta of the open shell in the initial state.

The form of this equation is intended to emphasize that more than one state (L_2S_2) may appear, in which case the total intensity given in equation (2-36) is shared between them.

(ii) Metals

In metallic systems, the positive hole created by photoionisation of a core orbital may interact with the mobile

conduction band. The main effect of this interaction is to produce asymmetry in the core-level PE signals.[23, 39, 40] Core-line asymmetries in the X-PE spectra of 4d and 5d transition metals have been shown[39] to be in quantitative agreement with the theoretical many-body lineshape function of Doniach and Sunjic[41]. The fact that, in transition metal oxides, it is only the metal core PE signals which possess asymmetry,[40, 42] is evidence of the local character of the many body interaction.

2.6 Calibration and charging effects

(i) Sample charging

Photoemission naturally implies the loss of electrons from the sample; in the case of solids, this can lead to the problem of sample charging. With respect to X-PES, the most adverse effect of sample charging is that it may be inhomogeneous and cause peaks to shift and broaden indiscriminately;[43] for UV-PES, it can leave one unable to record any spectrum at all.

The magnitude of the dynamic equilibrium charge on a PE sample depends on several factors. 'Holes' are produced at a constant rate by photoionisation processes, both primary and secondary, and are neutralised by two competing mechanisms: (i) conduction from the sample support; and (ii) capture of stray electrons from the vacuum system.[44, 45] Earthed conducting samples naturally take up electrons as required, thus preventing any charge build-up; however as the resistance between the sample surface and earth increases, the stray electron flux begins to play an increasingly important role, the emergent positive charge on the sample surface attracting slow electrons to the sample. One must be careful to

distinguish between the sources of stray electron flux that persist in a UV-PE or X-PE experiment. It has been shown[44,45] that in the case of X-PES, the major contribution of secondary flux arises from electrons streaming from the 'window' of the X-ray source. Under these conditions an insulating sample may acquire a potential of as much as +20V.[46] The absence of this stray electron source in UV-PES implies much more severe charging may occur.

Various techniques have been described in the literature to overcome the effects of sample charging when the sample is a non-conductor.[43] The most important ones are: (i) the use of a very thin sample which is in good contact with a conducting backing;[47] (ii) the quantitative application of electron 'flood' gun[46] (this tends not to be suitable for UV-PES where the photoelectrons have comparable energies to the slow (thermal) electrons from the gun); and (iii) the successive recording of rapid scans from freshly evaporated surfaces with extrapolation to zero time in order to counteract sample charging. (The UV-PE spectrum of crystalline NaCl has been recorded by this method).[48]

(ii) Calibration

Fig. 2-2 shows the energy level diagram for a conducting (metallic) sample in contact with an electron spectrometer. The binding energy (ϵ_F) of a core level is implicitly defined as the energy separation between that core level and the Fermi level (FL) of the sample. Consequently, we have the relationship

$$h\nu = T_s + \epsilon_F + e\phi_{sp} \qquad (2\text{-}37)$$

T_s is the measured K.E; and $e\phi_{sp}$ is the "spectrometer work

function". The Fermi level proves to be a convenient reference because a small number of electrons will have been transferred between any conducting sample and the spectrometer to make their Fermi levels coincident.

The FL is not, however, a fundamental reference point, in that calculations of the energies of electrons in solids are referred to the zero of potential within the solid: this zero is higher in energy than the FL by an amount known as the Fermi energy (E_F). It is important to distinguish Fermi energy and the work function of a material.[43] The work function $e\phi_{sa}$ is defined as the energy required to remove an electron from the Fermi level to a distance large compared with the interatomic spacing but small relative to the size of the crystal.[49] The potential energy of the electron after being so removed is the vacuum level (VL) of the surface concerned. The quantities $e\phi_{sa}$ and E_F are not necessarily identical because the work function includes not only a bulk term but also a surface term, which varies with the orientation and condition of the crystal surface.

It is convenient to define the work function ($e\phi_N$) of an insulator in precisely the same way (see Fig. 2.3). However, the precise position of the FL for an insulator is, in general, ill defined.

Various methods exist for the calibration of PE spectra.[43] Although this work is not particularly concerned with absolute spectral calibration, we have explored the feasibility of using the secondary emission edge as a means of calbrating He-I spectra. The essence of the method is to apply a potential bias to the end of the probe. Provided the sample is in good electrical contact with the probe, the whole spectrum should shift in a uniform manner in exact correspondence

with the magnitude and polarity of the applied potential.

Under normal running conditions, that is when the sample is earthed, the high binding energy (B.E) region of the spectrum, which is almost entirely due to secondary electron emission, is not observable due to the characteristics of the analyser transmission function (see section 3.3). Application of a negative potential (of magnitude ϕ_{bias}) shifts the secondary electron energy distribution (SEED) to higher K.E. This enables one to observe the step in PE flux associated with the onset of SEED; this step represents the true zero of the sample K.E scale. Fig. 2.4, which portrays the effects of probe biassing on a metallic sample, indicates how the respective energy parameters defined in Figs. 2.2 and 2.3 may be calculated.

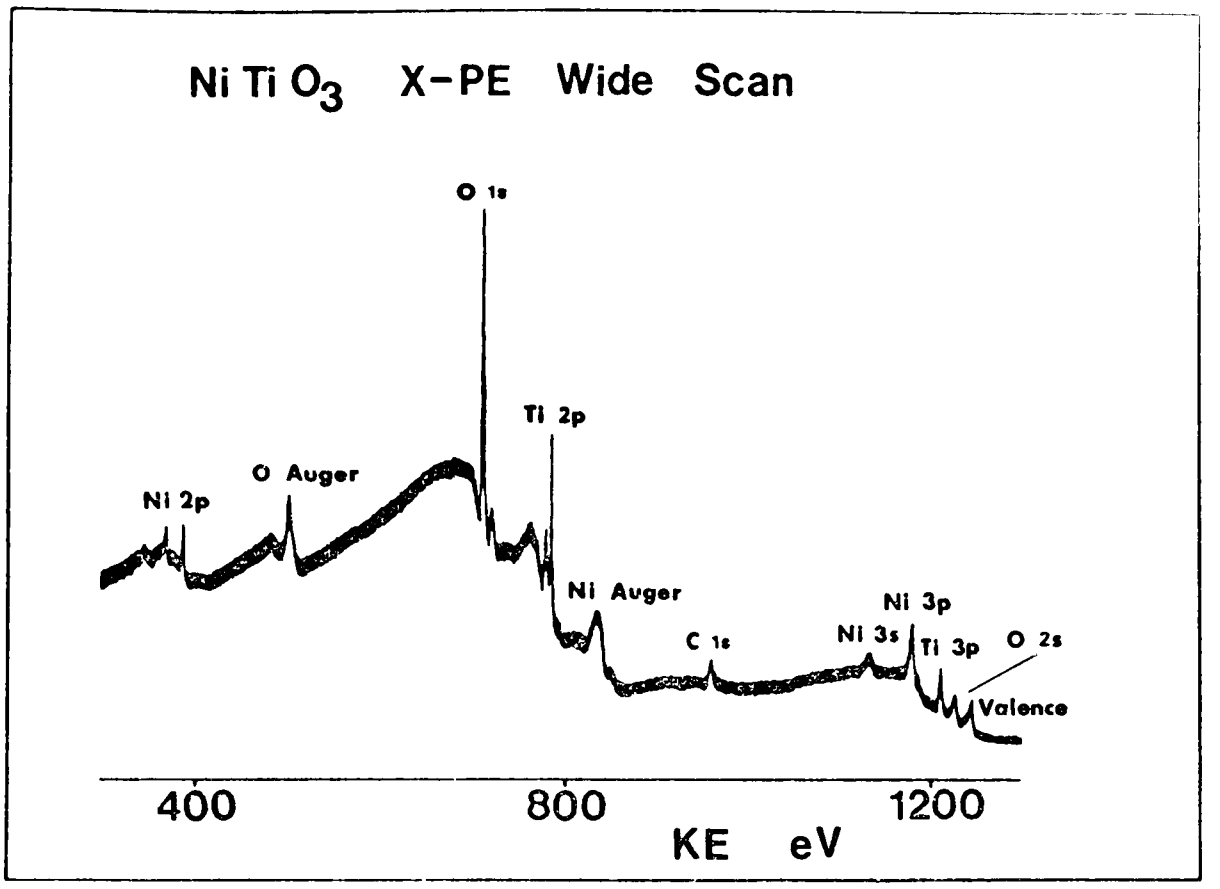


Fig. 2.1 Wide scan PE spectrum of $NiTiO_3$

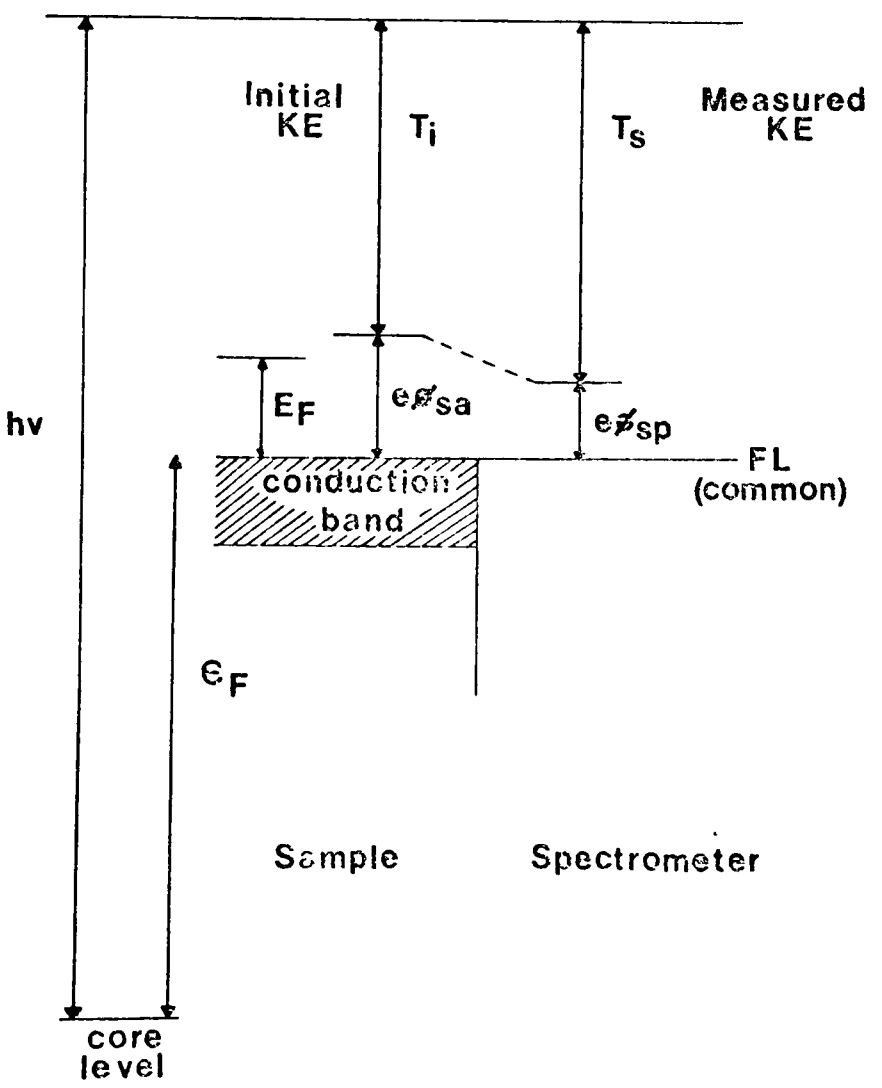


Fig. 2.2 Energy level scheme for a conducting (metallic) sample in electrical equilibrium with the spectrometer. Because ϕ_{sp}, as drawn, is less than ϕ_{sa}, photoelectrons are accelerated into the analyser by the contact potential difference ($\phi_{sa} - \phi_{sp}$) existing between the sample and the entrance slit of the analyser.

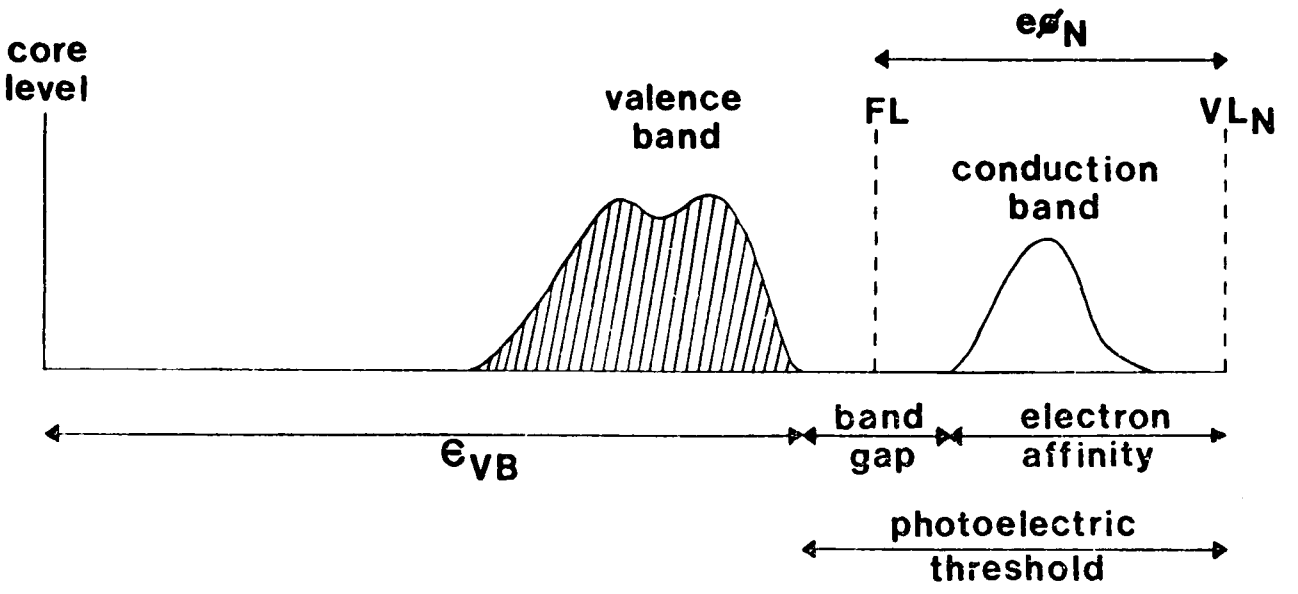


Fig. 2.3 Theoretical energy level scheme for a typical insulator, defining observable photoemission parameters

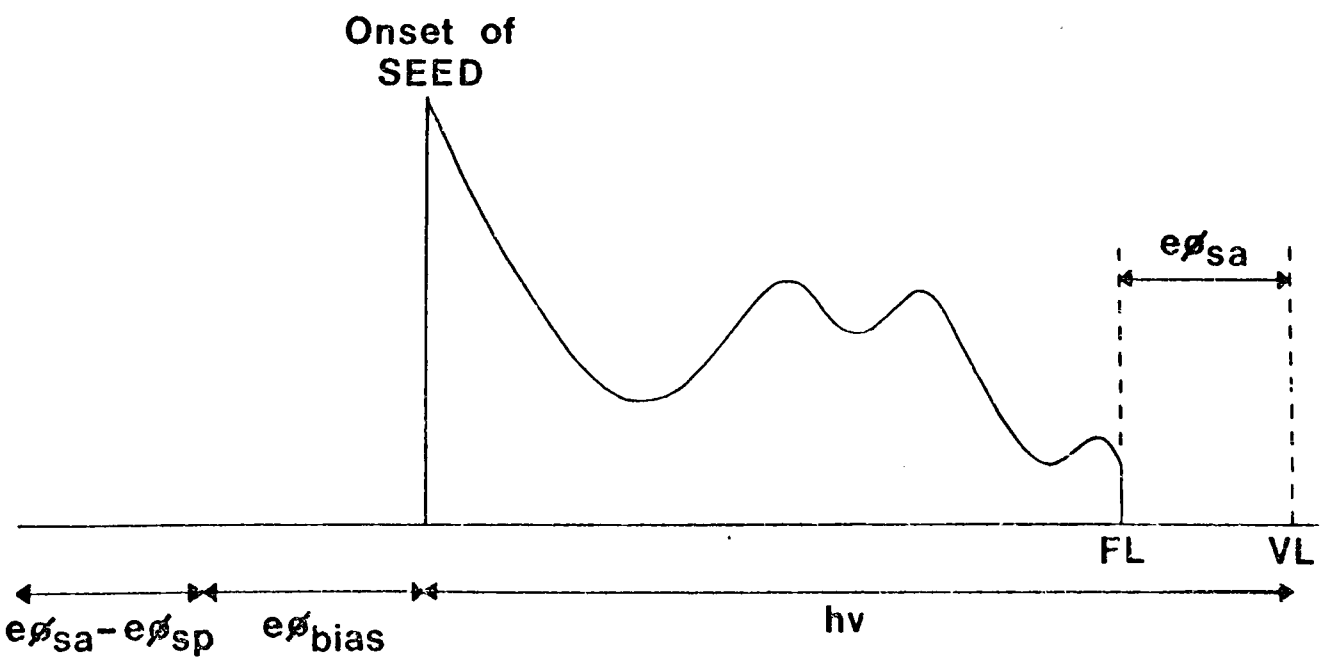


Fig. 2.4 Diagram illustrating the principle behind a probe biassing experiment on a metallic sample

REFERENCES FOR CHAPTER 2

1. P. G. Burke, p. 61 in "Photoelectron Emission: proceedings of the Daresbury Study Weekend, 6-7 March 1976" ed. I. H. Munro, G. V. Marr (1976) Science Research Council Publication DL/SRF/R8.
2. I. P. Grant, J. Phys. B7 (1974) 1458.
3. D. R. Brink, G. R. Satchler, "Angular Momentum" (1968), Oxford University Press, 2nd edition.
4. C. N. Yang, Phys. Rev. 74 (1948) 764.
5. G. V. Marr, p. 81 in "Photoelectron Emission: proceedings of the Daresbury Study Weekend, 6-7 March 1976" ed. I. H. Munro, G. V. Marr (1976) Science Research Council Publication DL/SRF/R8.
6. I. P. Grant, Adv. Physics 19 (1970) 747.
7. J. Berkowitz, J. L. Dehmer, Y.-K. Kim, J. P. Desclaux, J. Chem. Phys. 61 (1974) 2556.
8. N. S. Hush, S. Süzer, Chem. Phys. Lett. 46 (1977) 411.
9. R. L. Martin, D. A. Shirley, p. 75 in "Electron Spectroscopy: Theory, Techniques and Applications Vol. 1" (1977) Academic Press.
10. M. Ya. Amus'ya, N. A. Cherepkov, L. V. Chernyskeva, Soviet Physics JETP 33 (1971) 90.
11. M. Ohno, G. Wendin, Physica Scripta. 16 (1977) 299.
12. D. J. Kennedy, S. T. Manson, Phys. Rev. A5 (1972) 227.
13. P. G. Burke, W. D. Robb, Adv. in Atom. Molec. Phys. 11 (1975) 143.
14. P. G. Burke, K. T. Taylor, J. Phys. B8 (1975) 2620.
15. R. Manne, T. Åberg, Chem. Phys. Lett. 7 (1970) 282.
16. C. S. Fadley, J. Elect. Spec. 5 (1974) 895.

17. M. Mehta, C. S. Fadley, P. S. Bagus, Chem. Phys. Lett. 37 (1976) 454.

18. C. N. Berguind, W. E. Spicer, Phys. Rev. A136 (1964) 1030.

19. C. Kittel, "Quantum Theory of Solids" (1963), John Wiley & Sons, Inc.

20. W. Jones, N. H. March, "Theoretical Solid State Physics" Vols I + II (1973) Wiley-Interscience.

21. D. E. Eastman, p. 487 in "Electron Spectroscopy" ed. D. A. Shirley (1972) North-Holland.

22. N. V. Smith, G. K. Wertheim, S. Hüfner, M. M. Traum, Phys. Rev. B10 (1974) 3197.

23. A. Barrie, N. E. Christensen, Phys. Rev. B14 (1976) 2442.

24. R. J. Baird, L. F. Wagner, C. S. Fadley, Phys. Rev. Lett. 37 (1976).

25. D. E. Eastman, J. L. Freeouf, Phys. Rev. Lett. 34 (1975) 395.

26. W. Braun, A. Goldmann, M. Cardona, Phys. Rev. B10 (1974).

27. G. K. Wertheim, L. F. Mattheiss, M. Campagna, T. G. Pearsell, Phys. Rev. Lett. 32 (1974) 997.

28. J. M. Adams, S. Evans, J. M. Thomas, Chem. Comm. (1978) in press.

29. N. Beatham, Chemistry Part II Thesis, Oxford (1975).

30. C. Caroli, D. Lederer-Rozenblatt, B. Roulet, D. Saint-James, Phys. Rev. B8 (1973) 4552.

31. J. B. Pendry, Surf. Sci. 57 (1976) 679.

32. J. H. Scofield, p. 265 in "Atomic Inner-Shell Processes" Vol. I (1975) Academic Press.

33. E. J. McCruire, p. 293 in "Atomic Inner-Shell Processes" Vol. I (1975) Academic Press.

34. W. D. Robb, Comput. Phys. Commun. 6 (1973) 132.

35. N. C. Pyper, I. P. Grant, N. Beatham, Comput. Phys. Commun. (1978) to be published.

36. C. W. Nielson, G. F. Koster, "Spectroscopic coefficients for p^n, d^n and f^n configurations" Cambridge, Mass. (1963) M.I.T. Press.

37. J. S. Griffith, "Theory of transition and ions" (1964) Cambridge University Press.

38. P. A. Cox, Structure and Bonding 24 (1975) 59.

39. S. Hüfner, G. K. Wertheim, Phys. Rev. B11 (1974) 678.

40. M. Campagna, G. K. Wertheim, H. R. Shanks, F. Zumsteg, E. Banks, Phys. Rev. Lett. 34 (1975) 738.

41. S. Doniach, M. Sunjic, J. Phys. C3 (1970) 285.

42. J. Riga, C. Tenret-Noël, J. J. Pireaux, R. Caudano, J. J. Verbist, Y. Gobillon, Physica Scripta 16 (1977) 351.

43. S. Evans, p 121 in "Handbook of X-Ray and Ultraviolet Photoelectron Spectroscopy" ed. D. Briggs (1977) Heyden.

44. M. F. Ebel, H. Ebel, J. Elect. Spec. 3 (1974) 169.

45. J. F. McGilp, I. G. Main, J. Elect. Spec. 6 (1975) 397.

46. D. A. Huchital, R. T. McKeon, App. Phys. Lett. 20 (1972) 158.

47. J. A. Connor, M. Considine, I. H. Hillier, D. Briggs, J. Elect. Spec. 12 (1977) 143.

48. R. T. Poole, J. G. Jenkin, J. Liesegang, R. C. G. Leckey, Phys. Rev. B11 (1975) 5179.

49. N. D. Lang, Solid State Phys. 28 (1973) 225.

CHAPTER THREE

INSTRUMENTAL AND EXPERIMENTAL PROCEDURES

3.1 Sample Preparation and characterisation

3.2 The photoelectron spectrometer

3.3 The presentation of PE spectra

3.4 Computing facilities

3.1 Sample Preparation and Characterisation

NiO, ZnO, Cr_2O_3, Fe_2O_3, MnO_2, Nb_2O_5, MoO_3, WO_3, $Rh_2O_3 \cdot 5H_2O$ and $IrO_2 \cdot 5H_2O$ and $IrO_2 \cdot 2H_2O$ ("Specpure" grade) were obtained from Johnson-Matthey Chemicals Ltd. RuO_2 and CdO (both at least 99.9% pure) were purchased from Koch-Light Laboratories Ltd. Samples of VO_2 and V_2O_3 came from Ventron Alpha products.

The sample of $IrO_2 \cdot 2H_2O$ was initially found to contain small traces of sodium. This was indicated by the presence of Na KLL Auger signals in the X-PE spectrum (the Auger technique being particularly sensitive to Na). The sodium (presumably in the form of NaOH) had no doubt resulted from the preparative method[1] which entails the addition of alkali to a boiling solution of $IrCl_6^{2-}$. The Na KLL Auger signal could be removed from the X-PE spectrum by thorough washing with concentrated HNO_3 and then drying in vacuo[1].

The sample of VO_2 was characterised as $VO_2 \cdot yH_2O$ ($y \leqslant 0.04$)[2] by means of X-ray diffraction.

α-Mn_2O_3 was prepared by heating MnO_2 in air at ca. 1070K for 8 days[3]. $CaMnO_3$ was made by firing $CaCO_3$ and Mn_3O_4 (both Johnson-Matthey) in air at ca. 1250K for 3 weeks[4] (with 3 intermediate regrinds). Both compounds were characterised by the weight change during the reaction and by X-ray diffraction[3,5,6]. As a further check, four of the Mn-containing materials used in this work (Mn_3O_4, Mn_2O_3, MnO_2 and $CaMnO_3$) were analysed volumetrically by dissolving them in acid in the presence of excess I^-, followed by titration of the liberated iodine with standard thiosulphate solution. The respective stoichiometrics obtained were $MnO_{1.34 \pm 0.01}$, $MnO_{1.51 \pm 0.01}$, $MnO_{1.99 \pm 0.01}$ and

$CaMnO_{2.97\pm0.01}$.

$YMnO_3$ was prepared by dissolving high purity Mn (99.98%) and Y_2O_3 (99.97%) (both supplied by Koch-Light Laboratories Ltd.) in conc. HNO_3, evaporating the solution to dryness and then firing the mixed nitrate in air at ca. 1440K for 3 days[7]. $YbMnO_3$ (provided by I. L. Fragala) was prepared in similar fashion using 99.9% Yb_2O_3 (Rare Earth Products Ltd.). $YFeO_3$ was prepared from the corresponding ferricyanide[4,8]. A saturated solution of 'Analar' potassium ferricyanide was added to an equivalent quantity of warm neutral chloride solution prepared by dissolving Y_2O_3 in HCl. The precipitate was dried, heated to 870K and then fired in air for four days at 1470K. $YCrO_3$ (supplied by I. L. Fragala) was made by firing an equimolar mixture of Y_2O_3 and Cr_2O_3 in air at ca. 1670K for five days (with two intermediate regrinds). All four materials ($YMnO_3$, $YbMnO_3$, $YFeO_3$ and $YCrO_3$) gave diffraction patterns in essential agreement with the literature[9-11]. Volumetric analysis was precluded however by incomplete solubility of the samples in aqueous acid.

Ti_2O_3 (provided by Prof. C. N. R. Rao) was prepared by arc melting the correct stoichiometric mixture of Ti + TiO_2,[12] NbO_2 (supplied by P. G. Dunn) was made by hydrogen reduction of Nb_2O_5 at ca. 1300K for 24 hrs, and determined to be $NbO_{2.00}$ by means of thermogravimetric analysis. MoO_2 (provided by J. J. Birtill) was obtained by reduction of 'Analar' MoO_3 at 820K in a H_2/H_2O atmosphere (P_{H_2} = 25.8 torr, P_{H_2O} = 2.4 torr) over 4 days. The H_2/H_2O ratio used was that which renders MoO_2 the thermodynamically favoured product. WO_2 (supplied

by D. Palmer) was analogously prepared by reduction of WO_3 at ca 1020K under H_2/H_2O. Both dioxides were confirmed to be $MO_{2.00}$ by volumetric analysis[13] and X-ray diffraction[14] and, in the case of WO_2, this was further substantiated by thermogravimetric analysis.

Mo_4O_{11} (again provided by J. J. Birtill) was prepared by a sealed silica tube reaction at ca. 990K between α-Inorganics MoO_2 and Analar MoO_3 (with no temperature gradient)[15]. $W_{18}O_{49}$ (supplied by P. Wiseman) was similarly made by a sealed tube reaction between W and WO_3 at ca 1270K. In both cases the reactions were quenched by immersion in water. The stoichiometrics were determined by the standard techniques already mentioned, the sample of Mo_4O_{11} being established as $MoO_{2.741\pm0.002}$ (corresponding to 98.9% Mo_4O_{11}, 1.1% MoO_2).

The transition metal titanates ($MnTiO_3$, $FeTiO_3$, $CoTiO_3$, $NiTiO_3$) were provided by Mrs G. S. Bindaar. $MnTiO_3$ was made by heating together TiO_2 and MnO (prepared from Mn_3O_4 by hydrogen reduction at 1270K for 24 hours) in a horizontal furnace at 1220K for 12 hours under an atmosphere of CO_2. The product was then ground, made into a pellet and reheated at 1420K in CO_2 for 36 hours (using an alumina crucible).[16] $FeTiO_3$ was prepared by heating an intimate mixture of Fe_2O_3, Fe and TiO_2 (in the correct stoichiometric proportions) for 24 hours in an evacuated silica tube[17]. $CoTiO_3$ was made by firing $CoCO_3$ and TiO_2 in a platinum crucible in air at 1520 K for 32 hours with an intermediate regrind and pelletisation. Similarly $NiTiO_3$ was prepared from NiO and TiO_2 at ca 1570K.[16] The diffraction patterns of the materials were in essential agreement with the literature.[18-20]

In all cases, the X-PE spectra provided an additional check on the integrity of the samples.

3.2 The Photoelectron Spectrometer

The basic spectrometer used to measure all the PE spectra reported in this thesis is an AEI ES200B instrument. During the course of the work, the machine was updated by the successive additions of a sample pretreatment chamber and UV discharge lamp, respectively.

The general principle of operation of the spectrometer is illustrated in Fig. 3-1. The solid sample is irradiated by one of the two photon sources (X-ray gun or gas discharge lamp). The photoelectrons emitted pass through a slit into an electrostatic lens system, which retards them to respectively $^1/20$ or $\frac{1}{4}$ of their initial K.E, according to whether photoionisation is by X-ray or UV radiation. From the lens the electrons enter a 10" diameter double-focussing hemispherical analyser, which is screened from stray magnetic fields by a mu-metal shield. Those electrons possessing energies in the range ΔE pass through an adjustable collector slit to strike a channel electron multiplier ("channeltron") which generates one charge pulse per incident electron. The output from the multiplier is amplified and can then be plotted out on a X-Y pen recorder (the X-axis drive of the recorder being coupled to the scan unit of the spectrometer which sweeps the deflecting potential between the two hemispheres of the analyser). An additional option is that pulses may also be counted over given time intervals, and the results punched out onto paper tape.

The extreme surface sensitivity of PES necessitates UHV conditions ($\leqslant 10^{-9}$ torr) to avoid recontamination of a clean

sample surface. The main pumping is provided by an Edwards EO4 oil diffusion pump, in addition to which there is a Vacuum Generators titanium sublimation pump for occasional refinement of the vacuum conditions. The X-ray source and analyser are both separately pumped by 3 inch AEI Metrovac oil diffusion pumps. All oil diffusion pumps on the machine employ low vapour pressure polyphenylether oil and have attached liquid nitrogen traps to improve the pumping speed and ultimate vacuum performance; the backing always being provided by an Edwards ED50 rotary pump.

The complete vacuum system is constructed from machined stainless steel to allow it to be "baked" (i.e. degassing of volatile materials from the spectrometer walls) at ca 450K. Routine baking is essential if UHV conditions are to be maintained.

In addition to the two photon sources, the ionisation chamber holds an observation port, leak valve and a Vacuum Generators Q7 quadrupole mass spectrometer for residual gas analysis. Pressure measurements in the vacuum system were made variously by thermocouple, pirani and ionisation gauges. The principal pressure was measured using a V.G. VIG10 ionisation gauge.

The X-rays are generated by accelerating electrons, emitted from a hot tungsten filament, onto a water-cooled magnesium anode (see Fig. 3-2). The X-ray gun is usually operated at 228 watts, an electron current of 19mA being accelerated through 12 KV. The resulting achromatic Mg Kα radiation then emerges through an 0.08mm thick aluminium window, which prevents most of the secondary electrons produced at the magnesium target

from striking the sample.

UV radiation is produced in a windowless noble gas discharge lamp of the cold cathode type (see Fig. 3-3). The majority of UV spectra were recorded using a helium discharge (i.e. He-I and He-II) although occasionally it proved profitable to record Ne-I and Ne-II spectra. The helium passes from a cylinder through a liquid nitrogen trap, which removes impurities such as water, and into the discharge region. The gas is prevented from entering the ionisation chamber by efficient differential pumping of the lamp; the first stage is provided by an Edwards ED50 rotary pump and the second by an Edwards E02 oil diffusion pump.

In a helium discharge both He-I and He-II radiation are present, although under normal conditions He-II is a very minor component. The He-II photon flux can however be greatly enhanced by reducing the gas pressure in the lamp. In order to record He-I spectra, the operating pressure was routinely maintained at 0.05 torr, with a corresponding discharge voltage of 500V. The operation of the lamp in the He-II mode necessitates a compromise between photon flux and lamp stability. This is because the lower the operating pressure, the higher the amount of He-II radiation produced, but also the greater will be the risk that the lamp will extinguish. The exact conditions used for the measurement of the He-II spectra were dependent on many factors (e.g. state of the lamp, position of the cathode) although customarily the operating pressure was between 15 and 20 mtorr and the discharge voltage at about 600V.

In contrast to the standard AEI arrangement[21], the UV source is positioned at the front of the target chamber,

directly opposite to the X-ray source, and is inclined such that the UV photons are directed at an angle of about 135° to the X-ray beam. The photoelectrons produced in UV-PES characteristically have much lower K.E than in X-PES and as such are much more susceptible to deflection by stray magnetic fields. Consequently, with the advent of the UV lamp it proved essential to ensure the electrostatic lens and intermediate surroundings were completely demagnetised.

The sample. in the form of a powder, is contained in a specially constructed platinum tray fastened to the end of a rotatable (and translatable) Vacuum Generators P8 probe assembly. The rotation facility allows sequential measurement of UV and X-ray PE spectra: the translation mechanism, a retractable 18" bellows assembly, permits various kinds of sample treatment in a UHV chamber connected with, but isolable from, the main chamber. This preparation chamber (constructed by V.G. Scientific Ltd. according to a design conceived in this laboratory) is separately pumped by means of an Edwards E04 oil diffusion pump and this enables a high vacuum to be maintained inside the ionisation chamber while the sample is changed (see Fig. 3-4). The preparation chamber is normally pumped down to a pressure of the order of 10^{-8}torr before the isolation valve is opened and the probe introduced into the ionisation chamber. Facilities attached to the treatment chamber are as follows: (i) an RF coil for heating samples either <u>in vacuo</u> or under a variable pressure of suitable gases, (ii) a PHI 1 KV argon ion gun, which may be used to clean metallic surfaces, (iii) an observation port, (iv) a gold evaporator, (v) a general

sample manipulator (see Fig. 3-4).

Sample cleaning can be achieved by one of two methods. The probe itself contains a resistance-wound heater capable of providing a sample temperature of ca 870K. The temperature can be measured using a NiCr/NiAl thermocouple at the probe tip, which is capable of reading in the range 70-870K (the lower end of the scale being necessary as a liquid nitrogen cooling facility is available). In order to reach higher temperatures the RF coil must be used. This is connected to a 5 kW radiofrequency generator by means of a special lead-through (Ultek Ltd.). A 3" bellows assembly separates this lead-through from the chamber and enables the coil to be moved in and out of the translational axis of the probe. The platinum sample holder acts as the RF susceptor. The maximum temperature achieved using the coil depends on many factors but in excess of 1500K may be obtained in vacuum; however this temperature is lowered when heating in a gaseous atmosphere (e.g. 1000K for hydrogen). The gas used is passed through a molecular sieve (activated Al_2O_3) to remove any water present, and then through a leak valve (Varian Ltd.) into the preparation chamber.

It is only possible to estimate the temperature of the sample during heating in the RF coil. This is because (i) it is impossible to ensure absolutely uniform heating because normally it is the platinum and not the sample which is the receptor and this material nearer the edge of the tray will tend to be at a higher temperature; (ii) only temperatures up to 870K may be read on the thermocouple and even then there may well be a considerable temperature gradient between the sample and the thermocouple; and (iii) above 870K the

temperature can only be estimated by means of an optical pyrometer.

The essential aim in any sample treatment procedure is to reproduce the standard preparative conditions, the spectra then being recorded without the danger of surface recontamination. Under normal conditions, H_2O and CO_2 are expected to be incorporated by oxide surfaces. These can both be removed by heating but one must also ensure that no sample degradation or change in oxidation state occurs. In order to achieve this, extreme caution is necessary. For most of the samples studied in this work, we have been guided by both thermodynamic considerations and whether the PE spectra themselves are compatible with the known physical properties of the material. An example of the need for surface cleaning is provided by Fig. 3-5, which shows the effects on the UV and X-ray PE spectra of $FeTiO_3$. UV-PES is much more surface-sensitive than X-PES, and it is clear from Fig. 3-5, that under normal conditions any oxide UV-PE spectrum may well be completely unrepresentative of the material under investigation.

The effectiveness of *in situ* heating can often be gauged by the nature of the O 1s signal; this usually tends to become sharper and more symmetric after sample cleaning. For the majority of compounds studied in this work, clean O 1s signals could be obtained although for a few (e.g. RuO_2, CdO) this proved impossible. However, it should be pointed out that a symmetric O 1s signal is in itself no guarantee of surface integrity, as witnessed by the fact that all V and Mo oxides gave clean O 1s spectra even when it was clear from

the UV-PE spectra that there was still some surface contamination (vide infra).

The general methodology adopted was to heat the samples for approximately 2-3 hours. It was generally found that if a clean O 1s signal could not be obtained within this period, then it was unwise to continue heating. The reasons for this are essentially that (i) for all the cases where prolonged heating was investigated, there was little or no further affect on the shpae of the O 1s signal; (ii) during prolonged heating one runs the very serious risk of diffusion of impurities to the surface[22] (indeed for the sample of CdO traces of sulphur became apparent if heating was prolonged beyond 2 hours); (iii) the platinum tray (which measures 2.5 cm x 0.2 cm x 0.6 cm with an 0.1 cm well) has a very thin sliver of platinum at the sides which may become more exposed if there is sintering of the sample.

Whereas the UV photon beam is extremely well focussed (a circle of diameter 0.1 cm) and there is no danger of picking up any extraneous signal from the edge of the tray, the X-ray beam covers a much larger area and does strike the edges if the tray is not completely full. (The exact region exposed to the X-ray flux could be conveniently determined by utilising the fact that KCl turns purple when exposed to X-radiation). In the majority of cases, only a small trace (if any) of Pt could be detected. However, for a few samples (notably Ti_2O_3 and VO_2), an unacceptably high Pt signal was detected, mainly as a consequence of the fine nature of the material which prevented complete packing of the tray. The main problem is that the presence of Pt signals will affect the valence region X-PE spectrum; however, the shape and

intensity of the Pt valence band is well established, and may readily be subtracted out given a knowledge of the intensity of the Pt 4f signals.

It may be argued that, in order to circumvent this problem, either the platinum tray could have been enlarged, the X-ray source more effectively focussed or a pressed pellet used instead of the tray. However, barring complete redesign of the instrument, enlargement of the tray would prohibit rotation of the probe whilst the only way to produce finer focussing of the X-rays would be by recourse to a smaller X-ray window which would then reduce the X-ray flux to an unacceptably low level. Pelletisation of the sample would severely increase the probability of surface contamination.

3.3 The presentation of PE spectra

The facility for being able to record all PE spectra on both the X-Y pen recorder and on paper tape provides the opportunity to present the spectra either in their original form or by means of the Oxford computer graph plotter. The more satisfying approach is clearly to present the original spectra. However there are times when it is advantageous to make use of the data processing facilities afforded by the computer plotter.

For He-I and X-radiation the count rate was both sufficiently high and stable enough to realise good quality spectra in a single 2 to 3 hour scan. This was not the case when using He-II excitation where the count rates were frequently as low as of 15 counts/sec, a consequence of giving

preference to lamp stability over optimisation of photon flux. This sacrifice in count rate meant that characteristically four or five 3 hour scans (the slowest rate available on the instrument) were needed to ensure a satisfactory signal to noise ratio. In this case it was obligatory to use the computer to build up the spectrum.

As one frequently wishes to make direct comparison between He-I and He-II PE spectra it was felt desirable to present both spectra together by means of the computer plotter. An error bar is shown on the He-II spectra to provide an estimate of the signal-to-noise ratio of the integrated spectrum.

Having the data in digitised form enables PE spectra to be readily processed. All valence region X-PE spectra were routinely corrected for the effects of secondary electron emission and then deconvoluted by the Fourier Transform technique; the principles involved in each case are described in previous work.[23. 24] However, deconvoluted spectra are presented only in cases where they are particularly informative. For UV-PE spectra, the effects of analyser transmission function and secondary electron emission begin to assume major importance.

The transmission function of the hemispherical ES200B analyser was determined by a probe-biassing experiment on the He-I photoemission from a sample of clean metallic gold, with the angle $\theta = 0^{o}$ (vide infra, chapter 4). Assuming that the inherent intensity of a PE signal does not change with the bias applied to the sample, the analyser transmission function is given by the variation in the height of a given peak, after allowance for the effects of inelastic electron scattering, as the energy of the corresponding photoelectron changes. The

results of the experiment are shown in Fig. 3-6, where the data points represent heights of the most intense peak in the gold spectrum (in arbitary units). It can be seen that this function is effectively linear in the K.E above about 15eV, but that there is a marked fall-off below this energy. Similar behaviour appears to be characteristic of most deflection analysers,[25] and indeed an analogous relationship was found for the same analyser in the X-ray mode.[23]

With regard to secondary electron emission in UV-PES, the fact that one is dealing with relatively slow electrons, means that the Born approximation cannot be expected to apply to the electron-electron scattering event; and also that electron-phonon scattering assumes importance. These two factors make theoretical analysis difficult.[23, 26, 27] The empirical observation, however, is that there is usually a smooth but steeply rising background to lower K.E, assuming of course, a constant analyser transmission function.

The effects of both analyser transmittance and secondary electron emission can be gauged from Fig. 3-7, which shows the variation in the He-I spectrum of CdO with applied bias. The Cd 4d signal (labelled as peak a) can only be directly observed if a negative potential is applied to the sample.

To some extent the secondary electron and analyser transmission effects tend to cancel; and for this reason we thought it best to present the spectra in their original form. In view of the difficulties in accurately estimating each term, this is more satisfactory than the increasingly adopted practice of presenting only corrected UV-PE spectra.[28]

3.4 Computing Facilities

All the computer programmes employed in this thesis were coded in Fortran. With the exception of the MCDF suite of programmes, all computing was performed on the Oxford University ICL 1906A. The MCDF work was performed on the Science Research Council IBM 370/195 computer at the Rutherford Laboratory, Chilton. This was accessed via the remote job entry terminal in the Department of Nuclear Physics. A description of all computer programmes used in this thesis is provided in Appendix 2.

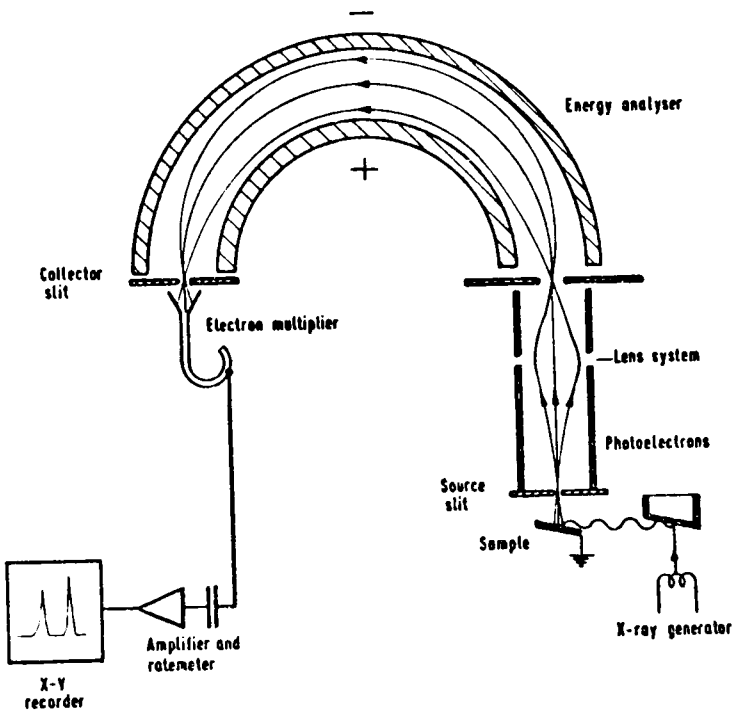


Fig. 3.1. Principle of operation of X-ray PE spectrometer

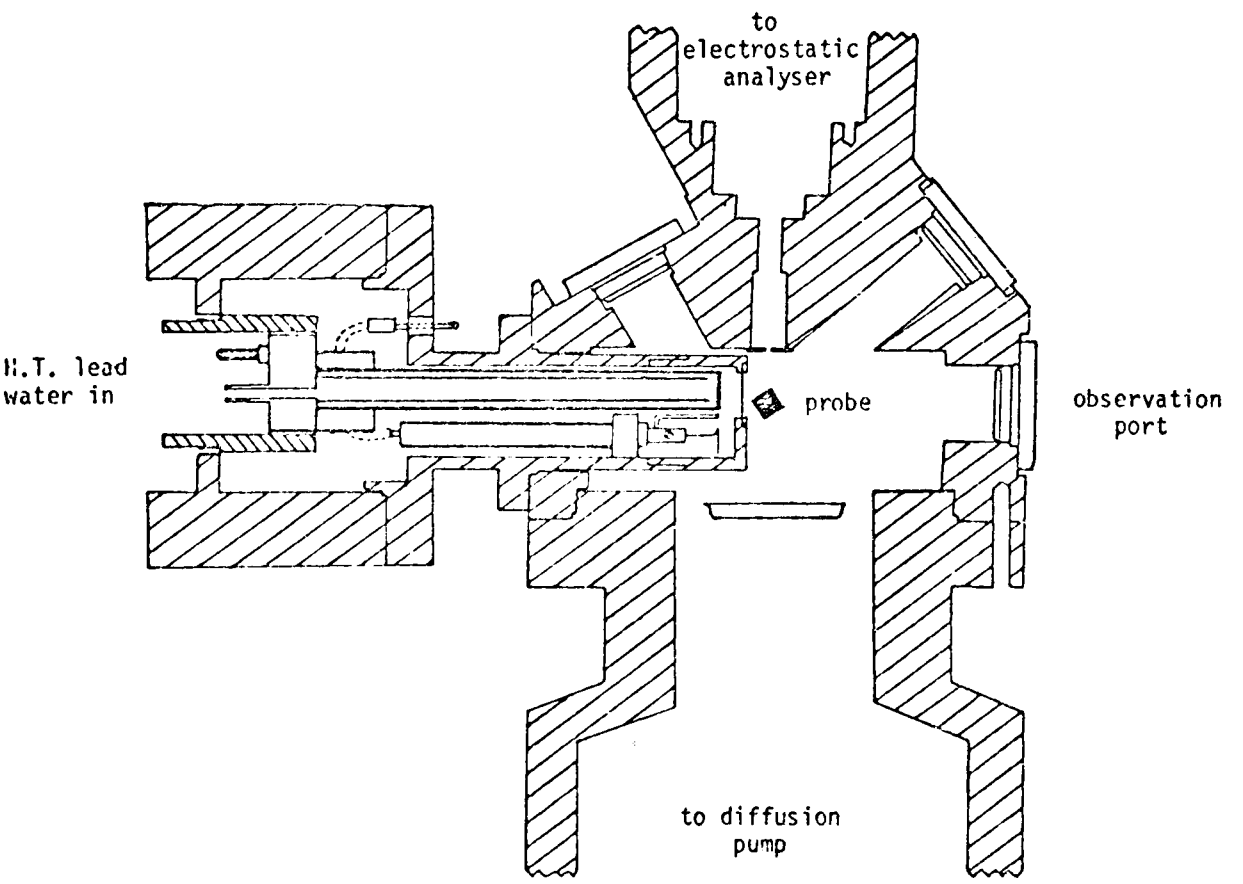


Fig. 3.2. Schematic diagram of the ES200B (before addition of UV lamp).

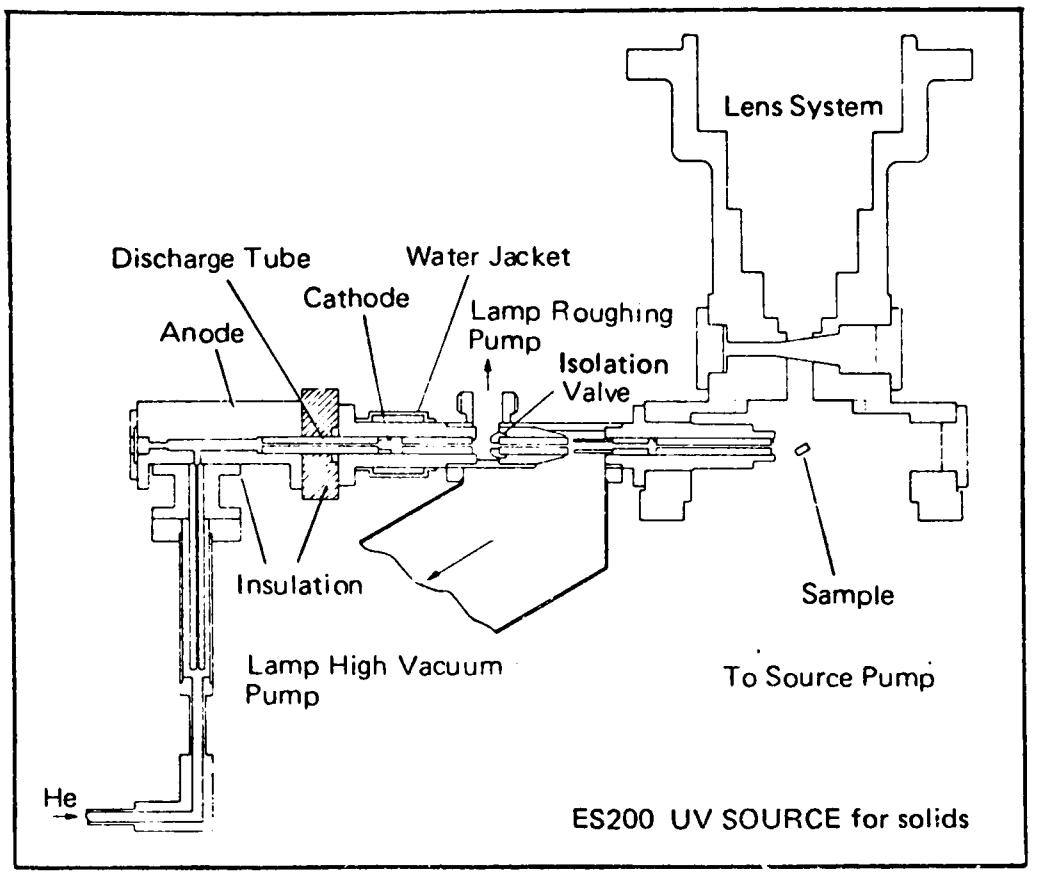


Fig. 3.3. The ES200 UV source (the lamp is shown as it would be in the standard AEI arrangement).

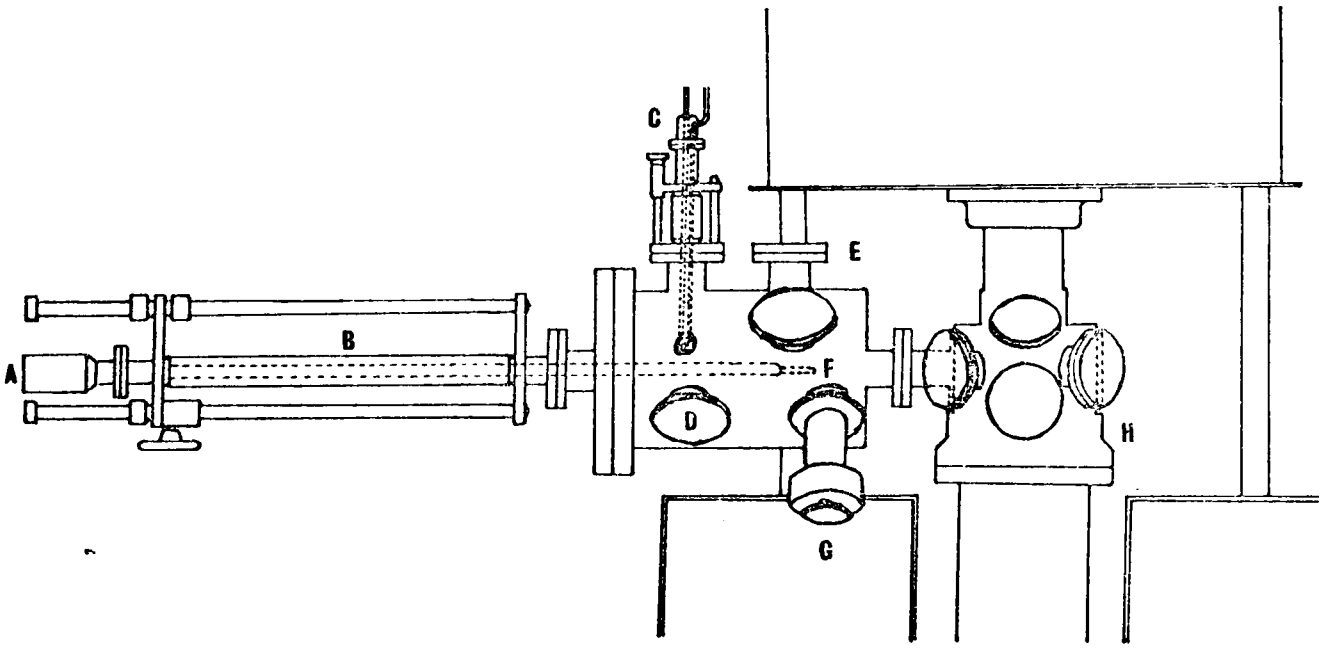
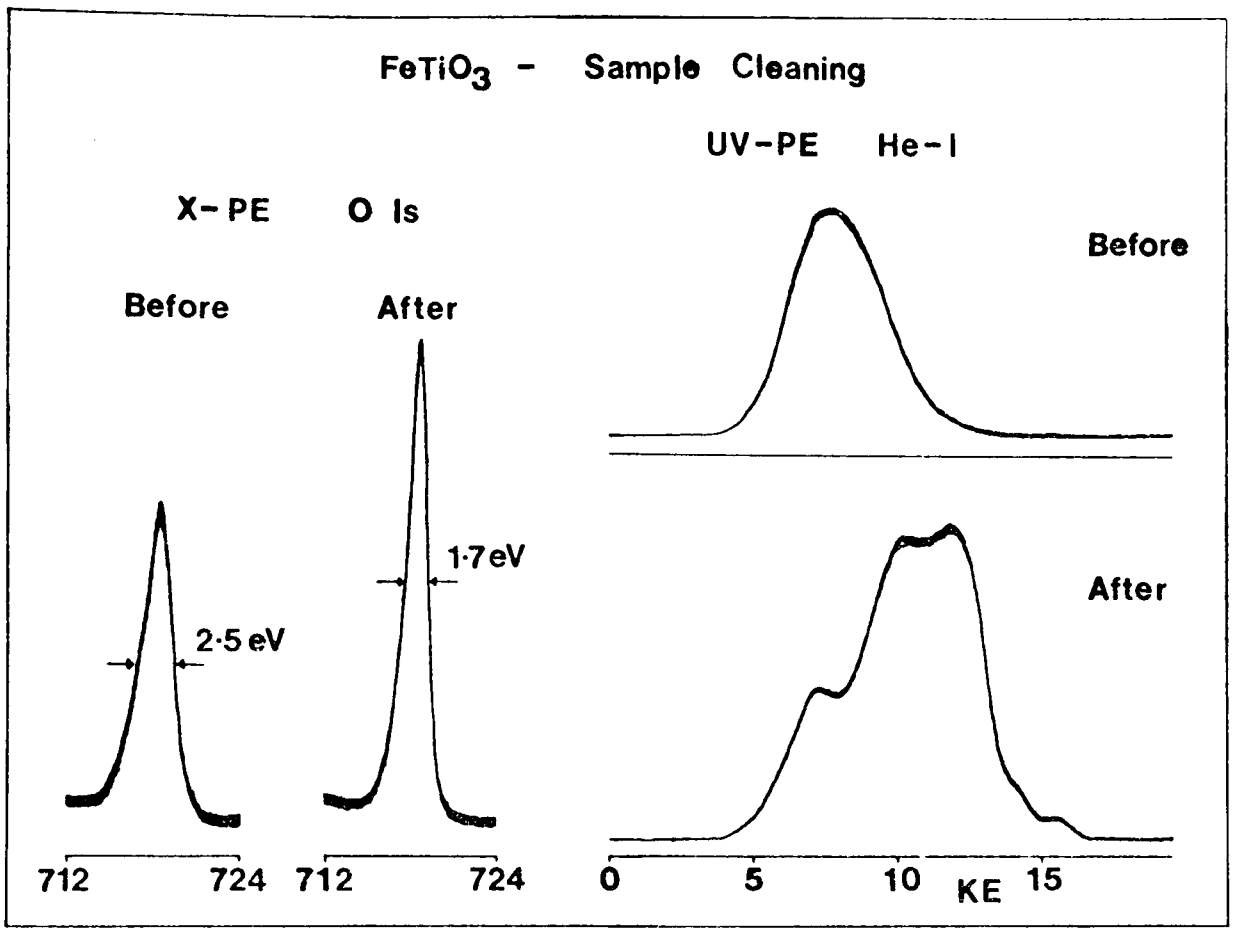


Fig. 3.4. The sample preparation chamber: (A) rotatable probe (B) bellows arrangement (C) retractable R.F coil (D) observation port (E) port containing gold evaporator (F) sample (G) isolation valve (H) main chamber.



g. 3.5. The effects of sample cleaning on the UV-PE and X-PE
ectra of $FeTiO_3$.

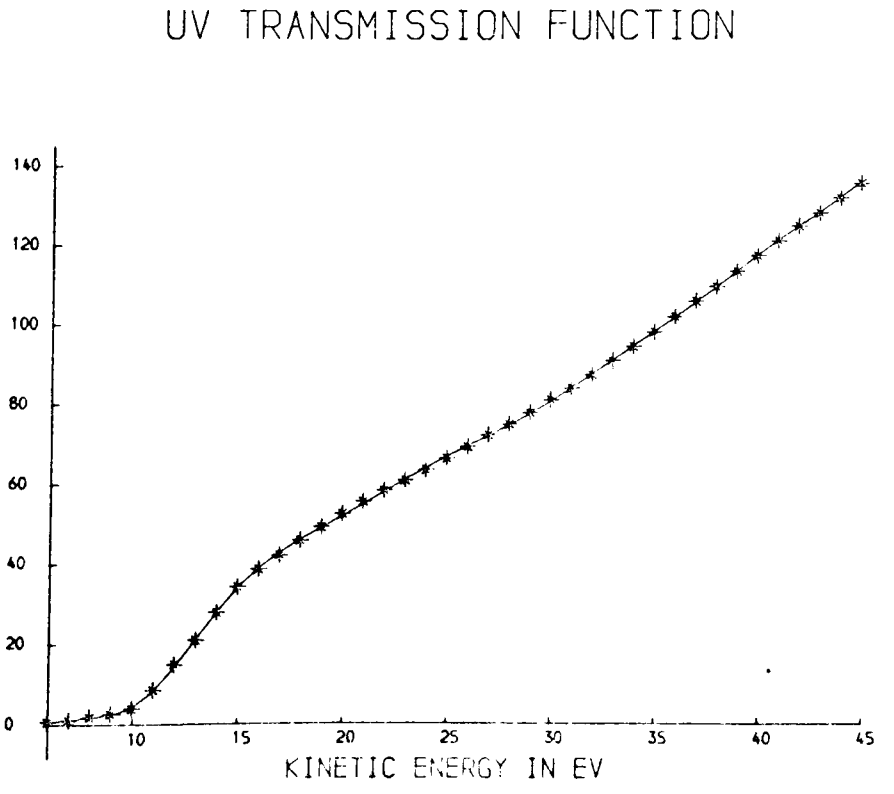


Fig. 3.6.

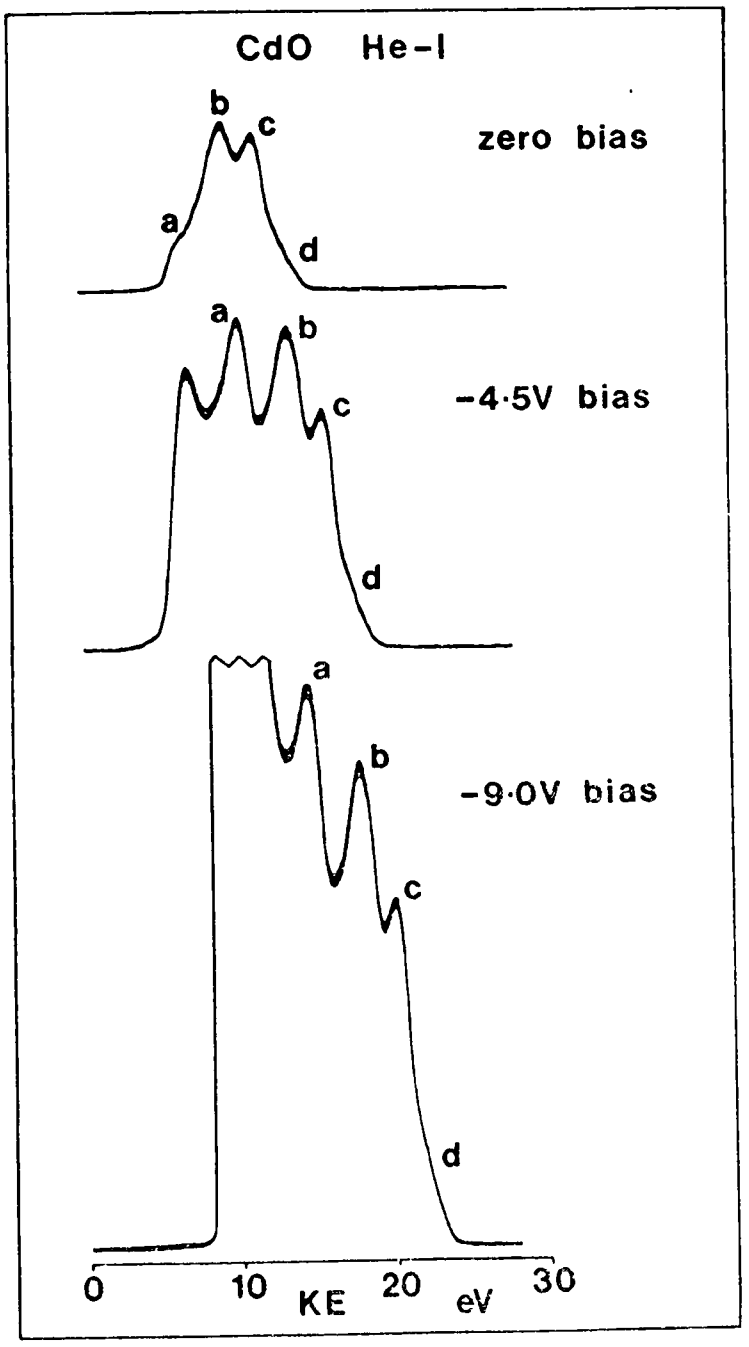


Fig. 3.7. The effects of probe-biassing on the He-I spectrum of CdO.

REFERENCES FOR CHAPTER 3

1. S. E. Livingstone, p 1163 in "Comprehensive Inorganic Chemistry" Vol 3, ed. A. F. Trotman-Dickenson (1973) Pergamon Press.
2. A. Deschanvres, G. Nouet, B. Raveau, Compt. Redn. 261 (1965) 3144.
3. J. Norrestam, Acta Chem. Scand. 21 (1967) 2871.
4. B. C. Tofield, B. E. F. Fender, J. Phys. Chem. Solids 31 (1970).
5. S. Geller, Acta Cryst. B27 (1971) 821.
6. E. O. Wollan, W. C. Koehler, Phys. Rev. 100 (1955) 545.
7. V. E. Wood, A. E. Austin, E. W. Collins, K. C. Borg, J. Phys. Chem. Solids 34 (1973) 859.
8. P. K. Gallagher, Mat. Res. Bull. 3 (1968) 225.
9. G. J. McCarthy, P. V. Gallagher, C. Sipe, Mat. Res. Bull. 8 (1973) 1277.
10. M. Eibschütz, Acta Cryst. 19 (1965) 337.
11. S. Geller, Acta Cryst. 10 (1957) 243.
12. "Handbook of preparative inorganic chemistry" ed. G. K. Brauer, trans. ed. R. F. Riley, 2nd Edit (1963) New York.
13. C. Choain, F. Marion, Bull. Soc. Chim. Fr (1963) 212.
14. D. B. Rogers, R. D. Shannon, A. W. Sleight, J. L. Gillson, Inorganic Chem 8 (1969) 841.
15. L. Kihlborg, Acta Chem. Scand. 13 (1959) 954.
16. J. J. Stickler, S. Kern, A. Wold, G. S. Heller, Phys. Rev. 164 (1967) 765.
17. S. Akimoto, T. Nagata, T. Katsura, Nature 179 (1957) 37.
18. E. Posnjak, T. F. W. Bath, Z. Krist 88 (1934) 277.
19. D. G. Sullivan, A. S. Pavlovic, Proc. W. Va Acad. Sci. 34 (1962) 173.

20. K. N. Raymond, H. R. Wenk, Beitr. Miner. Petrol. 30 (1971) 135.

21. J. A. Connor, M. Considine, I. H. Hillier, D. Briggs, J. Elect. Spec. 12 (1977) 143.

22. C. A. Shell, J. C. Riviere, "Analysis of segregation of phosphorous in iron", A.E.R.E. R7397, Harwell (1973).

23. N. Beatham, Chemistry Part II thesis, Oxford (1975).

24. N. Beatham, A. F. Orchard, J. Elect. Spec. 9 (1976) 129.

25. J. A. R. Samson, J. L. Gardener, J. Elect. Spec. 8 (1976) 35.

26. C. Caroli, D. Lederer-Rozenblatt, B. Roulet, D. Saint-James, Phys. Rev. B8 (1973) 4552.

27. M. Sunjic, D. Sokcevic, A. Lucas, J. Elect. Spec. 5 (1974) 963.

28. I. T. McGovern, R. H. Williams, J. Phys. C9 (1976) L337.

CHAPTER FOUR

GENERAL ASPECTS OF THE PHOTOELECTRON SPECTRA OF TRANSITION METAL OXIDES

4.1 The electronic structure of transition metal oxides

4.2 The effects of sample charging

4.3 Probe-biassing experiments

This chapter provides an overview of the more important theoretical and technical issues concerning the valence region PE spectra reported in this work.

4.1 The electronic structure of transition metal oxides

The electronic properties of the transition metal oxides have been the subject of recent theoretical interest and speculation.[1, 2] This interest has focussed mainly on the question of whether the d electrons in these oxides are in itinerant Bloch or localised Wannier states.[3] The phenomenological model proposed by Goodenough[1] has served to establish a conceptually attractive basis for discussion of the electronic properties in the absence of detailed calculations. The majority of calculations that have been performed to date have either utilised the APW-LCAO band method[4-7] or have resorted to an SCF Xα calcultion on the appropriate transition metal cluster (e.g. FeO_6^{9-} in Fe_2O_3).[8] However, the choice of computational method to apply to a particular system, tends to be governed more by prior knowledge of the electronic properties of the system than whether that method can satisfactorily explain why those properties should be found in the first place.

The fundamental parameter in the Goodenough LCAO model[1] is the transfer integral(b), which is a measure of the strength of interaction between neighbouring atoms. The most important transfer integrals for transition metal oxides are expected to be: (i) the M-O ($ds\sigma$, $dp\sigma$ and $dp\pi$) interactions; (ii) the O-O ($pp\sigma$ and $pp\pi$) interactions; and (iii) the M-M ($dd\sigma$ and $dd\pi$) interactions.[2] Relativistic effects (except for second and third row elements), polaron effects, anion distortion effects and more distant neighbour interactions are thought

not to be important in determining the qualitative features of the electronic structure, and are usually ignored.

The electronic structure of a material is thus expected to depend on both the relative and absolute order of magnitude of these transfer integrals. In table 4.1, we list values of these transfer integrals for NiO, RuO_2 and $SrTiO_3$. (These compounds exhibit the rock salt, rutile and perovskite structures respectively). The values are taken from APW-LCAO band structure calculations performed on these oxides by Mattheiss.[4, 6, 7] Although it is clear from these tables that the largest transfer integrals arise from M-O interactions, it must be remembered that there will be more O-O than M-O transfer integrals to consider. It is generally thought that the two peaks that are usually observed in the O2p band of the PE spectra of transition metal oxides can be assigned to M-O σ and M-O π interactions respectively. However, it is not perhaps widely realised that there must also be a considerable contribution to the O 2p band from the O-O interactions. In an attempt to examine the magnitude of this contribution, two semi-empirical band structure calculations were performed on a face-centred cubic(fcc) array of oxygen anions (see Appendix 3 for details). The results of these two calculations shown in fig. 4.1, where the DOS profiles have been broadened by the appropriate instrumental function. The top spectrum refers to a calculation performed on an O_6^{12-} cluster, whereas the bottom spectrum refers to a tight binding band structure calculation performed on the whole lattice. We have taken the parameter α (see Appendix 3) to be 8.0eV, which means that our transfer integrals are given as O-O ($pp\sigma$) = 1.95eV and O-O ($pp\pi$) = 0.82eV. These values are of course much larger

than those found in most oxides. However, it must be stressed that the purpose of this calculation is simply to show the qualitative form expected of the O 2p band. There are two main points concerning the spectra in fig. 4.1. (i) Both the cluster and band structure calculations produce the same qualitative profile although as we might anticipate, the band structure calculation gives a much broader spectrum. This result is quite pleasing because it helps to reconcile the two apparently quite different approaches to calculating the electronic structure of transition metal oxides - namely the cluster and APW-LCAO band structure calculations. Wolfram et al.[2] have recently examined the relationship between cluster and band states for the d-band perovskites. (ii) The O 2p band consists essentially of two peaks. If we examine the cluster calculation we find that these two bands have no simple interpretation. Neither peak, for instance, can be unequivocally assigned as having either σ or π symmetry with respect to the metal-oxygen axis.

It is interesting to compare directly the cluster spectrum in fig. 4.1, with the O 2p band in the He-II PE spectrum of CdO (see section 5.4). CdO has the rock salt structure in which the oxygen anions form an fcc array. In fact, the main contribution to the doublet structure of the oxygen 2p band in transition metal oxides possessing the rock salt structure (e.g. MgO, CaO, FeO, NiO, CdO) may well be mainly due to O-O rather than M-O interactions. This fact is supported by Xα cluster calculations[8, 9] on systems such as MgO_6^{10-} and FeO_6^{10-}. The ordering of orbitals in the O 2p region of these systems follows very closely the pattern predicted by our cluster calculation.

Although our semi-empirical calculations can only apply to those structures which contain a cubic close packed(ccp) array of oxide anions, it is not unreasonable to suppose that a similar partitioning of the oxygen 2p band into two peaks might be expected to occur in other oxide structures. Thus, if the PE spectrum of a compound which exhibits more covalency than the binary oxides, indicates that the oxygen band is split into two, then this splitting may well be due to a superimposition of two effects: (i) M-O ($dp\sigma$ and $dp\pi$) interactions; and (ii) O-O interactions.

The most important feature of the electronic structures of transition metal oxides, however, concerns whether the d electrons are in itinerant Bloch or localised Wannier states.

Hubbard's simplified model calculations predict that a metal to non-metal (MNM) transition should occur when $W \gtrsim U$. Here W is the unperturbed bandwidth of one-electron energy states and U is the Coulomb interaction energy between two electrons on the same atom.[3] If $U > W$, the electrons will be localised rather than itinerant.

It is clear that W will be dependent on the strength of the relevant transfer integral b which causes the band to broaden. In Goodenough's model he simply elects to define a critical value b_c for the transfer integral above which the electrons exhibit itinerant, rather than localised behaviour. The transfer integral b may in turn be related qualitatively to either the interatomic spacing (R) or to cation-anion covalent mixing parameters (λ_σ , λ_π).

There are essentially two types of interaction which may be strong enough in oxides to make $b > b_c$; these are (i) cation-cation and (ii) cation-anion-cation interactions. For

cation-cation interactions, the most useful parameter is the cation-cation separation R. Oxides that are metallic because of partially filled d bands resulting from $R < R_c$, i.e. $b > b_c$, are referred to as Class I metallic oxides and the d bands as cation-sublattice d bands. Oxides that are metallic because of partially filled d bands resulting from $\lambda > \lambda_c$, where $b \approx \lambda^2$, are referred to as Class II metallic oxides.

The great value of the phenomenological model is that it provides a means of rationalising trends in the electronic properties within an isostructural series. Thus the fact that Ti_2O_3 and V_2O_3 exhibit itinerant electron behaviour whilst Cr_2O_3 and Fe_2O_3 show localised electron behaviour can be correlated with the expected value of R_c.

In general, the PE spectra reported in chapter 5, are in good agreement with the Goodenough model and indeed with various APW-LCAO band structure calculations. However, there is one serious discrepancy between the results of PES and one-electron band schemes. It is that the band schemes often predict an O 2p - M nd energy band separation which is very rarely observed in the corresponding PE spectrum. The main reason for this is that a one-electron band scheme neglects electron correlation effects which may often be quite substantial. The APW-LCAO band structure method has the further drawback of not being self-consistent. APW-LCAO calculations on FeO, CoO and NiO[4] predict that there should be a ca 5eV separation between the bottom of the metal 3d band and the top of the O 2p band. PES data from these oxides[10] indicates, however, that these two bands overlap. Recently, calculations have been performed[11] on these oxides using the self-consistent Restricted Hartree-Fock method with subsequent allowance for

correlation effects. The results of these calculations would seem to be in qualitative agreement with the PE spectra of the oxides. Hence the fact that the one-electron description often predicts an O 2p - Mnd band separation for transition metal oxides which is not observed in the PE spectrum must be viewed as a serious deficiency of the method.

The foregoing discussion has concentrated solely on the bulk electronic structure of oxide materials. PES is essentially a surface technique and thus, in principle, there is no guarantee that the surface will be representative of the bulk.

Whenever a solid is terminated by a surface or interface, special electronic states occur whose wavefunctions are localised at and near the surface.

Surface states which occur in the absence of foreign atoms are called intrinsic surface states. The major factors which produce intrinsic surface states and which influence the energy of such states are: (i) missing neighbouring atoms; (ii) changes in the electrostatic potentials at a surface; (iii) changes in the covalent bonding interactions at the surface; (iv) relaxation of the surface layers and changes in the interlayer spacings; and (v) reconstruction of the surface structure.

One important point concerning surface states in oxides is that if there is a separation between the oxygen 2p and metal nd bands, then some of the surface energy levels may congregate in this region.[2]

Extrinsic surface states are caused by surface perturbations.[2, 12] It is these surface states which are probably more important as regards the oxide PE spectra reported in

this thesis. They will occur whenever: (i) a surface treatment procedure is not entirely effective; (ii) there is surface oxidation due to the presence of small traces of oxygen in the main chamber; or (iii) there is surface reduction through oxygen loss during heating of the sample in vacuo.

Thus, even if there is a band gap between the oxygen 2p and metal nd energy distribution, it may not be possible to observe it in PES when extrinsic surface states are present. It is therefore imperative to ensure that PE spectra are free from structure due to extrinsic surface states, before comparison is made with one-electron band schemes.

4.2 The effects of sample charging

The electrical conductivity of the sample completely determines whether or not it is possible to measure the UV-PE spectrum from a solid compound (see section 2.6). The oxide samples studied in this work possess a wide range of electrical conductivities. This has enabled us to determine more accurately the relationship between electrical conductivity and sample charging. We may summarise our observations as follows:

(i) When the sample was metallic, no difficulties were encountered in obtaining UV-PE spectra.

(ii) If the sample was a complete insulator e.g. Gd_2O_3 or $SrZrO_3$, then no UV-PE spectra could be obtained under any experimental conditions.

(iii) For many semi-conducting materials it was found that, although no UV-PE spectra could be recorded at room temperature, raising the temperature of the sample by means of the probe heater quite often permitted measurement of a UV-PE

spectrum. It was normally found that there was a narrow temperature range (ca 50°C), in which the intensity of the He-I spectrum would show a dramatic rise from below 10 counts/sec to ca. 3000 counts/sec - the normal photoelectron flux. This phenomenon was completely reversible and occurred at different temperatures for different samples. A corresponding, but much less pronounced change in the X-PE spectrum of the material was also found to occur near this temperature. This involved the shifting of the whole spectrum to higher K.E. by approximately 2-3eV. These results indicate that charging effects are much more pronounced in UV-PES than X-PES.

(iv) Whereas no room-temperature He-I PE spectrum could be obtained from a clean bulk sample of MoO_3, a spectrum representative of MoO_3 could be obtained at RT from a partially oxidised sample of MoO_2. The only difference between these two samples is their bulk electrical conductivity.

A strong correlation is found to exist between the electrical conductivity of a sample and the degree (if any) of sample charging (see Chapters 5 and 6). It is anticipated that the major contribution to the electrical conductivity of the semi-conducting oxide samples studied in this work, is due to deviations from stoichiometry. This can arise: (i) through non-stoichiometry in the bulk material (e.g. $CaMnO_{2.97}$); (ii) as a consequence of the pretreatment; or (iii) as a result of heating the sample to too high a temperature when one is attempting to observe a UV-PE spectrum.

The dangers of 'roasting' a compound until it produces a UV-PE spectrum are all too apparent. We may quote the

case history of $SrTiO_3$ which was examined during the course of the work. The sample surface was originally prepared by heating in an atmosphere of oxygen at ca 900K. The sample gave no UV-PE spectrum, even at 750K The oxide was then returned to the preparation chamber and heated in vacuo at ca. 1000 K. Although the sample still gave no UV-PE spectrum at room temperature, a spectrum could now be observed at 750K. However, this spectrum (not reported here) showed the presence of a not insignificant metal d band, indicative therefore of surface reduction.

For a few of the oxides studied here, independent conductivity measurements were also made on the same samples from which the PE spectra were recorded (see section 6.2). However, it would seem that the only way of establishing a quantitative relationship between electrical conductivity and sample charging phenomena is to make sequential conductivity and PE measurements on the sample within the main chamber.

4.3 Probe-biassing experiments

The technique of probe-biassing (see section 2.6) should in principle afford a relatively straightforward means of calibrating He-I PE spectra. During the course of the work it soon became apparent that the situation was much more complex than had been imagined.

It was found that the results from a probe-biassing experiment were critically dependent on the orientation of the sample, in particular the angle θ (see fig. 4.2). The experimental observations can be summarised as follows.

(i) If the sample is in or near to the horizontal plane (i.e. $|\theta| \leqslant 15^{\circ}$) then the results are in good agreement with what one would expect on the basis of the discussion present-

ed in section 2.6. That is for a metal, the separation between the SEED and Fermi edges remains constant for all values of applied bias (assuming of course that the bias is sufficiently negative that the SEED edge is visible) and that both edges take up the full bias. Our results for clean metallic gold with $\theta = 0^{o}$ (fig. 4 3) indicate a work function of 5.1 ± 0.1 eV, in good agreement with the literature values of 5.0,[13] 5.1[14] and 5.2 eV[15]. Similar results are obtained if the sample is a semi-conductor; the separation between the SEED and valence band (VB) edges is constant for low values of θ. For $YCrO_3$ (see fig. 4.4) this separation is 15.6eV, which implies that the photoelectric threshold for this oxide is 5.6 eV.

(ii) When $|\theta|$ is $> 15^{o}$, although the high K.E edge (the Fermi edge for a metal, the VB edge for a semi-conductor) apparently takes up the full bias, the separation between the high K.E edge and the SEED edge diminishes the larger the angle θ and the larger the value of the applied potential. Moreover, the total photoelectron flux is found to decrease correspondingly. This effect appears to be independent of whether the sample is a metal or a semi-conductor (see figs. 4.5 and 4.6).

A similar observation has recently been reported by another group[15] using an AEI ES200B spectrometer. Their lamp, however, is positioned in the same horizontal plane as the X-ray gun, the angle between them being 135^{o}. Thus it seems clear that the most important factor in the experiment is the orientation of the sample with respect to the analyser slit in the electrostatic lens system.

These observations can be rationalised if one takes into account the electric field surrounding the sample when a

negative bias has been applied to it. Although the field cannot be characterised exactly, it is not unreasonable to suppose that it is similar to that from a long thin strip.[16]

For photoelectrons to be detected they must pass normally through the centre of the analyser slit. In a probe-biassing experiment, the photoelectron leaves the sample with an initial kinetic energy eV_i, which is then accelerated by the bias voltage $(-V_b)$ between the sample and ground to a final energy $e(V_i + V_b)$. Although the photoelectron always takes up the full increase in K.E, its final direction is dependent on two factors: (i) the initial K.E of the electron as it leaves the surface; and (ii) the magnitude of the electric field.

Let us consider two limiting cases. (a) A large potential bais is applied to the sample to ensure that $V_b \gg V_i$. Here the path of the photoelectron will follow closely the electric field lines between the sample and earth. (b) A weak electric field is present ($V_i \gg V_b$). Here the final direction of the photoelectron will be little changed from its original direction.

In the limiting case (a), photoelectrons will only pass through the analyser system for low values of θ, the range of θ being defined by the slit dimensions and the exact nature of the electric field. As the conditions of limit (a) are relaxed, the final direction of the photoelectrons will not be so rigidly dictated by the electric field direction and will become dependent to some extent on their initial direction.

We are now in a position to explain the results shown in figs. 4.4 to 4.6. Take a particular angle, say $\theta = 40^{o}$; then, as V_b is raised although the high K.E electrons will be

largely unaffected, an increasingly greater proportion of the slow K.E electrons (i.e. those near the onset of SEED) will not reach the analyser slit at the necessary angle in order to reach the detector. As a consequence, the separation between the high K.E edge and the 'apparent' SEED edge will decrease with increasing external potential bias.

Thus it is vitally important in determining photoelectric thresholds or work functions from probe-biassing experiments, to ensure that the sample is in the horizontal position. Although probe-biassing experiments were performed on many of the oxides reported in this thesis, the importance of having the sample in the horizontal position was not fully realised until near the end of the work. For this reason, we present values of the photoelectric threshold (table 4.2) for only a selected number of oxides where this condition was met.

As can be seen from table 4.2, most of the values are only accurate to $\pm$ 0.2eV. This is due to the difficulty of determining the exact position of the valence band edge. We are led to conclude that probe-biassing experiments may not perhaps be the most accurate method for determining the various energy parameters illustrated in fig. 2.3. In the case of the semiconducting oxides studied here an alternative and more accurate method is the determination of the flat band potential using standard electrochemical tehcniques.[17]

Table 4.1. Comparison of transfer integrals for various transition metal oxides, obtained from APW-LCAO band structure calculations.

(All energies given are in eV)

Transfer Integral		NiO[4]	RuO_2[6]	$SrTiO_3$[7]
M-O	(ds σ)	1.21	2.22	2.49
M-O	(dp σ)	1.04	2.51	2.12
M-O	(dp π)	0.47	1.11	1.03
O-O	(ss σ)	0.07	0.25	0.13
O-O	(pp σ)	0.38	0.63	0.42
O-O	(pp π)	0.06	0.22	0.11
M-M	(dd σ)	0.10	0.50	-
M-M	(dd π)	0.01	0.05	-

Notes

(i) M-O for $SrTiO_3$ refers to Ti-O

(ii) For RuO_2, where there is more than one M-O near neighbour separation, we tabulate the transfer integrals only for the shortest M-O distance.

Table 4.2. Values of the photoelectric threshold for selected oxides, as determined from probe-biassing experiments.

Oxide	Photoelectric threshold (eV)
Cr_2O_3	5.05 ± 0.2
$YCrO_3$	5.6 ± 0.1
MnO_2	5.65 ± 0.1
CdO	5.75 ± 0.15
$FeTiO_3$	6.0 ± 0.3

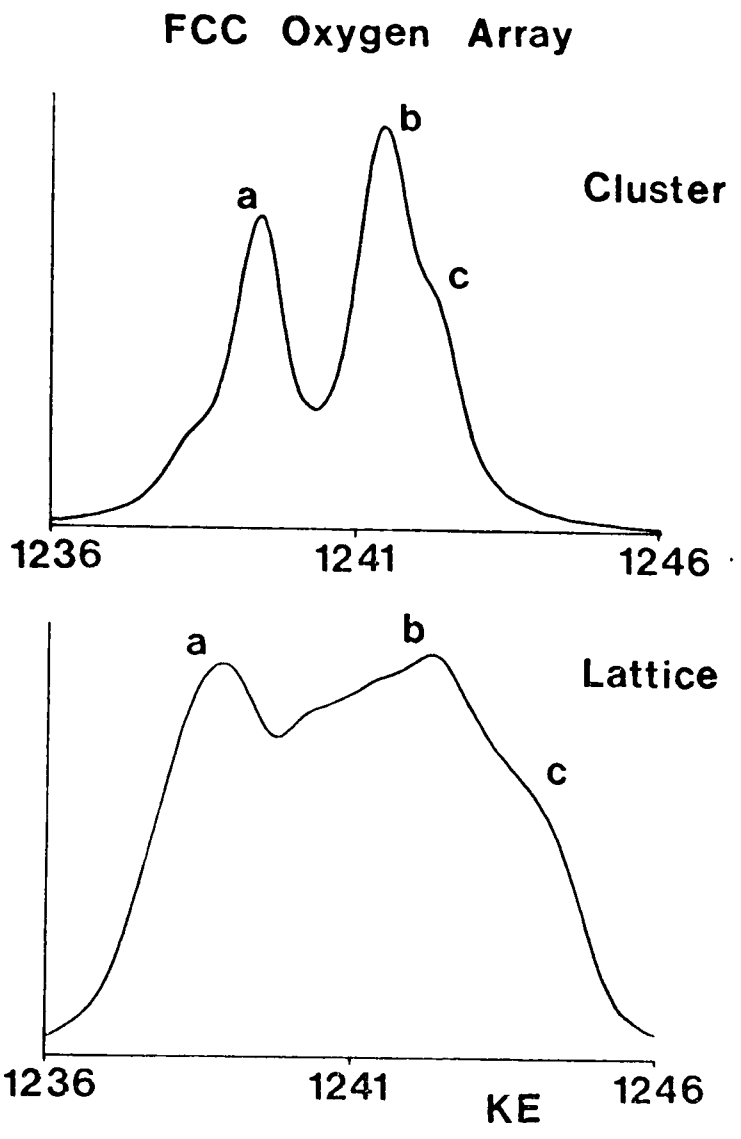


Fig. 4.1. Semi-empirical density of states for a face-centred cubic oxide framework.

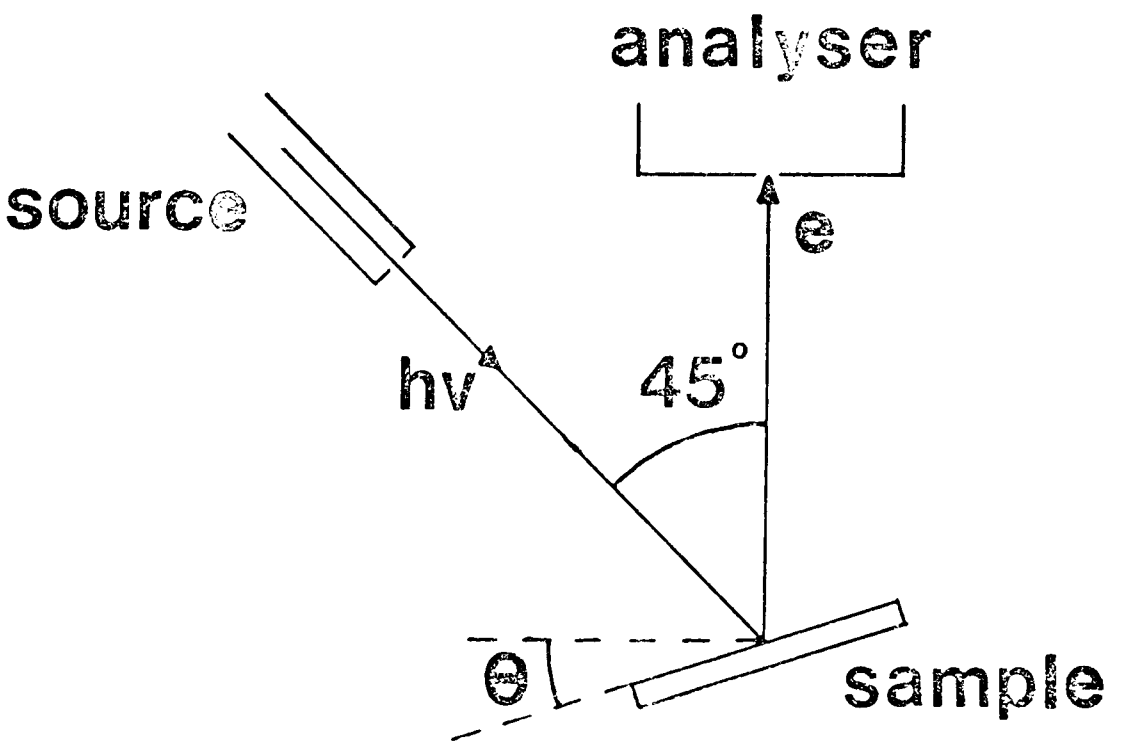


Fig. 4.2. Position of UV lamp in relation to both the sample and electron analyser.

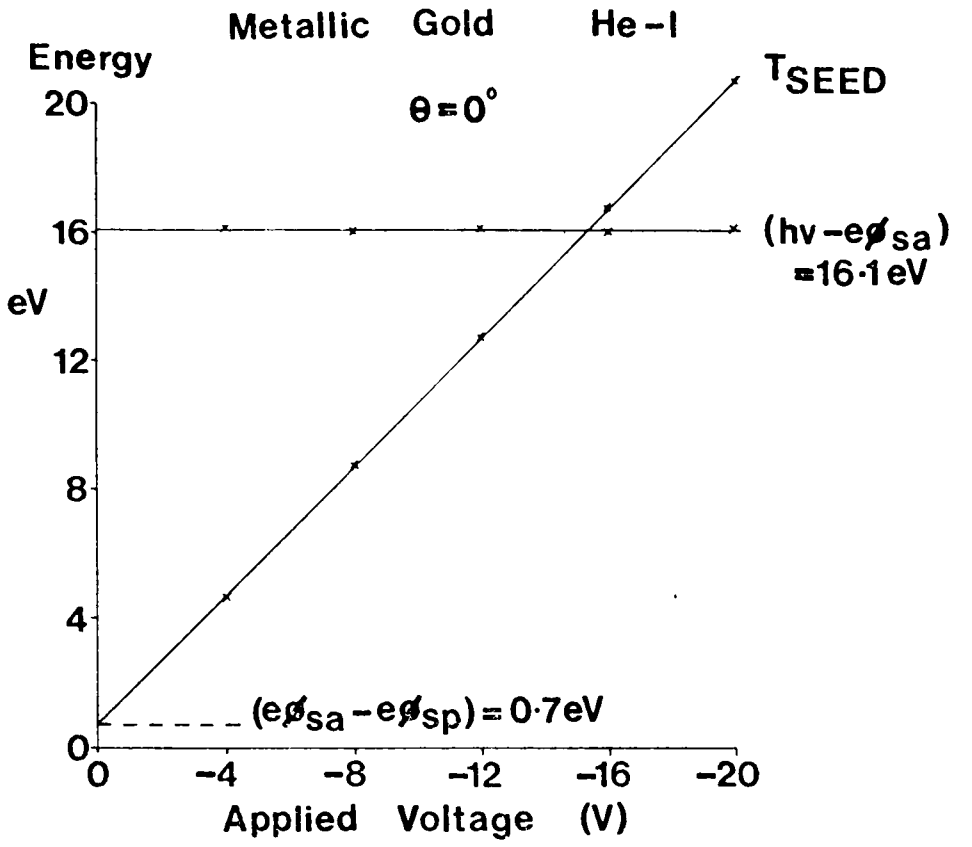


Fig. 4.3. Results from probe-biassing experiment on the He-I spectrum of metallic gold ($\theta = 0^{\circ}$).

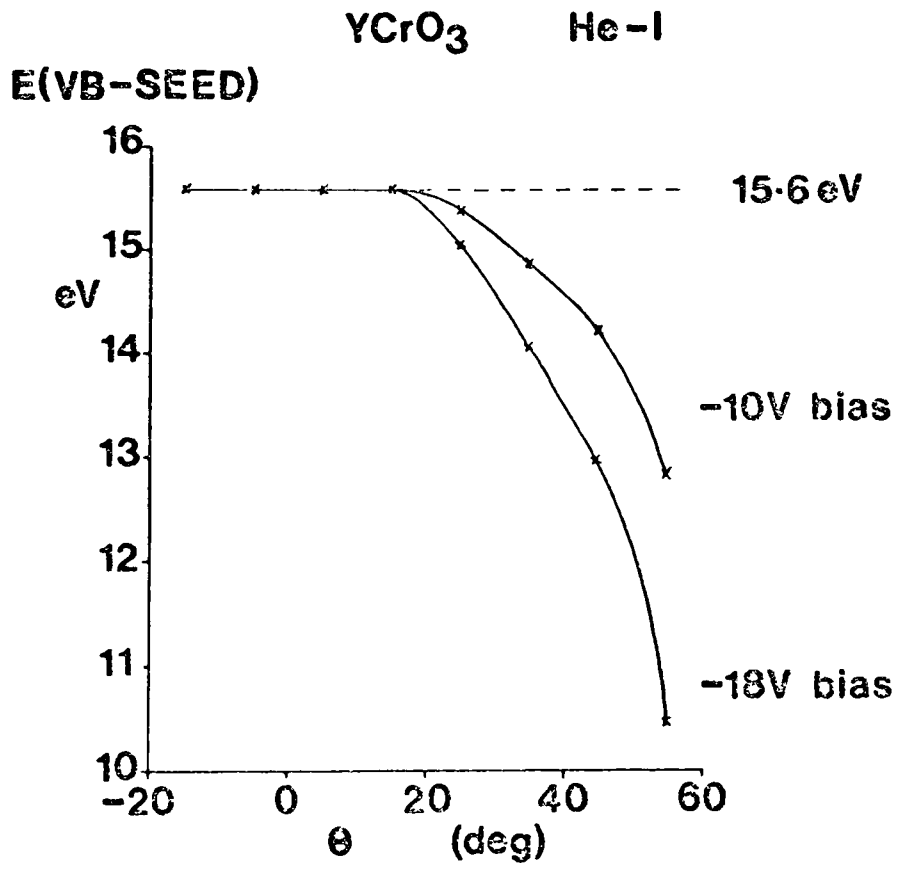


Fig. 4.4. Angular variation of the separation between the valence band and SEED edges in a probe-biassing experiment on the He-I spectrum of $YCrO_3$.

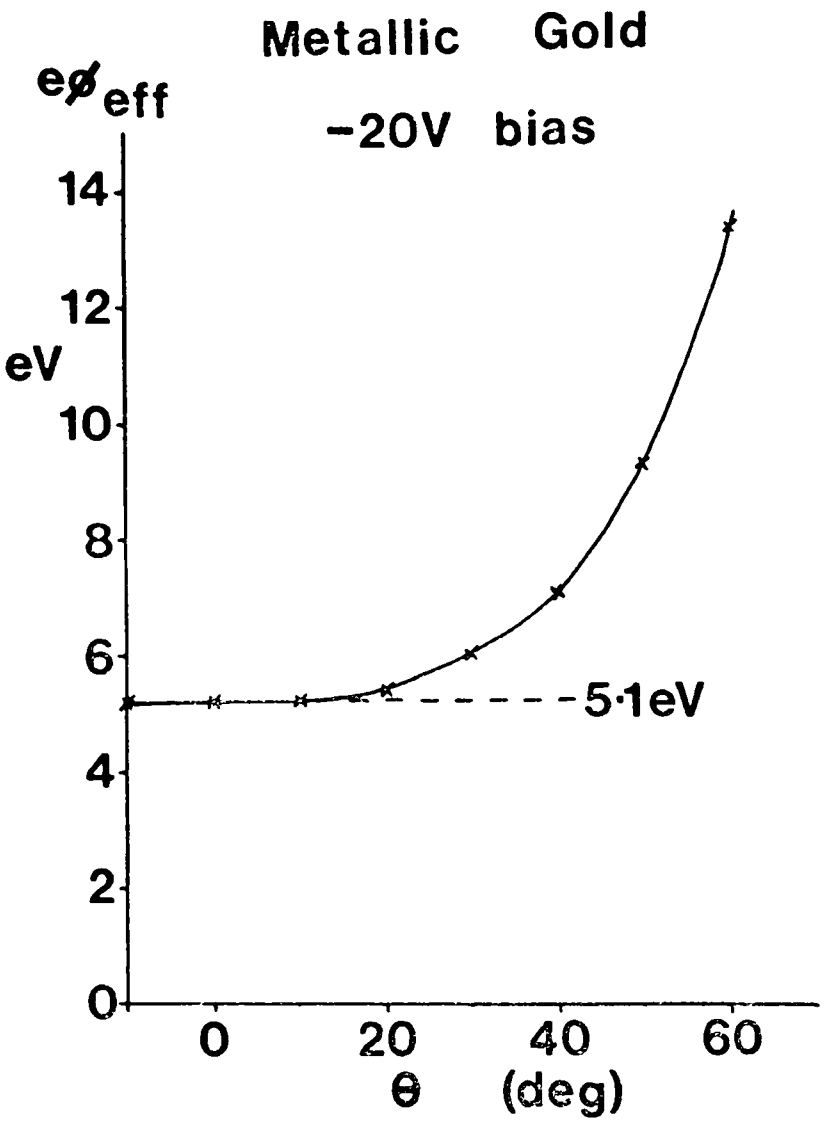


Fig. 4.5. Angular variation of the 'effective' work function in a probe-biassing experiment on the He-I spectrum of metallic gold.

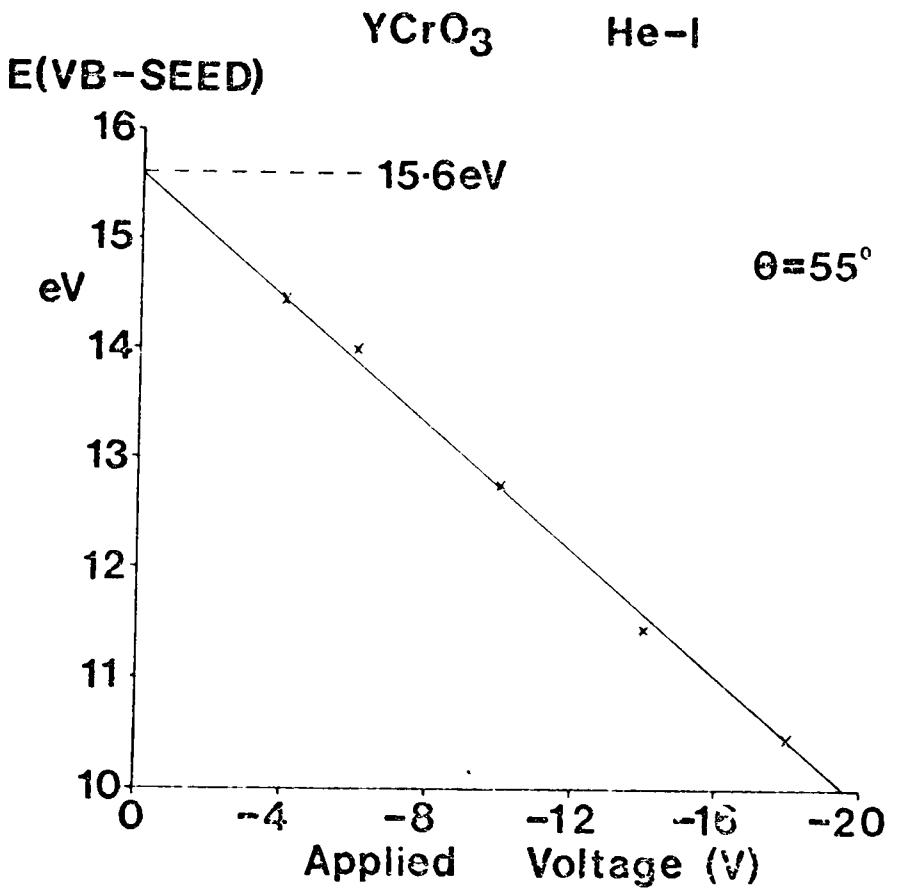


Fig. 4.6. Variation of the separation between the valence band and SEED edges as a function of applied potential when $\theta = 55^{o}$ in a probe-biassing experiment on the He-I spectrum of $YCrO_3$.

REFERENCES FOR CHAPTER 4

1. J. B. Goodenough, Prog. Solid State Chem. 5 (1971) 490.
2. T. Wolfram, F. J. Morin, R. Hurst, p 21 in NBS Special Publication 455, "Electrocatalysis on non-metallic surfaces" (1976).
3. J. Hubbard, Proc. Roy. Soc. (London) A281 (1964) 401.
4. L. F. Mattheiss, Phys. Rev. B5 (1972) 290.
5. L. F. Mattheiss, Phys. Rev. B5 (1972) 306.
6. L. F. Mattheiss, Phys. Rev. B6 (1972) 4718.
7. L. F. Mattheiss, Phys. Rev. B13 (1976) 2433.
8. J. A. Tossell, D. J. Vaughan, K. H. Johnson, Amer. Min. 59 (1974) 319.
9. J. A. Tossell, J. Phys. Chem. Solids 36 (1975) 1273.
10. D. E. Eastman, J. L. Freeouf, Phys. Rev. Lett. 34 (1975) 395.
11. A. B. Kunz, G. T. Surratt, Solid State Commun. 25 (1978).
12. V. E. Henrich, G. Dresselhaus, H. J. Zeiger, Phys. Rev. Lett. 36 (1976) 1335.
13. D. E. Eastman, Phys. Rev. B2 (1970) 1.
14. Y. Baer, Solid State Commun. 19 (1976) 669.
15. J. A. Connor, M. Considine, I. H. Hillier, D. Briggs, J. Elect. Spec. 12 (1977) 143.
16. B. I. Bleaney, B. Bleaney "Electricity and Magnetism" 2nd Edit. (1965) OUP.
17. V. A. Myamlin, Yu. V. Pleskov, "Electrochemistry of Semiconductors" (1967) Plenum Press, New York.

CHAPTER FIVE

PHOTOELECTRON SPECTRA OF BINARY OXIDES

5.1 Transition metal dioxides

5.2 The higher oxides of Nb, Mo and W

5.3 Transition metal sesquioxides

5.4 Transition metal monoxides

5.1 Transition metal dioxides

The transition-metal dioxides MO_2 are intriguing from the structural viewpoint since many of them have crystal lattices which show marked distortions from the tetragonal rutile (TiO_2) structure (fig. 5.1) containing chains of edge-sharing MO_6 octahedra, with a regular M-M spacing, orientated along the c-axis.[1, 2] The variants have commonly an axially distorted, monoclinic form of the regular rutile structure in which the M-M distances alternate along the c-axis so as to produce pairs of metal atoms.[1] In table 5.1 we classify the transition metal dioxides according to structural type, electronic and magnetic properties. Seven of these oxides have been investigated in this work: VO_2, MnO_2, NbO_2, MoO_2, RuO_2, WO_2 and IrO_2.

Once introduced into the spectrometer vacuum, and positioned in the sample preparation chamber, the samples were treated as follows.

(i) VO_2 was heated to ca 900K in vacuo for two hours.

(ii) MnO_2 was heated for two hours at 670K under one atmosphere of oxygen. At this temperature there is no danger of reduction to Mn_2O_3.[3]

(iii) NbO_2 was heated in vacuo for 7 hours at ca 900K, to eliminate any surface Nb_2O_5.[4]

(iv) MoO_2 was heated for 2 hours at ca 1050K in vacuo. This treatment should ensure the decomposition of higher oxides of molybdenum present at the surface.[4]

(v) RuO_2 was heated in one atmosphere of dry oxygen for three hours at ca 1050K. RuO_2 is known to be the only ruthenium oxide stable in air at this temperature.[5]

(vi) WO_2 was heated <u>in vacuo</u> at <u>ca</u> 900K for $2\frac{1}{2}$ hours in order to 'drive off' higher oxides from the surface.[4]
(vii) $IrO_2.2H_2O$ was dehydrated[6] to IrO_2 by heating the sample for 6 hours <u>in vacuo</u> at 650K by means of the probe-heater. During the dehydration, the pressure in the preparation chamber rose to 10^{-5} torr, and H_2O could be detected by means of the quadrupole mass spectrometer.

The most compelling evidence for the success of the sample pretreatment procedures that were applied to the dioxides comes from the fact that the UV-PE spectra are consistent with the known electrical properties of the materials.[1] The room-temperature He-I and He-II PE spectra of the dioxides are reproduced in figs. 5.2 to 5.6. (No problems with sample charging were encountered). For the majority of the compounds, we also present expansions of the metal d structure in the He-I spectrum (figs. 5.7 to 5.11). The room-temperature He-I spectra of the metals MoO_2, RuO_2, WO_2 and IrO_2 each show the expected Fermi edge. The absence of a Fermi edge in the room-temperature He-I spectra of VO_2, MnO_2 and NbO_2 are consistent with the fact that all are semiconductors at this temperature. Moreover, VO_2 undergoes a semiconductor $\longleftrightarrow$ metal transition (SMT) at 339K.[7] He-I spectra of VO_2 recorded above this transition temperature (figs. 5.6 to 5.8) reflect the fact that the sample is now metallic.

The progress of the sample treatment was in each case monitored by reference to the O 1s and principal metal core-electron signals in the X-PE spectrum. In figs. 5.12 to 5.13, we present the main core-level PE signals that were obtained from the second and third row transition metal dioxides at the end of the sample pretreatment procedure.

The samples of VO_2, MnO_2, NbO_2, MoO_2 and WO_2 all gave reasonably sharp O 1s PE signals. For IrO_2 and RuO_2 a slight asymmetry and a small shoulder, respectively, could be observed to higher binding energy. In an attempt to determine the origin of the shoulder on the O 1s PE signal from RuO_2, the sample was also heated to ca 1050K in vacuo for 1½ hours. However, no change was detected in either the O 1s PE signal or the UV-PE spectra. The shoulder has been reported before and attributed to a continuous evaporation of RuO_2 as RuO_3.[8] Although we have no reason to doubt this assertion, we were still able to resolve a fairly sharp Fermi edge in the He-I spectrum.

The effect of progressive surface 'cleaning' of the samples may be of interest. The valence region X-PE spectra (figs. 5.14 to 5.16 and 6.9) assumed their ultimate form at a quite early stage in the treatment; the main effect of continued heating on the samples of NbO_2, MoO_2 and WO_2 was to increase the relative intensity of the metal nd signal, rather than to improve the resolution of the spectra. In the He-I measurements, however, progressive treatment continued usually to yield both an increase in the intensity of the metal nd signal and in resolution, long after the X-PE spectrum had settled down. The UV-PE spectra recorded at early stages in the process were often of an exceedingly poor quality. These observations presumably reflect incomplete decomposition of higher oxides (especially for the earlier members of a transition row i.e. NbO_2, MoO_2 and WO_2) or of surface hydroxides, etc., in the early stages, the effects of this being more evident in the UV-PE spectra

due to the smaller electron escape depths involved.

VO_2 provides a particularly instructive case study. The He-I PE spectrum of VO_2 recorded at temperatures in excess of the semiconductor $\longleftrightarrow$ metal transition temperature, T_t, showed a Fermi edge only after the sample had been heated in vacuo above ca 970K. It was then possible to observe the marked changes in the valence electron structure that occur as the sample is taken through the SMT (fig.s 5.6 to 5.8). Above the transition temperature (T_t), a sharp Fermi edge is detected; this disappears as the temperature is lowered below T_t. The spectra also reveal that there is an alteration in the general profile of the essentially V 3d band through the transition whereas the oxygen 2p band remains constant. Changes were also noted in the O1s, V2$\overline{p}$ and V2p X-PE signals (see fig. 5-17). All the changes were perfectly reproducible; the sample was taken through the transition five times during the course of the investigation.

The temperature of the sample was measured by means of the NiCr/NiA1 thermocouple at the probe tip. We found that the SMT appeared to occur between ca. 358K and 373K. This is slightly higher than the accepted value of 339K,[7] but may be attributed to the fact that the temperature of the sample is likely to be less than at the end of the probe. Our present instrumentation is not such that we can make accurate determinations of the sample temperature.

As expected, the He-I PE spectra show much better resolution of the metal d structure than the spectra excited with the achromatic X-rays. The effective resolution of the UV-PE spectra at the Fermi edge is ca. 0.2 eV for He-I and ca. 0.3 eV For He-II. Our estimates are based upon the PE spectra

reported in this thesis and also from UV-PE spectra obtained with clean metallic gold and vanadium.[9]) The corresponding resolution for achromatic X-PE spectra at the Fermi edge is ca. 1.5 eV.

Thus, whereas in our UV-PES study of the SMT in VO_2, we were able to detect a sharp Fermi edge from the metallic phase this was not the case in a previous achromatic X-PES study of the transition.[10]

The principal core-level PE signals of the metallic dioxides MoO_2, RuO_2, WO_2 and IrO_2 all show a marked asymmetry (see fig. 5.12 and 5.13). In principle, some or all of this asymmetry could be due to the presence of higher oxides at the surface. In the case of MoO_2 (and also NbO_2 where the Nb 3d signals exhibit complex structure) a final check was carried out, after the valence band spectra had been recorded, to test this hypothesis. The samples were heated for 1 hour at ca. 600K in an atmosphere of hydrogen, but no further changes in the spectra were observed.

The core-level asymmetry is ascribed to the interaction between the positive hole created by photoionisation and the mobile conduction band[11-13] (see section 2.5). The asymmetry is expected to be proportional to the density of states at the Fermi level. Examination of the spectra indicates that there is a strong correlation between the height of the DOS at the Fermi level, as deduced from the He-I spectra and the degree of asymmetry in the core-level PE signal. Thus RuO_2, which has the highest DOS at the Fermi level possesses the greatest core-level asymmetry. From the general absence of asymmetric broadening in the O 1s PE signal it may be concluded that the interaction of the core hole with the conduction

electrons is a local effect,[12] directly related to the localisation tendencies of the wavefunctions forming the conduction band.

NbO_2 is a semiconductor, but still exhibits complex structure in the Nb 3d PE signals. As mentioned earlier, this structure cannot be ascribed simply to the presence of Nb_2O_5. We tentatively attribute this structure to the coupling of the core-hole with the Nb 4d band. (We recognise, however, that NbO_2 may not have any unpaired electrons - vide infra). It is also worth noting that the V2p PE signals from monoclinic VO_2 also show an asymmetry.

The structure we have observed in the Nb 3d PE signals is slightly different, however, to that reported in two previous studies.[16, 17] The form of the earlier spectra was closely similar to the structure observed in the Nb 3d signals of our sample of NbO_2 before sample pretreatment and thus may be attributed to surface contamination by Nb_2O_5.

Our interpretation is further strengthened by comparison of the X-PE spectra of the second row transition metal dioxides (fig. 5.14). The spectra show a satisfying correlation between the relative intensity of the 4d band and the number of d electrons present; that is, the 4d signal grows progressively in the sequence NbO_2 (d^1) - MoO_2 (d^2) - RuO_2 (d^4). The simplicity of the effect, which has been observed elsewhere (e.g. in a series of sodium tungsten bronzes, Na_xWO_3 [12]), depends in particular on the final state of the photoelectron lying in the continuum region of the one-electron energy level diagram.

NbO_2 undergoes a SMT at ca. 1081K.[19, 20] An earlier X-PES study on NbO_2 in this laboratory attempted to monitor

changes in the valence band PE structure with increasing the temperature.[17, 18] Apart from the fact that the spectra indicated contamination by Nb_2O_5 (vide supra), some particularly strange results were obtained that were not consistent with other physical measurements[7] - namely, the whole valence band appeared to broaden uniformly as a function of temperature. To check these results, we recorded PE spectra from our sample of NbO_2 at ca. 800K. No significant changes in the spectra were observed. It would appear that the broadening of the spectra in the earlier work was an artefact of the method used for heating the sample.

The valence region X-PE spectra of four of the other dioxides (MoO_2, RuO_2, WO_2 and IrO_2) have been reported using monochromatised Al Kα radiation.[13, 21, 22] Our PE spectrum from RuO_2 is in essential agreement with that reported in a recent study[13], whereas the spectra from MoO_2 and WO_2 show a distinct improvement upon the previously reported results.[21,22] Comparison between the X-PE spectra of IrO_2 indicates that there are slight differences.[13] Whereas the structure in the oxygen 2p bands are consistent, the Belgian workers[13] note a shoulder in the Ir 5d band just before the Fermi edge. The fact that we do not observe this feature in our 'raw' X-PE spectrum (fig. 5.16) is not too surprising because of the low resolution afforded by achromatic X-PES. However there is no indication of such a feature in the deconvoluted spectrum (not shown here). Nor does the shoulder in their spectrum correspond with the Ir 5d band observed in the UV-PE spectrum. Furthermore, it is not predicted in the Goodenough model.[23]

To confirm the authenticity of their spectrum, the Belgians refer to an APW-LCAO band structure calculation by

Mattheiss[24] which includes the effects of spin-orbit coupling. We find their argument somewhat unconvincing; the Ir 5d partial DOS in the calculation would appear to be in better agreement with the Ir 5d band that we observe in our He-I spectrum. This fact, coupled with the observation of a sharp Fermi edge in the UV-PE spectra leave us confident of the veracity of our spectra. If their X-PE spectrum is correct then we must suppose that the additional feature observed is one that disappears for cross-section reasons in the UV-PE spectrum.

The metal d bands show a dramatic increase in intensity, relative to the oxygen 2p bands, on changing from UV to X-ray excitation. This effect appears to be quite general for transition-metal compounds: it is observed not only in oxides,[25] but also in chalcogenides[26] and halides.[27]

The relationship between the structure and physical properties of the dioxides (in particular, electrical conductivity) is well understood, largely through the ideas of Goodenough.[23] In the regular, tetragonal rutile structure (fig. 5.1) the fused MO_6 octahedra are distorted in such a way as to leave the metal ions with D_{2h} site symmetry and to permit a degree of metal-metal bonding in the cation sub-lattice. Referring to the coordinate system shown in fig. 5.18, we may distinguish the following categories of metal d orbital: (i) d_{xy} (b_{1g}) and d_{Z^2} (a_g), which are involved in M-O σ bonding; (ii) d_{yz} (b_{3g}) and d_{xz} (b_{2g}), engated in M-O π bonding; and (iii) the $d_{x^2-y^2}$ (a_g) orbital, which can participate in metal-metal bonding by σ-overlap. (Recalling their parentage in octahedral symmetry, Goodenough[23]

labels these three sets of orbitals e, $t_{\perp}$ and $t_{\parallel}$, respectively). We are then led ultimately to a band scheme essentially of the form given in fig. 5.19. If, as shown there, the relatively narrow σ(M-M) band merges with the broader π^*(M-O) band then the dioxides which have d electrons should exhibit metallic conductivity. In this way we can understand the high temperature forms of VO_2 and NbO_2 (d^1) and the prevailing forms of RuO_2 (d^4) and IrO_2 (d^5) being metals.

Although β-MnO_2 posseses the perfect rutile structure, the Mn 3d electrons are localised rather than itinerant and thus this oxide does not exhibit metallic properties. In the axially-distorted variants of the rutile structure metal-metal bonding within the pairs of metal ions changes the picture dramatically. The σ-overlap of the metal $d_{x^2-y^2}$ orbitals becomes sufficiently large, between paired atoms, that the σ(M-M) band divides into bonding and anti-bonding bands, as illustrated in fig. 5.20. Goodenough has argued that the effect is large enough to produce a bonding σ(M-M) band lying at lower energy than (and separated from) the π^* (M-O) band. The width of the band being determined by the interaction between the pairs M_2, it is expected to be quite narrow.

Clearly, this bonding σ(M-M) band must be filled before the π^* (M-O) conduction band can be populated. It then follows that the room temperature forms of VO_2 and NbO_2 (both d^1) should be semiconductors, as indeed is observed; for, with two d electrons per pair of niobium atoms, the σ(M-M) band is precisely filled.

The semiconductor $\longleftrightarrow$ metal transitions in VO_2 and NbO_2 which occur at ca. 339K and 1081K respectively,

have been the subject of much theoretical and experimental study.[10,23,28-31] Unfortunately, the driving mechanism behind the transition is still not properly understood. A review of recent theories has been provided by Gupta et al.[31] In the monoclinic forms of both VO_2 and NbO_2, there is an antiferroelectric distortion; the metal-metal pairs are tilted with respect to the c-axis with a concomittant shortening of certain M-O distances.[28, 32] However, the driving force for the transition is currently thought to be due to phonon mode 'softening' (electron-phonon coupling)[33].

In the room-temperature UV-PE spectra fo both VO_2 and NbO_2 (figs. 5.7 and 5.9) we observe a single d band but no Fermi edge. The separation between the maxima of the O 2p and the metal d band in the He-II PE spectra of the dioxides (where the effects of the analyser transmittance are relatively small) is 4.5(5) eV for VO_2 and 4.9(5) eV for NbO_2. The general profiles of the He spectra are very similar for the two oxides, and they also correlate well with the X-PE spectra.[10] (The valence band separations for NbO_2 are listed in table 5.2).

In addition to possessing a Fermi edge, the V3d band in the He-I spectrum of VO_2 measured above T_t is consistent with the presence of two overlapping bands.

The separation between the maximum in the V 3d band and the Fermi edge is equal to 0.9 eV. Although there is an obvious change in the V 3d band through the SMT, the maximum of the band remains at much the same energy.

The Dutch workers[10] who examined the transition by X-PES, also noted a change in the O 1s, V $2\bar{p}$ and V 2p PE signals in passing through the SMT. We have observed

exactly the same changes in our study. The origin of these variations has been adequately discussed by these workers. Comparison of the two studies indicates that only UV-PES (by virtue of its enhanced resolution) can provide conclusive information on the changes in the V 3d band through the transition.

For MoO_2 and WO_2 (each d^2), which both possess the axially, distorted, monoclinic form of the regular rutile structure, the π^* (M-O) band becomes partially occupied. This results in metallic conductivity and also quenches any ferroelectric distortion from the basic rutile unit (as is found in VO_2 and NbO_2).

However, the high correlation that exists between the metal-metal distance in these rutile related dioxides and the number of electrons available for bonding[1] would seem to suggest a bond order[34] of 2 in both MoO_2 and WO_2. Rogers et al.[1] propose that in addition to the M-M σ-band, a π band is formed by utilising the metal b_{2g} orbitals. The b_{3g} orbital remains available for M-O π interactions. This bonding scheme is illustrated in fig. 5.21. One anticipates however, that there will be considerable interaction between the M-M and M-O π bands resulting in considerable cation-anion-cation bonding between the interacting M pairs.

The He-I PE spectra of both MoO_2 and WO_2 (figs. 5.9 and 5.10) show not only the presence of a Fermi edge but also a splitting of the essentially metal nd band. This is consistent with the proposed electronic structure. The separations between the two peaks in the metal d band and the Fermi edge are 0.4(5) and 1.5 eV for MoO_2, and 0.6 and 1.8eV for WO_2. These figures help to explain why the two peaks are more resolved in the X-PE spectrum of WO_2 than

of MoO_2. The larger splitting found in the case of WO_2 presumably reflects the much stronger metal-metal bonding along the c-axis for W. This is due presumably to the W 5d atomic wavefunctions having a larger spatial extension than the Mo 4d atomic wavefunctions. Relativistic effects may well be of importance also. The shortest M-M distance in WO_2 is 0.249 nm as compared with 0.251 nm for MoO_2.[1]

In RuO_2 one now has four outer d electrons per cation to occupy either the $t_{\parallel}$ or M-O π^* bands. Whereas the first three outer d electrons per cation can be considered to enter orbitals that are bonding with respect to the cationic array, all further electrons must enter anti-bonding orbitals. Any stabilisation resulting from cation-cation pairing in RuO_2 is precluded for this reason and RuO_2 retains the rutile structure, with an extended c-axis ensuring non-bonding $t_{\parallel}$ orbitals (see fig. 5.21).

In addition to the He-I, He-II and X-ray PE spectra of RuO_2 we also report Ne-I and Ne-II spectra (fig. 5.22). The well-resolved structure in the valence region PE spectra of RuO_2, together with the availability of both monochromatised X-PE spectra[13] and APW-LCAO band structure data[24], make RuO_2 an ideal case in which to compare the energy separations of the various features. This is done in table 5.3, where remarkable agreement is found.

IrO_2 (d^5) is metallic and possesses the undistorted rutile structure. As mentioned earlier, the profile of the Ir 5d band in the He-I PE spectrum of IrO_2 correlates well with the APW-LCAO band structure calculation performed by Mattheiss.[24] The broad nature of the 5d band can be ascribed to the number of d electrons in the band and also the influence of relativistic effects.

Finally, as regards MnO_2, the 3d electrons are localised, the $t_{\parallel}$ and $t_{\perp}$ orbitals being half-filled. We therefore ascribe the structure labelled c in the He-I and He-II PE spectrum of MnO_2 (fig. 5.2) to the final states of d^2 in D_{2h} symmetry.

5.2 The higher oxides of Nb, Mo and W

The PE spectra of the five oxides Nb_2O_5, Mo_4O_{11}, MoO_3, $W_{18}O_{49}$ and WO_3 have been recorded to complement the study of the corresponding dioxides of these transition metal elements. The main aim of this investigation was to provide more detailed information on the composition of the surface phases.

Nb_2O_5 has a narrow homogeneity range and exhibits extensive polymorphism.[4, 7] MoO_3 crystallises in an orthorhombic layer structure composed of MoO_6 octahedra.[4] Several mixed-valence oxides in the composition range MoO_2 to MoO_3 are known. We elected to study orthorhombic Mo_4O_{11}. The crystal structure of this can be described as distorted ReO_3 type containing both MoO_4 tetrahedra and MoO_6 octahedra.[4, 7] WO_3 also is a variant of the ReO_3 structure with a distorted WO_6 octahedra network extending in three dimensions. Substantial loss of oxygen from WO_3 results in a partial breakdown of corner-sharing to leave edge-sharing for some octahedra. This occurs for $W_{18}O_{49}$, for example.[4]

Sample pretreatment procedures for the d^0 oxides were as follows: Nb_2O_5 was heated in one atmosphere of oxygen for $2\frac{1}{2}$ hours at ca 950K; MoO_3 was heated in one atmosphere of oxygen for 2 hours at ca 870K (the oxide melts at 1068K); WO_3 was heated in one atmosphere of oxygen for $2\frac{1}{4}$ hours at ca 1000K. The sample cleaning procedures reflect the fact that these oxides contain the transition metal in the highest oxidation state.

The PE spectra of Mo_4O_{11} and $W_{18}O_{49}$ were recorded without sample pretreatment. Any attempts to heat Mo_4O_{11} in oxygen would partially oxidise the sample to MoO_3; when a sample of the oxide was heated *in vacuo* disproportionation occurred to give MoO_2 and MoO_3. $W_{18}O_{49}$ is metastable with respect to WO_2 and $W_{20}O_{58}$ below 860K and thus heat treatment is also precluded for this compound. These two oxides reveal a serious deficiency in our sample pretreatment preparation procedures - namely that we are unable to obtain clean surfaces from compounds which are unstable at the temperatures necessary to out-gas typical surface contaminants such as H_2O and CO_2.

All five samples however, provided reasonably sharp symmetrical O 1s PE signals, regardless of whether or not they had been pretreated. Thus, for these systems, the form of the O 1s signal is no guarantee of surface integrity.

The UV-PE spectra of the oxides are presented in figs. 5.3, 5.23 and 5.24. The spectra of Mo_4O_{11}, $W_{18}O_{49}$ and WO_3 were recorded at room temperature, while those of Nb_2O_5 and MoO_3 were recorded at *ca.* 700K and *ca.* 620K respectively in order to overcome the problems of sample charging (see section 4.2). These observations are consistent with the reported electrical conductivity data on these compounds.[7, 35] The valence region and principal core-level X-PE spectra are reproduced in figs. 5.12, 5.13, 5.15 and fig. 5.16.

As regards WO_3, the monochromatised X-PE spectrum has been reported[22] and is in essential agreement with the deconvoluted spectrum of WO_3 (not shown here). The energy separations between features in the valence band for the He-I, He-II and X-PE spectra are listed in table 5.4. The He-I and He-II PE spectra are in reasonable agreement with each other.

However, turning to the X-PE spectrum, not only does the peak b appear to move but there is a change in the general profile of the spectrum. This can be attributed to photoionisation cross-section modulation. A similar affect has been noticed for the d^o perovskite $SrTiO_3$.[36] The higher B.E part of the valence band is expected to have more d electron admixture than the lower B.E part. The X-PE spectrum is dominated by the d electron partial DOS (vide supra). Similar effects can be detected in the PE spectra of MoO_3 and $W_{18}O_{49}$. The energy separations between features in the valence band PE spectra of these two compounds are presented in tables 5.5 and 5.6, respectively.

The He-I PE spectrum of MoO_3 exhibits weak secondary structure in the metal 4d region, indicative of surface reduction. This may be attributed to the fact that the sample had to be heated to ca 620K in order to obtain the spectrum. The structure is compatible with that observed in the He-I PE spectrum of Mo_4O_{11}.

One might have thought then that the peak labelled x in the X-PE spectrum of MoO_3 (fig. 5.16) was also part of the Mo 4d structure. However, the situation is more complicated than this. Part of the structure is due to the $K\alpha_{3,4}$ radiation, but after this has been 'stripped away' from the spectrum, the peak x still has a sizeable intensity. Although the UV-PE spectrum of MoO_3 had to be recorded at elevated temperature, an X-PE spectrum recorded at room temperature striaght after sample pretreatment was exactly the same as shown in fig. 5.16. Further investigations revealed that the peak x was also present in the spectrum before the cleaning process and the effect was not peculiar to the sample of MoO_3 that we were using; similar results were

obtained from 'Analar' MoO_3.

Monochromatised X-PE spectra of both stoichiometric and substoichiometric MoO_3 have been reported by Rabalais et al.[37] The peak x is not present in their spectrum of stoichiometric MoO_3, but the authors remark that they used monochromatised radiation for the study because they feared that bremsstrahlung radiation might have a harmful effect on MoO_3. If reduction was caused by bremsstrahlung radiation, one might expect the intensity of the peak x to come up as a function of time, but this was not the case.

A similar peak has also been observed by Calabrese et al. in the achromatic X-PE spectrum of Na_2MoO_4.[38] They also mention that the same feature was present in PE spectra from MoO_3 and H_2MoO_4.

The most puzzling aspect of the peak x is that it does not correlate particularly well with the Mo 4d structure observed in the PE spectrum of substoichiometric MoO_3[37] or indeed with that observed in Mo_4O_{11}. The separation between the maxima in the O 2p band and the structure in the Mo 4d region is 5.7(5)eV for substoichiometric MoO_3, 6.3eV for Mo_4O_{11} and 7.0(5) for MoO_3. We are unable to provide any plausible explanation for these observations. The Mo 3d X-PE signals of MoO_3 (fig. 5.12) do not give any indication of a lower oxidation state of molybdenum being present, as they do in the case of Mo_4O_{11}.

Inspection of the He-II and X-ray PE valence region spectra from all five oxides, indicates that there is a remarkable similarity in the structure of the oxygen 2p band; three features (labelled a, b and c) can be discerned in each case. A similar O 2p profile has also been observed for the

tungsten bronzes (Na_xWO_3)[12] and ReO_3.[39] The three features a, b, c may be attributed to M-O σ, M-O π and O-O bands respectively.[36]

Whereas the PE spectra of Mo_4O_{11} are largely uninformative, as one might expect from a sample that has not been subjected to any 'cleaning' procedures, the PE spectra of $W_{18}O_{49}$ possess considerable structure. In fact, examination of the He-I spectrum of the compound (fig. 5.25) reveals a small Fermi edge.

Detailed physical properties of $W_{18}O_{49}$ are not known. However, $W_{18}O_{49}$ belongs to a series of mixed valency tungsten oxides ranging from WO_3 to WO_2, where there is a gradual breakdown of corner-sharing to edge-sharing on the part of the WO_6 octahedra. Electrical conductivity measurements have been reported on one of these mixed-valency oxides, namely $W_{20}O_{58}$, and metallic behaviour is indicated.[35]

It is particularly interesting (but also puzzling) why the He-I PE spectrum of an uncleaned sample of $W_{18}O_{49}$ should show a Fermi edge while that of uncleaned WO_2 does not. The presence of a Fermi edge from an 'uncleaned' oxide sample is contrary to the general conclusions of this thesis.

5.3 Transition metal sesquioxides

Six transition metal sesquioxides (Ti_2O_3, V_2O_3, Cr_2O_3, Mn_2O_3, Fe_2O_3, Rh_2O_3) are known to exist,[7] and all have been studied in this work. Apart from α-Mn_2O_3 which has the C-M_2O_3 structure,[2] these compounds possess the corundum structure at room temperature, although other polymorphs do exist.[2, 7]

The corundum structure consists of an approximate hexagonal close-packed (hcp) array of oxygen anions in which the

metal ions occupy two-thirds of the octahedral holes. However, electrostatic repulsion between cationic pairs along the c-axis results in a trigonal distortion of the oxygen environment of each metal.

Ti_2O_3 and V_2O_3 show collective electron behaviour and exhibit semiconductor $\longleftrightarrow$ metal transitions, whereas the later sesquioxides of the first transition series possess localised 3d electrons.[7, 23] The change from itinerant to localised electron behaviour along the series has been rationalised by Goodenough.[23] The physical properties of Rh_2O_3 are not so well characterised except that the compound exhibits semiconducting properties.[7]

Once inside the spectrometer the oxides were prepared as follows: Ti_2O_3 was heated *in vacuo* at *ca* 920K for two hours; V_2O_3 was heated *in vacuo* at *ca* 870K for two hours; Cr_2O_3 was heated for $2\frac{1}{2}$ hours at *ca* 820K under a dynamic partial pressure of 10^{-3} torr O_2; Mn_2O_3 was heated at *ca* 820K for two hours under one atmosphere of oxygen; Fe_2O_3 was heated *in vacuo* at *ca* 870K for two hours; $Rh_2O_3 \cdot 5H_2O$ was dehydrated to Rh_2O_3 by heating in one atmosphere of oxygen at *ca* 1000K for two hours.[40, 41] The sample cleaning procedures were sufficient to realise clean O 1s PE signals for Ti_2O_3, V_2O_3, Cr_2O_3 and Fe_2O_3. Slight asymmetries to higher B.E were still detected for Mn_2O_3 and Rh_2O_3. However, one is unable to heat Mn_2O_3 at a higher temperature than that employed without fear of reduction to Mn_3O_4.[7] Attempts to heat Rh_2O_3 *in vacuo*, resulted in reduction of the sample, as witnessed by the form of the Rh 3d X-PE signals.

Valence region PE spectra of the sesquioxides are

reproduced in figs. 5.26 to 5.33. The spectra of Ti_2O_3, V_2O_3 and Rh_2O_3 (unless otherwise indicated) were recorded at room temperature. Because of sample charging the spectra of Cr_2O_3, Mn_2O_3 and Fe_2O_3 had to be recorded at ca 690K, 600K and 670K, respectively, to ensure a reasonable He-I intensity. These observations are consistent with the reported electrical conductivity data on these compounds.[42]

Immediately after insertion into the spectrometer, the sample of Ti_2O_3 gave PE spectra that were consistent with a considerable overlayer of TiO_2. The Ti 2p signals (fig. 5.34) exemplify this point. (These core signals are much broader in Ti_2O_3 than TiO_2 due to the interaction of the core-hole with the Ti 3d band). The UV-PE spectra obtained before cleaning were essentially the same as those reported from TiO_2.[43]

Heating the sample in vacuo ensured the 'emergence' of the Ti 3d band (fig. 5.28). After approximately 30 mins at ca 870K, the band assumed its maximum intensity and exhibited a Fermi edge (though not as sharp as was observed for some of the dioxides).

The Ti_2O_3 surface proved to be extremely susceptible to reoxidation. When the sample was left at room temperature overnight, the Ti 3d band was found to have diminished to half its intensity. This extreme surface sensitivity appears to be characteristic of all the lower oxides of Ti.[44] This point seems to have been overlooked by previous workers[45] who attempted to record X-PE spectra from various Ti suboxides without any surface pretreatment.

Ti_2O_3 undergoes a SMT over the temperature range 400-470K; the transition is at least second order.[7, 46] Pure Ti_2O_3 in

the range 100-300K is an intrinsic semiconductor with a small band gap (0.03 to 0.05 eV). It is apparent from the wide spread in the electrical properties reported in the literature, that the transition is critically dependent on the exact stoichiometry of the sample.

We recorded the He-I PE spectrum of Ti_2O_3 at both room temperature and at ca. 730K; however, no significant change in the Ti 3d band could be detected. The room temperature He-I PE spectrum from a cleaved single crystal has recently been reported[43] and is in good agreement with our spectrum. We are then led to conclude that the surface sensitivity of Ti_2O_3 precludes direct observation of the high-order SMT.

V_2O_3 is a metal at room temperature, but undergoes a first-order phase transition to an antiferromagnetic, monoclinic, semiconducting state at ca 150K. Our room temperature He-I spectrum of V_2O_3 (fig. 5.29) possesses a sharp Fermi edge. In contrast to the sample of Ti_2O_3, the metal 3d band in V_2O_3 deteriorates little at room temperature.

On cooling the sample to ca. 135K, by passing liquid nitrogen through the probe assembly, we have seen some indication of the SMT transition. Fig. 5.30 shows the He-I spectrum of V_2O_3 cooled down to ca. 135K and then allowed to warm up to room temperature. The two spectra in fig. 5.30 show clear differences, but not quite as marked as for VO_2. The Fermi edge has almost disappeared at the lower temperature and there is also a decrease in the relative intensity of the maximum of the V 3d band with respect to the minimum between the V 3d and O 2p bands. However, the room temperature He-I spectrum obtained after the sample had been cooled down to ca. 135K, and then allowed to warm again (fig. 5.30),

shows signs of deterioration compared with the original spectrum (fig. 5.29). On taking the sample through several cooling cycles, surface contamination resulted in the complete loss of the Fermi edge. This phenomena is almost certainly due to contaminants condensing more readily on the cold sample surface.

Our experimental arrangement permitted little control over the exact temperature of the sample and we were unable to lower the temperature further than ca. 125K. It is also unclear whether the thermocouple reading reflects the true temperature of the sample and also whether the whole sample is at this temperature. Despite these difficulties, there are some reproducible changes in the V 3d band in crossing the SMT.

Goodenough[23] has proposed the following bonding scheme to explain the electronic properties of the sesquioxides. The trigonal distortion afforded by the corundum structure lowers the site symmetry of the transition metal from O_h to C_{3V}. Referring to the coordinate system adopted by Ashkenazi[47] (where the z-axis corresponds to the c-axis and the y-axis to the two fold axis of the lattice), it is possible to distinguish the following categories of metal d orbital: (i) a_1 (d_{z^2}) orbital, which is directed along the c-axis toward one near-neighbour through a common octahedral-site face; and (ii) two doubly-degenerate orbitals e (σ) and e (π), both consisting of combinations of d_{xz}, d_{yz}, $d_{x^2-y^2}$ and d_{xy}, whose lobes are directed either towards the oxygens (e (σ)) or toward three neighbouring cations in the puckered basal plane (e (π)). Goodenough[23] labels these three sets of orbitals a^T, e (σ) and e^T(π) respectively. It is important to stress the fact that, because of the deviation from cubic

symmetry, the e (σ) and e (π) orbitals here are not the ordinary e (σ) and e^{T}(π) bands in a cubic crystal, but certain admixtures of them. We are then led ultimately to a band scheme of the form given in fig. 5.35, which depicts the one-electron energies for the room-temperature form of Ti_2O_3 and α-Cr_2O_3 respectively. Whether the bonding a_1 and e(π)* bands overlap depends upon the widths of these bands and the magnitude of the crystallographic C_H/a_H ratio (hexagonal basis). With one outer d electron per Ti^{3+} ion, the small C_H/a_H ratio of Ti_2O_3 stabilises a filled, bonding a_1 band at the expense of empty e (π)* bands. With two 3d electrons per V^{3+} ion, the large C_H/a_H ratio of V_2O_3 stabilises the two bonding e(π)* oribtals per cation relative to the lower a_1 band. In fig. 5.36 we depict the one-electron energies for the rhombohedral (corundum) and monoclinic phases of V_2O_3.

We now turn our attention to the remaining sesquioxides of the first transition series, Cr_2O_3, Mn_2O_3 and Fe_2O_3. Both the He-II[25] and monochromatic X-PE[48] spectra of Cr_2O_3 have been reported previously and are in good agreement with the PE spectra presented here. All three sesquioxides exhibit localised electron behaviour. As such, we anticipate that the metal 3d structure in the PE spectra of these compounds may be interpreted using a ligand-field description of the localised $3d^{n-1}$ final states.

The site symmetry of the transition metal is not properly O_h in any of the oxides. (Mn_2O_3 possesses the c-M_2O_3 structure which contains two types of distorted octahedra). However these distortions (for both the corundum and c-M_2O_3 structures) are probably comparatively small and the transition metal ions may be treated as if they were in regular

octahedral environments.

The states arising upon ionisation of d^n configuration in cubic fields have conveniently been tabulated.[49] The features c and d in the He-I spectrum of Fe_2O_3 (high-spin d^5) may be attributed to the final states $^5T_2$ and ^5E, respectively.

It was hoped originally to prepare the sample surface of Fe_2O_3 by heating the compound in one atmosphere of oxygen. However, it proved impossible to record any UV-PE spectra from a sample that had been treated in this way (presumably because of sample charging effects). When the sample was heated *in vacuo*, no problems were encountered in measuring UV-PE spectra, provided that they were recorded at an elevated temperature (670K). One conclusion that may be drawn from these observations is that heating the sample *in vacuo* may have reduced it partially to Fe_3O_4. However, the core X-PE spectra were all consistent with an oxidation state of +3 for the metal. Furthermore, UV-PE spectra of Fe_3O_4 have been reported[50] and show significant differences when compared with our spectra. The satisfactory assignment of the spectrum in terms of final state structure from a d^5 ground state confirms that the spectrum is indeed representative of Fe_2O_3. Consideration of the relevant thermodynamic data for the Fe_3O_4/Fe_2O_3 system[51] gives *ca* 1000K as the temperature at which Fe_2O_3 would decompose if heated in *ca* 10^{-9} torr O_2.

The UV-PE spectra of Cr_2O_3 and Rh_2O_3 (fig. 5.27) exhibit similar well resolved structure. In tables 5.7 and 5.8 we list the energy separations of the various features in the valence band PE spectra for Cr_2O_3 and Rh_2O_3, respectively. The structure due to the metal 3d electrons in the spectrum of the Cr (III) compound is well resolved from the oxygen 2p

band because only one final state ($^3T_1$) can be reached by photoionisation of $t_{2g}{}^3$ ($^4A_2$).[49]

In the case of Rh_2O_3 it is apparently not known whether the d electrons are significantly delocalised; nor has the spin state of the Rh ion been determined, so far as we can discover. However, it is most likely that Rh^{3+} is low spin ($t_{2g}{}^6$) and, unless there is an unusual mutual perturbation between d electrons on different sites, one would again expect a single PE signal from the d subshell.

5.4 Transition metal monoxides

In the majority of transition metal oxides, there is considerable overlap between the O 2p and metal nd partial DOS. However once the metal d band is completely filled, there is a marked increase in its binding energy with the result that it separates from the O 2p band. For the d^{10} systems, ZnO and CdO, the metal nd band is still within the range of He-I and He-II radiation. This allows direct observation of the change in the relative nd to O 2p photo-ionisation cross-section with incident photon energy. The PE spectra of both these two oxides and also of NiO are reported in this section.

Sample pretreatment procedures for the oxides were as follows: ZnO was heated *in vacuo* at *ca.* 900K for $1\frac{1}{4}$ hours; CdO was heated under one atmosphere of oxygen at *ca.* 930K for two hours; NiO was heated under one atmosphere at *ca.* 900K for $2\frac{1}{2}$ hours. A symmetrical O 1s PE signal was observed for ZnO, but for both NiO and CdO there was some asymmetry to higher B.E. Several transition metal oxides, are found in fact to possess two O 1s PE signals, even after the sample has been heated to high enough temperature to ensure

the decomposition of surface hydroxides and carbonates. The peak corresponding to smaller B.E will be due to the lattice oxygen ions O^{2-}. The small peak to higher B.E usually corresponds to chemisorbed oxygen or oxygen ions in a partial lattice of a higher-valent oxide.[8] In the case of NiO the smaller peak is thought to correspond to Ni_2O_3 which is only stable in the surface region.[8, 52] In the case of both NiO and CdO, heating the sample in vacuo ensured that the O 1s signal became more symmetrical; however, it was clear from the other core PE signals that slight reduction of the sample had also taken place. It should also be pointed out that when the sample of CdO was subjected to prolonged heating, traces of sulphur could be detected in the wide scan X-PE spectrum (see section 3.2).

The He-I and He-II PE spectra (recorded at room temperature) of ZnO and CdO are reproduced in fig. 5.37. In the X-PE valence region spectra of these oxides much of the oxygen 2p band is obscured by the $K\alpha_{3,4}$ satellites of the Zn 3d band. For this reason, we present in fig. 5.38 both the observed and deconvoluted X-PE spectra of ZnO and CdO. Comparison of the spectra in figs. 5.37 and 5.38 shows that, for both ZnO and CdO, there is a marked increase in intensity of the metal nd relative to the oxygen 2p band on changing from UV to X-ray excitation. For ZnO we have measured the respective intensities of the Zn 3d and O 2p bands in the He-II and X-PE spectra. It is found that I(3d)/I(2p) = ca. 0.75 for He-II radiation and ca. 4.9 for X-radiation. In this analysis we have corrected for the analyser transmittance but have neglected any contribution of the Zn 4s electrons to the O 2p band.[53]

The energy separations between features in the valence region PE spectra of ZnO and CdO are listed in tables 5.9 and 5.10, respectively. These can only be determined really accurately for the He-II spectra. In the He-I spectra, the low K.E metal d signals are much affected by the analyser transmittance while, in the X-ray spectra, the $\alpha_{3,4}$ satellites have to be removed before the O 2p can be observed properly.

Both UV[53, 54] and X-PE[55] spectra from ZnO have been previously reported and are in agreement with those reported here. The metal nd signals in the He-II spectra of both ZnO and CdO show no sign of the expected spin-orbit coupling; this contrasts with the splittings of the d signals observed in the gas-phase He-II PE spectra from zinc and cadmium halides.[56] There are probably two reasons for this: (i) the perturbation of the crystal field may be of comparable magnitude to the multiplet splitting; and (ii) phonon broadening.

The oxygen 2p bands in both ZnO and CdO are very similar; in each case three features (labelled b, c and d) can usually be discerned. As has been mentioned previously (section 4.1), the form of the O 2p band in CdO (which has the rock salt structure) is similar to that predicted by the semi-empirical band structure calculation performed on a cubic close packed (ccp) array of oxygen anions (fig. 4.1). ZnO has the wurtzite structure which consists of hexagonal close packed (hcp) oxygen anions. The hcp and ccp structures have very similar near neighbour interactions (9 out of the 12 are exactly the same), and thus it is possible to rationalise the fact that similar O 2p structure is observed in the PE spectra of ZnO and CdO.

The He-I and X-ray PE spectra of NiO are presented in fig. 5.39. Both were recorded at room temperature and are in essential agreement with those reported from a cleaved single crystal.[25] This fact serves to emphasise that UV-PE spectra of comparable quality to those from single crystals can be obtained from the polycrystalline (powdered) material with appropriate sample preparation. The spectra have been adequately discussed in the literature, and no further comment is needed here.

Table 5.1 Rutile-type dioxides

d^0	d^1	d^2	d^3	d^4	d^5	d^6
TiO_2 [1,3,6]	VO_2 [2,7]	CrO_2 [2,5,8]	MnO_2 [1,3,9]			
	NbO_2 [2,7]	MoO_2 [2,5]	TcO_2 [2,5]	RuO_2 [1,5]	RhO_2 [1,4,5]	
		WO_2 [2,5]	ReO_2 [2,3,5]	OsO_2 [1,5]	IrO_2 [1,5]	PtO_2 [1,4,5]

Key to superscripts

1 = Rutile Structure

2 = Distorted Rutile structure

3 = Polymorphic

4 = Amorphous when prepared under atomspheric pressure, but crystallises under pressure.

5 = Metallic

6 = Semi-conductor

7 = Exhibits semiconductor $\longleftrightarrow$ metal transition. Below transition temperature, the dioxide possesses the distorted rutile structure and is a semicondcutor. Above transition temperature the dioxide possesses the perfect rutile structure and is metallic.

8 = Ferromagnet

9 = Antiferromagnet

Table 5.2 Energy separations between features in the valence band PE spectrum of NbO_2 (measured in eV)

Peak	He-II	X-ray
c	0	0
b	4.9	4.9(5)
a	6.5	6.5(5)

Table 5.3 Energy separations between features in the valence band PE spectrum of RuO_2 (measured in eV)

	Fermi edge	peak c	peak b
Ne-I	0.0	4.5*	-
He-I	0.0	4.8	6.7*
Ne-II	0.0	4.8	6.9
He-II	0.0	4.8	7.0
X-ray	0.0	4.7	6.9
Monochromatised X-ray[13]	0.0	4.7	6.9
APW-LCAO band calc.[24]	0.0	4.8	6.8

*These values are lower than expected due to the effects of the analyser transmittance.

Table 5.4 Energy separations between features in the valence band PE spectrum of WO_3 (measured in eV)

Peak	He-I	He-II	X-ray
c	0.0	0.0	0.0
b	2.0	2.0(5)	2.4
a	4.9(5)	4.8	4.8

Table 5.5 Energy separations between features in the valence band PE spectrum of MoO_3 (measured in eV)

Peak	He-II	X-ray
c	0.0	0.0
b	1.9(5)	1.8
a	3.7	3.5

Table 5.6 Energy separations between features in the valence band PE spectrum of $W_{18}O_{49}$ (measured in eV)

Peak	He-I	He-II	X-ray
c	0.0	0.0	0.0
b	2.9	2.2	2.5(5)
a	5.2(5)	5.2(5)	4.4

Table 5.7 Energy separations between features in the valence band PE spectrum of Cr_2O_3 (measured in eV)

Peak	He-I	He-II	X-ray
c	0.0	0.0	0.0
b	2.9(5)	2.4(5)	3.1
a	4.2	3.7	5.1

Table 5.8 Energy separations between features in the velence band PE spectrum of Rh_2O_3 (measured in eV)

Peak	He-I	He-II	X-ray
d	0.0	0	0
c	2.7(5)	2.7	3.0
b	5.0	5.1	6.0(5)

Table 5.9 Energy separations between features in the valence band PE spectrum of ZnO (measured in eV)

Peak	He-II	X-ray
c	0.0	0.0
b	2.6(5)	2.2
a	5.7	5.4

Table 5.10 Energy separations between features in the valence band PE spectrum of CdO (measured in eV)

Peak	He-I	He-II	X-ray
c	0.0	0.0	0.0
b	2.1	2.4	2.0
a	5.4(5)*	6.0	5.4

*Taken from probe-biassing experiments, where the position of the Cd 4d signal can be more accurately determined (see fig. 3.7).

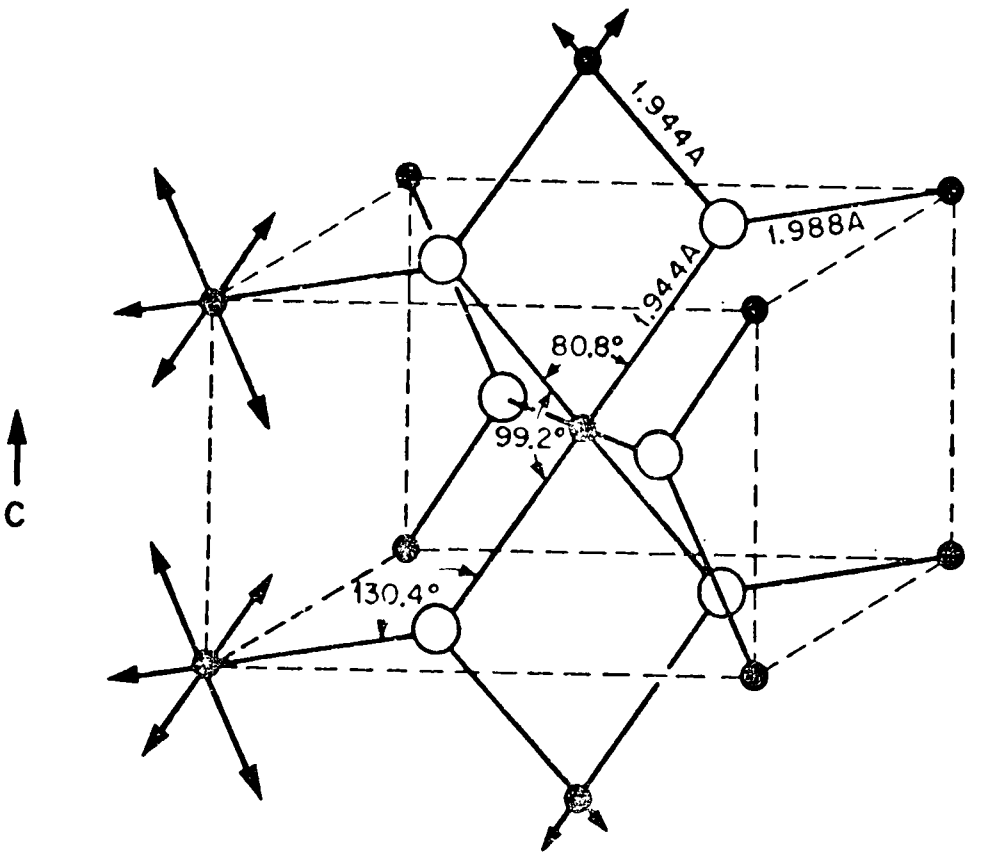


Fig. 5.1. The tetragonal structure of rutile TiO_2

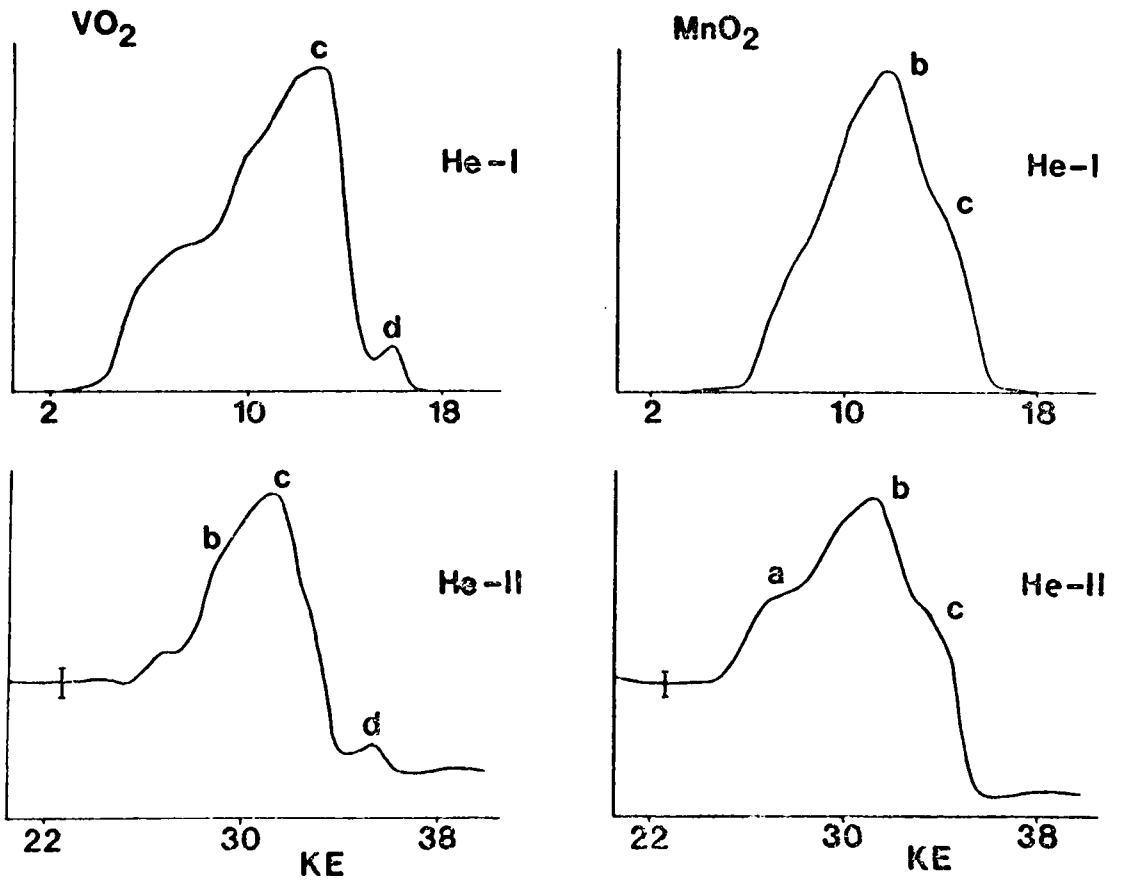


Fig. 5.2. He-I and He-II PE spectra of VO_2 and MnO_2

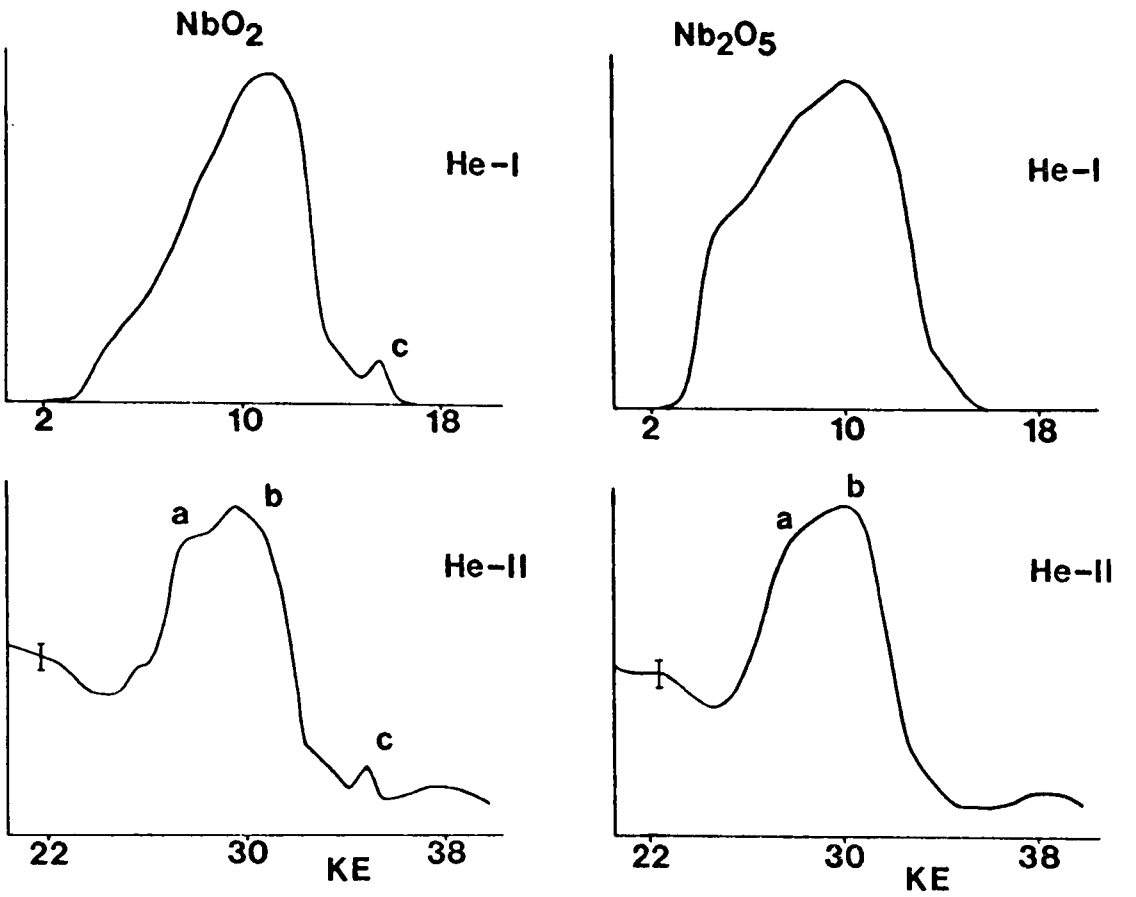


Fig. 5.3. He-I and He-II PE spectra of NbO_2 and Nb_2O_5

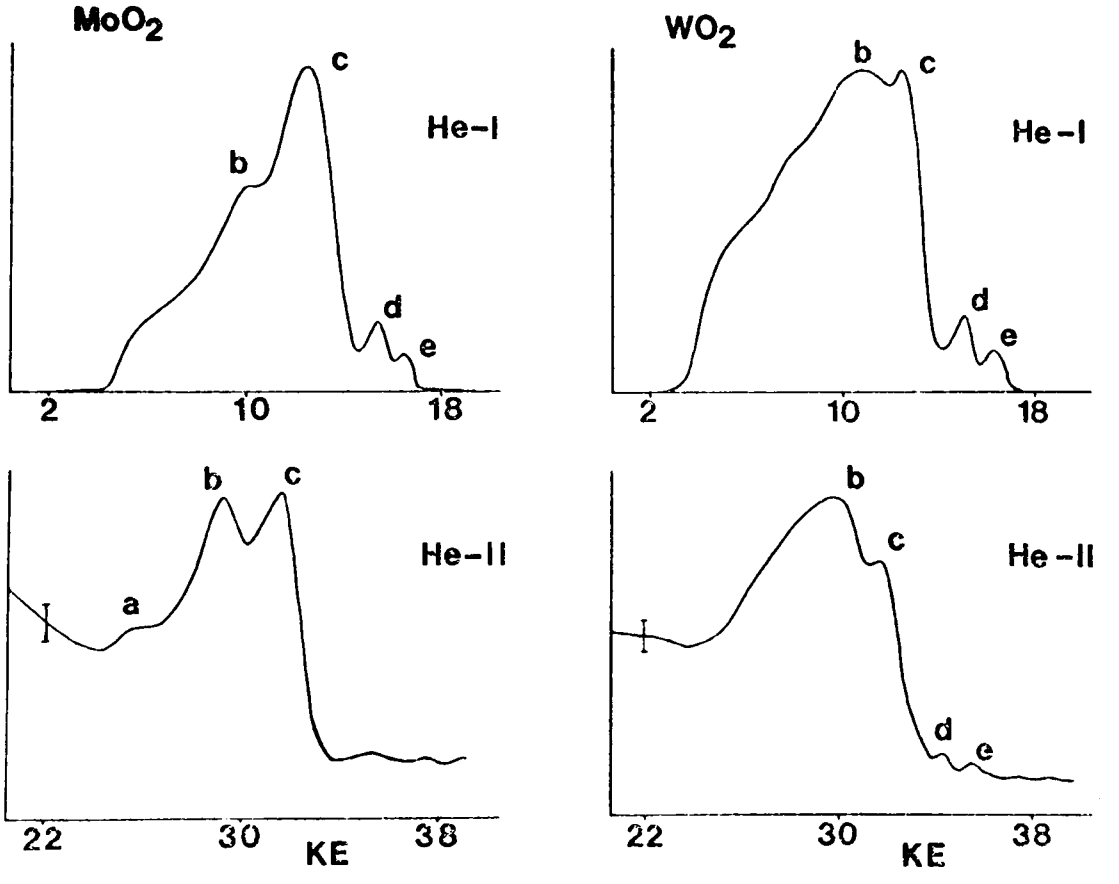


Fig. 5.4. He-I and He-II PE spectra of MoO_2 and WO_2

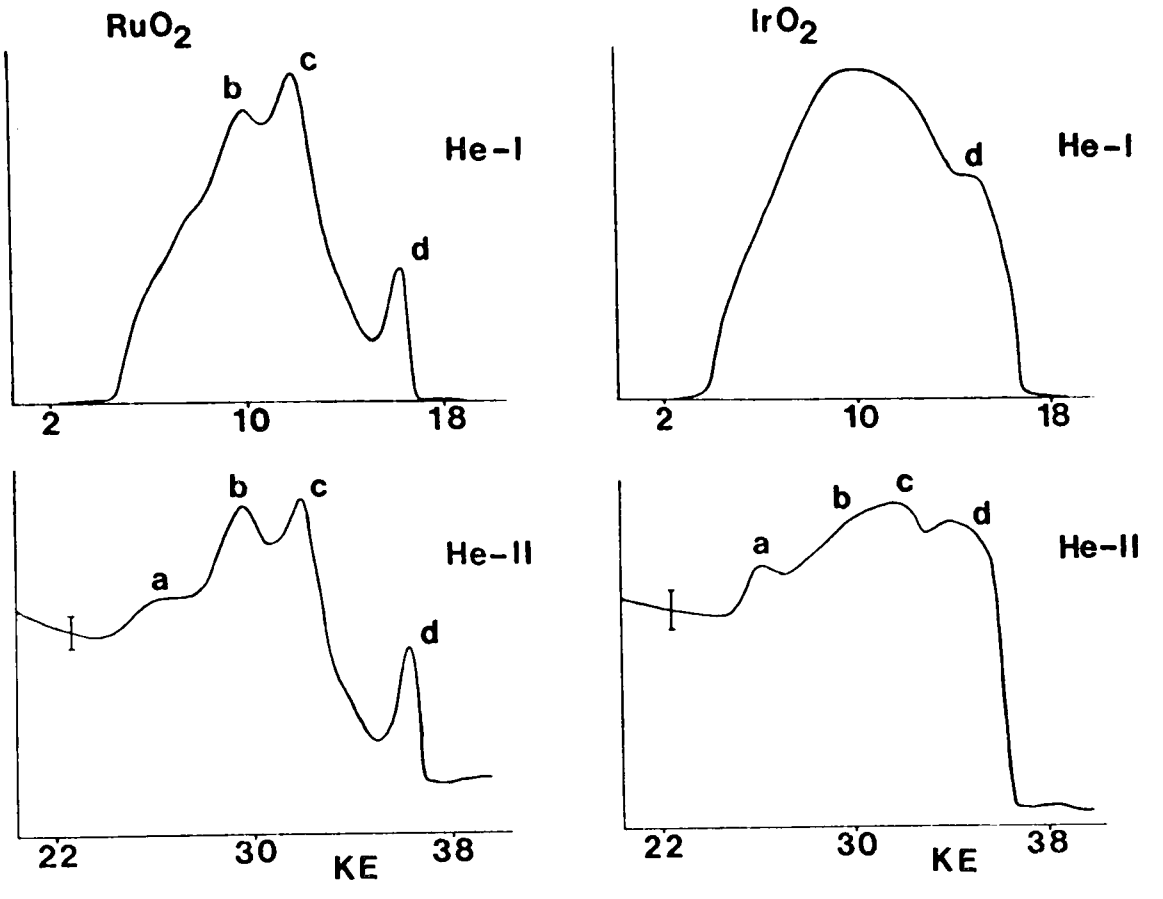


Fig. 5.5. He-I and He-II PE spectra of RuO_2 and IrO_2

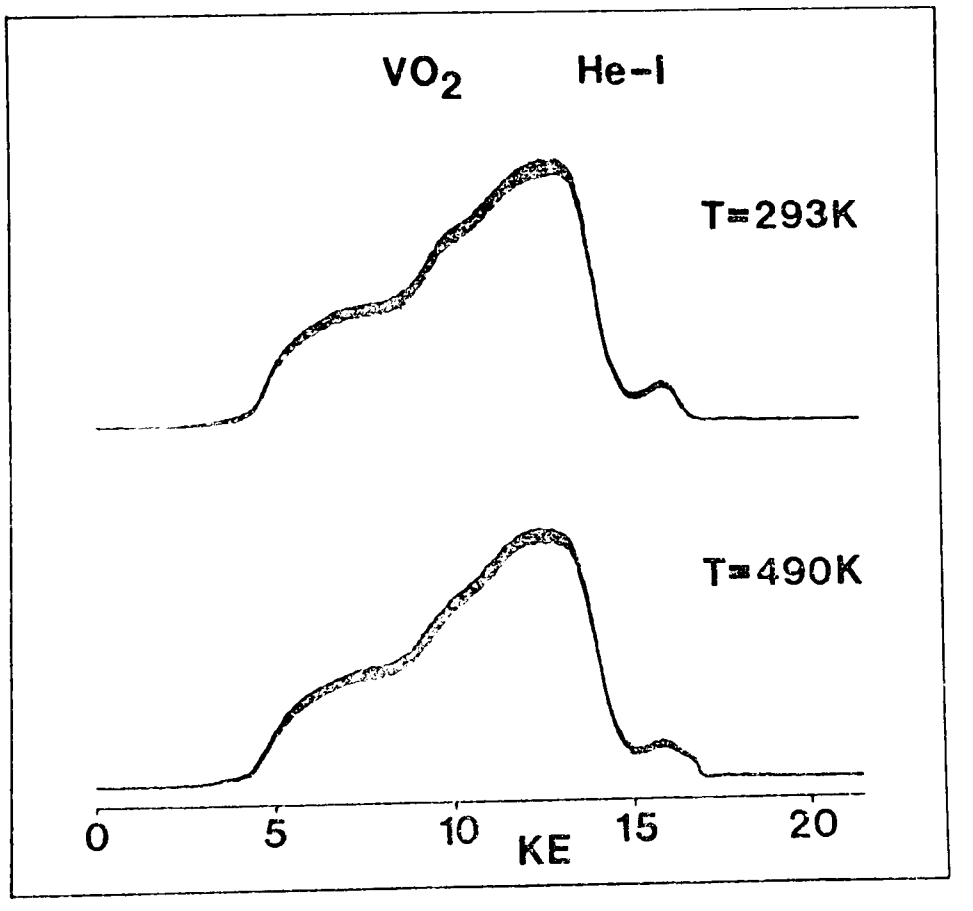


Fig. 5.6. He-I PE spectrum of VO_2 below and above the semiconductor $\longleftrightarrow$ metal transition temperature

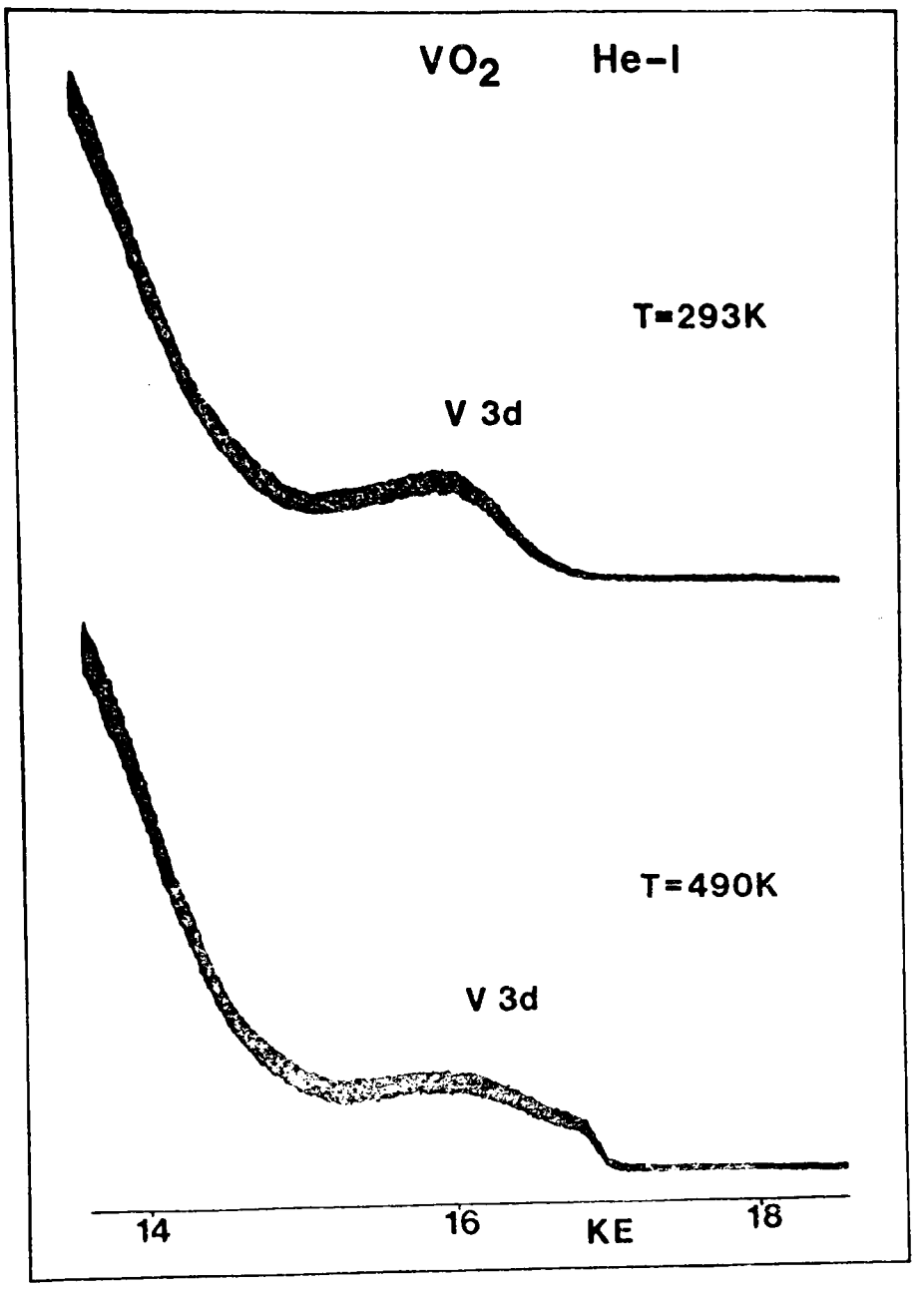


Fig. 5.7. The metal 3d structure in the He-I PE spectrum of VO_2 below and above the semiconductor $\longleftrightarrow$ metal transition temperature.

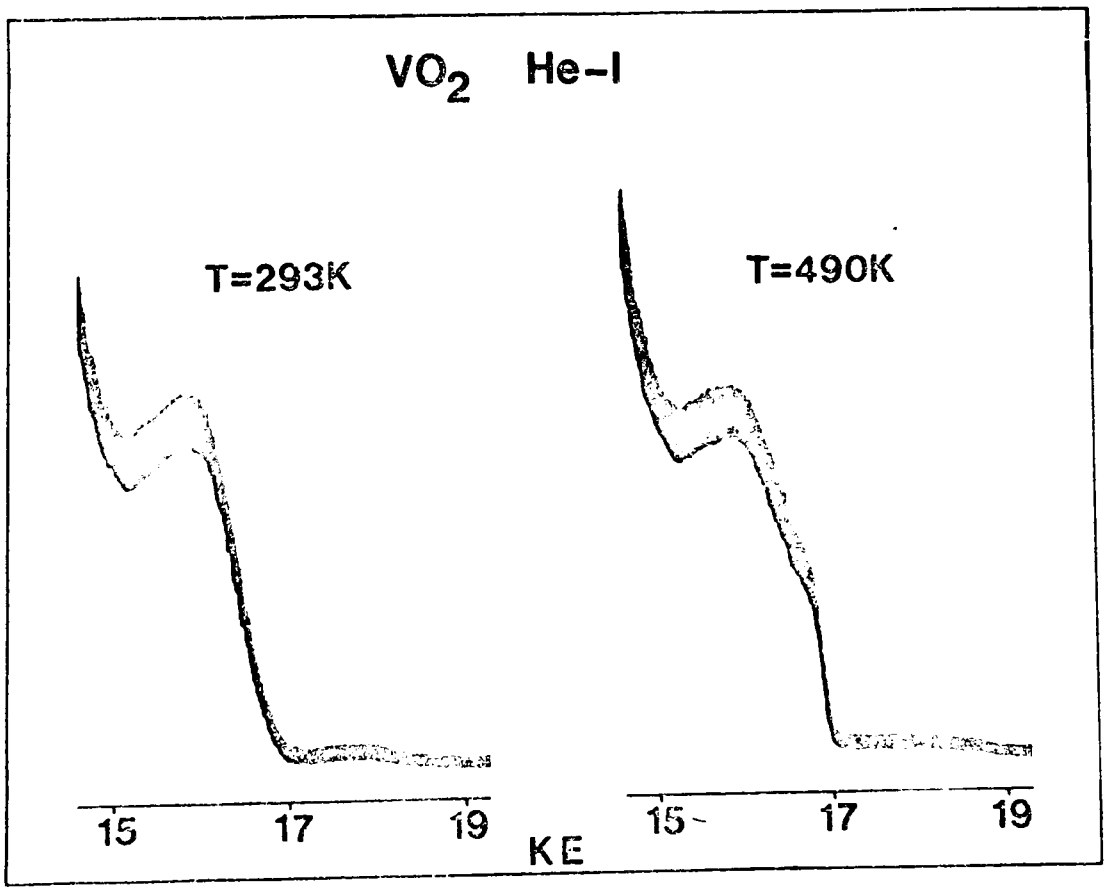


Fig. 5.8. Expansion of the V 3d structure in the He-I PE spectrum of VO_2 illustrating the semiconductor $\longleftrightarrow$ metal transition

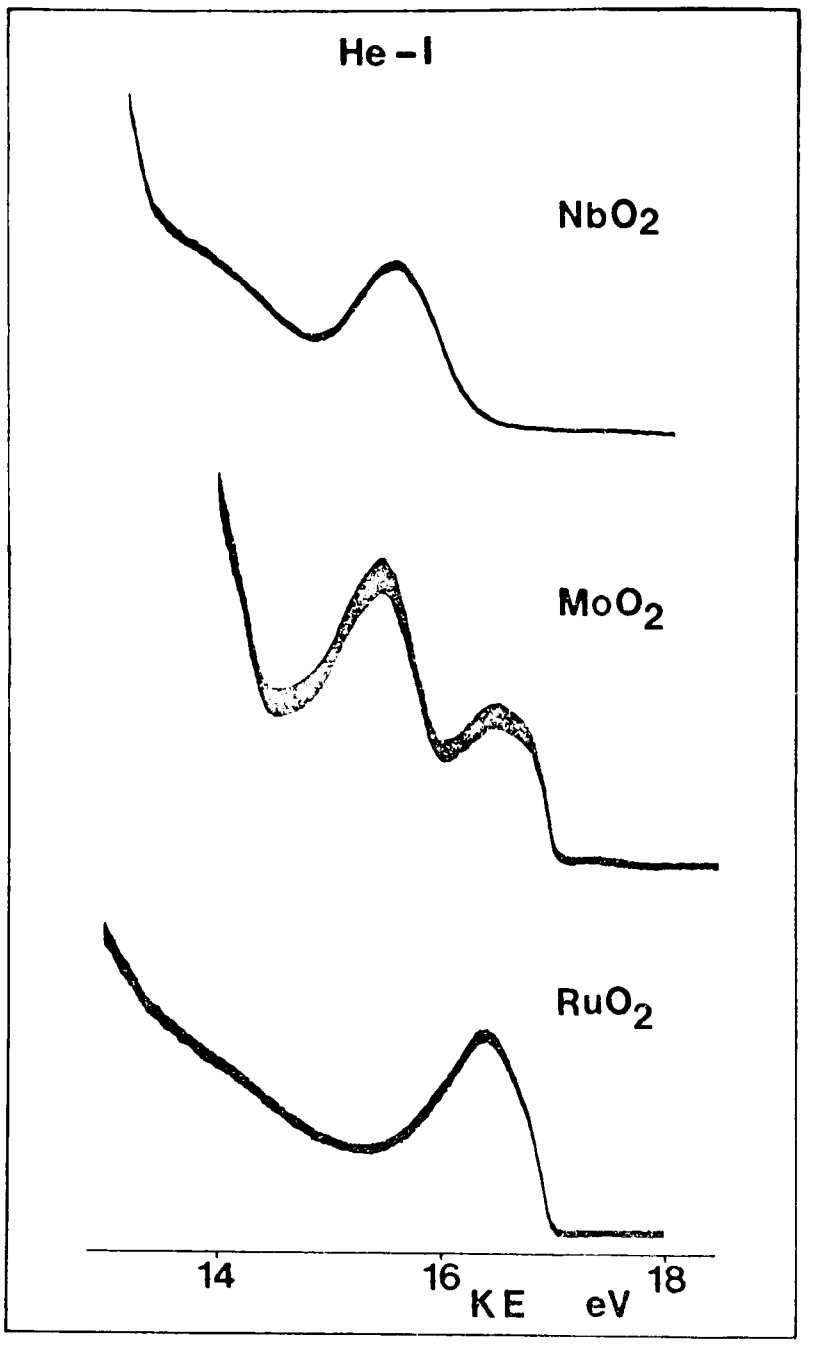


Fig. 5.9. The metal 4d structure in the He-I PE spectra of NbO_2, MoO_2 and RuO_2

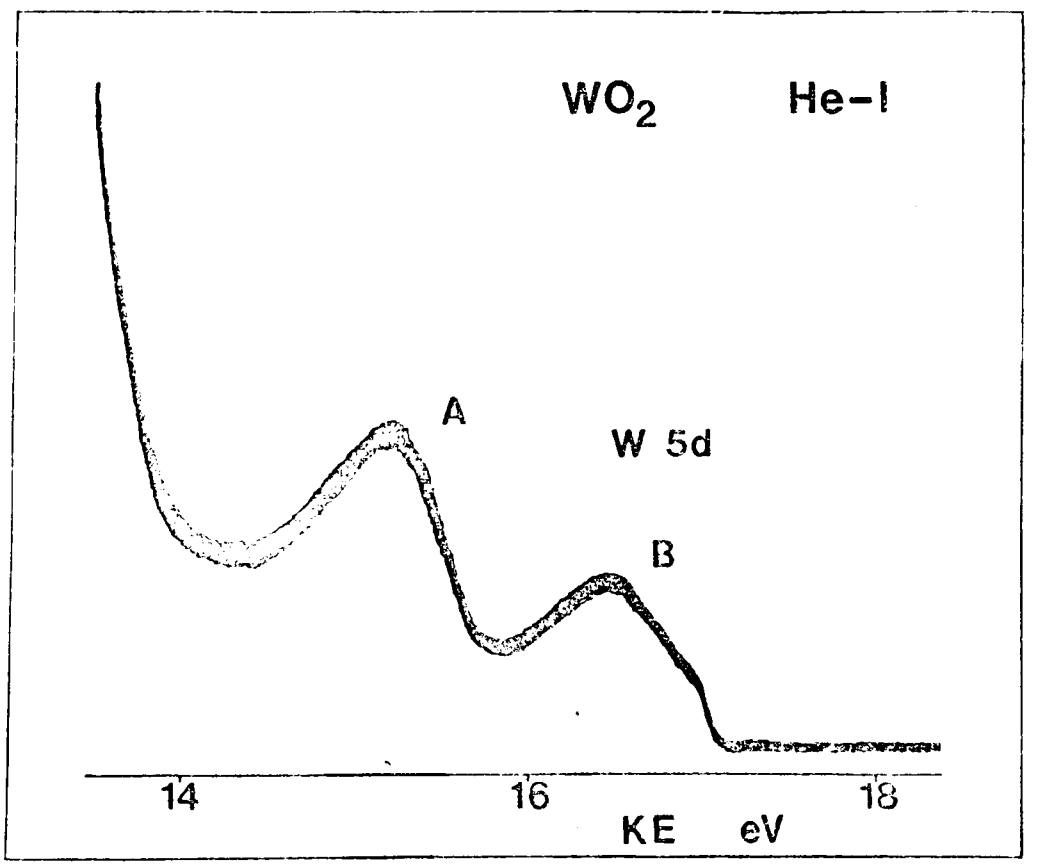


Fig. 5.10. The metal 5d structure in the He-I PE spectrum of WO_2

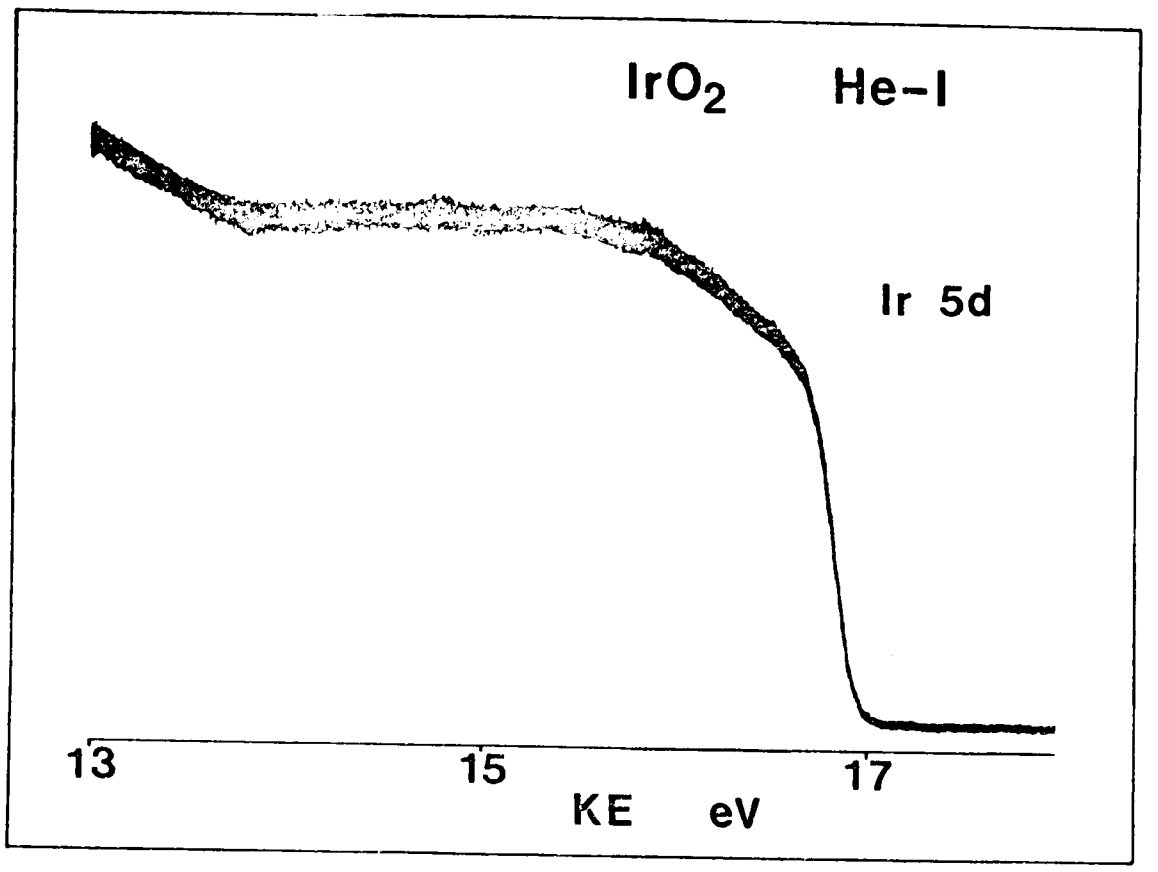


Fig. 5.11. The metal 5d structure in the He-I PE spectrum of IrO_2

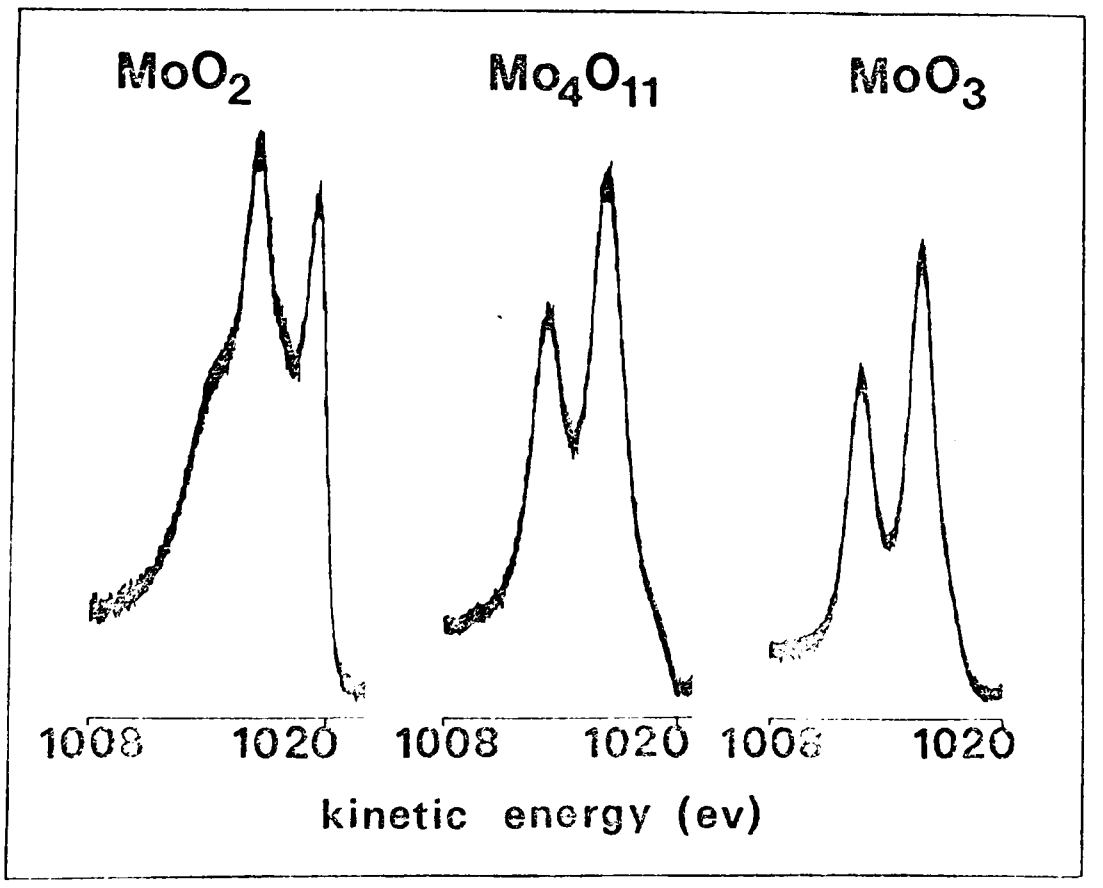


Fig. 5.12. The Mo 3d X-PE spectra of MoO_2, Mo_4O_{11} and MoO_3

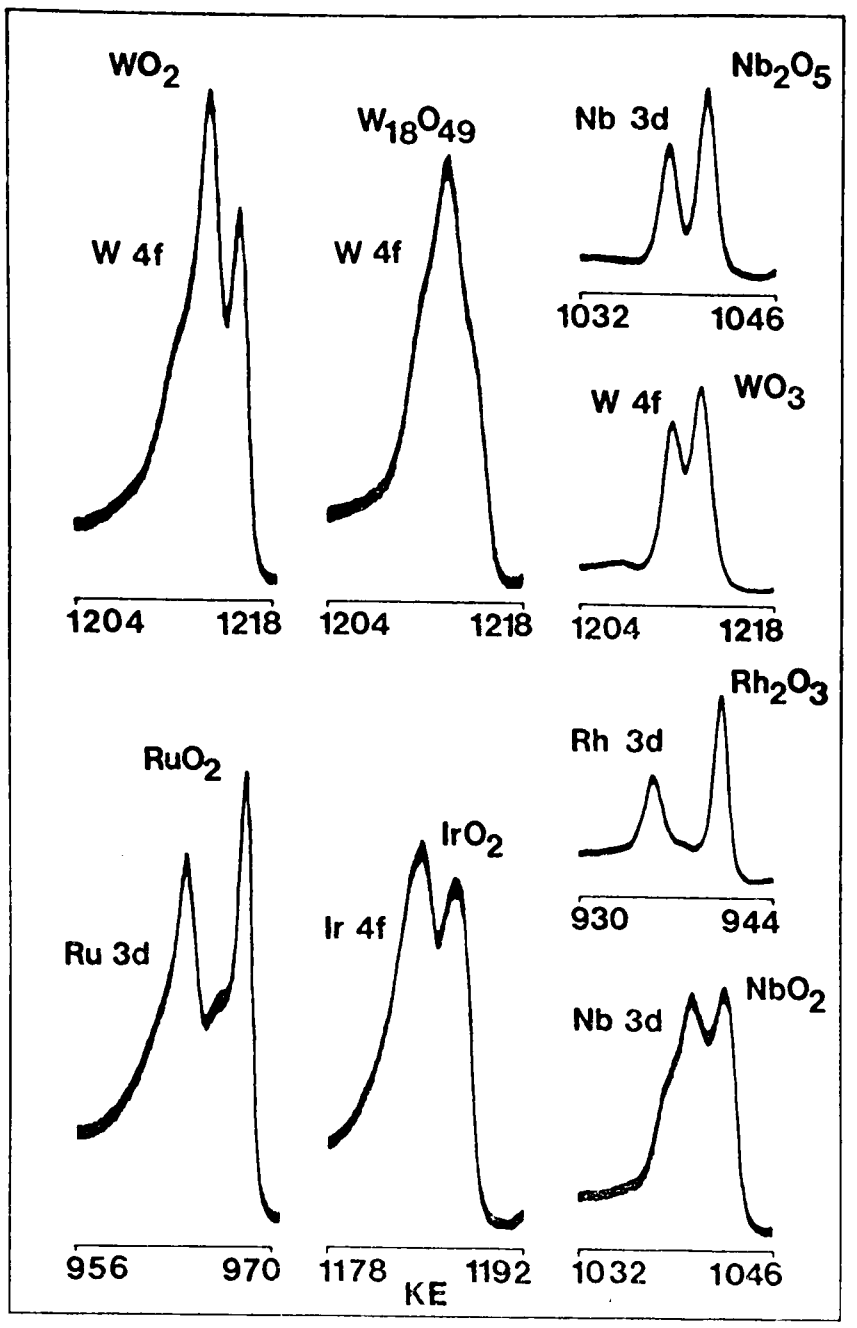


Fig. 5.13. The principal core-level PE signals from WO_2, $W_{18}O_{49}$, Nb_2O_5, WO_3, RuO_2, IrO_2, Rh_2O_3 and NbO_2

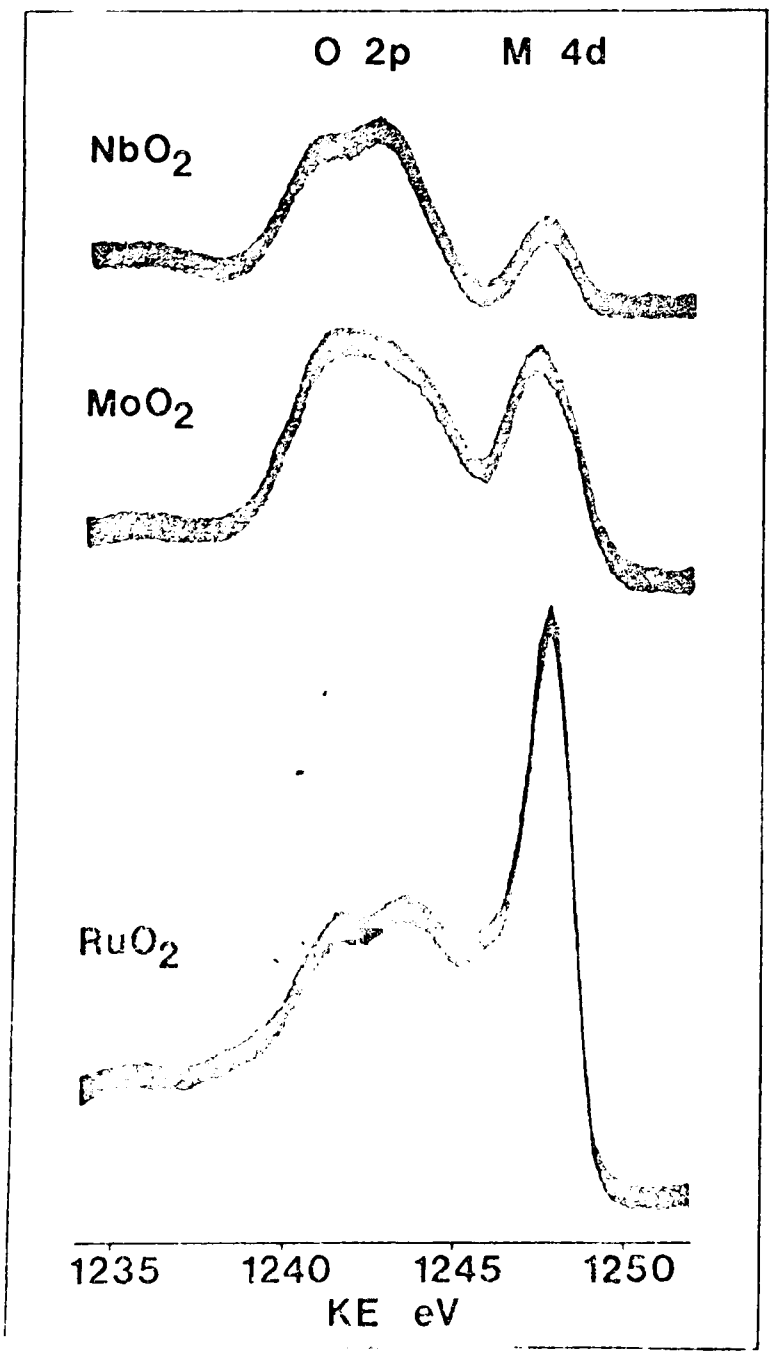


Fig. 5.14. Valence region X-PE spectra of NbO_2, MoO_2 and RuO_2

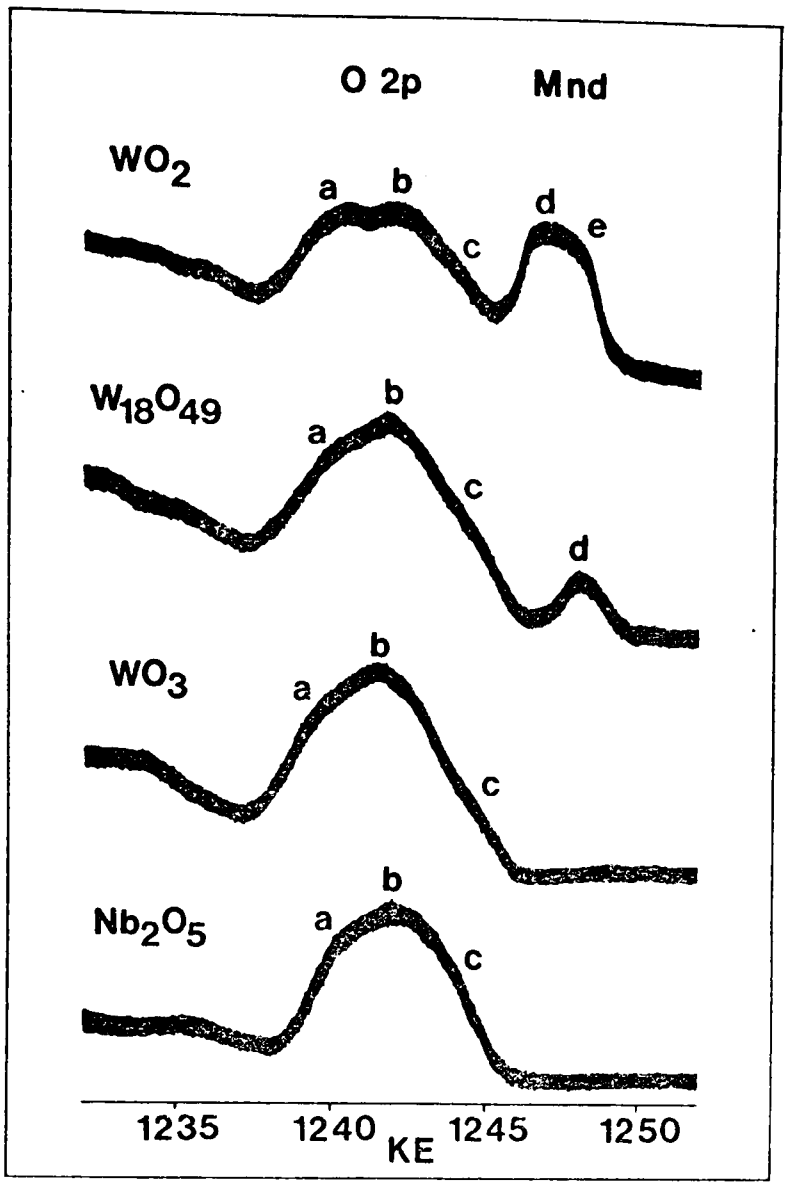


Fig. 5.15. Valence region X-PE spectra of WO_2, $W_{18}O_{49}$, WO_3 and Nb_2O_5

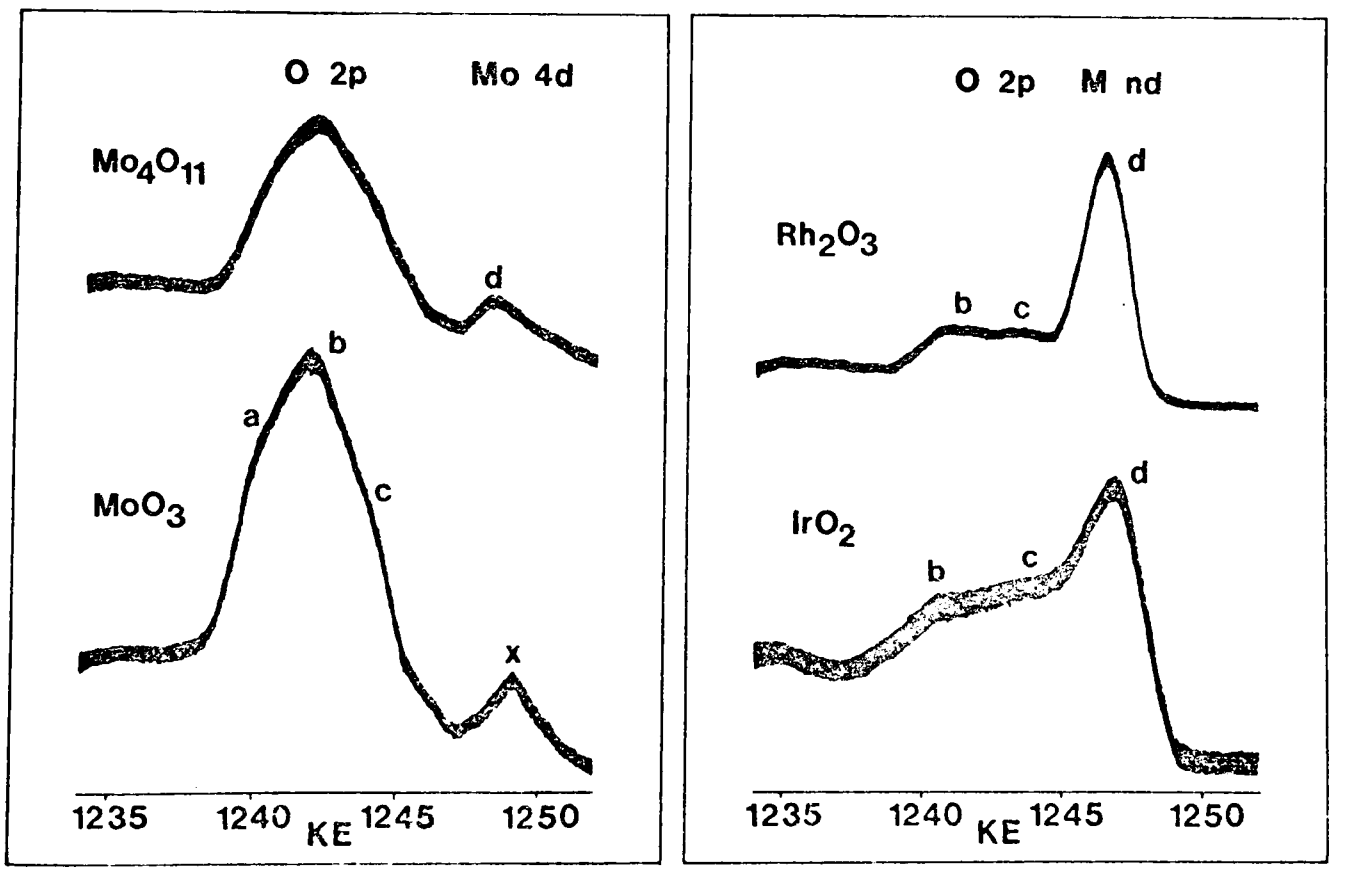


Fig. 5.16. Valence region X-PE spectra of Mo_4O_{11}, MoO_3, Rh_2O_3 and IrO_2

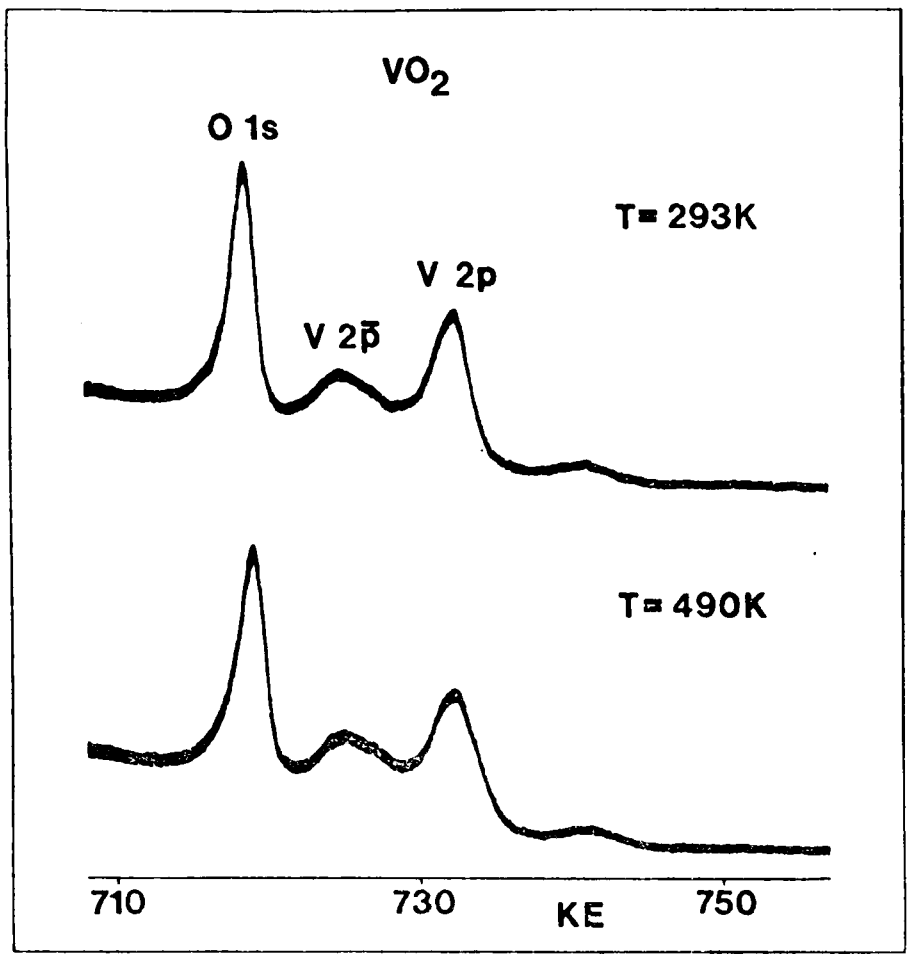


Fig. 5.17. The O 1s and V 2p PE signals from VO_2 below and above the semi-conductor —— metal transition

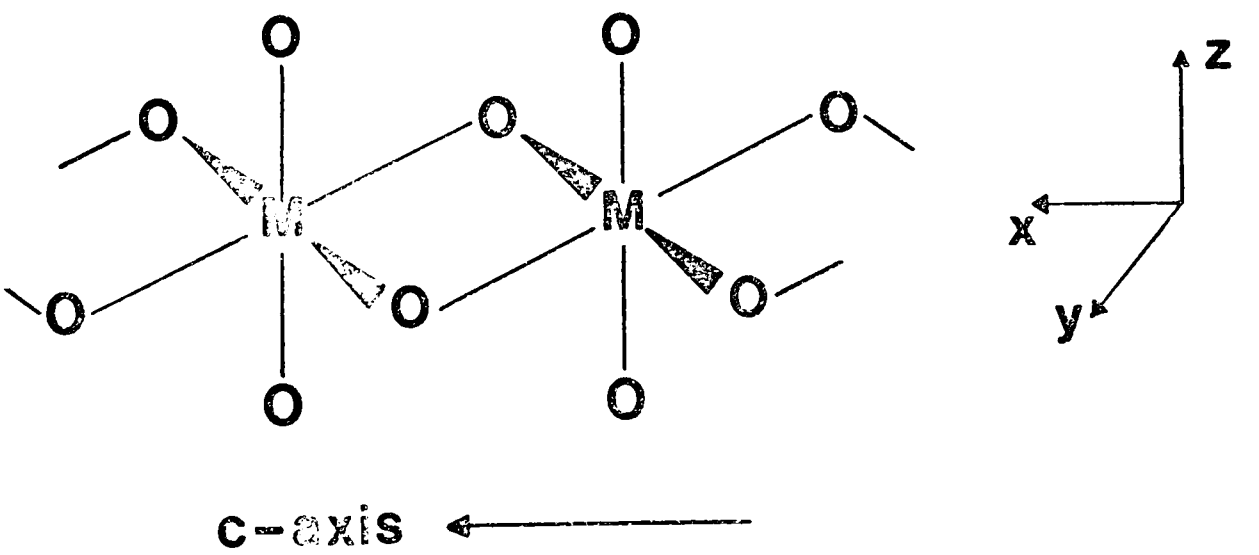


Fig. 5.18. Part of the chain of edge-sharing MO_6 octahedra in the undistorted rutile (TiO_2) structure, with a convenient choice of local cartesian axes for the metal ions

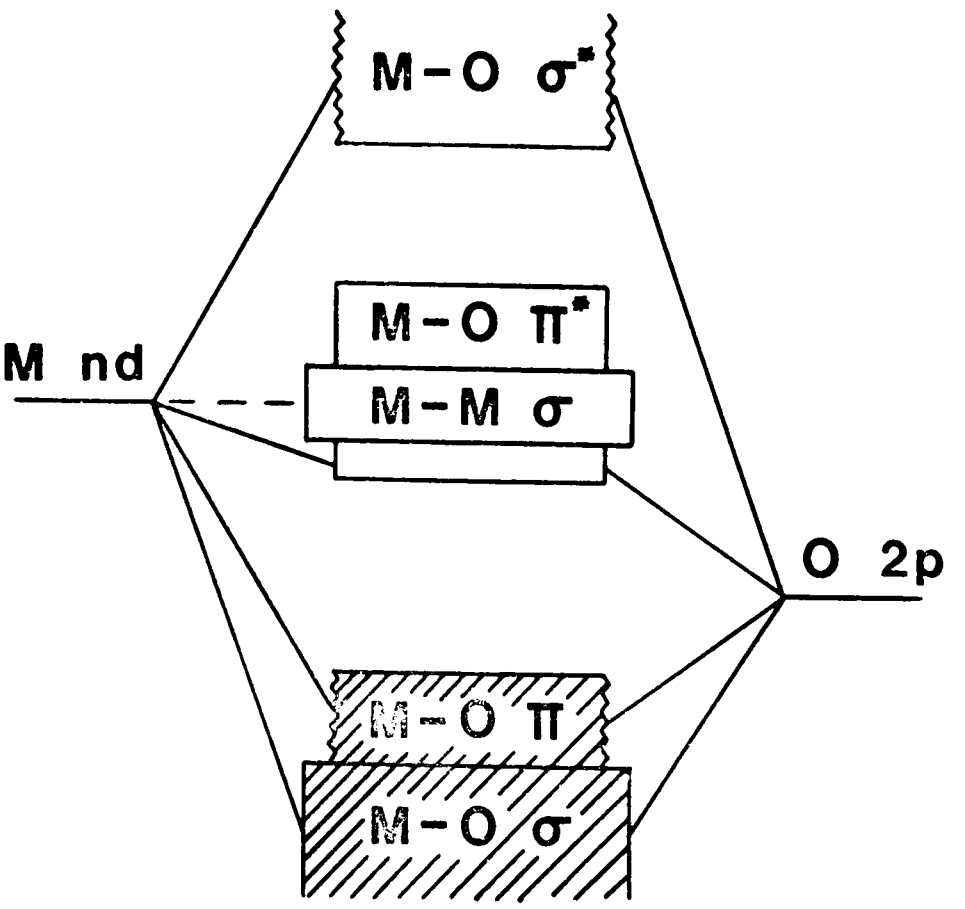


Fig. 5.19. Partial one-electron energy level diagram for a transition metal dioxide MO_2 having the regular, tetragonal rutile structure. The electron occupancies indicated by hatching are those appropriate to TiO_2 (d^0)

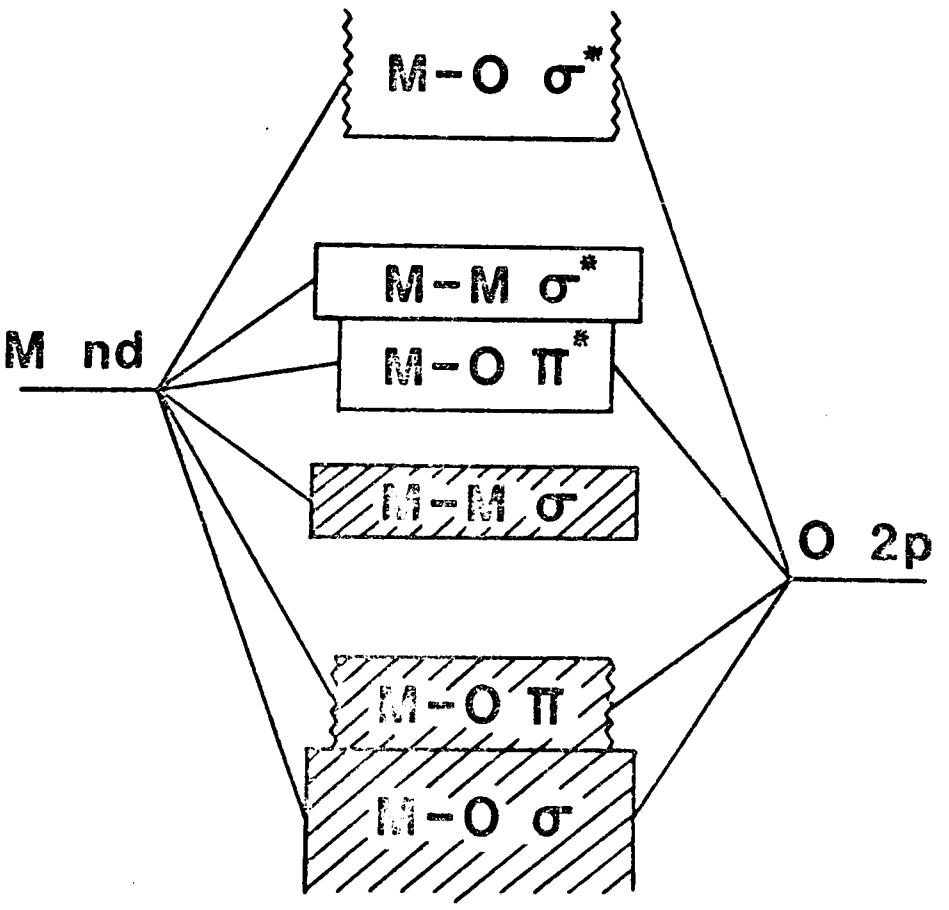


Fig. 5.20. Partial one-electron energy level scheme for a MO_2 species with the axially distorted form of the rutile structure. The electron occupancies, as indicated by hatching, are those for the room temperature form of VO_2 or NbO_2 (d^1)

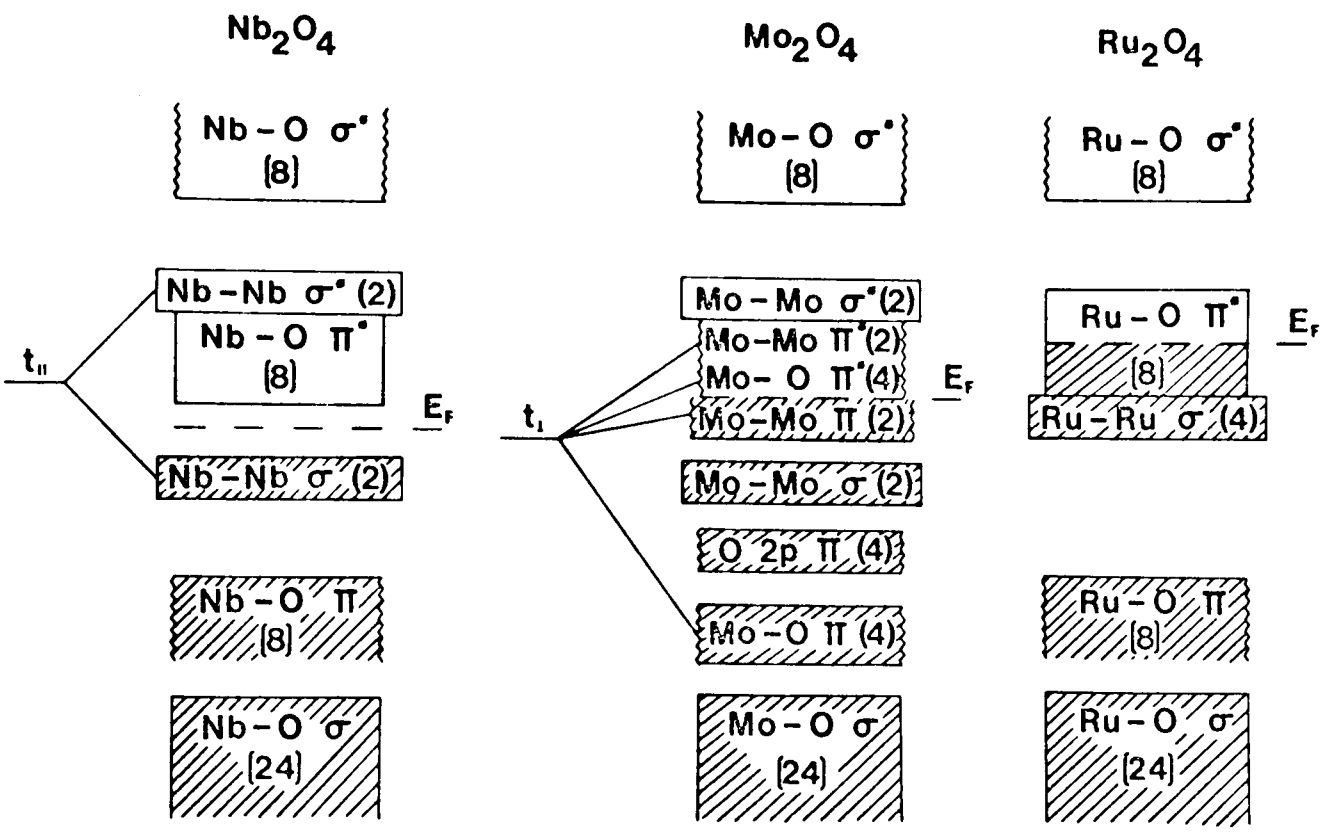


Fig. 5.21. Schematic one-electron energy diagrams for rutile-related dioxides NbO_2, MoO_2 and RuO_2 respectively. All diagrams are drawn on the basis of a doubled formula, i.e. M_2O_4

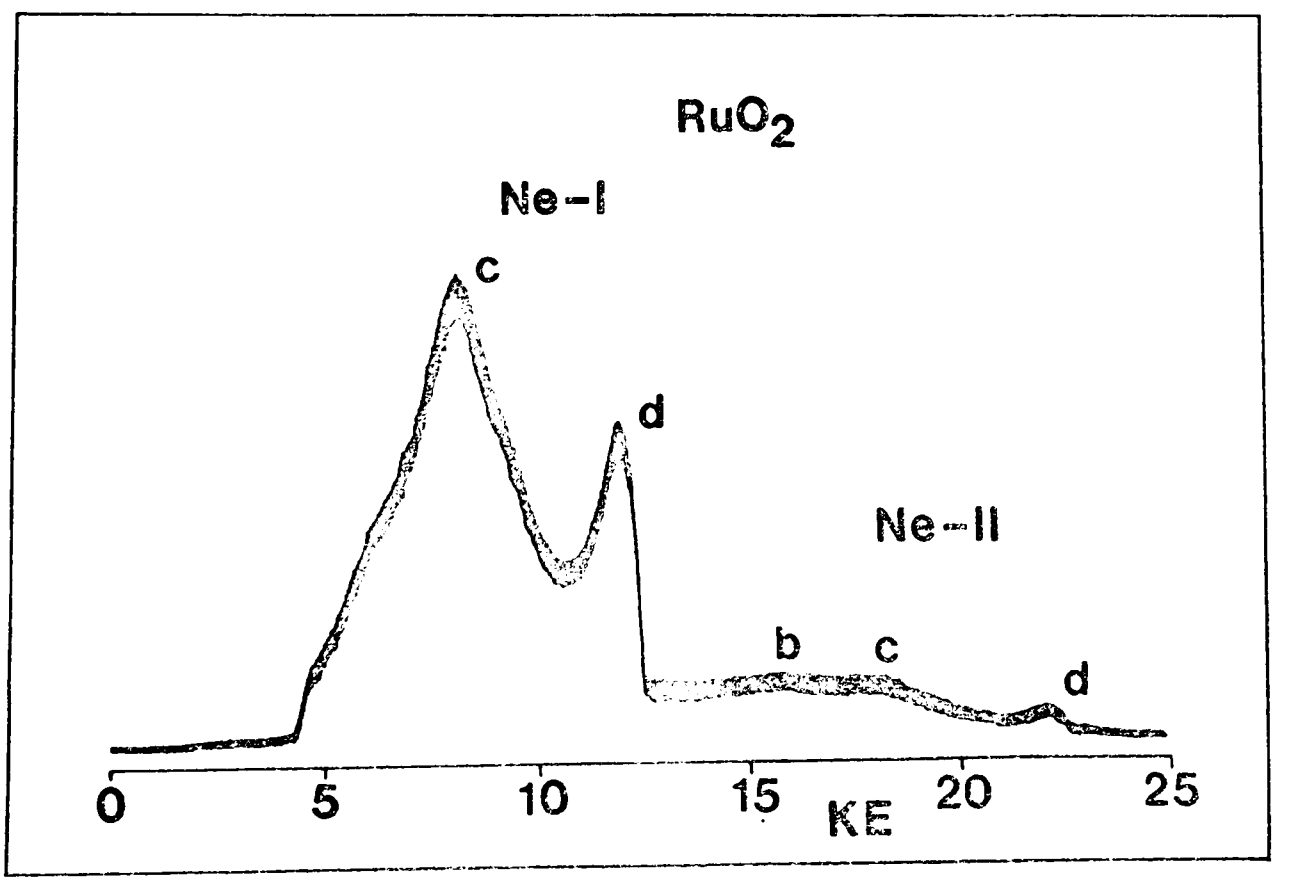


Fig. 5.22. Ne-I and Ne-II PE spectra of RuO_2

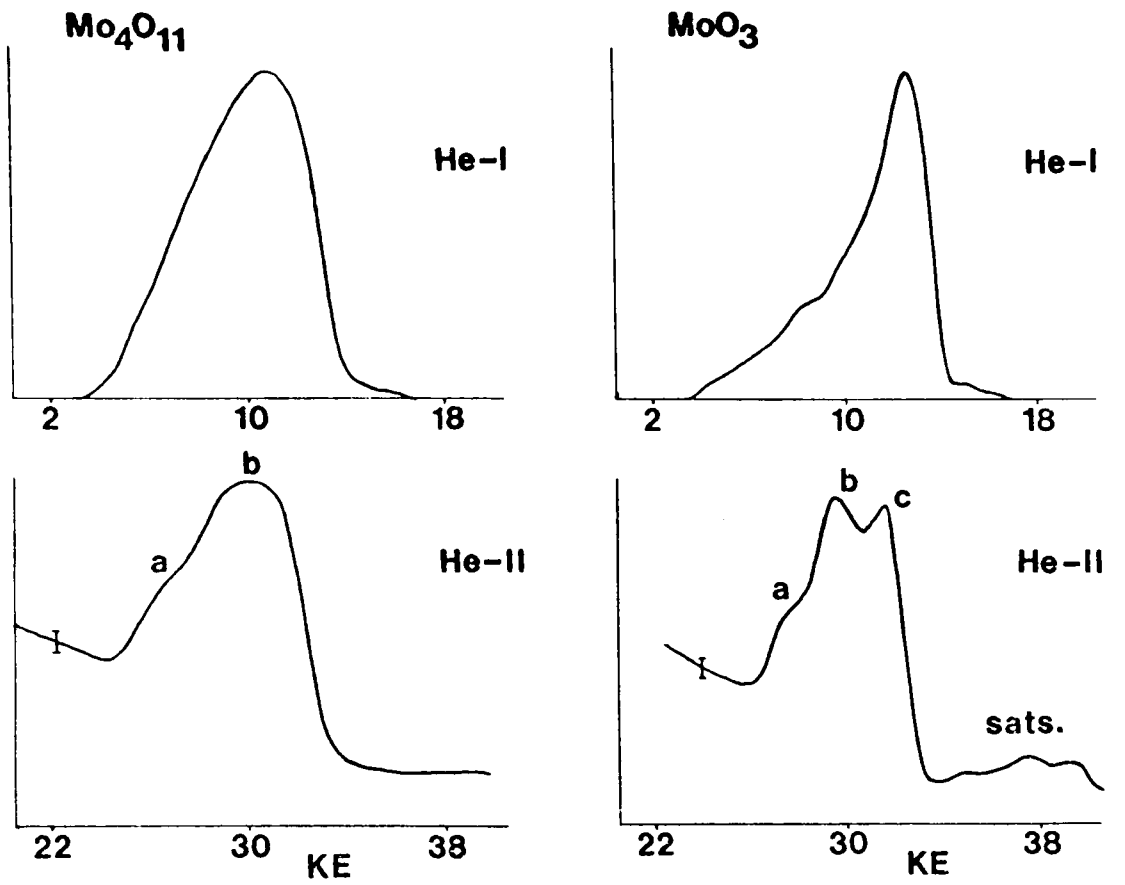


Fig. 5.23. He-I and He-II PE spectra of Mo_4O_{11} and MoO_3

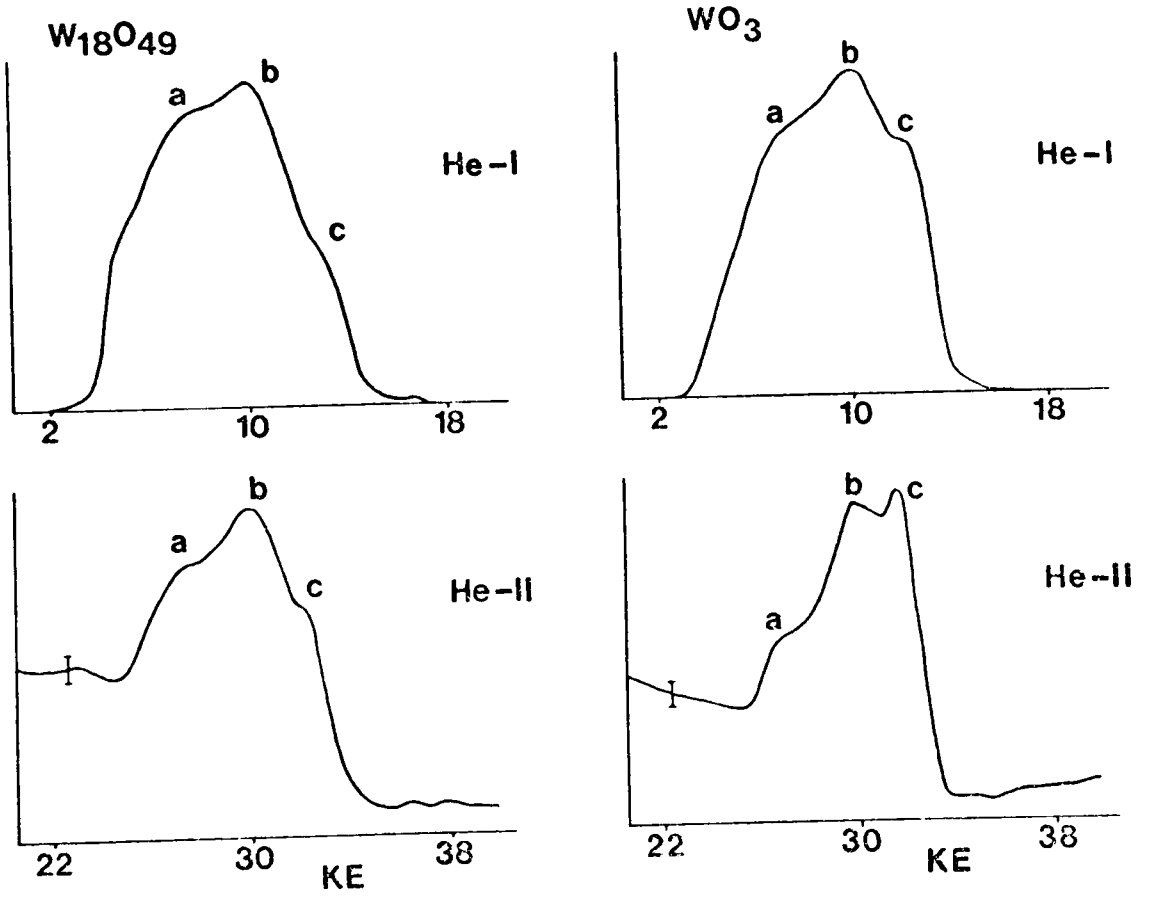


Fig. 5.24. He-I and He-II PE spectra of $W_{18}O_{49}$ and WO_3

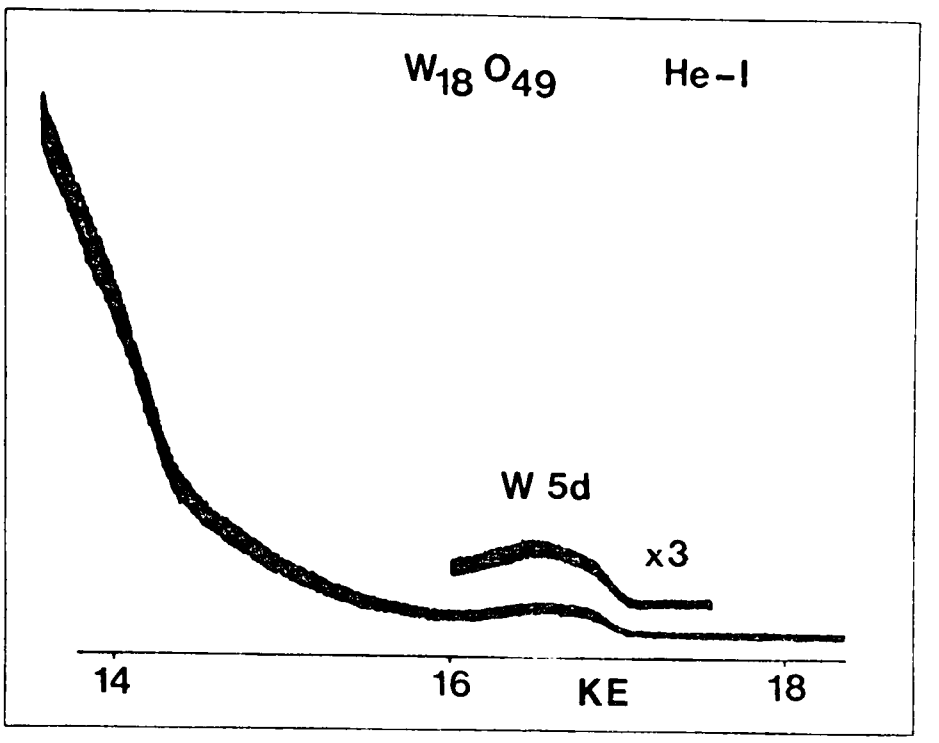


Fig. 5.25. The W 5d structure in the He-I PE spectrum of $W_{18}O_{49}$

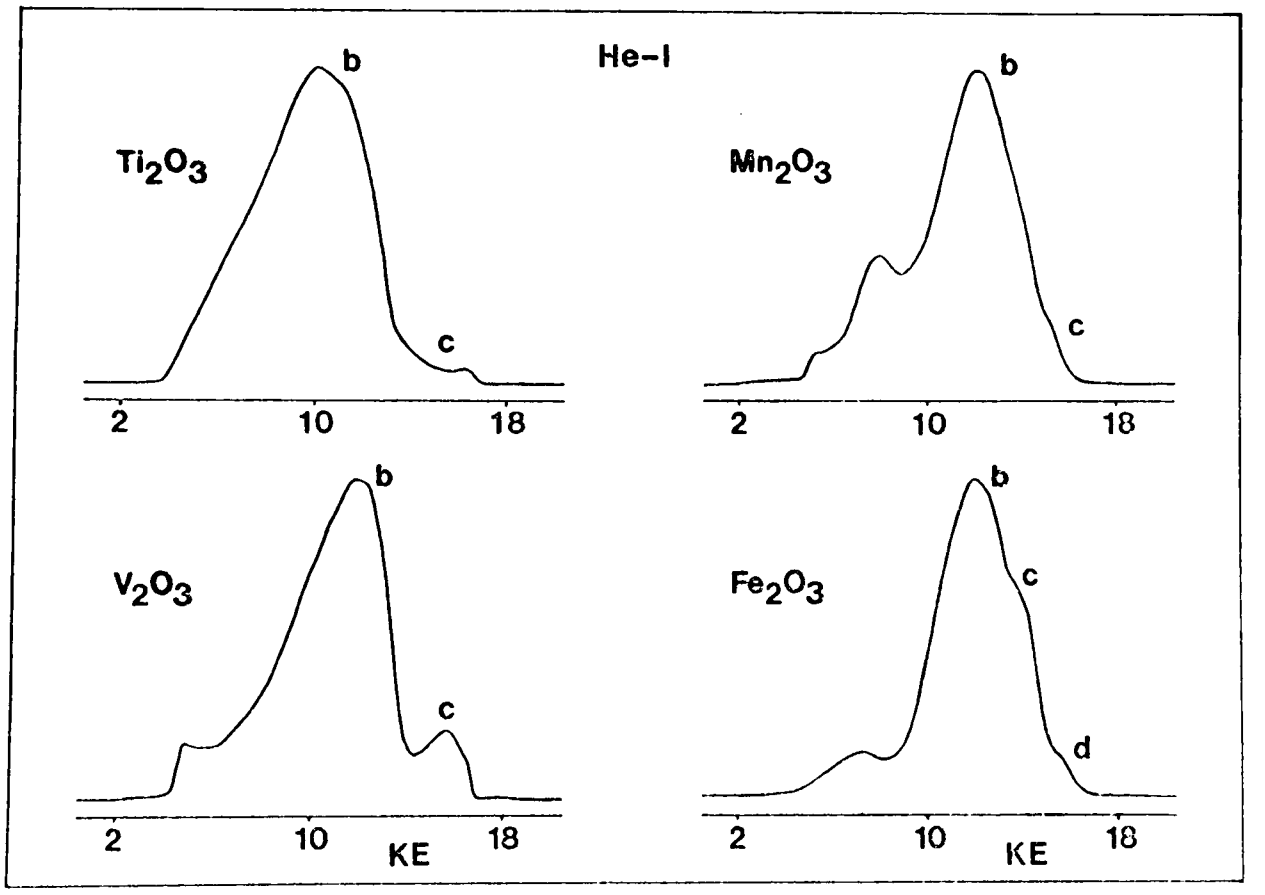


Fig. 5.26. He-I PE spectra of Ti_2O_3, V_2O_3, Mn_2O_3 and Fe_2O_3

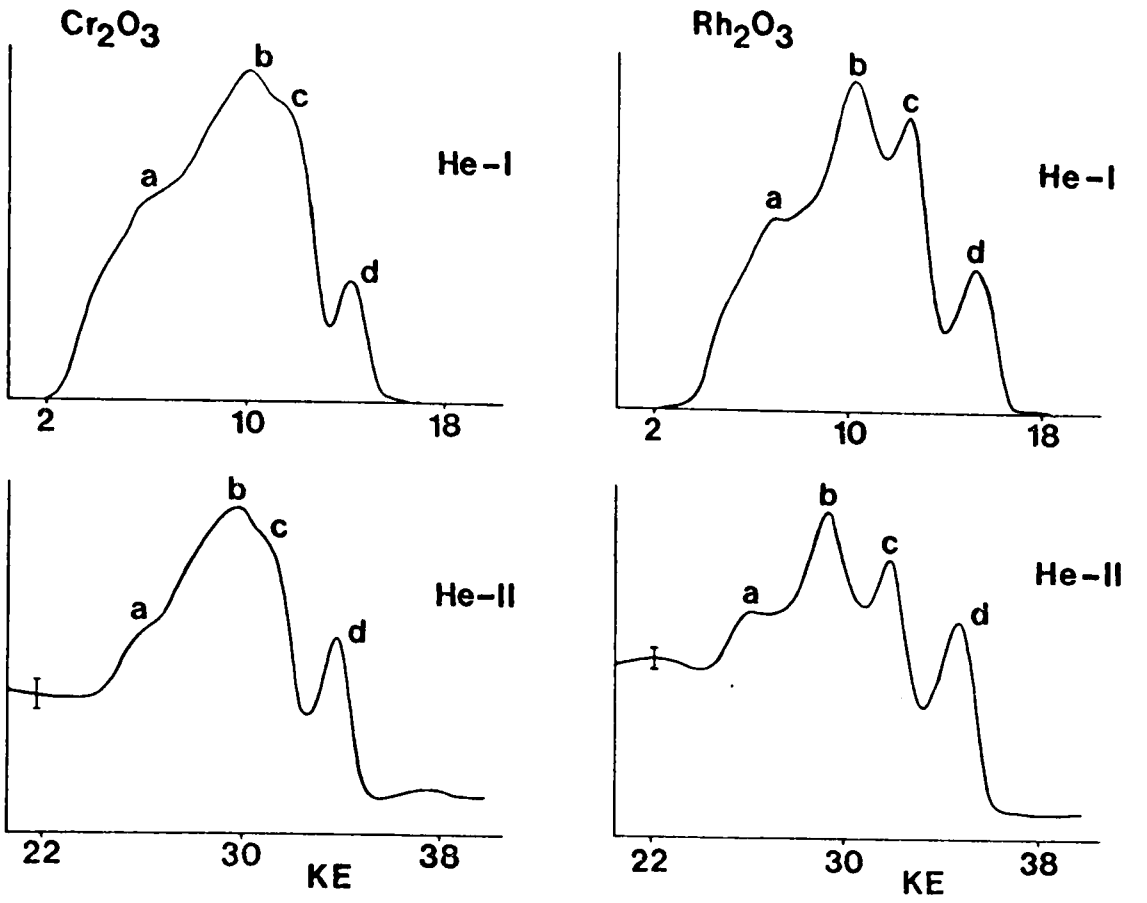


Fig. 5.27. He-I and He-II PE spectra of Cr_2O_3 and Rh_2O_3

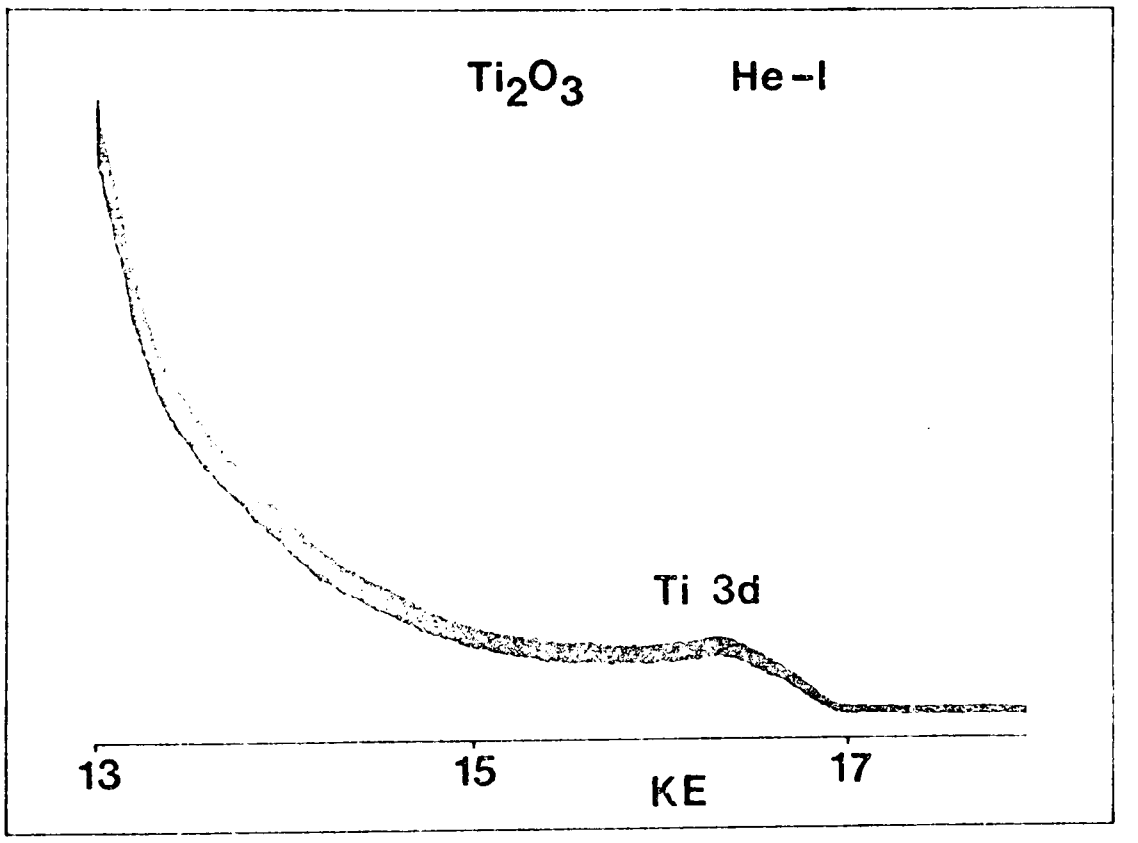


Fig. 5.28. The Ti 3d structure in the He-I PE spectrum of Ti_2O_3

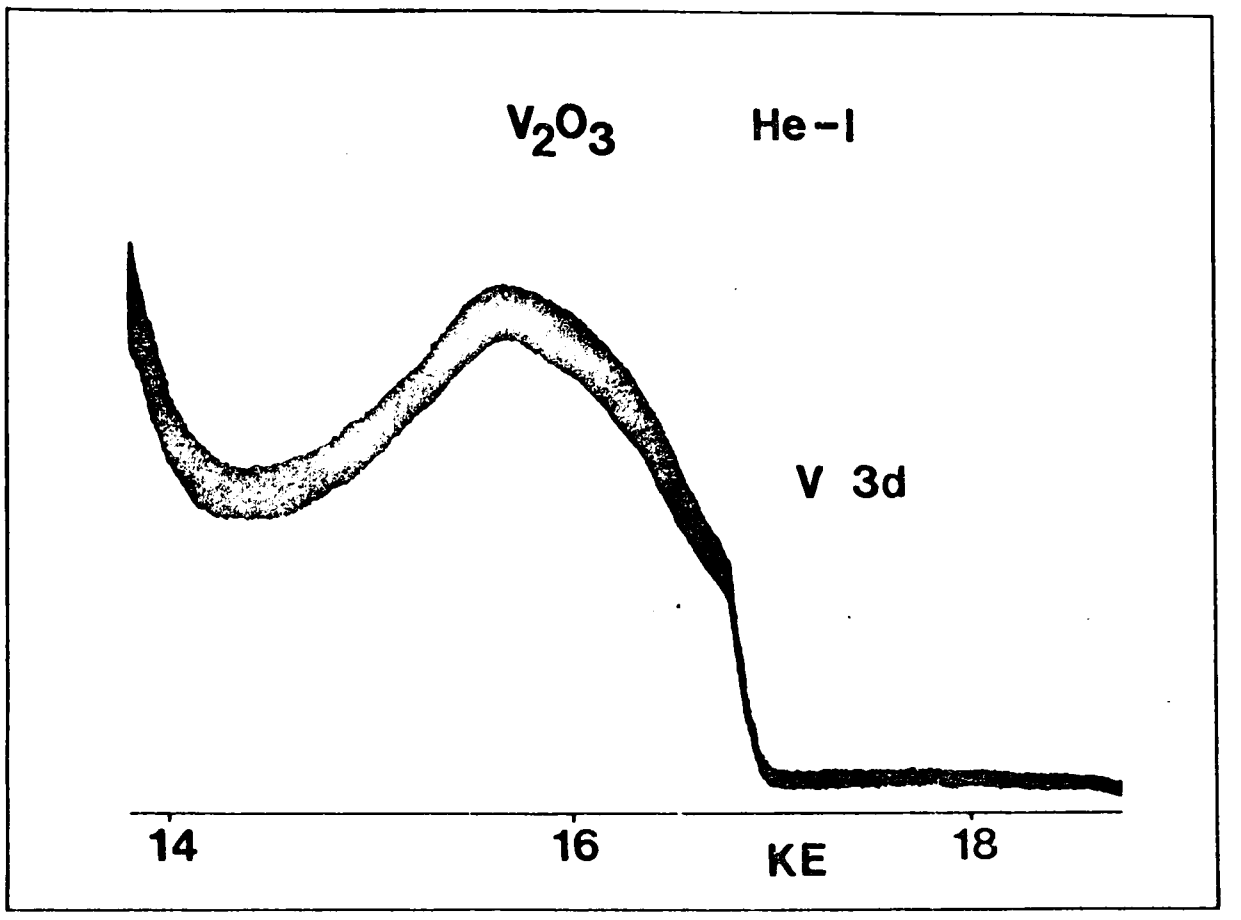


Fig. 5.29. The V 3d structure in the He-I PE spectrum of V_2O_3

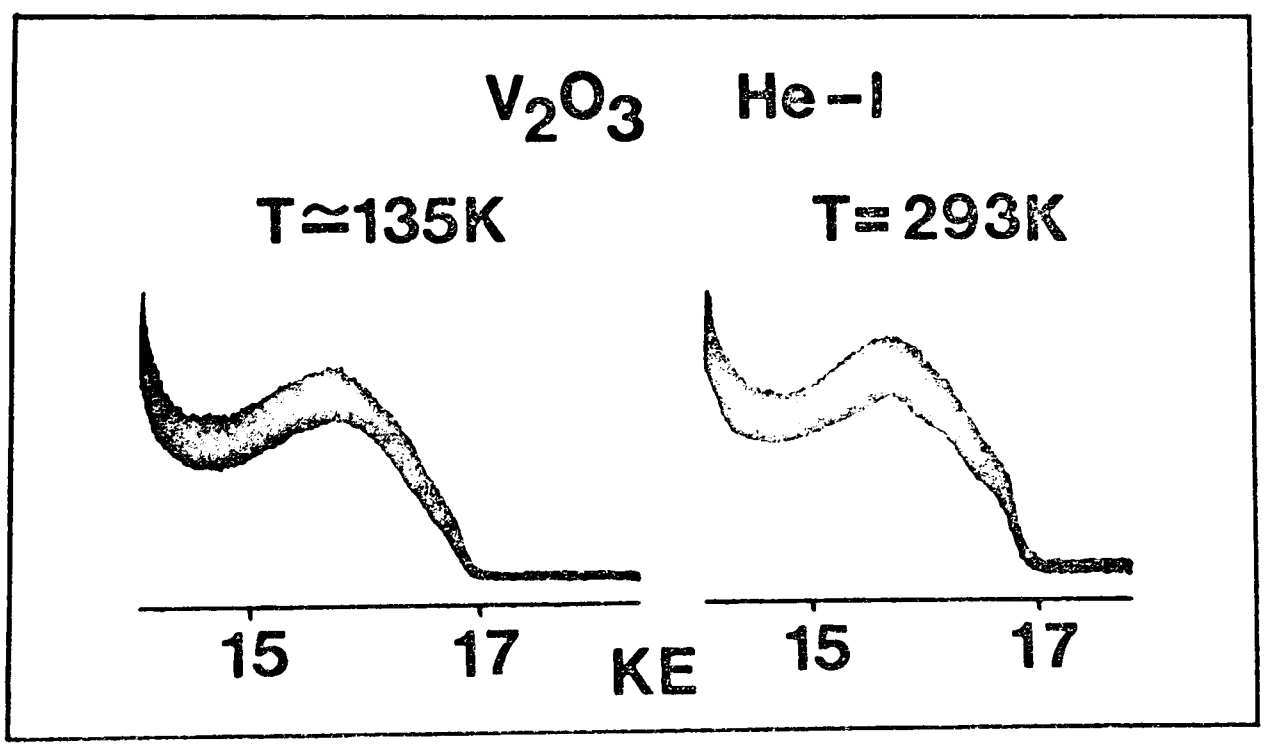


Fig. 5.30. Temperature dependence of the He-I PE spectrum of V_2O_3

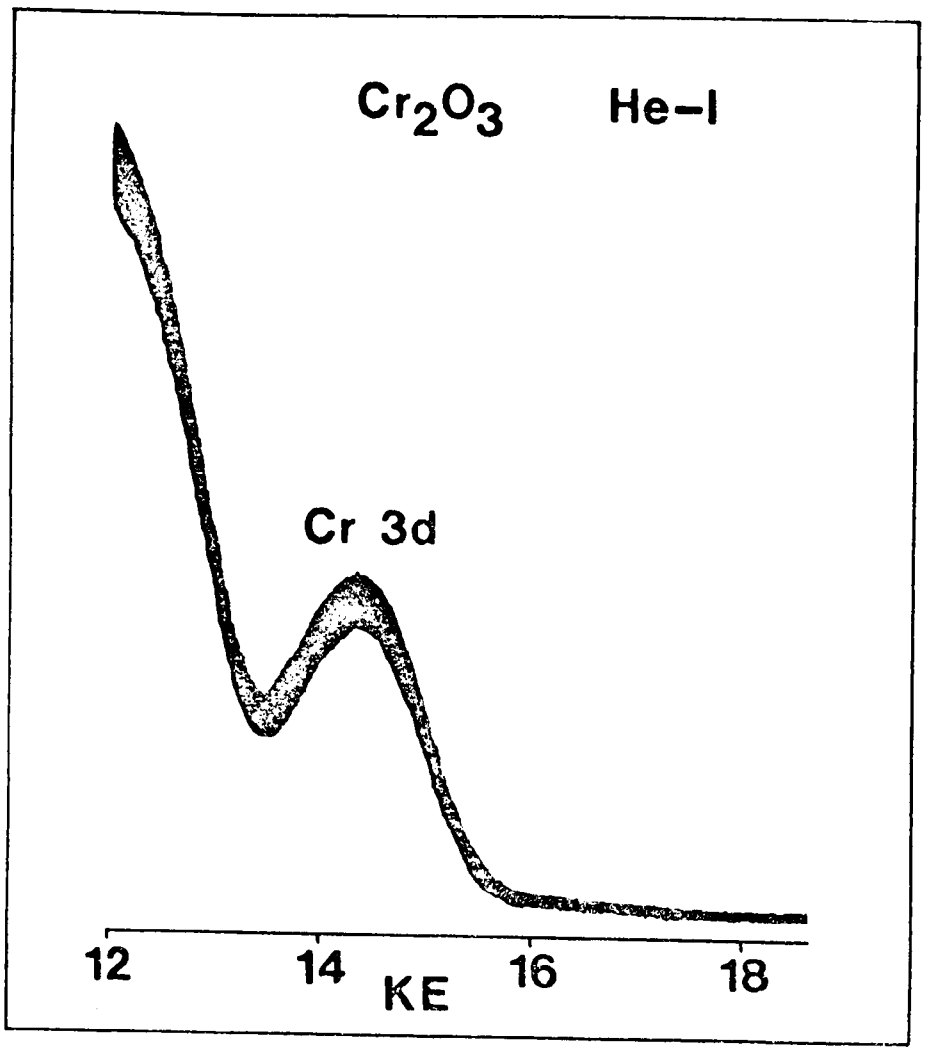


Fig. 5.31. The Cr 3d structure in the He-I PE spectrum of Cr_2O_3

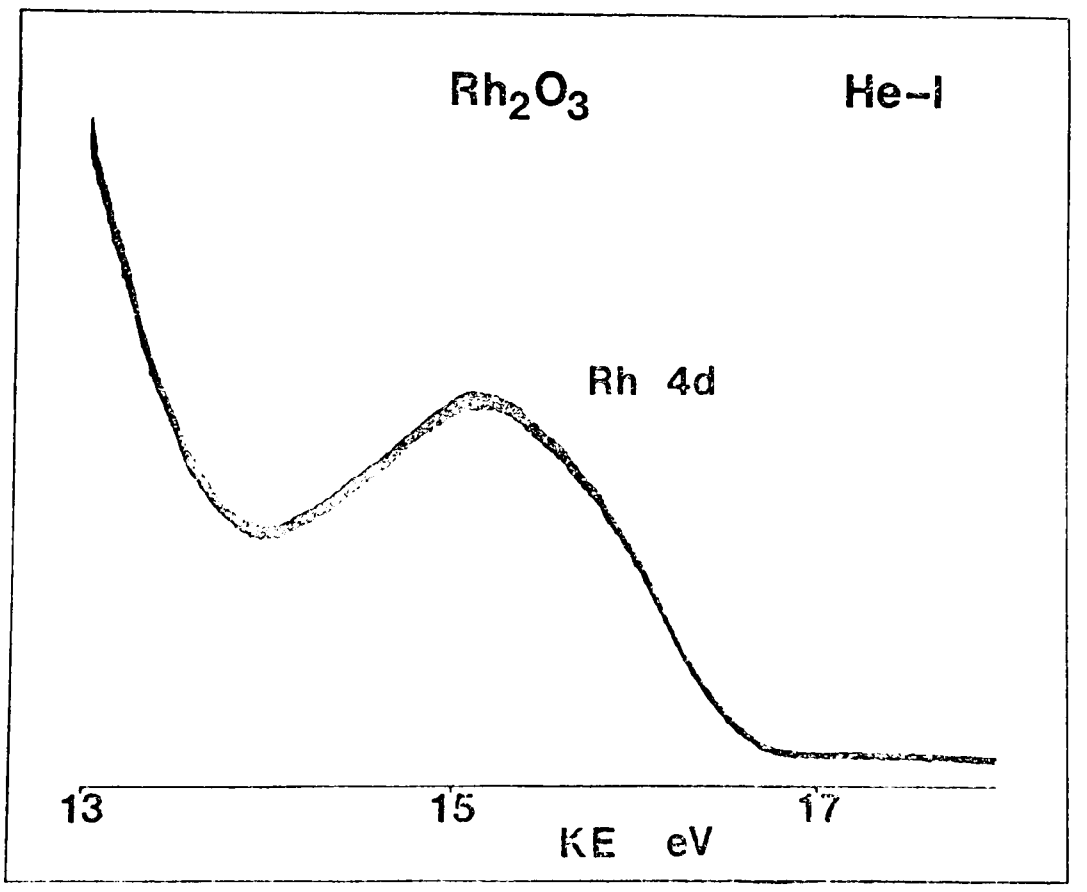


Fig. 5.32. The Rh 4d structure in the He-I PE spectrum of Rh_2O_3

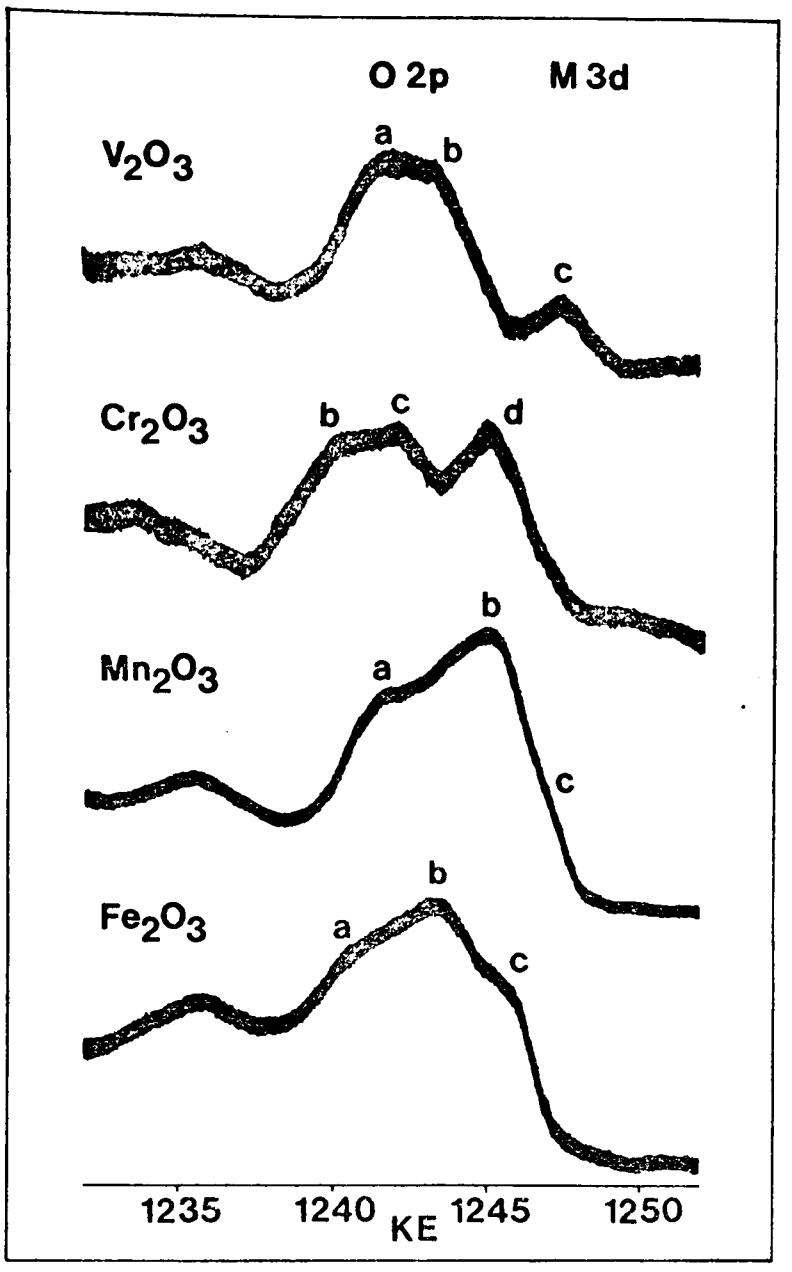


Fig. 5.33. Valence region X-PE spectra of V_2O_3, Cr_2O_3, Mn_2O_3 and Fe_2O_3

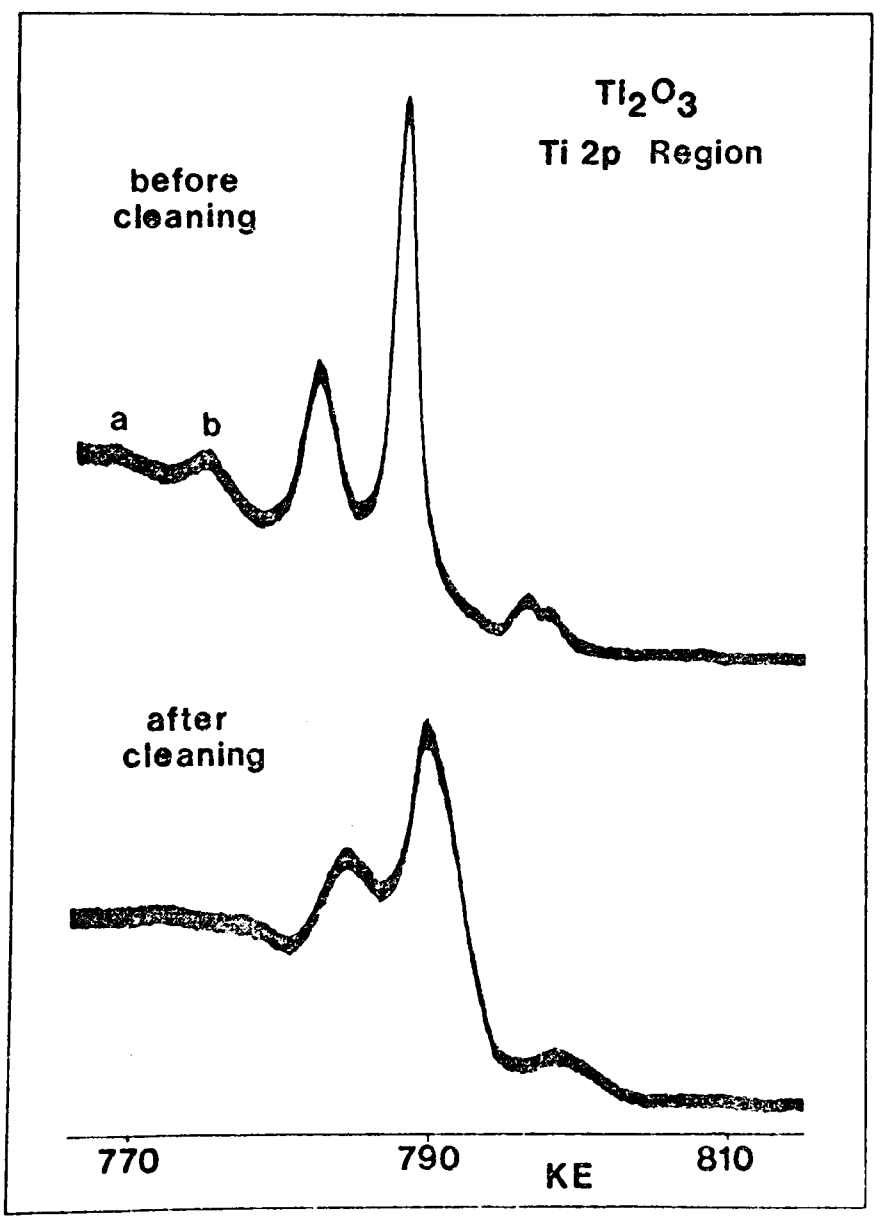


Fig. 5.34. The effect of sample cleaning on the Ti 2p PE signals from Ti_2O_3

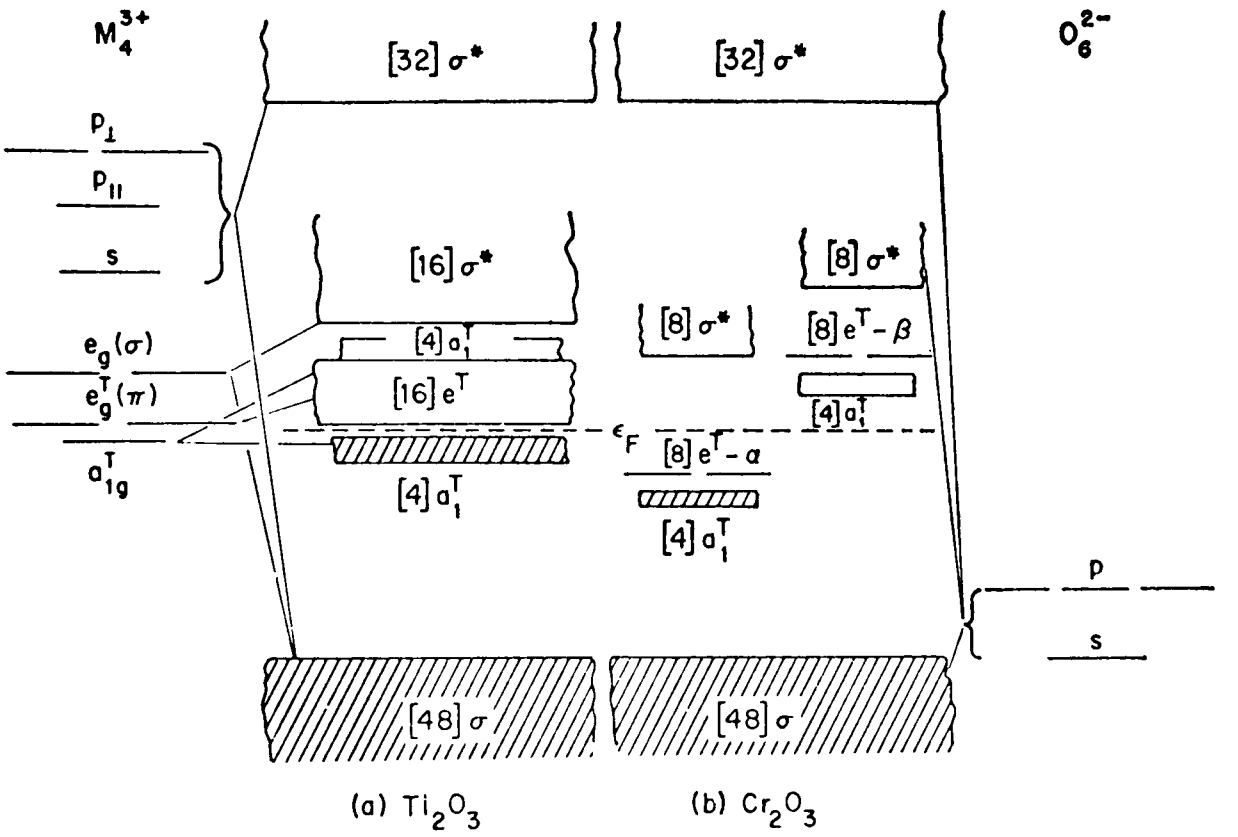


Fig. 5.35. Schematic one-electron diagrams for Cr_2O_3 and Ti_2O_3 (after Goodenough)[23]

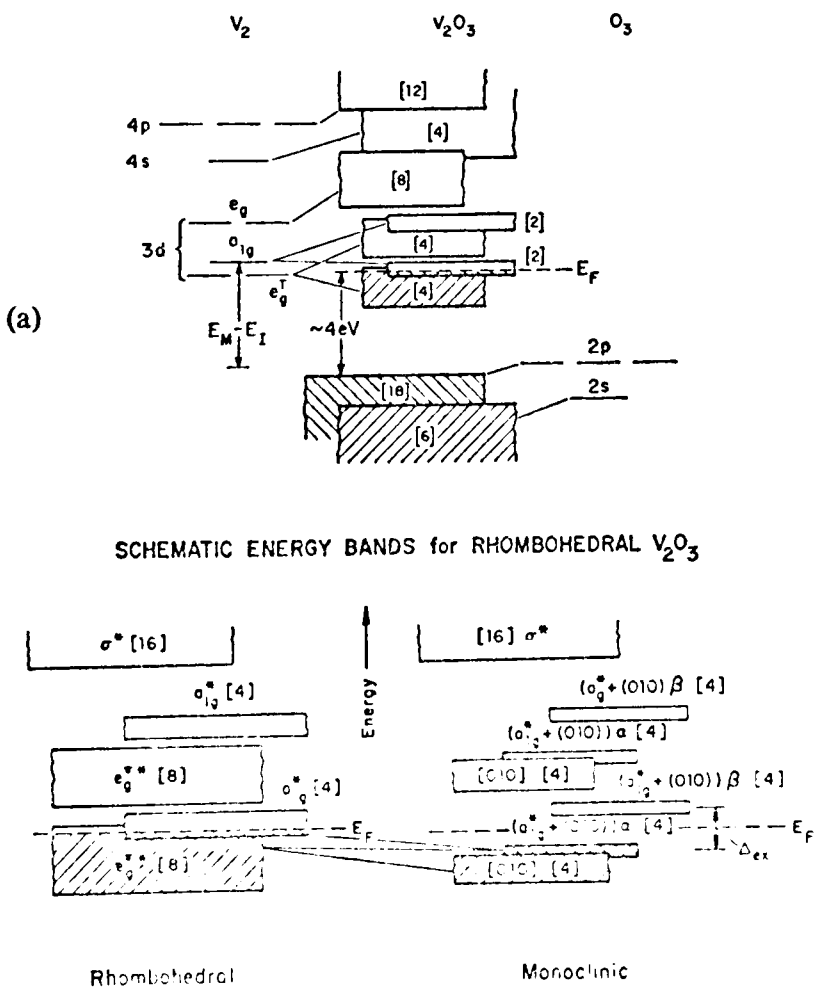


Fig. 5.36. Schematic one-electron diagrams for rhombohedral and monoclinic V_2O_3 (after Goodenough)[23]

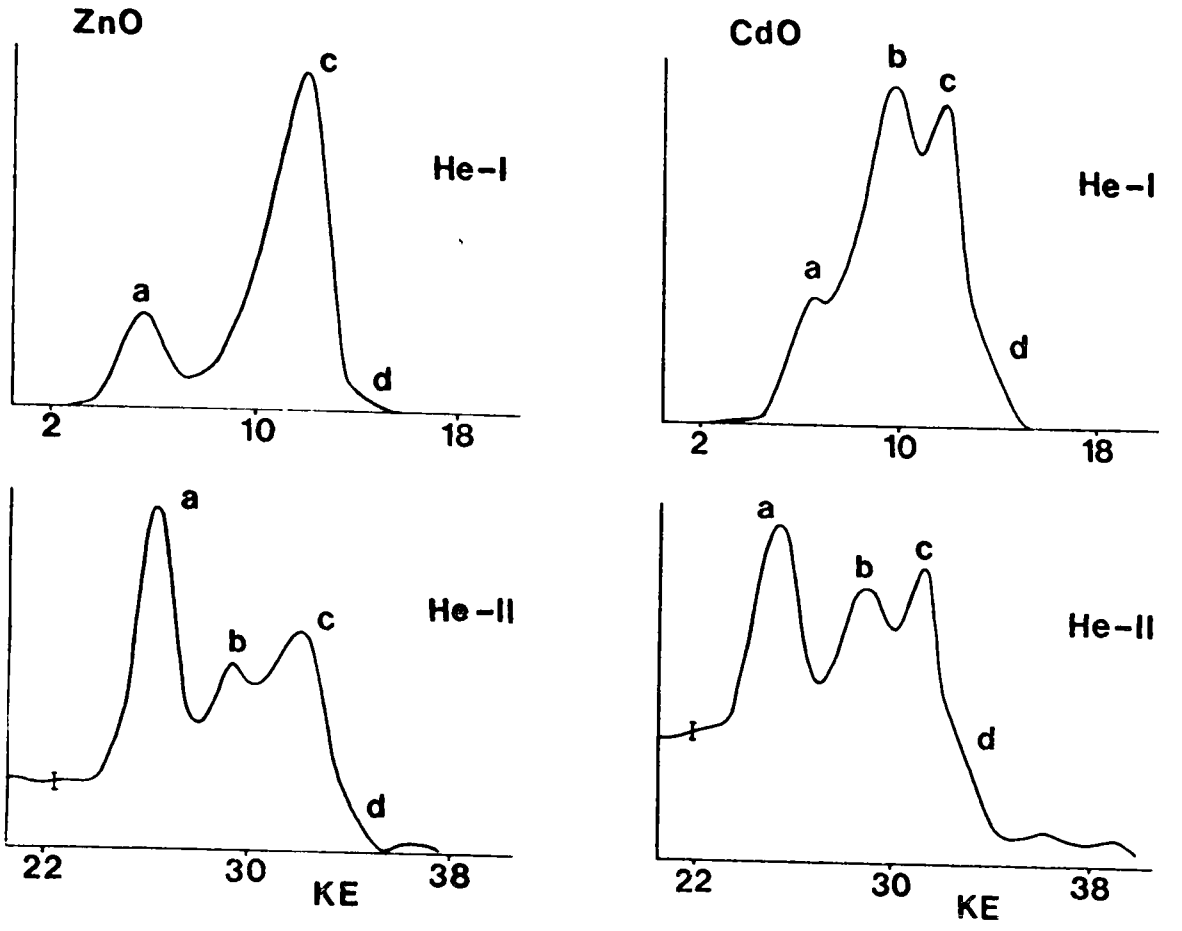


Fig. 5.37. He-I and He-II PE spectra of ZnO and CdO

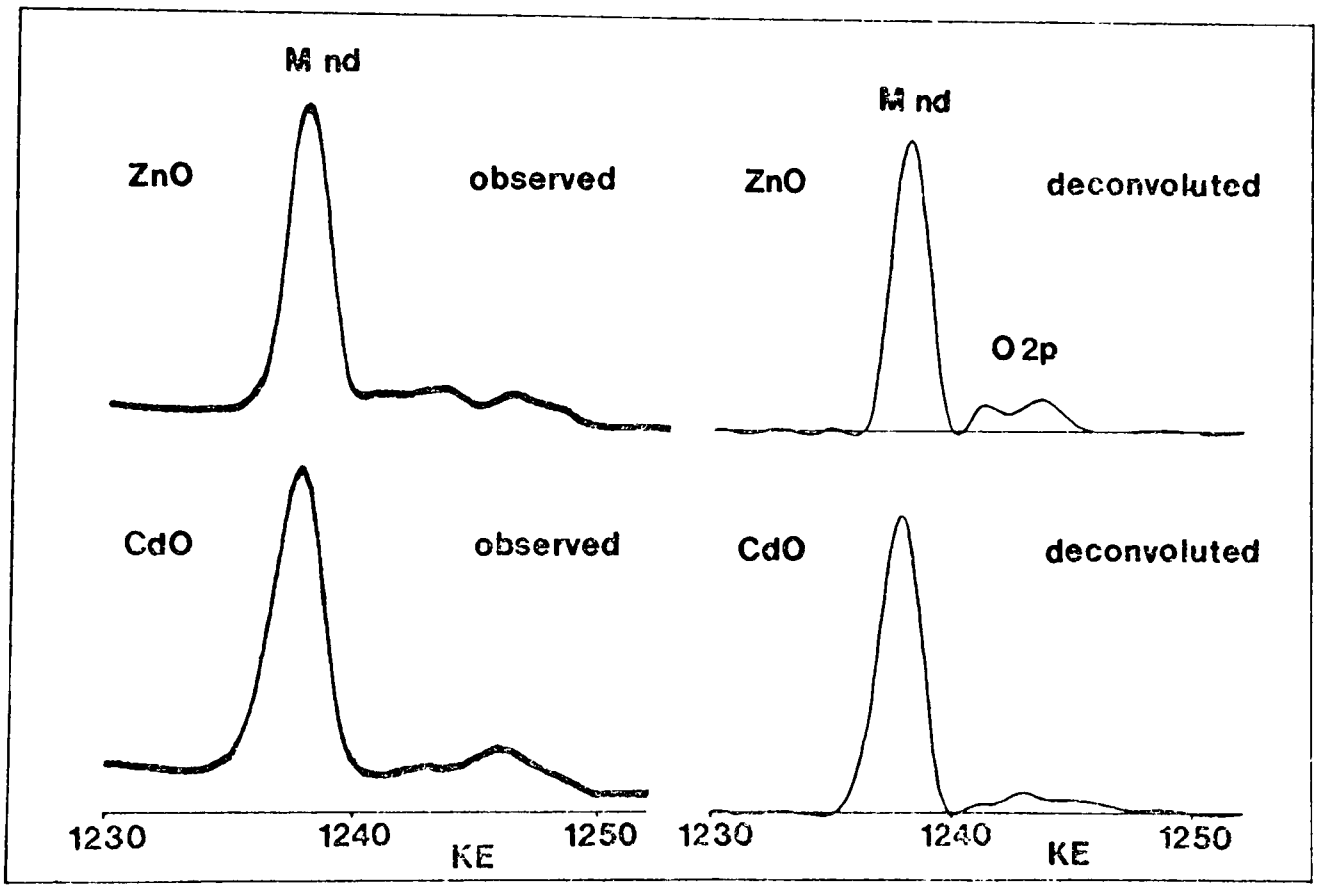


Fig. 5.38. Valence region X-PE spectra of ZnO and CdO

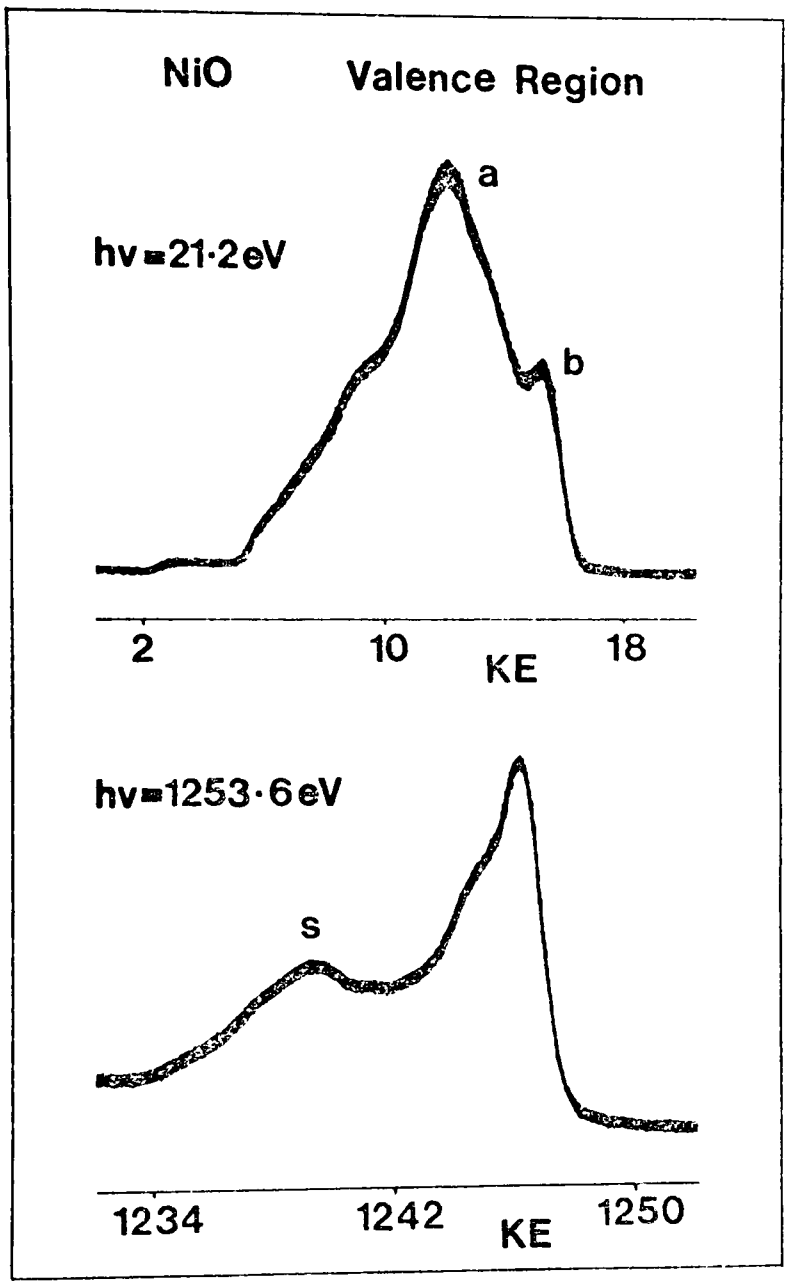


Fig. 5.39. He-I and X-ray PE spectra of NiO

REFERENCES FOR CHAPTER 5

1. D. B. Rogers, R. D. Shannon, A. W. Sleight, J. L. Gillson, Inorg. Chem. 8 (1969) 841.
2. A. F. Wells, 'Structural Inorganic Chemistry' 4th Edition (1975) Clarendon Press, Oxford.
3. J. Norrestam, Acta Chem. Scand. 21 (1967) 2871.
4. L. L. Y. Chang, B. Phillips, J. Amer. Ceram. Soc. 52 (1969) 527.
5. C. L. McDaniels, S. J. Schneider, J. Res., Nat. Bur. Stand., U.S.A. 73A (1969) 213.
6. S. E. Livingstone, p 1163 in 'Comprehensive Inorganic Chemistry' Vol 3, ed. A. F. Trotman-Dickenson (1973) Pergamon Press.
7. C. N. R. Rao, G. V. Subba Rao, 'Transition metal oxides' (1974) NBS-NSRDS-49, Nat. Bur. Stand., Dept. Commerce, Washington, D.C. 20234, U.S.A.
8. K. S. Kim, W. E. Baitinger, J. W. Amy, N. Winograd, J. Elect. Spec. 5 (1974) 351.
9. G. Thornton, personal communication.
10. C. Blaauw, F. Leenhouts, F. van der Woude, G. A. Savatzky, J. Phys. C8 (1975) 459.
11. S. Hüfner, G. K. Wertheim, Phys. Rev. B11 (1974) 687.
12. M. Campagna, G. K. Wertheim, H. R. Shanks, F. Zumsteg, E. Banks, Phys. Rev. Lett. 34 (1975) 738.
13. J. Riga, C. Tenret-Noël, J. J. Pireaux, R. Caudano, J. J. Verbist, Y. Gobillon, Physica Scipta 16 (1977) 351.
14. S. Doniach, M. Sunjic, J. Phys. C3 (1970) 285.
15. A. Kotani, Y. Toyazawa, J. Phys. Soc. Japan 37 (1974) 912.

16. M. K. Bahl, J. Phys. Chem. Solids 36 (1975) 485.

17. G. Thornton, A. F. Orchard, C. N. R. Rao, Phys. Lett. 54A (1975) 235.

18. G. Thornton, D. Phil. Thesis, Oxford (1976).

19. K. Sakata, I. Nishida, M. Matsushima, T. Sakata, J. Phys. Soc. Japan 27 (1969) 506.

20. C. N. R. Rao, G. R. Rao, G. V. Rao, J. Solid State Chem. 6 (1973) 340.

21 J. Horkans, M. W. Shafer, R. Peekema, p 305 in NBS Special Publication 455, 'Electrocatalysis on non-metallic surfaces' (1976).

22. R. J. Colton, J. W. Rabalais, Inorg. Chem. 15 (1976) 236.

23. J. B. Goodenough, Prog. Solid State Chem. 5 (1971) 490.

24. L. F. Mattheiss, Phys. Rev. B13 (1976) 2433.

25. D. E. Eastman, J. L. Freeouf, Phys. Rev. Lett. 34 (1975) 395.

26. I. T. McGovern, R. H. Williams, J. Phys. C9 (1976) L337.

27. A. Goldmann, J. Tejeda, N. J. Shevchik, M. Cardona, Phys. Rev. B10 (1974) 4388.

28. J. B. Goodenough, J. Solid State Chem. 3 (1971) 490.

29. J. M. Honig, L. L. Van Zandt, Ann. Rev. Mater. Sci. 5 (1975) 225.

30. M. Gupta, D. E. Ellis, Phys. Rev. B13 (1976) 3405.

31. M. Gupta, A. J. Freeman, D. E. Ellis, Phys. Rev. B16 (1977) 3338.

32. A. K. Cheetham, C. N. R. Rao, Acta Cryst. B32 (1976) 1579.

33. W. Paul, Mat. Res. Bull. 5 (1970) 691.

34. F. A. Cotton, Quart. Rev. (London) 20 (1966) 389.

35. J. M. Berak, M. J. Sienko, J. Solid State Chem. 2 (1970) 109.

36. T. Wolfram, Ş. Ellialtioğlu, Phys. Rev. Lett. in press.

37. J. W. Rabalais, R. J. Colton, A. M. Guzman, Chem. Phys. Lett. 29 (1974) 131.

38. A. Calabrese, R. G. Hayes, Chem. Phys. Lett. 43 (1976) 263.

39. G. K. Wertheim, L. F. Mattheiss, M. Campagna, T. P. Pearsall, Phys. Rev. Lett. 32 (1974) 997.

40. O. Muller, R. J. Roy, J. Less-Common Metals 16 (1968) 129.

41. J. W. M. Biesterbos, J. J. Horustia, J. Less-Common Metals 30 (1973) 121.

42. G. V. Subba Rao, B. M. Wanklyn, C. N. R. Rao, J. Phys. Chem. Solids 32 (1971) 345.

43. V. E. Henrich, G. Dresselhaus, H. J. Zeiger, Phys. Rev. Lett. 36 (1976) 1335.

44. V. E. Henrich, H. J. Zeiger, T. B. Reed, Phys. Rev. B17 (1978) 4121.

45. K. Iohikawa, O. Terasaki, T. Sagawa, J. Phys. Soc. Japan 36 (1974) 706.

46. J. M. Honig, T. B. Reed, Phys. Rev. 174 (1968) 1020.

47. J. Ashkenazi, T. Chuchem, Philos. Mag. (GB) 32 (1975) 763.

48. L. Fiermans, R. Hoogewijs, J. Vennik, Surface Sci. 47 (1975) 1.

49. P. A. Cox, Structure and Bonding 24 (1975) 59.

50. S. G. Bishop, P. C. Kemeny, Solid State Comm. 15 (1974) 1877.

51. G. C. Allen, M. T. Curtis, A. J. Hooper, P. M. Tucker, J. C. S. Dalton (1974) 1675.

52. S. Evans, J. Pielaszek, J. M. Thomas, Surface Science 55 (1976) 644.

53. W. Ranke, Solid State Comm. 19 (1976) 685.

54. R. A. Powell, W. E. Spicer, J. C. McMenamin, Phys. Rev. B6 (1972) 3056.

55. L. Ley, R. A. Pollak, F. R. McFeely, S. P. Kowalczyk, D. A. Shirley, Phys. Rev. B9 (1974) 600.

56. R. G. Egdell, D.Phil. Thesis, Oxford (1977).

CHAPTER SIX

PHOTOELECTRON SPECTRA OF TERNARY OXIDES

6.1 Introduction

6.2 Transition metal titanates

6.3 Transition metal perovskites

6.1 Introduction

Compounds of the general stoichiometry ABO_3, where A is a large divalent or trivalent ion and B is a transition element, frequently possess the perovskite structure (see fig. 6-1). Few compounds, however, have the ideal cubic perovskite structure. The physical origins of the crystallographic distortions can be variously ascribed to (i) relative mismatching of ionic sizes (ii) electron ordering among localised electrons (iii) electron ordering among collective electrons.[1]

The role of relative ionic size can be conveniently discussed by introducing the concept of the tolerance factor.[2]

$$t = \frac{(r_A + r_o)}{\sqrt{2}(r_B + r_o)}$$

where r_A, r_B, r_o are the empirical radii of the respective ions. By geometry, the ideal cubic structure should have t=1. In practice the perovskite structure occurs only within the range $0.75 < t < 1.00$, although for the ideal cubic structure t must be greater than 0.89. A further constraint is that the A and B cations must, in themselves, be stable in twelve-fold and six-fold coordinations, respectively - that is $r_A >$ 0.090 nm and $r_B >$ 0.051 nm.

Nine ternary oxides have been examined in this work: $CaMnO_3$, $YCrO_3$, $YMnO_3$, $YFeO_3$, $YbMnO_3$, $MnTiO_3$, $FeTiO_3$, $CoTiO_3$ and $NiTiO_3$. $CaMnO_3$ is almost cubic ($t \simeq 1.00$) with only a slight orthorhombic distortion. $YCrO_3$ and $YFeO_3$ exhibit more pronounced orthorhombic deformations of the perovskite structure while $YMnO_3$ and $YbMnO_3$ are hexagonal.[3] In the four titanates $ATiO_3$ (A = Mn, Fe, Co, Ni), the A cation is too small to

accommodate twelve-fold coordination, and, as a consequence, the titanates adopt the ilmenite structure. This structure is directly related to the corundum structure,[2] both the A and Ti cations being in approximate octahedral coordination. The physical properties of all these compounds appear to suggest that the transition metal 3d electrons are localised.[3, 4]

In this work, we have attempted to exploit several of the physical properties afforded by the ternary oxide lattice. The most general feature of ternary oxides is that they commonly stabilise oxidation states of transition metals which may be 'unstable' or 'non-existent' in the binary oxide (compare $Fe_{1-x}O$ and $FeTiO_3$). Secondly, the increased thermal stability of the ternary oxide lattice with respect to that of the binary oxide leaves more scope for the surface pretreatment procedure that can be employed (compare MnO_2 and $CaMnO_3$). Ternary oxides also have the advantage that they may possess different values of electrical conductivity to those of the corresponding binary oxide.

In connection with the work described in section 7.4, concerning 4f photoionisation from lanthanoid compounds, it was hoped to record the He-II PE spectra of the lanthanide sesquixoides. Unfortunately no UV-PE spectra could be obtained, presumably because of the insulating nature of these materials. The electrical conductivity of $YbMnO_3$ is considerably larger than that of the parent rare-earth oxide and this proved sufficient to realise a He-II spectrum from the compound. Yb oxides represent the optimum lanthanide system in which to explore the final state PE structure associated with photoionisation of a 4f electron by He-II radiation. This is because: (i) there is a choice of 13 f electrons to ionise;

and (ii) the 4f region of the spectrum is well separated from the O 2p and transition metal nd regions.[5]

The transition metal titanates have been of interest recently in this laboratory because their electronic properties would appear to suggest that they may be better photoelectrolytic catalysts than TiO_2 or $SrTiO_3$.[6] In this connection, it is important to have a knowledge of the electronic properties of their surfaces together with the energetics of the bulk valence and conduction bands.

6.2 Transition metal titanates

Once inside the spectrometer, the titanates were prepared as follows: $MnTiO_3$ was heated for two hours *in vacuo* at *ca* 920K; $FeTiO_3$ was fired *in vacuo* at *ca* 1000K for two hours; $CoTiO_3$ was heated *in vacuo* for two hours at *ca* 950K; $NiTiO_3$ was heated in a 79% N_2/21% O_2 mixture for $2\frac{1}{2}$ hours at *ca* 920K. The sample cleaning procedures essentially reflect the bulk preparative conditions and for all materials, reasonably sharp symmetrical O 1s PE signals were obtained. The effects of surface cleaning on $FeTiO_3$ are shown in fig. 3.5. As for the samples that were heated *in vacuo*, the pressure was monitored and in no case was found to rise above 5×10^{-7} torr.

The He-I and He-II PE spectra of $MnTiO_3$ and $FeTiO_3$ are presented in fig. 6.2 while those of $CoTiO_3$ and $NiTiO_3$ are reproduced in fig. 6.3. The spectra of $FeTiO_3$ were recorded at room temperature, while those of $CoTiO_3$ and $NiTiO_3$ were measured at 690K. UV-PE spectra could be obtained from $CoTiO_3$ at room temperature, but the detectable photoelectron flux was an order of magnitude less than that observed at 690K. These observations were consistent with electrical conduct-

ivity measurements made by A. Hamnett, on the same samples from which the PE spectra were recorded. The resistivities of the samples of $CoTiO_3$ and $NiTiO_3$ at 731K were ca 10^6 and 10^8 ohm cm respectively, while that of $FeTiO_3$ was ca 200 ohm cm at 373K.

As regards $MnTiO_3$, the original sample provided by Mrs G. S. Bindaar was not sufficiently conducting to yield UV-PE spectra. Moreover, charging effects were noticed in the X-PE spectrum of the compound. For instance, if a small positive potential was applied to the end of the probe, the sample would only take up part of this bias.

A further sample of $MnTiO_3$ was provided. This time the compound had been heated under flowing hydrogen for two days at ca 1170K. The resulting non-stoichiometry induced in the material proved to be sufficient to enable UV-PE spectra to be recorded from the sample. It was not, however, enough to affect significantly the valence band structure of the compound, the X-PE spectra recorded from both samples of $MnTiO_3$ being identical. Although the new sample of $MnTiO_3$ provided UV-PE spectra at room temperature, the spectra shown in fig. 6.2 were recorded at 640K. This was because of a slightly improved photoelectron flux at this temperature.

The valence region and the transition metal 2p X-PE spectra of the titanates are presented in figs. 6.4 and 6.5 respectively. The valence region X-PE spectra of $MnTiO_3$, $CoTiO_3$ and $NiTiO_3$ are corrected for the small presence ($< 5\%$) of Pt signals. These arose from the X-rays hitting the edge of the platinum tray supporting the sample (see section 3.2).

The analysis of the valence region PE spectra of the titanates is much facilitated if we compare our X-ray spectra

with the UV-PE spectra of the corresponding transition metal monoxides (i.e. MnO, FeO, CoO and NiO), which have been reported recently by Eastman.[7] The energy of the exciting UV photons in this case was 30.0eV, a synchrotron radiation source being employed. The X-PE spectra of the titanates and the UV-PE spectra of the monoxides are remarkably similar after allowance has been made for the lower resolution inherent in X-PES.

This observation has a very simple explanation. The 3d electrons in both the titanates and the monoxides exhibit localised behaviour and might be expected to give rise to similar PE structure. It is also anticipated that the widths and profile of the oxygen 2p band in MO and $MTiO_3$ are comparable. If this is so, then the three-fold reduction in the ratio of the number of 3d electrons to O 2p electrons in going from the monoxides to the titanates might be expected to counterbalance a comparable increase in the M 3d to O 2p partial photoionisation cross-section in passing from UV to X-PES.

Obviously, such an assumption is a drastic oversimplification of the physical situation. However, some justification is provided by the facts that: (i) MgO and $SrTiO_3$ (albeit a perovskite) have the same band-width (6.5eV);[10] and (ii) the average M-O separations in MO and $MTiO_3$ are very similar (the average Co-O distance in $CoTiO_3$ is 0.212 nm and in CoO is 0.213 nm).[8, 11]

The structure in the PE spectra of the titanates arising from the ionised metal 3d electrons may be interpreted using a ligand-field description of the localised $3d^{n-1}$ final states.

The site symmetry of the transition metal in the ilmenite

structure is not properly O_h, there being a trigonal distortion to C_{3V}. (The ilmenites have an ordered corundum structure.[4]) However, this trigonal distortion is probably comparatively small and, if so, the transition metal ions may be treated as if they were in an octahedral environment. The ground states of Mn^{2+}, Fe^{2+}, Co^{2+} and Ni^{2+} are then $^6A_{1g}$, $^5T_{2g}$, $^4T_{1g}$ and $^3A_{2g}$ respectively.

The ligand field analysis of the final state PE structure arising from photoionisation of these ions has been performed before in connection with the PE spectra of transition metal monoxides[7] and dihalides[12] respectively. We therefore do not propose to repeat the calculation, but note that the analysis by Eastman[7] contains one error (concerning the ionisation of high-spin d^5).

The final state structure due to metal 3d photoionisation is understandably weak in the UV-PE spectra, but some of the features in the spectra compare favourably with those in the UV-PE spectra of the corresponding transition metal dihalides.[12] Although there are usually many final states accessible following metal 3d photoionisation in these systems, the states tend to group together. The Japanese workers[12] have analysed their PE spectra of the transition metal dihalides in terms of such final state groupings. We propose, therefore, that the PE spectra of the ilmenites may be explained in terms of the same groupings. In table 6.1 we present the component final states and relative intensities of each of the groupings.

Turning again to figs. 6.2 and 6.3, the peaks c and d in the He-I PE spectrum of $MnTiO_3$ are thought to be due to

the final states $^5T_{2g}$ and ^5Eg respectively. Three features due to metal 3d photoionisation can be observed in the He-I PE spectrum of $FeTiO_3$, although the first one overlaps considerably with the oxygen 2p band. These are the peak c and the two peaks labelled d; we attribute these to the final state groupings X, Y and Z respectively (see table 6.1). In the UV-PE spectra of both $CoTiO_3$ and $NiTiO_3$ it is only possible to discern the Y groupings and these have been labelled as c in the spectrum.

6.3 Transition metal perovskites

Sample pretreatment procedures for the oxides were as follows: $YCrO_3$ was heated at ca 920K for $2\frac{1}{2}$ hours under a dynamic pressure of 10^{-4} torr oxygen; $YMnO_3$ was heated in a 79% N_2/21% O_2 atmosphere for $2\frac{1}{2}$ hours at ca 1050K; $YFeO_3$ was fired at ca 1000K for 2 $^3/4$ hours under an atmosphere of oxygen; $YbMnO_3$ was heated for three hours at ca 870K under an atmosphere of oxygen; $CaMnO_3$ was fired at ca 970K for $3\frac{1}{2}$ hours under an atmosphere of oxygen. The samples of $YCrO_3$, $YMnO_3$ and $YFeO_3$ gave reasonably sharp O 1s PE signals, while that of $CaMnO_3$ and, to a lesser extent, $YbMnO_3$ still exhibited shoulders to higher binding energy. Prolonged heating of these two samples, had no further effect however.

The valence region PE spectra of the compounds are presented in figs. 6.6 to 6.10. The X-PE spectra have been corrected for the small presence of Pt signals (cf. section 3.2). The PE spectra of $YCrO_3$, $YMnO_3$, $YFeO_3$ and $YbMnO_3$ were recorded at 750K, 695K, 530K and 690K, respectively, to overcome sample charging. These observations are consistent with the reported electrical conductivity data on these compounds.[3] All are p-type semiconductors with conductivities of the order of 10^{-3}

mho cm^{-1} at 77OK. The PE spectra of $CaMnO_3$ were recorded at room temperature. Although this compound is expected to be an intrinsic insulator, non-stoichiometric samples exhibit high conductivities. A resistance of 1.6 ohm cm has been reported[13] for $CaMnO_{2.98}$; our sample analysed as $CaMnO_{2.97}$.

The structure of $CaMnO_3$ is the nearest of the five oxides to the cubic perovskite ideal. Both the UV-PE spectra of the material (fig. 6.10) reveal that the oxygen 2p band is split into two, the separation between the peaks being 2.0eV. A similar O 2p profile has been observed in the He-I PE spectrum of the perovskite $SrTiO_3$;[14] the separation between the two peaks in that compound was 1.9eV.

The peak labelled d in fig. 6.10 must be due to Mn 3d photoionisation. Once again we note that in the case of a localised d^3 configuration, the oxygen and metal nd bands are partially resolved. The origin of the peak labelled a is uncertain. It may conceivably be an impurity peak such as carbon 2s (recall that we could not completely 'clean up' the O 1s signal). However, it does bear resemblance to some of the structure that Eastman observed in the UV-PE spectra of the transition metal monoxides[7] and which he attributed to multi-electron processes. The peak a is separated from the Mn 3d band by ca 9eV. This compares favourably with the values of 8-10eV that Eastman obtained for the features in his spectra.

An analytical model has recently been proposed by Wolfram et al.[14, 15] to explain the PE spectra of d-band perovskites. Essentially they derive formulae for the oxygen 2p and metal nd partial DOS (ρ_p and ρ_d respectively) in terms of LCAO parameters. These parameters may be obtained from APW-LCAO band structure calculations. Although such an analytical model

cannot be as accurate as a full calculation it is of considerable didactic value. We have used it to rationalise the intensity changes that occur in the valence PE spectrum of $CaMnO_3$ with varying photon energy (see fig. 6.10).

For perovskites containing first row transition elements, the ratio of σ_d (the metal 3d photoionisation cross-section) to σ_p (that of the oxygen 2p) is expected to be roughly equal to unity for He-I radiation and ca 3 for X-radiation. This is consistent with the results obtained for the titanates in the last section.

The two peaks in the mainly oxygen 2p part of the PE spectrum are attributed to photoionisation from a bonding and a non-bonding oxygen band respectively. The higher binding energy bonding band will have a much larger metal 3d contribution than the non-bonding band.

The UV-PE spectra (where $\sigma_d = \sigma_p$) are representative of the total DOS, while the X-PE spectrum is dominated by the metal 3d PDOS ($\sigma_d / \sigma_p = 3$). Consequently, the oxygen 2p band at higher K.E is apparently 'lost' in changing from He-II to X-radiation. The separation between the peaks b and d should remain constant as the photon energy is varied. The observed separations are 4.8eV for the He-II spectrum and 4.6eV for the X-ray spectrum.

In contrast to $CaMnO_3$, the PE spectra of the other perovskite-related materials are much less informative. The gross features in the spectra of $YCrO_3$, $YMnO_3$ and $YFeO_3$ are consistent with those of the corresponding transition metal sesquioxide, if one allows for the two-fold reduction in the number of 3d electrons. This observation supports the proposed localised description of the transition metal 3d electrons

in both series of compounds.

Only in the case of the chromium oxides is it possible to make any direct comparison of features in the various spectra. The separation between the maxima in the oxygen 2p and metal nd regions of the He-II spectra is 3.3eV for Cr_2O_3 and 3.1eV for $YCrO_3$.

The UV-PE spectra of $YMnO_3$ and $YbMnO_3$ are very similar (fig. 6.7). This is a little surprising, because the X-PE valence region spectrum of $YbMnO_3$ (fig. 6.9) is dominated by Yb 4f signals.[3] From examination of the X-ray PE spectrum, one might have expected similar 4f structure between 21 and 31eV kinetic energy in the He-II spectrum. The fact that no such structure can be detected, must be attributed to the extremely low photoionisation cross-section that the 4f electrons in lanthanoid compounds have to He-II radiation. A similar conclusion has been reached by Egdell[16] in his gas phase UV-PE study of $Hf(BH_4)_4$. $YbMnO_3$ would certainly be a very interesting compound to investigate using synchrotron radiation.

Table 6.1. Final state intensities for the photoionisation process $3d^{n} \longrightarrow 3d^{n-1}$ as predicted from ligand field theory.[12]

Ground State Ion	$Mn^{2+}(^6A_1)$		$Fe^{2+}(^5T_2)$			$Co^{2+}(^4T_1)$		$Ni^{2+}(^3A_2)$	
Labels for Final state groupings	X	Y	X	Y	Z	X	Y	X	Y
Component final states in each group	$^5T_2$	^5E	$\begin{pmatrix}^4T_1, ^4E\\ ^4T_2, ^4A_1\end{pmatrix}$	$(^4T_2, ^4T_1)$	$^6A_1$	$\begin{pmatrix}^3A_2, ^3E\\ ^3T_2, ^3T_1\end{pmatrix}$	$\begin{pmatrix}^3T_2, ^3T_1\\ ^5T_2\end{pmatrix}$	$^2T_1$	$(^2E, ^4T)$
Relative intensities of Final state groupings	3.0	2.0	2.8	2.0	1.2	2.5	4.5	2.0	6.0

Note: (i) All final states are necessarily of even parity.

(ii) The photoionisation cross-section is assumed to be the same for the t_{2g} and e_g orbitals.

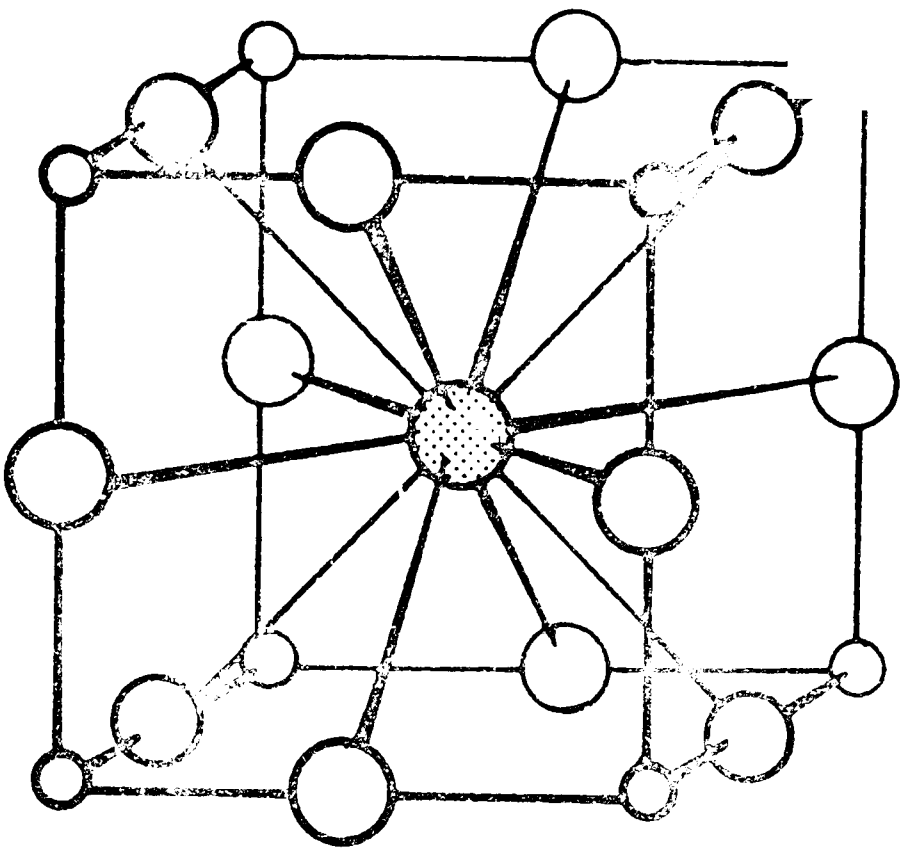


Fig. 6.1. The perovskite structure for compounds ABO_3. Large open circles represent O ions, the shaded circles A, and the small circles B ions.

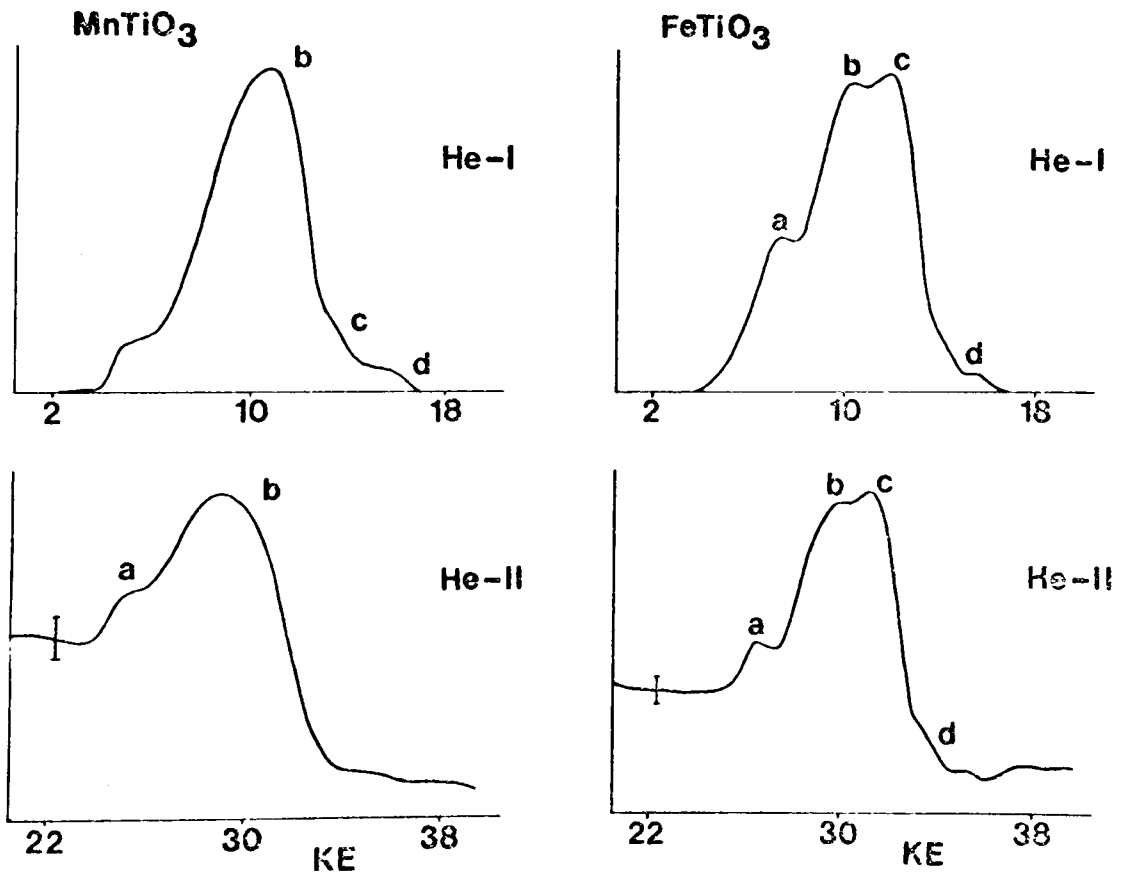


Fig. 6.2. He-I and He-II PE spectra of $MnTiO_3$ and $FeTiO_3$.

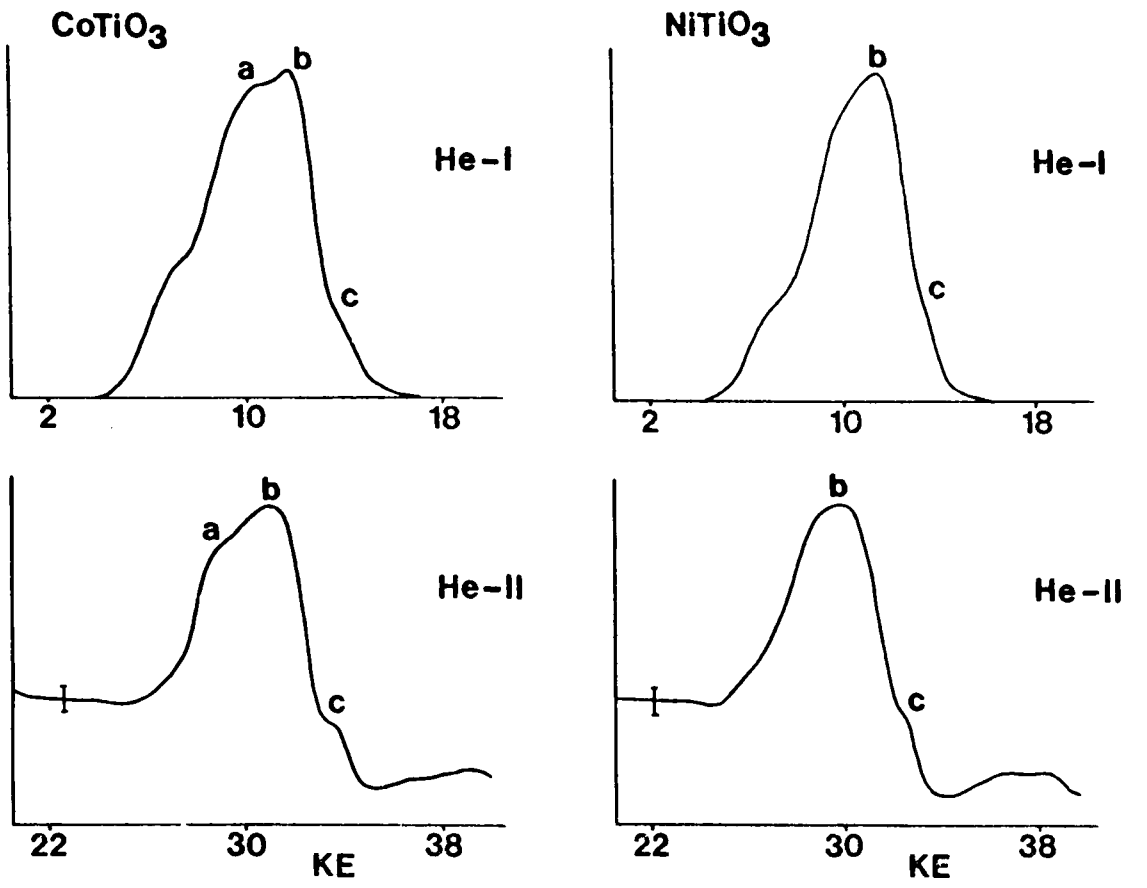


Fig. 6.3. He-I and He-II PE spectra of $CoTiO_3$ and $NiTiO_3$.

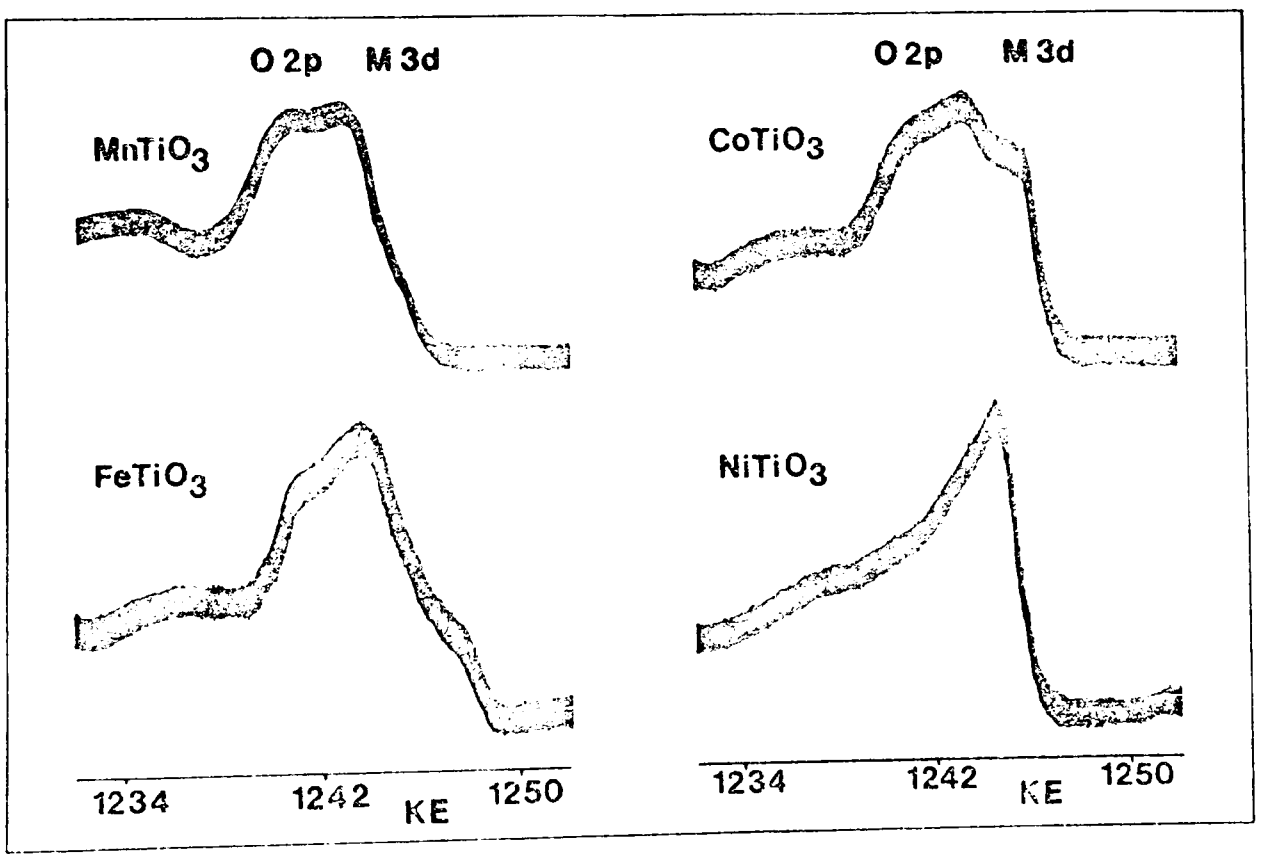


Fig. 6.4. Valence region X-PE spectra of $MnTiO_3$, $FeTiO_3$, $CoTiO_3$ and $NiTiO_3$.

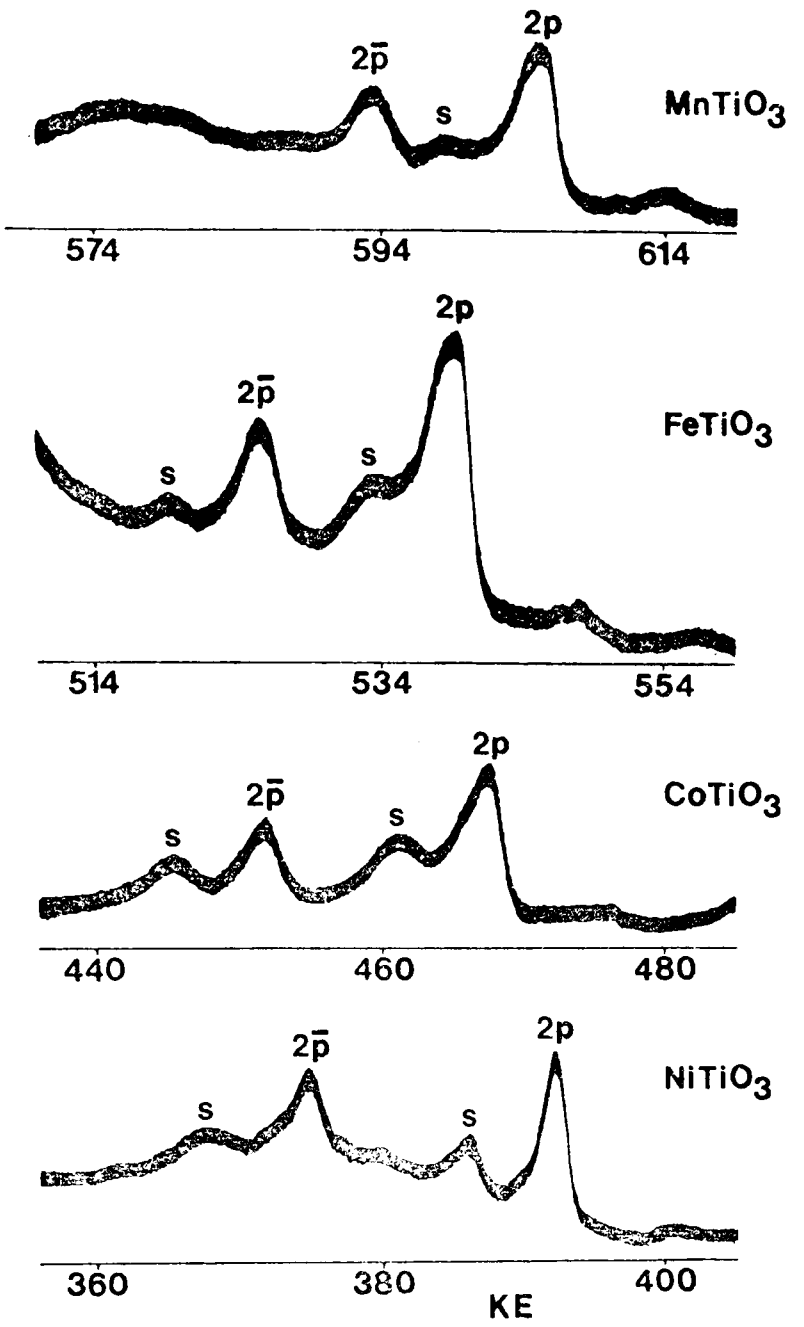


Fig. 6.5. The metal 2p X-PE spectra of $MnTiO_3$, $FeTiO_3$, $CoTiO_3$ and $NiTiO_3$.

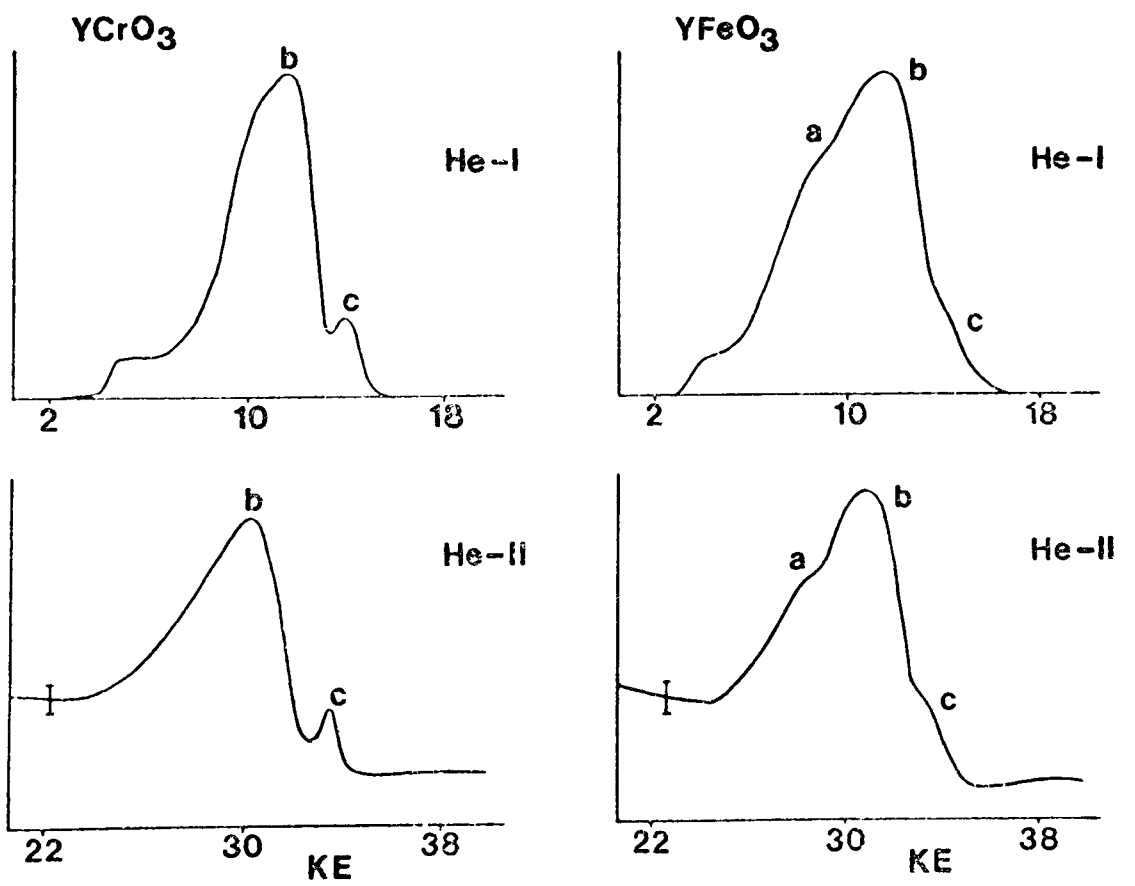


Fig. 6.6. He-I and He-II PE spectra of $YCrO_3$ and $YFeO_3$.

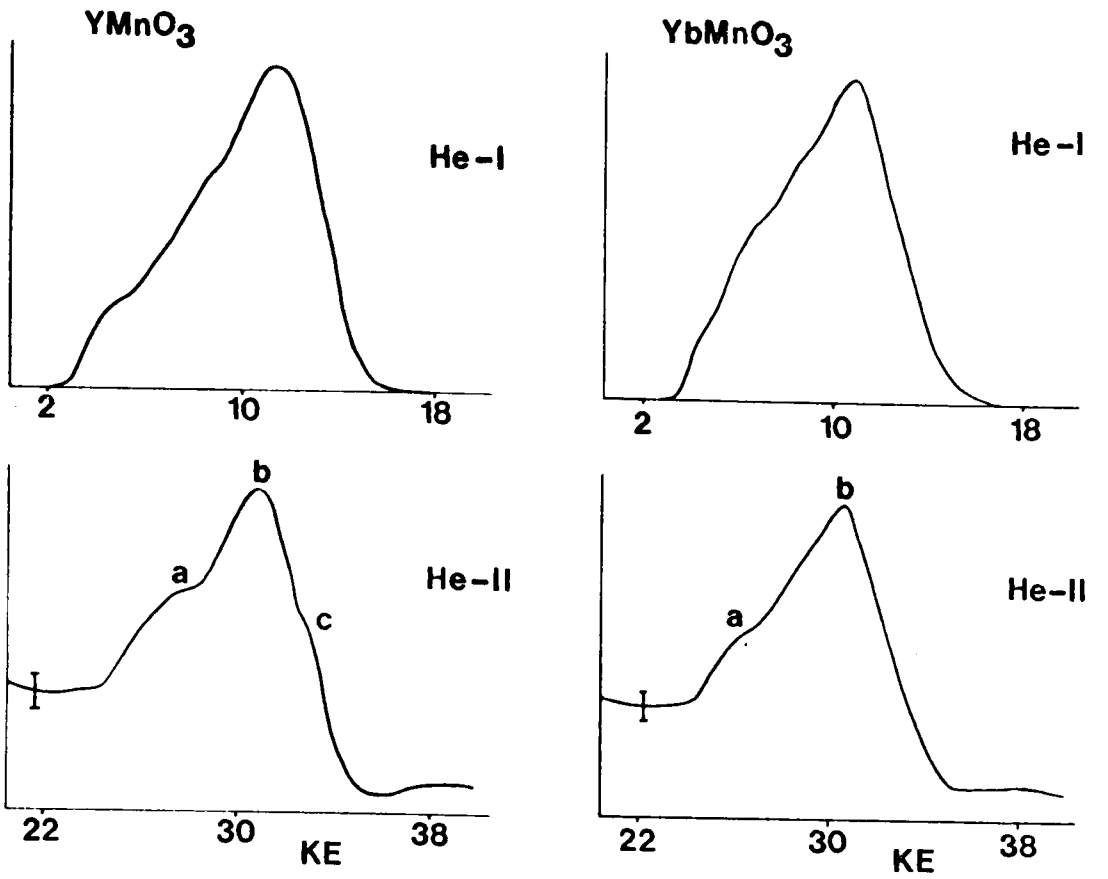


Fig. 6.7. He-I and He-II PE spectra of $YMnO_3$ and $YbMnO_3$.

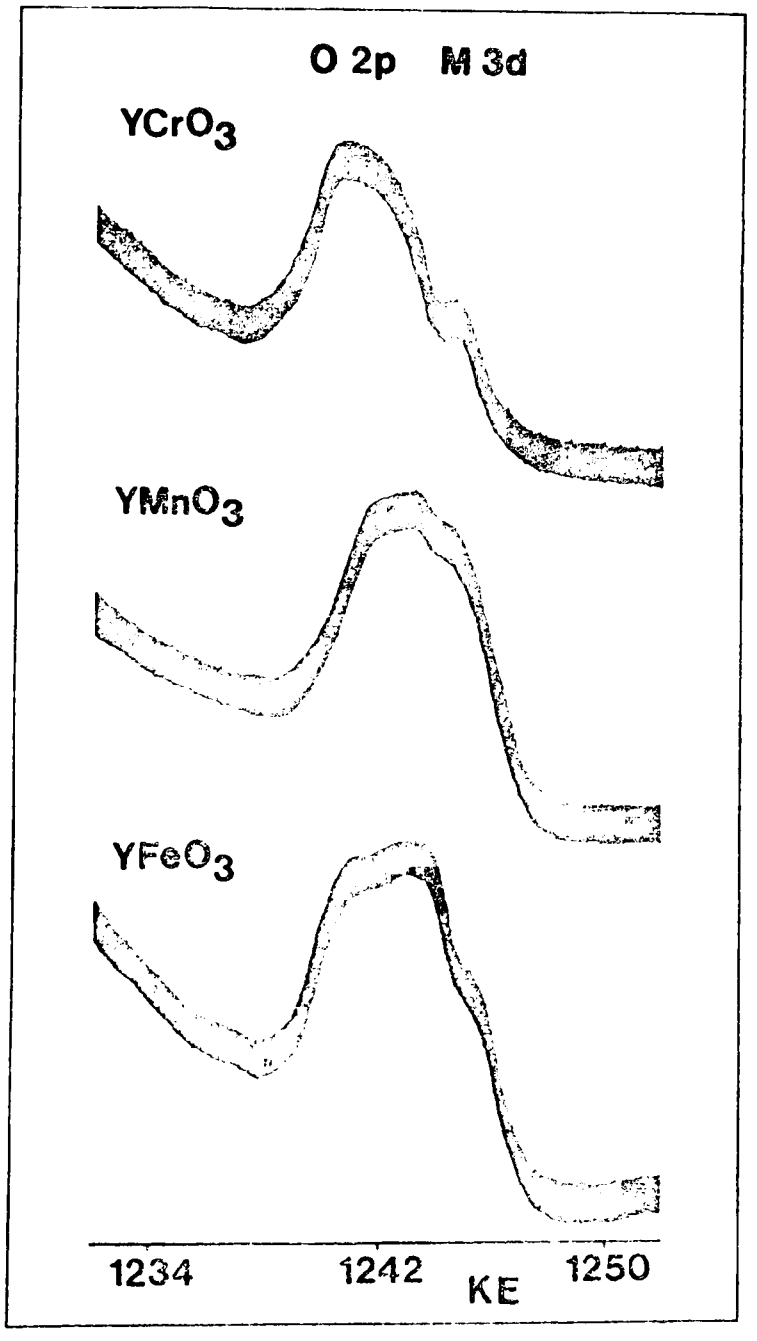


Fig. 6.8. Valence region X-PE spectra of $YCrO_3$, $YMnO_3$ and $YFeO_3$.

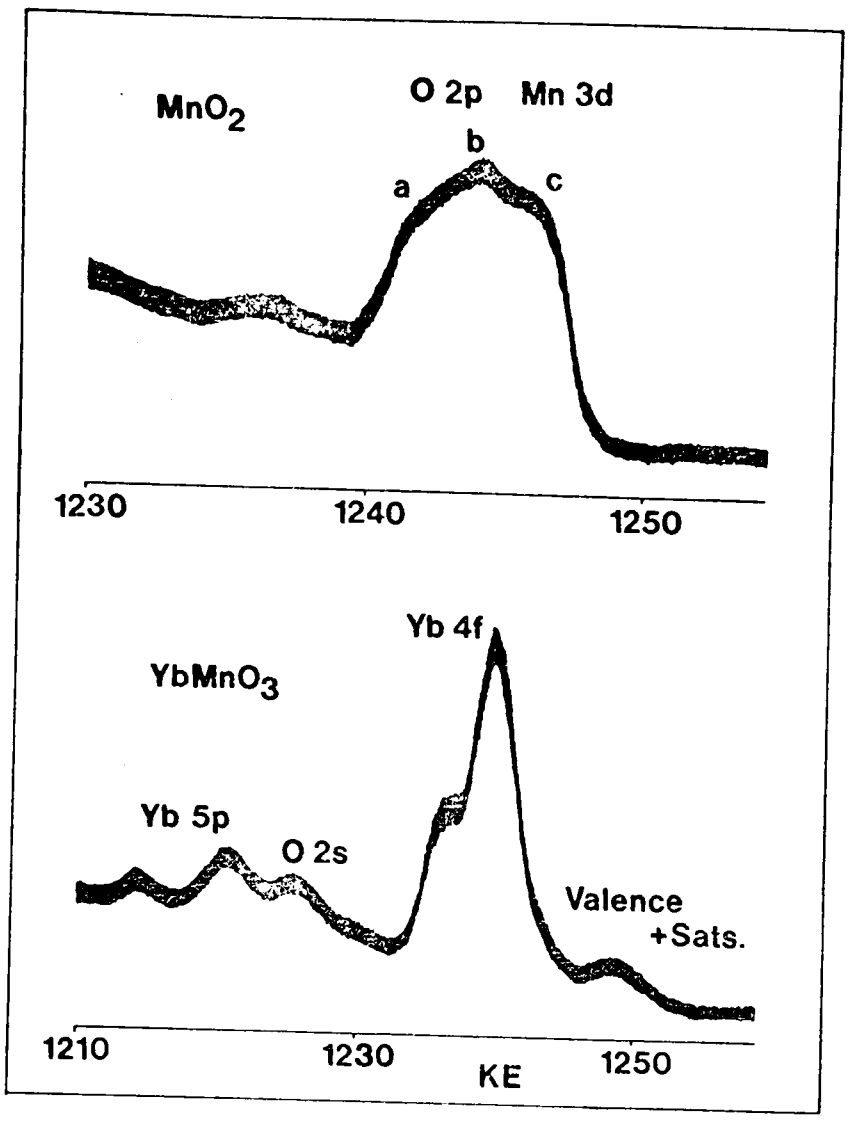


Fig. 6.9. Valence region X-PE spectra of MnO_2 and $YbMnO_3$

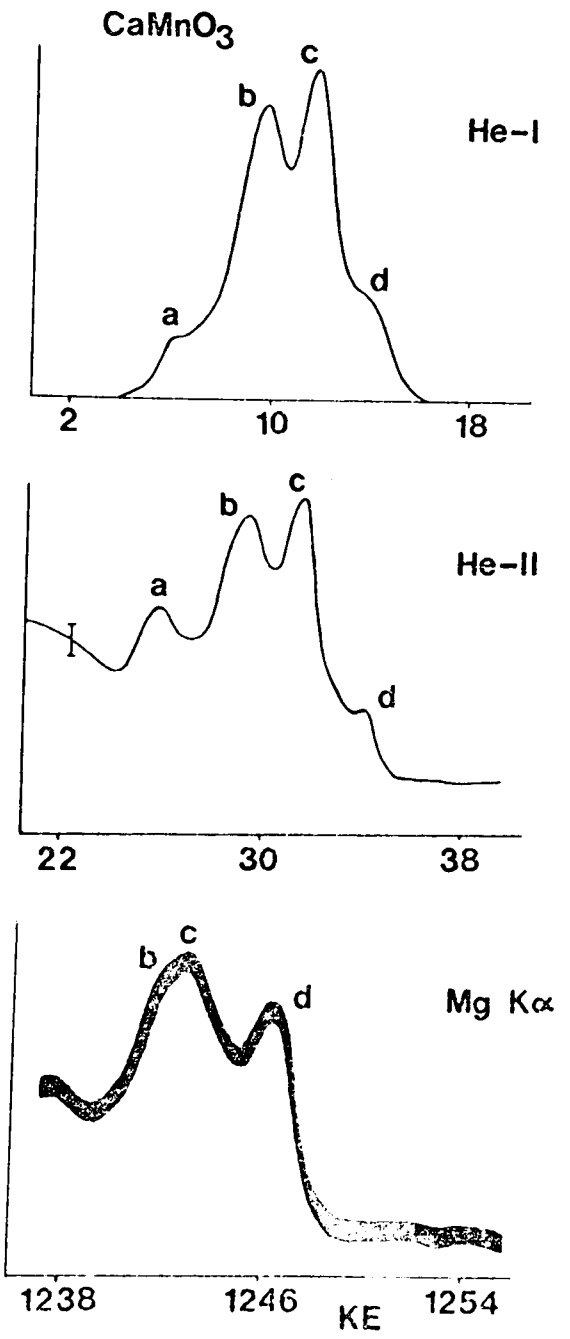


Fig. 6.10. He-I, He-II and X-PE valence region PE spectra of $CaMnO_3$

REFERENCES FOR CHAPTER 6

1. J. B. Goodenough, J. M. Longo "Landolt-Bornstein, New Series Group III" Vol. 4a (1970) Springer-Verlag, New York.
2. A. F. Wells, "Structural Inorganic Chemistry" 4th Edition (1975) Clarendon Press, Oxford.
3. G. V. Subba Rao, B. M. Wanklyn, C. N. R. Rao, J. Phys. Chem. Solids 32 (1971) 345.
4. J. B. Goodenough, J. J. Stickler, Phys. Rev. 164 (1967) 768.
5. G. Thornton, D. Phil. Thesis, Oxford (1976).
6. D. S. Ginley, M. A. Butler, J. App. Phys. 48 (1977) 2019.
7. D. E. Eastman, J. L. Freeouf, Phys. Rev. Lett. 34 (1975) 395.
8. L. F. Mattheiss, Phys. Rev. B5 (1972) 306.
9. J. B. Goodenough, Prog. Solid State Chem. 5 (1971) 490
10. S. P. Kowalczyk, F. R. McFeely, L. Ley, V. T. Gritsyna, D. A. Shirely, Solid State Commun. 23 (1977) 161.
11. R. E. Newnham, J. H. Fang, R. P. Santoro, Acta Cryst, 17 (1964) 240.
12. T. Ishii, S. Kono, S. Suzuki, I. Nagakura, T. Sagawa, R. Kato, M. Watanabe, S. Sato, Phys. Rev. B12 (1975) 4320.
13. J. B. MacChesney, H. J. Williams, J. F. Potter, R. C. Sherwood, Phys. Rev. 164 (1967) 779.
14. T. Wolfram, Ş. Ellialtioğlu, Phys. Rev. Lett. in press.
15. Ş. Ellialtioğlu, T. Wolfram, Phys. Rev. B15 (1977) 5909.
16. A. J. Downs, R. G. Egdell, A. F. Orchard, P. D. P. Thomas, JCS Dalton in press.

CHAPTER SEVEN

APPLICATION OF MULTICONFIGURATIONAL DIRAC-FOCK THEORY TO PHOTOELECTRON SPECTROSCOPY

7.1 Dirac-Fock theory

7.2 Implementation of the MCDF method

7.3 Relativistic formulation of final state structure in PES

7.4 Ionisation of a 4f electron from lanthanoid compounds

7.5 Structure in the core-level X-PE spectra of lanthanoid and transition metal compounds

7.6 Valence electron structure in the UV-PE spectra of metal atom vapours

7.1 Dirac-Fock theory

(i) The Dirac equation

The Schrödinger equation for a single electron in a central potential is not invariant under the Lorentz transformation and does not provide a description of electronic structure which satisfies the principles of special relativity. (The basic assumptions and implications inherent in the special theory of relativity are described briefly in Appendix 4). The Dirac equation, however, has the proper behaviour under the Lorentz transformation.[1]

The Dirac Hamiltonian, in atomic units is[2]

$$H_D = c\,\underline{\alpha}.\,\underline{p} + \beta c^2 + V(\underline{r}) \qquad (7\text{-}1)\ \text{a.u}$$

where $\underline{r}$ is the position vector of the electron, $V(\underline{r})$ is its potential energy, c is the velocity of light, and $\underline{p} \equiv -i\nabla$ is the linear momentum operator. The operators $\underline{\alpha}$ and $\underline{\beta}$ are 4 x 4 matrices

$$\alpha_\mu = \begin{pmatrix} 0 & \sigma_\mu^P \\ \sigma_\mu^P & 0 \end{pmatrix} \qquad \beta = \begin{pmatrix} I & 0 \\ 0 & -I \end{pmatrix} \qquad (7\text{-}2)$$

where μ = x, y or z, I is the 2 x 2 unit matrix and σ_μ^P are the Pauli spin matrices

$$\sigma_x^P = \begin{pmatrix} 0 & 1 \\ 1 & 0 \end{pmatrix} \quad \sigma_y^P = \begin{pmatrix} 0 & i \\ -i & 0 \end{pmatrix} \quad \sigma_z^P = \begin{pmatrix} 1 & 0 \\ 0 & -1 \end{pmatrix} \qquad (7\text{-}3)$$

As a result the wavefunction must be taken to be an object with four components (a four-component spinor).

For a central field, H_D is invariant under rotation and reflection

$$[H_D, \underline{j}\ ] = 0 \quad ; \quad [H_D, \underline{P}] = 0 \tag{7-4}$$

where j is the total angular momentum operator

$$\left.\begin{aligned} \underline{j} &= \underline{r} \wedge \underline{p} + \tfrac{1}{2}\underline{\sigma} \\ \sigma_\mu &= \begin{pmatrix} \sigma_\nu^\rho & 0 \\ 0 & \sigma_\nu^\rho \end{pmatrix} \end{aligned}\right\} \tag{7-5}$$

and $\underline{P} \equiv \beta P$ is the Dirac equivalent of the ordinary parity operator P. The term $\frac{1}{2}\underline{\sigma}$ represents the intrinsic (spin) angular momentum operator;the prediction of electron spin is one of the great triumphs of the Dirac equation. It follows that central field wave-functions can be classified in terms of the eigenstates of j^2, j_z and P. In addition, however, the operator

$$\underline{k} = \beta(\ \underline{\sigma}.\underline{l} + I) \tag{7-6}$$

is also a conserved quantity. The eigenvalues of j^2, j_z and $\underline{k}$ are $j(j+1)$, m_j and k respectively, the eigenvalues j and k being related by

$$\left.\begin{aligned} k &= -(j + \tfrac{1}{2})\ a \\ \text{where} \quad a &= +1 \quad \text{for} \quad j = l + \tfrac{1}{2} \\ \text{and} \quad a &= -1 \quad \text{for} \quad j = l - \tfrac{1}{2} \end{aligned}\right\} \tag{7-7}$$

The quantum numbers k and m_j prove to be sufficient to describe both the spin and angular part of the wavefunction.

The four component wave-function (single particle spinor) Ψ_{nkm} can be shown to have the form[1]

$$\Psi_{nkm}(\underline{r}) = \begin{pmatrix}\psi_+\\ \psi_-\end{pmatrix} = \frac{1}{r}\begin{pmatrix} P_{nk}(r) & \chi_{k,m}(\theta,\phi)\\ Q_{nk}(r) & \chi_{-k,m}(\theta,\phi)\end{pmatrix} \tag{7-8}$$

where ψ_+ and ψ_- are two-component functions. The two-component spin-orbital function $\chi_{k,m}$ is given by[1]

for k positive $$\chi_{km} = \begin{pmatrix} C_1^+ & Y_{j-1/2,\,m_j-1/2}\\ C_2^+ & Y_{j-1/2,\,m_j+1/2}\end{pmatrix} \tag{7-9}$$

for k negative $$\chi_{km} = \begin{pmatrix} C_1^- & Y_{j+1/2,\,m_j-1/2}\\ C_2^- & Y_{j+1/2,\,m_j+1/2}\end{pmatrix} \tag{7-10}$$

$Y_{l,m}$ is a spherical harmonic. The coefficients are as follows

$$C_1^+ = \left[\frac{j+m_j}{2j}\right]^{1/2} \qquad C_2^+ = \left[\frac{j-m_j}{2j}\right]^{1/2}$$

$$C_1^- = \left[\frac{j-m_j+1}{2(j+1)}\right]^{1/2} \qquad C_2^- = -\left[\frac{j+m_j+1}{2(j+1)}\right]^{1/2} \tag{7-11}$$

The radial wavefunctions P and Q in equation (7-8) are referred to as the large and small components respectively. In the non-relativistic (NR) limit $c \longrightarrow \infty$, P goes over into the NR radial wavefunction and Q tends to zero. The radial wave-equations for P and Q involve a pair of coupled first order differential equations.[2]

The conventional nomenclature for describing one-electron central-field solutions of Dirac's equation is shown in Table 7-1. The notation $\bar{l}$, l refers respectively to the $j = l - \frac{1}{2}$, $j = l + \frac{1}{2}$ states which both have the same value of l.

For bound states, we also need to introduce the principal quantum number n, related to the number of nodes n_r in the radial function $P_{nk}(\underline{r})$ by

$$n = n_r + |k| \qquad (7\text{-}12)$$

Subshells belonging to the values $j = l \pm \frac{1}{2}$ are degenerate in the NR limit; l is then the usual orbital angular momentum.

(ii) Relativistic modification of hydrogenic wavefunctions

In order to facilitate comparison with non-relativistic theory, it is necessary to subtract the rest mass energy, $m_o c^2$ (see Appendix 4) from the Dirac equation. The non-relativistic reduction of the Dirac equation may then be effected by several methods.[3, 4] In the Pauli theory,[4] the large component may be considered as satisfying a Schrödinger equation with effective Hamiltonian

$$\left.\begin{aligned} H_{eff} &= H_o - \frac{p^4}{8c^2} + \frac{1}{4c^2}\frac{1}{r}\frac{dV}{dr}(\underline{s}\cdot\underline{L}) + \cdots \\ H_o &= \tfrac{1}{2}\underline{p}^2 + V(r) \end{aligned}\right\} \quad \begin{matrix}(7\text{-}13)\\ \text{a.u}\end{matrix}$$

other terms being $O(\frac{1}{c^4})$

The term H_o is the usual NR Hamiltonian, the second term is just the relativistic K.E correction, and the third term is the spin-orbit coupling term.

Relativity gives rise to two major qualitative effects.[5,6] (i) The relativistic charge cloud is contracted relative to corresponding non-relativistic distributions. The effect is most marked for penetrating orbitals ($k = \pm 1$) and falls off as n and $|k|$ increase. (ii) The nodes of $P_{nk}(r)$ and $Q_{nk}(r)$ interlace except for nodeless cases with $k = -n$ and, consequently, relativistic electron probability densities are never zero.

(iii) The many-electron case

As may be anticipated, exact solutions for many-electron systems are just as impossible within a relativistic, as in a non-relativistic framework. Consequently, attempts to study many-electron atoms relativistically, have relied mainly upon self-consistent field procedures. The most commonly used Hamiltonian is

$$H = \sum_{i=1}^{N} H_i + \sum_{i>j} \frac{1}{r_{ij}} \qquad (7\text{-}14) \text{ a.u}$$

where

$$H_i = c\,\underline{\alpha}\cdot\underline{p}_i + (\beta-1)c^2 - \frac{Z}{r_i} \qquad (7\text{-}15) \text{ a.u}$$

The term $(\beta-1)c^2$ ensures that the energy origin has been shifted from $+m_o c^2$ (c^2 in a.u) to zero, in order to facilitate comparison with non-relativistic theory.

The above Hamiltonian suffices for most purposes, even though the Coulomb interaction $1/r_{12}$ is not even approximately Lorentz covariant. A more complete treatment is afforded by quantum electrodynamics (QED);[7] the Coulomb interaction appears as the leading term in an expansion of the interaction energy in powers of α (the fine structure constant).

7.2 Implementation of the MCDF method

As is customary in self-consistent field procedures, the orbital approximation is invoked. The wavefunction, which is referred to as a configuration state function (CSF), is assumed to be a linear combination of antisymmetrised products of single article spinors $\Psi_a(\underline{r})$.

The electrons are coupled together to give an eigenstate of total angular momentum

$$\underline{J} = \sum_{i=1}^{N} \underline{j}_i \qquad (7\text{-}16)$$

These CSF, to be denoted by $\Phi_r(\gamma_r PJM)$, are eigenfunctions of $\underline{J}^2$ and J_z belonging to the eigenvalues $J(J+1)$ and M, and of parity P. The label γ_r denotes the set of symmetry labels (subshell occupation numbers, angular-momentum coupling schemes, seniority numbers, or other group-theoretical labels) necessary to define an orthonormal N-electron basis. An open-shell atomic state will in general be expressible as a linear combination of CSF belonging to the same parity and total angular momentum. Such a linear combination is referred to as an atomic state function (ASF) and written

$$\Psi_\alpha(PJM) = \sum_{r=1}^{N_c} C_{r\alpha}\, \Phi_r(\gamma_r PJM) \qquad (7\text{-}17)$$

The essence of the multiconfigurational Dirac-Fock (MCDF) method is to choose configurational-mixing coefficients, $C_{r\alpha}$, and the orbitals, $\Phi_a(\underline{r})$, by applying the variational method to the expectation value of the Hamiltonian with respect to the ASF Ψ_α (PJM), subject to orbital orthonormality constraints.

One important aspect of calculating atomic structure within the framework of Dirac-Fock theory is that one is frequently dealing with situations which are close to Russell-Saunders coupling and consequently there will be considerable interaction between the relativistic states. As a result, it proves expedient to introduce the notion of a manifold of relativistic states. The l^n manifold is defined as the set of jj configurations $T^q\, l^{n-q}$ $(0 \leqslant q \leqslant n)$.

Such manifolds degenerate into the states of the non-relativistic l^n configuration in the formal limit $c \longrightarrow \infty$. It is helpful to list the allowed values of J in the configuration $(j)^r$; this is done in table 7.2. We can thus see (table 7.3) that the f^2 manifold gives rise to a total of 13CSF.

The results presented in this thesis were obtained using an existing suite of SCF programmes (see Appendix 2). There are three different variants of the MCDF procedure and these are distinguished by the criteria used to determine both the orbitals and the mixing coeffs $C_{r\alpha}$. In decreasing order of effort, we may use the following schemes:

(i) OL (optimal level) calculations - where the orbitals and mixing coefficients are determined simultaneously for each atomic state α in turn.

(ii) AL (average level) calculations where the orbitals are determined by using an energy functional given by the average energy of all CSF with a fixed value of J contributing to equation (7-17). This mean energy is proportional to the trace of the corresponding J sub-matrix of the atomic Hamiltonian and is independent of the mixing coefficients $C_{r\alpha}$. The latter can be determined for all atomic states involved by diagonalising the Hamiltonian submatrix with the optimised orbitals.

(iii) EAL (extended average level) calculations - where the orbitals are determined from an energy functional given by the weighted sum of the traces of several submatrices with different J values. Each submatrix is subsequently diagonalised to determine the mixing coefficients. The complete set of atomic states is conveniently built from a common set of orbitals in this method. In this work, extensive use was

made of the AL and EAL schemes.

Dirac-Fock calculations have revealed that relativity can significantly modify the orbitals in heavy many-electron atoms. Such changes can be interpreted as being the result of the interplay between two separate effects.[6] There is the direct effect (see section 7.1.ii) which causes all orbitals to contract, and the indirect effect which arises from the relativistic modification of other orbitals in the atom affecting the screening of the electron in question. In the inner-core shells of an atom, the motion of the electrons is primarily affected by the nuclear potential and the direct effect dominates. In the valence shells the modification depends on the angular momentum characterising the orbital. Comparison of relativistic and non-relativistic Hartree-Fock solutions for s and $\bar{p}$ electrons shows that the relativistic orbital is normally more tightly bound than the corresponding non-relativistic one, and that for p electrons the effect of relativity is small. For $\bar{d}$, d, $\bar{f}$ and f electrons the relativistic orbital is more loosely bound than the non-relativistic orbital.

7.3 Relativistic formulation of final state structure in PES

The tensor algebra associated with the relativistic formulation of photoionisation is very similar to that described for the non-relativistic case (see section 2.2). The reduced matrix element for photoionisation from a single open shell defined by $|(j^r)\alpha J\rangle$ is given by [9]

$$\langle j^r(\alpha J)\| \sum_i^N T^1(i) \| j^{r-1}(\alpha'' J''), j'_\beta j(\alpha' J')\rangle$$
$$= [j]^{1/2}[J']^{1/2} W(j'_\beta K J'' J; j J') \times \Gamma^{1/2}$$
$$\times \langle (\alpha J)\{|(\alpha'' J''), j\rangle \langle j \| T^1 \| j'_\beta\rangle$$

(7-18)

We have adopted an analogous notation to that described in section 2.2; the subscript to the continuum orbital j' is to indicate that it must be of opposite parity to j. The term $\langle(\alpha J)\{|(\alpha'' J''), j\rangle$ represents the <u>coefficient</u> of <u>fractional parentage</u> (cfp) for jj coupled electrons. These coefficients have been conveniently tabulated for cases up to $j = \frac{7}{2}$, although certain of the earlier compilations have inconsistent relative phases. Anyone interested in using such coefficients should see the recent note by Grant.[10] The explict form of the one-electron reduced matrix element of the electric dipole operator, $\langle j \| T^1 \| j\beta\rangle$, between two relativistic orbitals has not been used in this work; consequently, we do not present it here but refer to another paper by Grant.[11] The electric dipole operator only connects orbitals of opposite parity.

The total photoionisation cross-section for production of the ionic state $(\alpha'' J'')$ is obtained by summing over all values of j' and J'. By analogy to section 2.5, we end up with

$$\sigma_{tot} = \tau |\langle (\alpha J)\{|(\alpha'' J''), j\rangle|^2 \bar{\sigma}_j \qquad (7\text{-}19)$$

where the sub-shell photoionisation cross-section ($\bar{\sigma}_j$) is given by

$$\bar{\sigma}_j = \frac{4\pi^2\alpha C}{3}\left\{|\langle j \| T^1 \| j_\beta - 1\rangle|^2 + |\langle j \| T^1 \| j_\beta\rangle|^2 + |\langle j \| T^1 \| j_\beta + 1\rangle|^2\right\}$$

(7-20)

Equation (7-20 indicates that in general, three continuum channels are available to the photoelectron. An $\bar{f}$ ($j = \frac{5}{2}$) electron may be ionised into a $\bar{d}$ ($j = \frac{3}{2}$), d ($j = \frac{5}{2}$) or $\bar{g}$ ($j = \frac{7}{2}$) continuum orbital. The weighted average of the $\bar{f}$ and f electron photoionisation cross-section as $c \longrightarrow \infty$.

The simple form of these relativistic photoionisation equations is perhaps misleading beacuse if the system is still close to Russell-Saunders coupling, it will be necessary to include all the interactions between relativistic states belonging to the same manifold. What this means is that we will invariably have to deal with cases where ionisation occurs from one of several open shells in the system.

Let us consider photoionisation from a state J belonging to the manifold 1^n. This state can be written as

$$|J\rangle = \sum_a c_a \left| j_1^{\tau}(J_3), j_2^{n-\tau}(J_1); J\right\rangle$$

(7-21)

where the c_a are the mixing coefficients which may be typically obtained from an SCF calculation; j_1 and j_2 are the two relativistic components of the orbital 1; and the coupling scheme indicates that J_3 and J_2 are the total angular momentum of the j_1 and j_2 subshells respectively. We have dropped group theoretical labels from the notation to aid clarity. The final

system of ion plus continuum electron may be similarly described as

$$|J'\rangle = \sum_b C_b \left|\left(j_1^{s}(J_4), j_2^{n-s-1}(J_2); J''\right), j'; J'\right\rangle \qquad (7\text{-}22)$$

The reduced matrix element of the electric dipole operator between these two states is given by

$$\langle J \| \sum T^1(i) \| J' \rangle =$$

$$\left([j_2][J']\right)^{1/2} W(k j' J'' J; j_2 J')$$

$$\times \left\{ \sum_{ab} C_a C_b \delta_{rs} \delta_{J_3 J_4} [J_1]^{1/2} [J'']^{1/2} W(J_2 j_2 J_3 J; J_1 J'') \right.$$

$$\left. \times r^{1/2} \langle J_1 \{ | J_2, j_2 \rangle \langle j_2 \| T^1 \| j' \rangle \right\}$$

$$+ \left([j_1][J']\right)^{1/2} W(k j' J'' J; j_1 J')$$

$$\times \left\{ \sum_{ab} C_a C_b \delta_{r,s+1} \delta_{J_1 J_2} [J_3]^{1/2} [J'']^{1/2} W(J_4 j_1 J_1 J; J_2 J'') \right.$$

$$\left. \times (n-r)^{1/2} \langle J_3 \{ | J_4, j_1 \rangle \langle j_1 \| T^1 \| j' \rangle \right\}$$

(7-23)

In order to determine the total photoionisation cross-section for photoionisation into the ionic state J" we must sum the squares of reduced matrix elements over all possible values of j' and J'. The resulting formula is slightly simplified by the following orthogonality relation[9]

$$\sum_{J'} [J'][j_2] W(kj'J''J; j_2 J') W(kj'J''J; j_1 J') = \delta_{j_1 j_2} \tag{7-24}$$

The total photoionisation cross-section is then given by

$$\sigma_{tot} = \delta_{rs}\,\delta_{J_3 J_4}\left[\sum_{ab} C_a C_b [J_1]^{1/2}[J'']^{1/2} T^{1/2} W(J_2 j_2 J_3 J; J_1 J'') \times \langle J_1 \{ | J_2, j_2 \rangle\right]^2 \sigma_{j_2}$$

$$+ \delta_{r,s+1}\,\delta_{J_1 J_2}\left[\sum_{ab} C_a C_b [J_3]^{1/2}[J'']^{1/2} (n-T)^{1/2} W(J_4 j_1 J_1 J; J_3 J'')\right] \sigma_{j_1} \times \langle J_3 \{ | J_4, j_1 \rangle \tag{7-25}$$

Although this formula remains formidable, it can readily be evaluated on the computer (see Appendix 2). The most important feature of this equation is that there are no interference terms between the two sub-shell cross-sections. This is a general result and is completely independent of the internal coupling schemes in either the initial or final ion state.

It is instructive to provide a simple example. Consider the cross-section for photoionisation from the ground state J = 4

of Pr^{3+} ($4f^2$) to the J = $^5/_2$ level of Pr^{4+} ($4f^1$).

The ground state will be a linear combination of CSF with J = 4, that is

$$|J=4\rangle = C_1|\bar{f}^2\rangle_4 + C_2|\bar{f}f\rangle_4 + C_3|f^2\rangle_4 \qquad (7\text{-}26)$$

Hence the cross-section to $(\bar{f})J = {}^5/_2$ is given by

$$\sigma = 2C_1^2\bar{\sigma}_{\bar{f}} + C_2^2\bar{\sigma}_f \qquad (7\text{-}27)$$

It has not been our intention in this work to calculate absolute photoionisation cross-sections. In all the analysis of final-state structure presented in sections 7.4 and 7.5, we have assumed that the cross-sections, $\bar{\sigma}_{\bar{l}}$, $\bar{\sigma}_l$ for both relativistic orbitals derived from the same value of l are equal. This must obviously be a poor approximation if the situation is remote from a Russell-Saunders coupling.

Relativity has two important effects[12, 13] on the partial cross-sections $\bar{\sigma}_{\bar{l}}$ and $\bar{\sigma}_l$. The first is a result of the direct effect: the photoelectrons from the $j = l+\frac{1}{2}$ component have slightly increased K.E with respect to the $j = l-\frac{1}{2}$ component. The second is that the two bound orbitals have slightly different radial wavefunctions, and hence different dipole matrix elements with the continuum orbitals.

7.4 Ionisation of a 4f electron from lanthanoid compounds

In a completely non-relativistic framework, when an open shell of f electrons is ionised, final states are expected to appear with a probability proportional to the square of the respective LS coefficient of fractional parentage (see section 2.5).

$$\sigma_\iota(\alpha''L''S'' \leftarrow \alpha LS) = n\left|\langle \alpha LS\{|(\alpha''L''S''), \iota\rangle\right|^2 \bar{\sigma}_\iota$$

(7-28)

This formula may be extended[14,15] to include the effects of weak spin-orbit coupling; this gives

$$\sigma_\iota(\alpha''L''S''J'' \leftarrow \alpha LSJ) = n\left|\langle \alpha LS\{|\alpha''L''S'', \iota\rangle\right|^2 \times [J''][S][L] \sum_j [j] \begin{pmatrix} \frac{1}{2} & \iota & j \\ S & L & J \\ S' & L' & J' \end{pmatrix}$$

(7-29)

Cox[15] has tabulated the relative PE intensities for final states arising from ionisation of an f electron, using equation (7-29). These intensity patterns have proved to be of value in the interpretation of the X-PE spectra of lanthanoid oxides, but it is clear that there are still some discrepancies.[16] The aim of this section is to extend the intensity rules to include more explicitly the effects of relativity.

We have restricted our attention to the beginning and end of the lanthanide series (Pr^{3+}, Nd^{3+}, Yb^{3+}) to avoid situations where the number of CSF becomes too large to handle in an SCF calculation. We are also performed calculations on the actinide ions U^{3+}, U^{4+} and No^{3+} to observe more fully the trend in expected PE final state structure as one moves towards the limit of jj coupling.

It is also possible to perform non-relativistic calculations using the MCDF package; this is done by increasing the velocity of light by a factor of 10^4. This serves two purposes:

(i) it is possible to generate the mixing coefficients for the LS limit without further need to angular recoupling methods; and (ii) it provides a sensitive test of the correctness of our calculation, because we should be able to reproduce the values tabulated by Cox.

In Tables 7.4, 7.5 and 7.6 we list the calculated values of the final state intensities for the photoionisation processes $f^2 \longrightarrow f^1$, $f^3 \longrightarrow f^2$ and $f^{13} \longrightarrow f^{12}$ respectively.

The intensities were calculated solely from the mixing coefficients generated from MCDF calculations on the f^n and f^{n-1} manifolds respectively. In each table we present the results for the limits of both the LS and jj coupling schemes along with those from the corresponding lanthanide and actinide ions. It is assumed throughout both this and the next section that only the ground level of the initial system is populated before photoionisation; thus the ground states for f^2, f^3 and f^{13} have total angular momentum $J = 4$, $^9/_2$ and $^7/_2$ respectively. We have labelled each final state by $^{2S+1}L_J$, this is simply meant to indicate how that state behaves in the limit of each coupling scheme. In all cases, our NR results are in perfect agreement with the values tabulated by Cox.

In the f^2 manifold, the ground state will approach the pure CSF $\bar{f}^{\,2}(J=4)$ as relativistic effects become more important. The calculations reveal that U^{4+} is close to the jj limit with a $^2F_{5/2}$: $^2F_{7/2}$ intensity ratio of 37.5:1. This probably explains why only one 5f electron signal is detected in the gas phase UV-PE spectrum of $U(BH_4)_4$;[17] a compound which is formally f^2.

Turning our attention to the f^3 manifold, we find that because of the fortuitous similarity in the values of the

non-relativistic cfp for $f^3(^4I \longrightarrow {}^3H$ and $^3F)$ and the relativistic cfp for $\bar{f}^{\,3}(J=^9/_2 \longrightarrow J=4$ and $J=2)$ we find that there is little change in the overall pattern of final state intensity as we change from one coupling scheme to another. It is worth mentioning, however, that in intermediate coupling certain states (those with J=2, 4 or 6) may acquire a slight intensity, which they would not possess in either the LS or jj limit.

Ionisation of an electron from the f^{13} manifold (table 7.6) is a much more interesting case because there is a definite change in overall intensity distribution as we move between the various coupling situations. In fig. 7.1, we compare the different theoretical PE intensity distributions with the previously reported valence region X-PE spectrum of Yb_2O_3 excited by Al Kα radiation. The theoretical spectra were generated as follows: (i) the energy of each final state was determined from a relativistic EAL calculation on the Yb^{4+} $4f^{12}$ manifold; (ii) the final state intensity distribution was taken from table 7.6 for the LS, intermediate (e.g. $Yb^{3+} \longrightarrow Yb^{4+}$) and jj coupling schemes in turn; and (iii) the calculated spectra then broadened by the appropriate instrumental function (corresponding to excitation by Al Kα radiation). It was found that the spectra required further broadening (by a Lorentzian function, FWHM=1.0eV) in order that experimental and calculated spectra were of comparable resolution. The discrepancy between the KE scales in fig. 7.1 which is ca 25eV is due to the lattice site potential of the Yb^{3+} ion in Yb_2O_3.

Although the theoretical PE spectrum obtained using the intensity pattern of the LS limit is in qualitative agreement with the Yb_2O_3 spectrum, better agreement can be obtain-

ed using the intensity distribution derived from either the intermediate or jj coupling scheme.

We may conclude that the intensity patterns tabulated by Cox for f electron ionisation may be expected to be systematically improved by taking full account of relativistic effects. There are technical difficulties, however, in extending the tabulation into the middle of the lanthanide series because of the prohibitively large number of CSF that have to be included (there are 369 CSF in the f^7 manifold, for example).

7.5 Structure in the core-level X-PE spectra of lanthanoid and transition metal compounds

The metal core-electron PE spectra of lanthanoid and transition metal compounds exhibit extensive, and often detailed, many-electron structure.[20-22] Although it is clear that part of this structure derives from covalency effects e.g. charge transfer processes,[23] it is anticipated that much of it should be interpretable within a purely ionic framework. In order to analyse properly the effects of the electrostatic coupling of the core hole with the open-shell valence electrons, it is essential to include relativistic effects. To date, these have only been included by perturbation methods.[18, 24, 25]

Within a relativistic formulation of photoionisation, the ground state $|J\rangle$ of the open-shell manifold l^n can be written as

$$|J\rangle = \sum_a c_a \left| j_1^{\ T}(J_3),\ j_2^{\ n-T}(J_1);\ J \right\rangle \qquad (7\text{-}30)$$

where j_1 and j_2 are the two relativistic components of the orbital l.

We now consider the photoionisation of an electron characterised by l', with relativistic components j_3 and j_4, to produce an ion state of total angular momentum J'' which belongs to the manifold $l^{n_l}\,(2l'+1)$

$$|J''\rangle = \sum_b C_b \left|\left(j_1^{s}(J_4)\, j_2^{n-s}(J_2);\, J_5\right), j_3^{(2j_3+1)};\, J''\right\rangle$$

$$+ \sum_d C_d \left|\left(j_1^{t}(J_6)\, j_2^{n-t}(J_7);\, J_8\right), j_4^{(2j_4+1)};\, J''\right\rangle \qquad (7\text{-}31)$$

Note, in both equations (7-30) and (7-31), that when an orbital is completely filled it is omitted from the description of the state.

The photoionisation cross-section for production of the ionic state J'' is thus given by

$$\sigma_{J''\leftarrow J} = \left(\sum_{ab} C_a C_b \delta_{J_3 J_4} \delta_{J_1 J_2} \delta_{J J_5}\right)^2 \frac{[J'']}{[J]}\ \bar{\sigma}_{j_3} +$$

$$\left(\sum_{ad} C_a C_d \delta_{J_3 J_6} \delta_{J_1 J_7} \delta_{J J_8}\right)^2 \frac{[J'']}{[J]}\ \bar{\sigma}_{j_4} \qquad (7\text{-}32)$$

The mixing coefficients C_a, C_b and C_d are generated from MCDF calculations on both the ground state and final ion state. As in the previous section, electron relaxation effects have been ignored.

We have examined the final state PE structure expected for: (i) photoionisation of a 4d electron from the lanthanide ions Yb^{3+}, Tm^{3+} and Pr^{3+}; and (ii) photoionisation of a 2p

electron from the transition metal ions Mn^{2+} and Fe^{3+}. In figs. 7.2 to 7.6 we compare our theoretical spectra with the corresponding core level X-PE spectra of Yb_2O_3, Tm_2O_3, Pr_2O_3, $MnTiO_3$ and Fe_2O_3 respectively. The lanthanoid spectra, which were recorded using Al Kα X-radiation, are taken from earlier work in this laboratory.[18] In all calculations, we have assumed the two relativistic orbitals $j_3(\bar{1})$ and $j_4(1)$ have the same photoionisation cross-section. In each of figures 7.2 to 7.6 we show three spectra. (i) The broadened theoretical spectrum; the broadening function consisted of the appropriate instrumental contribution plus an additional Lorentzian function (FWHM = 2.0eV for the transition metal ions and 3.0eV for the lanthanide ions). (ii) The observed PE spectrum. (iii) The deconvoluted PE spectrum (this has the effects of inelastic scattering removed from the experimental spectrum).

The K.E. scale at the bottom of each figure refers only to the observed and deconvoluted spectra. Because we have not included the effects of the lattice potential in our calculation, the convoluted spectrum must be displaced in KE to match with experiment.

In all cases, there is reasonable agreement between the observed and predicted spectra. This indicates that for these systems, core-electron photoionisation can be interpreted satisfactorily within an ionic framework. For Tm_2O_3 and Yb_2O_3, the fact that the theoretical spectra underestimate the intensity of the high K.E signal may be attributed to the occurrence of charge-transfer co-excitation in these compounds.[18]

The case of photoionisation of a 4d electron from Yb^{3+} is sufficiently simple to permit detailed analysis. The ground state of Yb^{3+} is $\bar{f}^6f^7$ and thus, for any final state in the $4d^94f^{13}$ manifold to gain appreciable PE intensity, it must

contain a sizeable contribution from either a $[\bar{d}f]$ or $[df]$ CSF. (We have adopted the square bracket notation to indicate where the holes in the d^9f^{13} manifold are). As expected the high K.E part of the spectrum derives mainly from contributions from $[df]$ CSF whilst the low K.E part mainly from $[\bar{d}f]$ CSF. Although for all states, except those with J = 0 and J = 6, there is appreciable interaction between the CSF, we can assign the five peaks in the spectrum as follows:

(a) $[\bar{d}f]_{J=5}$; (b) $[\bar{d}f]_{J=2,3,4}$; (c) $[df]_{J=1,3,5}$;

(d) $[df]_{J=2,4}$; and (e) $[df]_{J=6}$.

4d photoionisation from Tm^{3+} (f^{12}) is much more complicated. However, the ground state is given by

$$|J=6\rangle = 0.3016\ |\bar{f}^5f^7\rangle_{J=6} + 0.9535\ |\bar{f}^6f^6\rangle_{J=6} \qquad (7\text{-}33)$$

Hence only final states containing $[(f^2)_{J=6}\ \bar{d}]$ or $[(f^2)_{J=6}d]$ CSF can gain appreciable PE intensity. The fact that there is considerably more interaction between CSF in the final state for this case than for Yb^{3+} makes it less meaningful to describe final state structure in terms of pure CSF. As regards their J values the seven peaks in the spectrum are made up mainly as follows: (a) $J = {}^{15}/_2$ (b) $J = {}^{13}/_2$ (c) $J = {}^{9}/_2$ (d) $J = {}^{13}/_2 + J = {}^{7}/_2$ (e) $J = {}^{15}/_2 + J = {}^{11}/_2$ (f) $J = {}^{15}/_2$ (g) $J = {}^{11}/_2 + J = {}^{17}/_2$. The spread of J values does, however, bear a strong resemblance to those expected for the simple coupling of a $\bar{d}$ ($j = {}^{3}/_2$) or d ($j = {}^{5}/_2$) electron to a state with J=6.

With respect to the Pr^{3+} spectrum (fig. 7.4), the most important question is the origin of the peaks labelled a and b. The ground state of Pr^{3+} is

$$|J=4\rangle = 0.9320\,|\bar{f}^2\rangle_{J=4} + 0.3466\,|\bar{f}f\rangle_{J=4} - 0.1063\,|f^2\rangle_{J=4}$$

(7-34)

It is found that peak a corresponds to a single final state with J = $^5/_2$, and that peak b corresponds to a single final state with J = $^7/_2$. Both of these states contain large admixtures (ca 0.55) of $|\bar{f}^2(J=4)\ \bar{d}^3d^6\rangle_{J''}$ (where J'' = $^5/_2$ or $^7/_2$ as appropriate), and thus can be reached by photo-ionisation of a $4\bar{d}$ electron.

Finally, turning to Fe_2O_3 and $MnTiO_3$ (figs. 7.5 and 7.6), both compounds exhibit almost identical structure in the transition metal 2p region. Gupta and Sen[24, 25] have performed calculations on these systems using an ionic approach, but they only included relativistic effects as a perturbation. They started by treating the system non-relativistically. The ground state of Mn^{2+} (or Fe^{3+}) is then $3d^5\ ^6S$ and ionisation of a 2p electron gives rise to one ^7P and three ^5P states. They then included spin-orbit coupling, but only on these four states. This gave them 12 levels ($^7P_{1,2,3}$ once and $^5P_{1,2,3}$ three times) for their calculation. Our results indicate that not only are these 12 levels reached by photo-ionisation but that several other levels arising from the $3d^52p^5$ manifold acquire appreciable PE intensity.

This probably accounts for the better agreement with experiment obtained here. A detailed analysis of the $3d^5$ system is extremely complex. However, in essence, the peaks a and c in the spectrum correspond mainly to $2\bar{p}$ and $2p$ photo-

ionisation respectively, whilst peak b is a result of the considerable electronic interaction between the final state CSF.

7.6 Valence electron structure in the UV-PE spectra of metal atom vapours

In addition to the normal transitions to the ionic states $ns\ ^2S$ and $(n-1)d^9ns^2D_{3/2,5/2}$, the UV-PE spectra of group IIB metal atom vapours Zn, Cd and Hg exhibit weak satellite structure corresponding to formation of the excited $np\ ^2P_{1/2,\ 3/2}$ ionic states.[26-28] This structure has been attributed to admixture of the configuration np^2 into the ground state. Similar correlation satellites have also been observed for Cs^-,[29] lead[30] and the group IIA atoms Ca, Sr and Ba.[27] For the heavier elements, the intensity ratio of the $^2P_{1/2}$: $^2P_{3/2}$ signals deviates markedly from the statistical value 2 given in the LS coupling limit. Because the effects of electron correlation and relativity terms are intimately related in these systems, MCDF theory would appear to be an appropriate method for analysing the satellite structure.

We have performed (ns^2+np^2) EAL calculations on the group IIA and group IIB elements. The advantage of the EAL method is that provided (2J+1) weightings are applied to each CSF, calculations performed with the speed of light increased by a large factor (e.g. 10^4), correctly reproduce the non-relativistic results,[8] but still retain the concept of the $\bar{p}$ and p orbital. This is useful because comparison between relativistic and non-relativistic EAL calculations permits one to disentangle the relativity and correlation terms. Both sets of results are presented in table 7.7.

Examination of the non-relativistic results reveals that within each group the mixing coefficients remain essentially constant. The difference in mixing coefficients between group IIA and IIB is due to the ineffective screening of the increased nuclear charge by the intervening d electrons. We also note that the ratio of C_2:C_3 is 1: $\sqrt{2}$ as expected for LS coupling.

Turning to the relativistic calculations, the direct effect widens the energy separations between the s, $\bar{p}$ and p orbitals. This is reflected by the changes in the mixing coefficients. The effect is more important for the heavier elements, and for mercury, in particular, it is observed that: (i) the total amount of configuration interaction is reduced; and (ii) the $^2P_{1/2}$ and $^2P_{3/2}$ PE signals are expected to be comparable in magnitude.

In table 7.8 we compare the results of our relativistic calculations with the experimentally observed PE satellite intensities.[27, 28] There is reasonable agreement with experiment for the group IIA elements, although our calculations are unable to reproduce the marked decrease in satellite intensity as we descend the group. The observed satellite intensities from the group IIB atoms, however, are much stronger than those predicted by the MCDF work. The Hg satellites which we calculate to be the least intense are in fact quite strong. Our only consolation is that the $^2P_{1/2}$: $^2P_{3/2}$ intensity ratio is much removed from that expected for LS coupling, even though it is considerably larger than our computed value.

The discrepancies between experiment and theory are not too surprising. Firstly, there is still considerable uncertain-

ty in the experimental intensities. The second reason is that our theoretical analysis neglects certain terms which may in fact give rise to sizeable contributions to the satellite intensity.

(i) We are close to threshold which might result in large differences between the $\bar{s}$, $\bar{p}$ and p photoionisation cross-sections (our analysis has assumed that they are all the same).

(ii) Admixture of other configurations e.g. $\bar{d}^2$, d^2 into the ground state.

(iii) Effects due to autoionisation.

We still consider, however, that initial state CI is the dominant mechanism for the satellite processes.

Two other atomic systems Pb and Cs^- have aroused interest because of the intensity of their satellite peaks.[29, 30] Unfortunately, difficulties were encountered in getting the outermost orbitals to converge in the SCF programme. For Cs^-, however we may readily extrapolate values of the mixing coefficients from calculations performed on systems where the nuclear charge was intermediate between that of Cs and Ba. The ground state is extrapolated to be

$$|J=0\rangle = 0.9358|s^2\rangle_0 + 0.2308|\bar{p}^2\rangle_0 + 0.2665|\ldots\rangle_0$$

The extensive CI in this system is probably a major contributing factor to the unusually intense $^2P_{1/2}$, $^2P_{3/2}$ PE satellite peaks.

Table 7.1. Relativistic one-electron orbitals.

Orbital	s	$\bar{p}$	P	$\bar{d}$	d	$\bar{f}$	f
k	−1	1	−2	2	−3	3	−4
l	0	1	1	2	2	3	3
a	+1	−1	+1	−1	+1	−1	+1
j	$\frac{1}{2}$	$\frac{1}{2}$	$\frac{3}{2}$	$\frac{3}{2}$	$\frac{5}{2}$	$\frac{5}{2}$	$\frac{7}{2}$
Parity	+	−	−	+	+	−	−

Table 7.2. Allowed values of J in the configuration $(j)^r$.

j	l_j	r	J
$\frac{1}{2}$	s, $\bar{p}$	1	$\frac{1}{2}$
$\frac{3}{2}$	p, $\bar{d}$	1	$\frac{3}{2}$
		2	0, 2
$\frac{5}{2}$	d, $\bar{f}$	1	$\frac{5}{2}$
		2	0, 2, 4
		3	$\frac{3}{2}$, $\frac{5}{2}$, $\frac{9}{2}$
$\frac{7}{2}$	f, $\bar{g}$	1	$\frac{7}{2}$
		2	0,2,4,6
		3	$\frac{3}{2}$, $\frac{5}{2}$, $\frac{7}{2}$, $\frac{9}{2}$, $\frac{11}{2}$, $\frac{15}{2}$
		4	0, $(2)^2$, $(4)^2$, 5, 6, 8

Note: For the sake of simplicity seniority numbers and other group-theoretical labels have been omitted.

Table 7.3. Relativistic states arising from the f^2 manifold.

Three jj configurations are possible, and these give rise to a total of 13 CSF.

Configuration	Allowed values of J
$\bar{f}^2$	0, 2, 4
$\bar{f}f$	1, 2, 3, 4, 5, 6
f^2	0, 2, 4, 6

Table 7.4. Final state intensities for the photoionisation process $f^2 \longrightarrow f^1$

State	LS coupling	$Pr^{3+}(4f^2)$	$U^{4+}(5f^2)$	jj coupling
$^2F_{5/2}$	1.7143	1.8573	1.9480	2.0000
$^2F_{7/2}$	0.2857	0.1427	0.0520	0.0000

Table 7.5. Final state intensities for the photoionisation process $f^3 \longrightarrow f^2$

State	LS coupling	$Nd^{3+}(4f^3)$	$U^{3+}(5f^3)$	jj coupling
$^3H_6$	0.0192	0.0099	0.0050	0.0
$^3H_5$	0.4237	0.3086	0.1872	0.0
$^3H_4$	1.8904	2.0110	2.1374	2.3571
$^3F_4$	0.0054	0.0026	0.0102	0.0
$^3F_3$	0.0984	0.0747	0.0451	0.0
$^3F_2$	0.5629	0.5866	0.6116	0.6429
$^3P_2$	0.0	0.0	0.0	0.0
$^3P_1$	0.0	0.0	0.0	0.0
^3P_o	0.0	0.0	0.0	0.0
$^1I_6$	0.0	0.0002	0.0005	0.0
$^1G_4$	0.0	0.0065	0.0030	0.0
$^1D_2$	0.0	0.0	0.0001	0.0
^1S_o	0.0	0.0	0.0	0.0

Table 7.6. Final state intensities for the photoionisation process $f^{13} \longrightarrow f^{12}$

State	LS coupling	$Yb^{3+}(4f^{13})$	$No^{3+}(5f^{13})$	jj coupling
$^3H_6$	3.0179	3.1071	3.1688	3.2500
$^3H_5$	1.3750	1.3750	1.3750	1.3750
$^3H_4$	0 3214	2.2081	2.2462	2.2500
$^3F_4$	1.7678	0.9503	1.0909	1.1250
$^3F_3$	0.8750	0.8750	0.8750	0.8750
$^3F_2$	0.3571	0.7782	1.1398	1.2500
$^3P_2$	0.8036	0.3578	0.1194	0.0000
$^3P_1$	0.3750	0 3750	0.3750	0.3750
^3P_o	0.1071	0.1635	0.2102	0.2500
$^1I_6$	1.8571	1.7679	1.7060	1.6250
$^1G_4$	1.2858	0.2166	0.0379	0.0000
$^1D_2$	0.7143	0.7390	0.6158	0.6250
^1S_o	0.1429	0.0865	0.0398	0.0000

Table 7.7. Mixing coefficients obtained for the group IIA and group IIB elements using non-relativistic and relativistic EAL calculations.

$$|J=0\rangle = c_1 |s^2\rangle_o + c_2 |\bar{p}^2\rangle_o + c_3 |p^2\rangle_o$$

(i) Non-relativistic

	c_1	c_2	c_3
Ca	0.9548	0.1715	0.2426
Sr	0.9547	0.1718	0.2430
Ba	0.9483	0.1832	0.2591
Zn	0.9716	0.1366	0.1931
Cd	0.9685	0.1439	0.2035
Hg	0.9690	0.1427	0.2018

(ii) Relativistic

	c_1	c_2	c_3
Ca	0.9556	0.1717	0.2393
Sr	0.9576	0.1728	0.2304
Ba	0.9554	0.1864	0.2293
Zn	0.9732	0.1358	0.1857
Cd	0.9732	0.1421	0.1809
Hg	0.9820	0.1356	0.1314

Table 7.8. Comparison of intensities of satellite peaks in the UV-PE spectra of group IIA and IIB atoms with those predicted from MCDF calculations.

$$|J=0\rangle = c_1|s^2\rangle_{J=0} + c_2|\bar{p}^2\rangle_{J=0} + c_3|p^2\rangle_{J=0}$$

Mixing coeffs in this table are normalised to $c_1^2 = 1.0$

	Experiment[27,28]			Calculation		
	I_s	$I_{\bar{p}}$	I_p	c_1	c_2	c_3
Ca	1.00	0.103		1.00	0.032	0.063
Sr	1.00	0.065		1.00	0.033	0.057
Ba	1.00	0.047		1.00	0.038	0.058
Zn	1.00	0.04	0.08	1.00	0.019	0.036
Cd	1.00	0.03	0.07	1.00	0.021	0.035
Hg	1.00	0.22	0.07	1.00	0.019	0.018

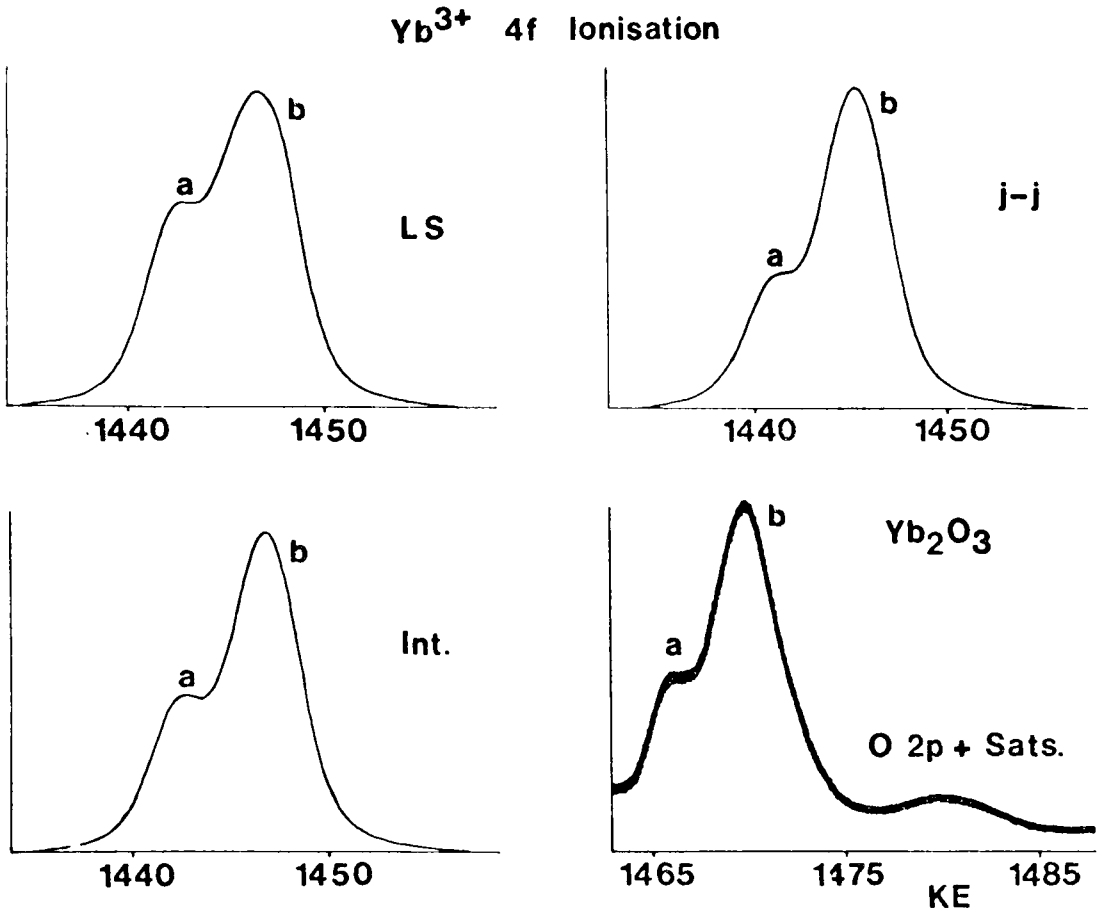


Fig. 7.1. Theoretical metal 4f PE spectra of the free ion Yb^{3+} compared with the Al Kα PE spectrum of Yb_2O_3.

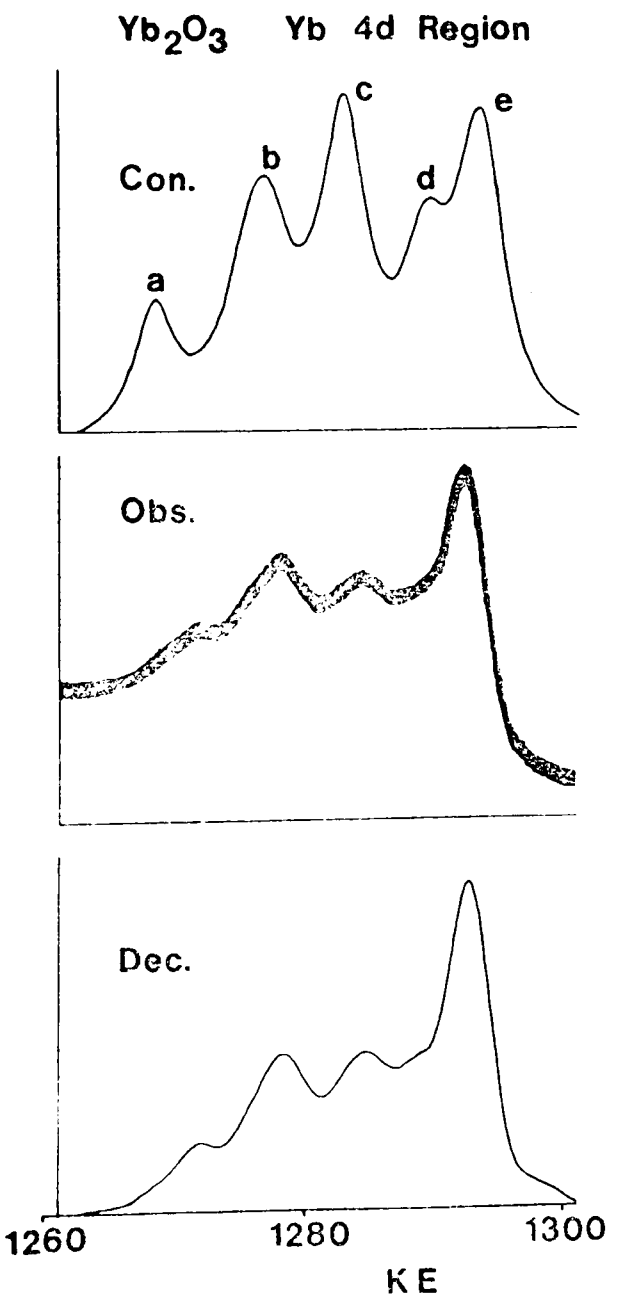


Fig. 7.2. Theoretical and experimental (Al Kα) PE spectra of the Yb 4d region of Yb_2O_3.

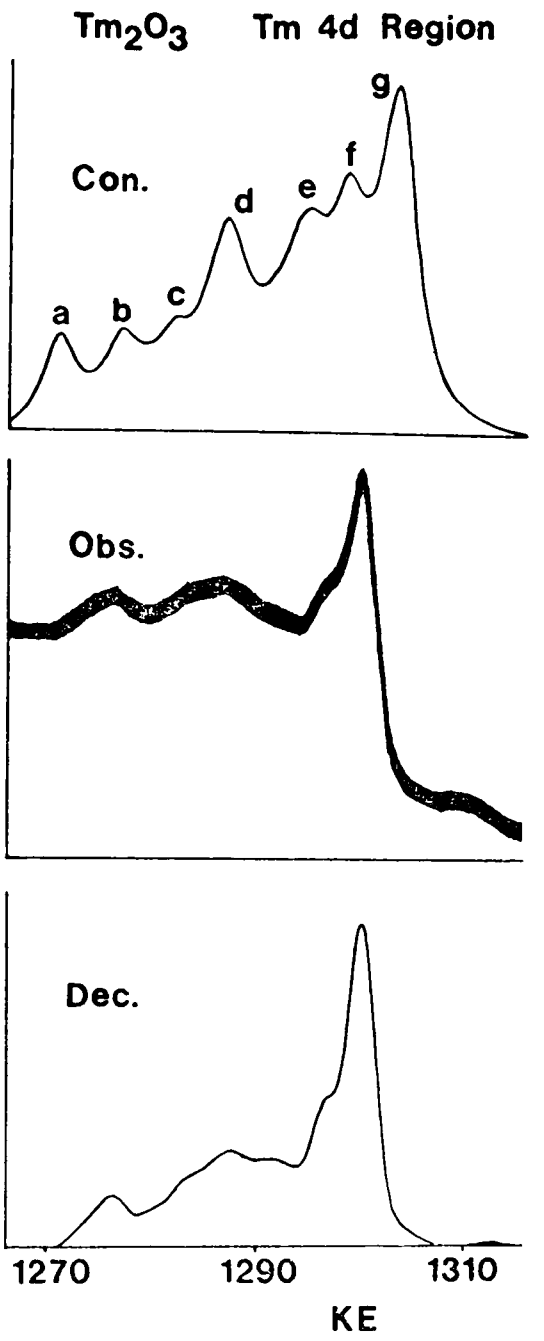


Fig. 7.3. Theoretical and experimental (Al Kα) PE spectra of the Tm 4d region of Tm_2O_3.

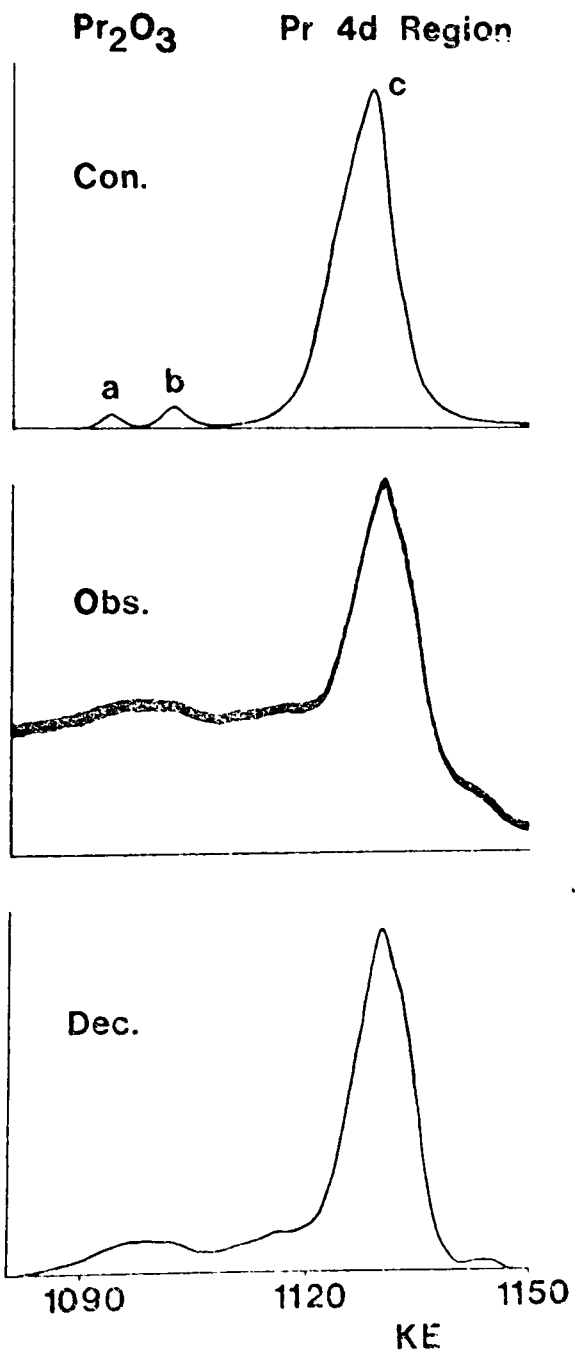


Fig. 7.4. Theoretical and experimental (Al Kα) PE spectra of the Pr 4d region of Pr_2O_3.

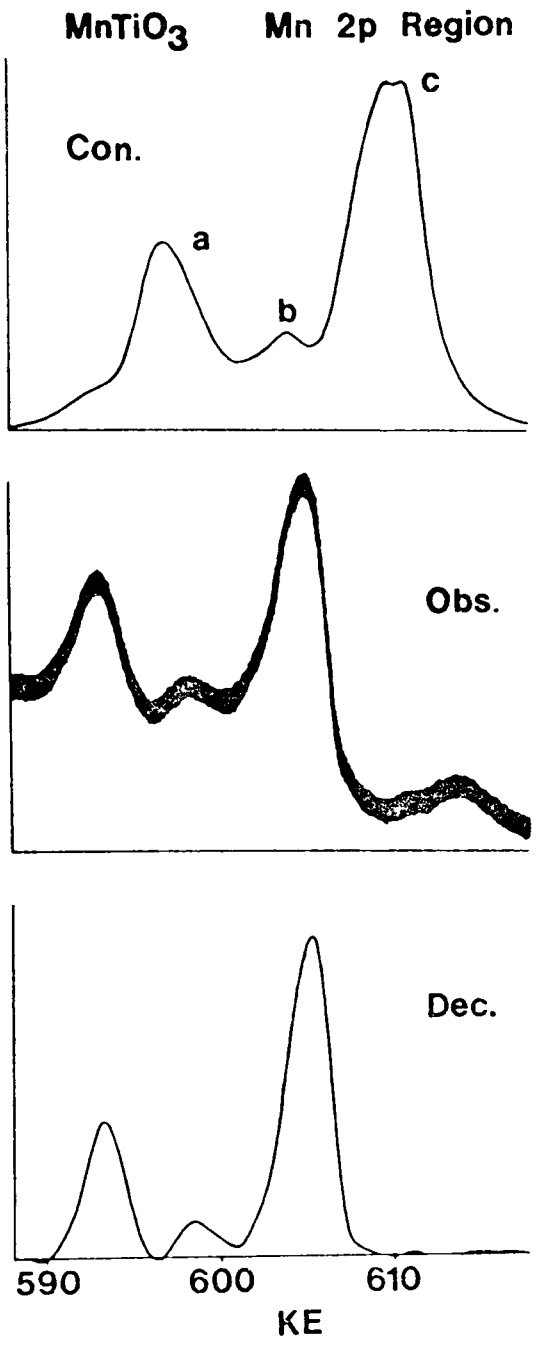


Fig. 7.5. Theoretical and experimental (Mg Kα) PE spectra of the Mn 2p region of $MnTiO_3$.

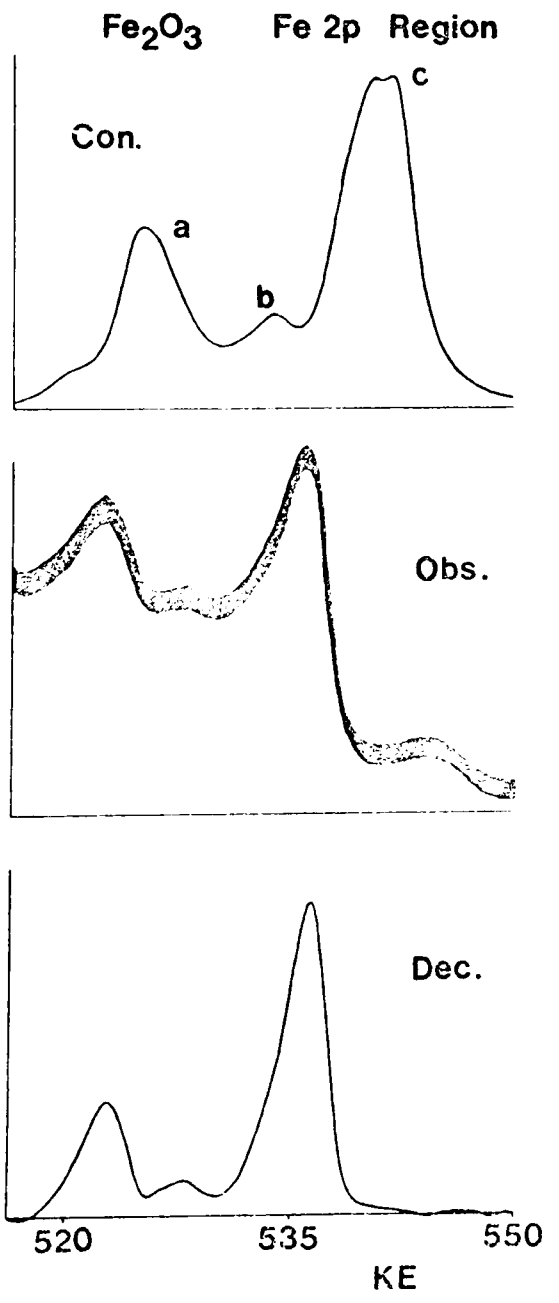


Fig. 7.6. Theoretical and experimental (Mg Kα) PE spectra of the Fe 2p region of Fe_2O_3.

REFERENCES FOR CHAPTER 7

1. R. E. Moss, "Advanced Molecular Quantum Mechanics" (1973) Chapman and Hall, London.
2. I. P. Grant, Adv. Phys. 19 (1970) 747.
3. S. J. Rose, Chemistry Part II thesis, Oxford (1976).
4. A. Messiah, "Quantum Mechanics" (1961) Wiley, New York.
5. V. M. Burke, I. P. Grant, Proc. Phys. Soc. 90 (1967) 297.
6. S. J. Rose, I. P. Grant, N. C. Pyper, J. Phys. B11 (1978) 1171.
7. A. I. Akhiezer, V. B. Berestetskii, "Quantum Electrodynamics" (1965) Wiley-Interscience, New York.
8. I. P. Grant, D. F. Mayers, N. C. Pyper, J. Phys. B9 (1976) 2777.
9. D. M. Brink, G. R. Satchler, "Angular Momentum" (1968), Oxford University Press, 2nd edition.
10. I. P. Grant, Comput. Phys. Commun. 14 (1978) 311.
11. I. P. Grant, J. Phys. B7 (1974) 1458.
12. T. E. H. Walker, J. T. Waber, J. Phys. B6 (1973) 1165.
13. T. E. H. Walker, J. T. Waber, J. Phys. B7 (1974) 674.
14. P. A. Cox, D. Phil. Thesis, Oxford (1973).
15. P. A. Cox, Structure and Bonding 24 (1975) 59.
16. A. F. Orchard, G. Thornton, J. Elect. Spec. 10 (1977) 1.
17. A. J. Downs, R. G. Egdell, A. F. Orchard, P. D. P. Thomas, JCS Dalton, in press.
18. G. Thornton, D. Phil. Thesis, Oxford (1976).
19. N. Beatham, Chemistry Part II Thesis, Oxford (1975).
20. B. Wallbank, I. G. Main, C. E. Johnson, J. Elect. Spec. 5 (1974) 259.
21. N. Spector, C. Bonnelle, G. Dufour, C. K. Jørgensen, H. Berthou, Chem. Phys. Lett. 41 (1976) 199.

22. A. F. Orchard, G. Thornton, J. Elect. Spec. 13 (1978) 27.

23. P. Burroughs, A. Hamnett, A. F. Orchard, G. Thornton, J. Chem. Soc. Dalton Trans. (1976) 1696.

24. R. P. Gupta, S. K. Sen, Phys. Rev. B10 (1974) 71.

25. R. P. Gupta, S. K. Sen, Phys. Rev. B12 (1975) 15.

26. J. Berkowitz, J. L. Dehmer, Y.-K. Kim, J. Chem. Phys. 61 (1974) 2556.

27. S. Süzer, S.-T. Lee, D. A. Shirley, Phys. Rev. A13 (1976) 1842.

28. N. S. Hush, S. Süzer, Chem. Phys. Lett. 46 (1977) 411.

29. A. Kasdan, W. C. Lineberger, Phys. Rev. A10 (1974) 1658

30. S. Süzer, M. S. Banna, D. A. Shirley, J. Chem. Phys. 63 (1975) 3473.

CHAPTER EIGHT

APPLICATION OF THE SUDDEN APPROXIMATION TO PHOTOELECTRON SPECTROSCOPY

8.1 Theoretical analysis of the sudden approximation

8.2 Core-electron ionisation from closed shell systems

8.3 Core-electron ionisation from open shell systems

8.1 Theoretical analysis of the sudden approximation

The sudden approximation (see section 2.2) has been widely used to interpret the satellite structure associated with core-electron photoionisation[1-4]. The underlying assumption is that when a core electron is photoionised the coulombic potential experienced by the outer shell electrons undergoes an abrupt change. This sudden perturbation may induce a 'shake-up' transition, involving the excitation of a valence electron to a higher, previously unoccupied orbital. Such a transition must obey the monopole selection rule (see section 2.2).

At first sight, it is not particularly obvious how the physical assumptions inherent in the sudden approximation can be accommodated within the general theory of photoionisation described earlier in the thesis. The main inconsistency is that the sudden approximation discusses photoelectron peak intensities as if the system contained (N-1) rather than N electrons. In order to explain this apparent anomaly, let us return to equation (2-12) which gives the photoionisation cross-section for the N-electron atomic system as

$$\sigma_{L',L'} = \delta_{SS'} \frac{4\pi^2 \alpha C}{3} \times \left| \langle l^n(\alpha L S) \| \sum_i^N T^1(i) \| l^{n-1}(\alpha'' L'' S''), l'; \alpha' L' S' \rangle \right|^2$$

(8-1) a.u

The notation is the same as before. Although the analysis in section 2.2 was based upon the fact that all electron orbitals were spatially invariant to photoionisation, the derivation of equation (2-12) involves only geometrical

considerations and consequently still holds even if we relax the orbital orthogonality constraint. In order to derive the sudden approximation, we now define: (i) the initial state orbitals as those given by an SCF Hartree-Fock calculation on the neutral N-electron system; and (ii) the bound orbitals of final state as those provided by an SCF Hartree-Fock calculation on the (N-1) electron ion state. Although we do not explicitly require the radial wave-equation of the continuum electron, we assume that it could be obtained by solving within the potential of the 'frozen' ion core.

We are now faced with having to compute matrix elements between two non-orthogonal basis-sets. This is a particularly difficult problem,[5] which is reflected by the dearth of atomic calculations adopting such an approach. P.-O Löwdin has however produced rules for evaluating such matrix elements.[6]

The matrix element of the qth component of the one-electron tensor operator of rank k with respect to two N-electron Slater determinants is given by

$$M_{f \leftarrow i} = \langle \Psi^{i}(N) \left| \sum_{i=1}^{N} T^{k}_{q}(i) \right| \Psi^{f}(N) \rangle$$

$$= \sum_{mn} \langle \phi_m | T^{k}_{q} | \phi'_n \rangle \times D_{if}(\phi_m | \phi_n') \qquad (8\text{-}2)$$

The spin-orbital set $\{\phi_1, \phi_2 \ \ldots\ldots\}$ belongs to the initial state, whilst the spin-orbital set $\{\phi_1', \phi_2' \ \ldots\ldots\}$ belongs to the final state. If the effects of relaxation are small, these two spin-orbital sets will closely resemble each other. The double summation in equation (8-2) is over all spin-orbitals. $D_{if}(\phi_m | \phi_n')$ is the <u>cofactor</u>, formed by removing the mth row and nth column from the N x N determinant D_{if}. The elements

of D_{if} are the overlaps between initial- and final-state one-electron spin-orbitals; that is, the element in the uth row and vth column of D_{if} is given by $\langle \phi_u | \phi_v' \rangle$. If we adapt equation (8-2) to the case of photoionisation one of the final state spin orbitals, which we refer to as χ, belongs to the continuum. If we assume that this continuum orbital χ is associated with ϕ_1 (i.e. ionisation takes place from the spin orbital ϕ_1) then we may rewrite equation (8-2) as

$$M_{f \leftarrow i} = \langle \phi_1 | T_q^1 | \chi \rangle D_{if}(\phi_1 | \chi) + \sum_{m=2}^{N} \langle \phi_m | T_q^1 | \chi \rangle D_{if}(\phi_m | \chi) + \sum_{m=1}^{N} \sum_{n=2}^{N} \langle \phi_m | T_q^1 | \phi_n' \rangle D_{if}(\phi_m | \phi_n') \qquad (8\text{-}3)$$

The first term in this expression has the usual one-electron interpretation; an electron in the spin-orbital ϕ_1 makes a dipole transition to the continuum. The factor $D_{if}(\phi_1 | \chi)$ multiplying this one-electron matrix element is the overlap of the "passive orbitals", i.e. those not directly involved in the ionisation. If we had made Koopmans' assumption - i.e. $\phi_m = \phi_m'$ $(m \geq 2)$, then $D_{if}(\phi_1 | \chi)$ would be unity, and we would be left with the one-electron approximation

$$M_{f \leftarrow i} = \langle \phi_1 | T_q^1 | \chi \rangle \qquad (8\text{-}4)$$

The second term represents dipole transitions from the other spin-orbitals in the initial state, to the continuum

orbital. The third term represents cases where the electron appears to make a monopole transition ($\phi_j \longrightarrow \chi$) and the passive orbitals rearrange themselves via a dipole excitation. This process has been termed conjugate shake-up.[7]

The sudden approximation is equivalent to neglecting the second and third terms in equation (8-3), viz.

$$\langle \Psi^i(N) | \sum_{i=1}^{N} T_q^1(i) | \Psi^f(N) \rangle$$

$$\simeq \langle \phi_1 | T_q^1 | \chi \rangle \times D_{if}(\phi_1 | \chi)$$

(8-5)

Unfortunately, because we have not been in a position to calculate continuum wavefunctions, we are unable to provide estimates as to the relative size of each term in equation (8-3). Some work has, however, been done on this problem.[8] The implications are that one expects the contribution from the second term to be relatively small over the whole range of electron K.E, and the third only to be significant close to threshold.

Equation (8-3) only refers to matrix elements between two single Slater Determinants; the calculation of photo-ionisation cross-section requires the evaluation of reduced matrix elements. Whereas the Löwdin formula for single Slater Determinants has been referred to in previous discussions of the sudden approximation[2,8], there have been no rigorous attempts to extend the formulation to the general case where

both initial and final states are invariably linear combinations of Slater Determinants.

Let us consider the case of photoionisation from a closed-shell system; the initial and final (ion plus continuum electron) states will have ^1S and ^1P symmetry respectively. If, for the purpose of our discussion, we assume that a 2p electron is ionised, then the relevant reduced matrix element (see equation 8-1) for photoionisation to continuum orbital with l' angular symmetry (l' must either be s or d) is given in the sudden approximation by

$$\langle (^1S) \| T^1 \| (^2P), l'; {}^1P \rangle = D_{if}(\phi_{2p} | \chi_{l'}) \times n \langle 2p \| T^1 \| l' \rangle \qquad (8\text{-}6)$$

n is the number of electrons in the subshell (which is this case is 6). The fact that we have denoted the cofactor in this expression by $D_{if}(\phi_{2p} | \chi_{l'})$ serves to emphasise that the numerical value of the cofactor does not depend on the magnetic quantum numbers of the spin-orbital which is deleted from the determinant of overlaps (i.e. it could be either p_1^+, p_o^+, p_{-1}^+, p_1^-, p_o^- or p_{-1}^-). Indeed it is this very property on which the derivation of equation (8-6) depends; because when we average over the initial state magnetic quantum numbers and sum over the final state magnetic quantum numbers (see section 2.2) the appropriate cofactor will in each case correspond to a different 2p spin-orbital being deleted from the N x N determinant of overlaps.

The total photoionisation cross-section for production

of the ionic state (^2P) is obtained by summing the contributions from both continuum channels (χ_s and χ_d). Hence

$$\sigma_{tot} = n[D_{if}\ (\phi_{2p} \mid \chi_{l'})]^2\ \bar{\sigma}_{l} \qquad (8\text{-}7)$$

The overlap factor $D_{if}\ (\phi_{2p} \mid \chi_{l'})$ cannot be greater than unity and so the "relaxed" sub-shell photoionisation cross-section will always tend to be less than the "unrelaxed" sub-shell photoionisation cross-section. This fact must be taken into account if one wishes to compare experimental cross-sections with theoretical predications based upon the one-electron model.[9]

A further corollary of the sudden approximation analysis concerns the total probability for <u>shake-up</u> and <u>shake-off</u> (P_{ss}) which is given by [10]

$$P_{ss} = 1 - \left\{D_{if}\ (\phi_{nl} \mid \chi_{l'})\right\}^2 \qquad (8\text{-}8)$$

This relationship depends upon the photoionisation cross-section for the satellite peaks being the same as for the primary peak; this will only be a good approximation if $h\nu$ is much in excess of the threshold ionisation energy.

Evaluation of the overlap factor $D_{if}\ (\phi_{nl} \mid \chi_{l'})$ is a relatively straightforward procedure, the elements in the determinant being given by

$$\langle \phi_{nlm_l m_s} \mid \phi'_{n'l'm_{l'}m_{s'}} \rangle = \delta_{ll'}\,\delta_{m_l m_{l'}}\,\delta_{m_s m_{s'}} \int_0^\infty P_{nl}\,P_{n'l}\,dr \qquad (8\text{-}9)$$

Thus we only need to compute radial overlap integrals in constructing the overlap factor.

In sections 8.2 and 8.3 we present calculations of the % total shake-up/shake-off probability (% TSSP) for various atomic systems. We expect the sudden approximation to be really applicable only to systems where: (i) one is well above ionisation threshold; and (ii) a core electron is being ionised (this is in order to ensure that electron correlation effects are small).

The sudden approximation is not very accurate for predicting the intensity of satellite peaks resulting from photoionisation of helium. We compute the % TSSP to be only 3.23% and the PE intensity ratio $He^+(2s)/He^+(1s)$ as 0.0236. Experimental and theoretical work indicate that this ratio should be 0.0482 in the high energy limit.[11-13] For the other noble gases, the experimental results suggest that application of the sudden approximation is justifiable,[10] although direct comparison between experiment and theory is made difficult by the fact that it is hard to determine the contribution from electron shake-off to the satellite intensity. One expects the probability for electron shake-up (as compared with that for electron shake-off) to be very small for inner shells, but to become comparable in magnitude as one goes to the outermost shell.[14]

8.2 Core-electron ionisation from closed shell systems

In this section, we present the results of both non-relativistic and relativistic calculations of the % total shake-up/shake-off probability (% TSSP) for core-electron ionisation from closed-shell atomic systems. The wavefunctions required to evaluate the overlap factor D_{if} $(\phi_{nl} | \chi_{l'})$

were generated by performing separate SCF calculations (Hartree-Fock or Dirac-Fock, as appropriate) on both the initial and final ion states, respectively (see Appendix 2). An element in the relativistic overlap factor D_{if} $(\phi_{nk} \mid \chi_{l'})$ is given by

$$\langle \phi_{nkm_j} \mid \phi'_{n'k'm_{j'}} \rangle = \delta_{kk'}\delta_{m_j m_{j'}} \int_0^\infty (P_{nk}P_{n'k} + Q_{nk}Q_{n'k})\, d\tau \qquad (8\text{–}10)$$

Previous work on the subject has concentrated on neutral systems[3,14]. It is our aim to extend such calculations to the rest of the isoelectronic series of which the noble gases are members. These ionic systems (i.e. K^+, Zr^{4+}) may be expected to be chemically representative of compounds containing that element.

In tables 8.1, 8.2 and 8.3 we present the results of non-relativistic calculations on the $3d^o$, $3d^{10}$ and $4d^o$ isoelectronic series. For the $5d^o$ isoelectronic series (table 8.4), where relativistic effects are expected to be more important, the calculations were performed using Dirac-Fock wavefunctions. However, it is clear from tables 8.5 and 8.6, which compare the results of relativistic and non-relativistic calculations on argon and xenon respectively, that in the main relativistic effects are unimportant.

Where the case permits (Ar, Kr, Xe), our results are in excellent agreement with previous calculations.[3, 14] This includes comparison with the statistical product method of Carlson and Nestor.[14] (see table 8.6).

Three major trends can be discerned in the figures for % TSSP: (i) the extent of relaxation decreases as the charge on the ion increases; (ii) the extent of relaxation increases as photoejection occurs from more deeply lying core levels;

and (iii) in general for equivalent orbitals the value of % TSSP increases in going from the $3d^0 \longrightarrow 4d^0 \longrightarrow 5d^0$ isoelectronic series. These trends are consistent with the notion that the % TSSP for a particular orbital depends on how tightly the orbital is bound. There does, however, appear to be a limit to the extent of relaxation that is possible following photoionisation; this seems to be dependent on the nuclear charge, but is approximately 20% for neutral atoms. This 'levelling off' in the value of % TSSP for deep core holes is probably the main reason why relativistic effects tend not to be too important.

There would appear to be a very strong correlation between the mean radius of the orbital in the initial system and the extent of relaxation. In table 8.6 we compare these quantities and find that, for all orbitals, the smaller the value of $\langle r \rangle$ the greater the extent of relaxation. This relationship would appear to be a completely general one; in all the non-relativistic calculations the % TSSP for a 2p orbital is greater than that for a 2s orbital, in keeping with the values of $\langle r \rangle$ for the respective orbitals. The fact that mean radius of an orbital does not always correlate with the inverse of the orbital eigenvalue can be attributed to the shape of the radial wavefunction.[15]

We have attempted to analyse this phenomenon further by examining the main contributions to the values of % TSSP for argon (see table 8.7). To a good approximation, the value of the overlap factor is given by the diagonal product of radial overlaps.[3] For each of the four ionisations examined in table 8.7 the 1s, 2s and 2p radial overlaps deviate only slightly from unity and thus the values of % TSSP are mainly determined by the diagonal product of 3s and

3p radial overlaps. Thus we can see that the reason why there is more relaxation for 2p photoionisation than for 2s, is the greater 3s orbital relaxation in the former case.

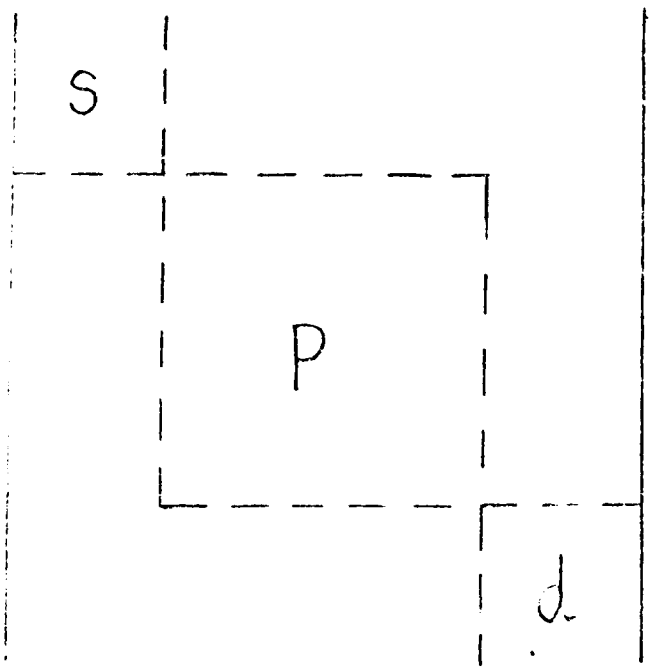
Comparison of the values of % TSSP for the ionic members of the isoelectronic series with the experimentally observed satellite peaks in compounds such as KCl, CaO,[16] La_2O_3[17] unfortunately reveals very little correlation between the two. Certainly both the K 2p and Cl 2p region of the X-PE spectrum of crystalline KCl exhibit similar (albeit broader) satellite structure to the 2p region of the X-PE spectrum of gaseous argon, but it would appear that the reasonably intense satellite structure in oxides such as TiO_2 and La_2O_3 must be due to charge-transfer processes.[17]

8.3 Core-electron ionisation from open-shell systems

The metal core-electron PE spectra of transition metal oxides often exhibit pronounced satellite structure (see for instance fig. 6.5 which shows the metal 2p X-PE spectra of $MnTiO_3$, $FeTiO_3$, $CoTiO_3$ and $NiTiO_3$). It is anticipated that much of this structure may be interpretable within a purely ionic framework. In the last chapter, we analysed some of the effects due to the electrostatic coupling of the core hole with the open-shell valence electrons. In this section, we wish to employ the sudden approximation to estimate the effects of electronic relaxation. Of particular interest are the trends along a transition series. Our attention is confined to the first row for two reasons: (i) this is where we should expect an ionic approach to be most viable; and (ii) it is where relativistic effects on the total shake-up/shake-off probability may safely be neglected. The advantage of working within a non-relativistic framework is that both initial and final states can be represented by a single-configuration.

Application of the sudden approximation to open-shell systems poses additional difficulties. The first is that, in general, many different ionic states are accessible when a core electron is ionised. Occasionally there will be cases where several states may exist having the same symmetry. There is also the problem of constructing the overlap factor. However, provided that the two open-shells in the final ionic state do not possess the same value of l, it is again possible to use only one overlap factor D_{if} $(\phi_{nl} \mid \chi_{l'})$ as in the closed-shell problem. The reason is that the numerical value of this co-factor is still invariant to which core-electron spin-orbital is deleted from the N x N determinant of overlaps.

This can readily be seen by rearranging the determinant by successive permutations of rows and columns to produce a series of block diagonals; each block diagonal contains only overlaps between spin-orbitals having the same angular symmetry. e.g.



All entries outside the block diagonal are necessarily equal to zero. It is now apparent that the choice of which spin-orbital to delete from say the p-block is independent of which spin-orbitals are missing in the d-block. The case where the two open shells have the same azimuthal quantum

number, does not lend itself to such a simple analysis.

For the first row of the transition series, none of the core electrons has the same angular symmetry as the open-shell valence electrons.

2p photoionisation from an open-shell system will give rise to six ion states and 2s photoionisation two ion states (ignoring any configuration interaction effects).

In principle, one can calculate total shake-up/shake-off probabilities for each of the various ion states derived by ionisation of the same type of electron. This would involve separate SCF calculations for each ion state; not only would this be computationally expensive but it would also unduly complicate the presentation of results. However, provided that there is little variation in the % TSSP for each of the various ion states, it is more convenient to average over all these states (weighting according to their spin-orbit degeneracies) and present a value which is characteristic simply of the core-electron being ionised. This is particularly helpful in comparing results for two different transition metal ions. We can also save computer time if we only perform one SCF calculation on all of these ion states. This compromise can be achieved by performing a single calculation on a system which represents an average of all ion states derived by photoionisation from the same core orbital. We may refer to this as a ACI calculation.

In table 8.8 we compare the results of the various types of calculations for the case of photoionisation of a 3p electron from Cu^{2+} (^2D). We may make two observations: (i) there is little variation in the % TSSP over the range of final ion states; and (ii) the ACI calculation is in very good agreement with that obtained by averaging the individual % TSSP

calculations.

Encouraged by these and similar results from other systems, we have performed ACI calculations on all the chemically significant doubly and triply ionised transition metal atoms. The results are presented in Tables 8.9 and 8.10 respectively.

For any given transition metal ion, the values of % TSSP follow much the same pattern as they do for any closed shell system: (i) the probabilities decrease in the order 1s > 2p > 2s > 3s > 3p; and (ii) for members of an isoelectronic series, the extent of relaxation decreases as the charge on the ion increases.

Examination of the trends along each transition metal series indicates that there are no very significant changes in % TSSP as we traverse the row. Certainly no abrupt changes in the extent of relaxation for 2p ionisation are found between Cu^{2+} (d^9) and Zn^{2+} (d^{10}) which would have accounted for the more intense satellite structure in Cu^{II} compounds than in Zn^{II} compounds.[18] We must again conclude that such an observation is a result of charge-transfer phenomena.

Certain slowly varying trends can be discerned for both the M^{2+} and M^{3+} series. Examination of table 8.9 indicates that for the M^{2+} ions the values of % TSSP for all core-electron ionisations are increased for the earlier members of the transition row in relation to Ca^{2+}. This can be attributed to the filling of the 3d shell. Although core-electron relaxation is smaller in say Ti^{2+} than in Ca^{2+}, these effects are outweighed by the effects of 3d electron relaxation.

The increase in % TSSP in passing from Ca^{2+} to Ti^{2+} is more marked for 2s and 2p photoionisation than for 1s photoionisation. Again the dominant reason is 3d electron relaxation. The Ti^{2+} 3d radial overlap $\langle \phi_{3d} | \phi'_{3d} \rangle$ is equal to

0.9811, 0.9792, 0.9794, 0.9907 and 0.9920 for 1s, 2s, 2p, 3s and 3p ionisation respectively. These figures are slightly surprising because they imply that the 3d electrons relax more for 2s and 2p photoionisation than for 1s photoionisation. This effect, however, tends to be perfectly general for all M^{2+} and M^{3+} ions.

The values of % TSSP along each series often show slight maxima. This is caused by two opposing effects: (i) the diagonal radial overlaps tend to approach unity along the series, this effect being more pronounced for the 3d radial overlap; and (ii) an increase in the number of 3d electrons. The contribution of the 3d electron relaxation term to the % TSSP is given exactly by the diagonal product $\langle \phi_{3d} \mid \phi'_{3d} \rangle^{n}$. In tables 8.11 and 8.12 we present the values of the diagonal product for 2p photoionisation from the M^{2+} and M^{3+} ions respectively. These values provide essential insights into the particular trends along each row.

Table 8.1. % TSSP for the $3d^0$ isoelectron series (obtained from non-relativistic SCF calculations).

Vacancy	Cl^-	Ar	K^+	Ca^{2+}	Sc^{3+}	Ti^{4+}	V^{5+}
1s	29.55	21.73	17.17	14.05	11.75	10.04	8.71
2s	22.30	14.81	10.87	8.38	6.68	5.48	4.57
2p	22.64	15.23	11.33	8.83	7.12	5.90	4.95
3s	7.75	3.96	2.54	1.80	1.33	1.04	0.86
3p	6.40	3.45	2.33	1.69	1.30	1.03	0.86

Table 8.3. % TSSP for the $4d^0$ isoelectronic series (obtained from non-relativistic SCF calculations).

Vacancy	Br^-	Kr	Rb^+	Sr^{2+}	Y^{3+}	Zr^{4+}
1s	27.15	20.35	16.56	14.07	12.24	10.84
2s	24.20	17.37	13.71	11.29	9.61	8.33
2p	24.57	17.72	14.09	11.65	9.99	8.65
3s	19.50	12.69	9.22	7 10	5.70	4.69
3p	19.32	12.61	9.21	7.09	5.72	4.71
3d	19.52	12.84	9.49	7.38	6.04	5.02
4s	7.44	3.80	2.40	1.65	1.28	0.96
4p	6.01	3.20	2.07	1.51	1.18	0.92

Table 8.2. % TSSP for the $3d^{10}$ isoelectronic series (obtained from non-relativistic SCF calculations).

Vacancy	Cu^+	Zn^{2+}	Ga^{3+}
1s	16.38	13.11	11.07
2s	15.14	11.48	9.25
2p	15.26	11.66	9.50
3s	7.58	4.75	3.30
3p	6.98	4.36	3.11

Table 8.4. % TSSP for the $5d^0$ isoelectronic series (obtained from relativistic SCF calculations).

Vacancy	I^-	Xe	Cs^+	Ba^{2+}	La^{3+}	Ce^{4+}	Hf^{4+}
1s	26.52	20.23	16.80	14.55	12.93	11.62	9.98
2s	24.53	18.19	14.78	12.58	11.07	9.82	9.21
$2\bar{p}$	24.84	18.53	15.16	12.94	11.41	10.19	9.32
2p	24.71	18.39	15.00	12.82	11.24	10.03	9.20
3s	21.81	15.38	12.04	9.90	8.44	7.33	8.14
$3\bar{p}$	21.87	15.49	12.15	10.03	8.57	7.45	8.25
3p	21.72	15.34	11.98	9.89	8.42	7.31	8.06
$3\bar{d}$	22.15	15.79	12.46	10.28	8.83	7.68	8.32
3d	22.08	15.68	12.38	10.26	8.72	7.66	8.24
4s	18.00	11.61	8.41	6.51	5.28	4.38	5.16
$4\bar{p}$	17.81	11.41	8.35	6.43	5.19	4.30	5.08
4p	17.53	11.25	8.12	6.24	5.03	4.15	4.69
$4\bar{d}$	17.05	10.86	7.82	6.05	4.91	4.03	4.56
$4\bar{d}$	17.02	10.80	7.73	5.98	4.84	4.01	4.39
$4\bar{f}$	–	–	–	–	–	–	3.82
4f	–	–	–	–	–	–	3.71
5s	7.22	3.69	2.33	1.60	1.26	0.96	1.07
$5\bar{p}$	6.26	3.25	2.13	1.51	1.20	0.95	0.98
5p	5.47	2.90	1.93	1.35	1.08	0.87	0.80

Table 8.5. Comparison between values of % TSSP obtained for argon using relativistic and non-relastivistic SCF calculations.

Vacancy	Relativistic	Non-Relativistic
1s	21.79	21.72
2s	14.86	14.80
$2\bar{p}$	15.34	15.24
2p	15.25	
3s	4.00	3.99
$3\bar{p}$	3.51	3.46
3p	3.46	

Table 8.6. Comparison of the values of % TSSP for xenon using different computational methods.

Vacancy	$\langle r \rangle$ (a.u)	Carlson-Nestor [14] (Statistical Product)	Relativistic	Non-Relativistic[3]
1s	0.0267	20.3	20.23	20.06
2s	0.1140	18.1	18.19	18.07
$2\bar{p}$	0.0963	18.5	18.53	18.38
2p	0.1021	18.3	18.39	
3s	0.3046	15.0	15.38	15.29
$3\bar{p}$	0.2953	15.1	15.49	15.36
3p	0.3066	14.9	15.34	
$3\bar{d}$	0.2779	15.3	15.79	15.78
3d	0.2815	15.3	15.68	
4s	0.7173	11.2	11.61	11.49
$4\bar{p}$	0.7474	11.0	11.41	11.27
4p	0.7731	10.8	11.25	
$4\bar{d}$	0.8699	10.1	10.86	10.92
4d	0.8805	10.1	10.80	
5s	1.9050	4.3	3.69	3.46
$5\bar{p}$	2.2417	3.0	3.25	2.97
5p	2.3516	2.5	2.90	

Table 8.7. Analysis of contributions to % TSSP in argon (obtained from non-relativistic calculations).

$a_{3s} = \langle \phi_{3s} \mid \phi'_{3s} \rangle$	$a_{3p} = \langle \phi_{3p} \mid \phi'_{3p} \rangle$
2s ionisation	2p ionisation
$a_{3s} = 0.9956$	$a_{3s} = 0.9947$
$a_{3p} = 0.9882$	$a_{3p} = 0.9882$
$a_{3s}^2 a_{3p}^6 = 0.9231$	$a_{3s}^2 a_{3p}^6 = 0.9214$
$D_{if}(2s \mid \chi_1) = 0.9230$	$D_{if}(2s \mid \chi_1) = 0.9207$
3s ionisation	3p ionisation
$a_{3s} = 0.9986$	$a_{3s} = 0.9992$
$a_{3p} = 0.9969$	$a_{3p} = 0.9968$
$a_{3s} a_{3p}^6 = 0.9802$	$a_{3s}^2 a_{3p}^5 = 0.9826$
$D_{if}(2p \mid \chi_1) = 0.9800$	$D_{if}(2p \mid \chi_1) = 0.9826$

Table 8.8. Comparison between calculations of % TSSP for ionisation of a 3p electron from $Cu^{2+}(^2D)$

Final ion state	Degeneracy	% TSSP
^3F	21	4.68
^3D	15	4.36
^3P	9	4.39
^1F	7	3.99
^1D	5	4.63
^1P	3	4.02
$\therefore$ Average % TSSP		= 4.44
% TSSP as given by ACI calculation		= 4.42

Table 8.9. % TSSP for doubly ionised transition metal atoms (obtained from non-relativistic ACI calculations).

Vacancy	Ti^{2+}	V^{2+}	Cr^{2+}	Mn^{2+}	Fe^{2+}	Co^{2+}	Ni^{2+}	Cu^{2+}	Zn^{2+}
1s	16.03	15.85	15.51	15.02	14.87	14.59	14.24	13.53	13.11
2s	12.50	12.82	12.85	12.62	12.75	12.66	12.44	11.81	11.48
2p	12.77	13.10	13.11	12.85	12.95	12.84	12.65	12.00	11.66
3s	4.52	4.77	4.85	4.80	5.12	5.26	5.31	4.80	4.75
3p	4.05	4.27	4.38	4.31	4.62	4.80	4.89	4.42	4.36

Table 8.10. % TSSP for triply ionised transition metal atoms (obtained from non-relativistic ACI calculations).

Vacancy	Ti^{3+}	V^{3+}	Cr^{3+}	Mn^{3+}	Fe^{3+}	Co^{3+}	Ni^{3+}
1s	12.46	12.69	12.62	12.51	12.27	12.17	11.99
2s	8.25	9.02	9.41	9.59	9.65	9.80	9.84
2p	8.63	9.36	9.71	9.89	9.90	10.06	10.06
3s	2.20	2.62	2.85	3.03	3.10	3.36	3.48
3p	2.03	2.39	2.62	2.76	2.86	3.09	3.19

Table 8.11. Analysis of 3d orbital relaxation following 2p ionisation from doubly ionised transition metal atoms.

Element	$\langle \phi_{3d} \mid \phi'_{3d} \rangle$	n = no. of d electrons	$\langle \phi_{3d} \mid \phi'_{3d} \rangle^n$
Ti	0.9794	2	0.9592
V	0.9839	3	0.9524
C	0.9870	4	0.9490
Mn	0.9893	5	0.9476
Fe	0.9905	6	0.9443
Co	0.9917	7	0.9433
Ni	0.9927	8	0.9431
Cu	0.9938	9	0.9457
Zn	0 9945	10	0.9463

Table 8.12. Analysis of 3d orbital relaxation following 2p ionisation from triply ionised transition metal atoms.

Element	$\langle \phi_{3d} \mid \phi'_{3d} \rangle$	n = no. of d electrons	$\langle \phi_{3d} \mid \phi'_{3d} \rangle^n$
Ti	0.9843	1	0.9843
V	0.9875	2	0.9795
Cr	0.9896	3	0.9691
Mn	0.9912	4	0.9653
Fe	0.9925	5	0.9630
Co	0.9932	6	0.9598
Ni	0.9940	7	0.9587

REFERENCES FOR CHAPTER 8

1. R. Manne, T. Åberg, Chem. Phys. Lett. 7 (1970) 282.
2. C. S. Fadley, J. Elect. Spec. 5 (1974) 895.
3. M. Mehta, C. S. Fadley, P. S. Bagus, Chem. Phys. Lett. 37 (1976) 454.
4. D. P. Spears, H. J. Fischbeck, T. A. Carlson, Phys. Rev. A9 (1974) 1603.
5. A. P. Jucys, Int. J. Quant. Chem. 1 (1967) 311.
6. P-O. Löwdin, Phys. Rev. 97 (1955) 1474.
7. J. Berkowitz, J. L. Dehmer, Y. K. Kim, J. P. Desclaux, J. Chem. Phys. 61 (1974) 2556.
8. R. L. Martin, D. A. Shirley, p 75 in "Electron Spectroscopy: Theory Techniques and Applications Vol. 1" (1977) Academic Press.
9. F. Wuilleumier, M. O. Krause, Phys. Rev. A10 (1974) 242.
10. T. A. Carlson, M. O. Krause, W. E. Moddenman, J. Phys. (Paris) C2 (1971) 102.
11. T. Åberg, Phys. Rev. A2 (1970) 1726.
12. V. L. Jacobs, P. G. Burke, J. Phys. B4 (1972) L67.
13. M. O. Krause, F. Wuilleumier, J. Phys. B5 (1972) L143.
14. T. A. Carlson, C. W. Nestor, Jr., Phys. Rev. A8 (1973) 2887.
15. E. U. Condon, G. H. Shortley, "Theory of Atomic Spectra" (1963) Cambridge University Press.
16. M. J. Gordon, Chemistry Part II Thesis, Oxford (1976).
17. P. Burroughs, A. Hamnett, A. F. Orchard, G. Thornton, J. Chem. Soc. Dalton Trans. (1976) 1686.
18. B. Wallbank, I. G. Main, C. E. Johnson, J. Elect. Spec. 5 (1974) 259.

APPENDICES

A.1 Conventions adopted in this thesis

A.2 Description of computer programmes used in this thesis

A.3 Description of the semi-empirical band structure calculations performed on a face-centre cubic oxide framework

A.4 The special theory of relativity

APPENDIX 1

Conventions adopted in this thesis

(i) Units

The majority of equations in this thesis use the rationalised MSKA system of units (SI).

The SI system adopts the metre, kilogramme and second as the fundamental mechanical units, and uses the definition that the permeability of free space μ_o is exactly equal to $4\pi \times 10^{-7}$ henry m^{-1} in order to specify the electrical properties.

However in PES, it has been customary to retain two non-SI units. These are the electron volt (eV) as the unit of energy and the torr as the unit of pressure.

The conversion factors are as follows

$$1 \text{ torr} = 133.3 \text{ Nm}^{-2}$$

$$1 \text{ eV} = 1.602 \times 10^{-19} \text{J}$$

$$= 9.648 \times 10^{4} \text{ KJ Kmol}^{-1}$$

It also proves convenient in theoretical discussions and calculations to adopt the Hartree set of atomic units.[1] In this system, $e^2/4\pi\epsilon_o$, μ (the reduced mass), and $\hbar$ each have the numerical value of unity, and are then subsequently omitted from the relevant equations.

The basic units of reduced mass, length and time are given by

$$\text{unit reduced mass} = 9.105 \times 10^{-31} \text{Kg (for H atom)}$$

$$\text{unit length} = 5.292 \times 10^{-11} \text{ m}$$

$$\text{unit time} = 2.419 \times 10^{-17} \text{ s}$$

and hence

unit of energy = 27.21 eV (for H atom)

velocity of light = $\frac{1}{\alpha}$ = 137.036 a.u

Equations denoted with a.u after them indicate that they have been formulated in atomic units.

(ii) Wigner-Eckart Theorem

The Wigner-Eckart theorem can be written in a variety of ways depending upon the definition of the reduced matrix element. We have adopted the form given in Brink and Satchler[2] which is

$$\langle \alpha JM | T^K_q | \alpha' J' M' \rangle = (-1)^{2K} \langle \alpha J \| T^K \| \alpha' J' \rangle \times \langle JM | J' K M' q \rangle$$

As a consequence reduced matrix elements connecting the same two states are related by

$$\sqrt{(2J+1)} \langle J \| T^K \| J' \rangle = (-1)^{J-J'} \sqrt{(2J'+1)} \langle J' \| T^K \| J \rangle^*$$

(iii) Reciprocal Space

We follow the usual notation of solid state physics and define a plane wave as $\exp(i\underline{k}.\underline{x})$ where $\underline{K} = \frac{2\pi}{\lambda}$ is the circular wave number.

APPENDIX 2

Description of computer programmes used in this thesis

(i) Programmes on the ICL 1906A

(a) Atomic SCF procedures

Single configuration SCF Hartree-Fock and Dirac-Fock calculations were performed using programmes kindly provided by D. F. Mayers.

(b) Atomic relaxation calculations

Separate SCF calculations were performed on the respective initial and final (ionised) state atomic systems, and the resulting radial wavefunctions stored away in separate files. The % shake-up/shake-off probability was then determined by reading back both sets of wavefunctions and evaluating the determinant of radial overlaps by means of the NAG library routine F03AAF.

(c) Two-centre atomic overlap programme

The general strategy employed in this programme is essentially that outlined in Ballhausen and Gray[3] (page 134); this utilises elliptical co-ordinates. The relevant atomic wavefunctions were provided from the aforementioned SCF procedures, with the integration over the co-ordinates λ and μ being performed numerically. The programme evaluates all the possible types of overlap (i.e. σ, π, δ etc.) that are allowed by symmetry. The numerical procedures were rigorously tested by means of evaluating overlaps between Slater Type Orbital wavefunctions and then comparing the results with the tabulated analytical master formulae.

(d) Semi-empirical band structure calculations

A detailed description of the method is provided in Appendix 3. The DOS profiles were generated by sampling the irreducible wedge of the respective Brillouin zone using standard Monte-Carlo techniques. For each chosen value of K, the respective secular determinant was constructed and then evaluated by application of the NAG library routine F02AEF. The DOS profile was built up from the ensuing energy eigenvalues and finally broadened by means of the convolution programme.

(e) X-PE deconvolution and convolution procedures

These are both based on the Fourier Transform method which has been adequately described previously.[4, 5]

(ii) Programmes on the IBM 370/195

(a) MCDF-SCF routines

The existing suite of multiconfigurational Dirac-Fock (MCDF) programmes has been developed by I. P. Grant, D. F. Mayers and N. C. Pyper.[6] The main SCF programme requires the relevant open-shell jj-coupled angular momentum coefficients, the closed-shell coefficients being generated internally. These extraneous coefficients are precalculated by means of the MCP package[7] and are stored in a disc file for input at run time.

The main SCF procedure is essentially an extended version of that described by D. F. Mayers and F. O'Brien.[8] Initial orbital estimates can either be screened Coulomb wavefunctions or solutions of the Dirac equation in a Thomas-Fermi potential. Alternatively, some or all of the orbitals may be taken from previous calculations on other systems. Diagonalisation of

the Hamiltonian matrix to provide the energy eigenvalues and eigenvectors is achieved by means of the QR process.[9, 10]

Some of the general principles of numerical HF calculations have been recently discussed by C. Froese Fischer.[11]

(b) MCDF final state relative PE intensity programme

Separate MCDF-SCF calculations were performed on the respective initial and final (ionised) state atomic systems, and the wavefunctions stored in separate files. The intensity programme requires as input data the energy eigenvalues and CSF mixing coefficients for each system; this information is extracted from the appropriate file at run time. The relative PE intensity pattern is then constructed by examining each possible final state in turn, and searching through each of its constituent CSF for instances where that CSF is connected to a ground state CSF by a single electron ionisation. Any coefficients of fractional parentage or recoupling coefficients needed to effect the calculation were evaluated using existing routines.[12, 13]

The intensity profiles was finally broadened via the convolution programme on the ICL 1906A.

APPENDIX 3

Description of the semi-empirical band structure calculations performed on a face-centred cubic oxide framework.

(i) O_6^{12-} Cluster

Consider an octahedral cluster AB_6 of six oxygen ions surrounding a central metal atom (e.g. M^{2+}) with a M-O separation of a. In our model we shall ignore any metal-oxygen interaction and consider only the interactions of the oxygen 2p orbitals with each other.

The 18 oxygen 2p orbitals span the representations t_{1g}, t_{2g}, t_{1u}, t_{2u} (π symmetry with respect to the metal oxygen axis and a_{1g}, t_{1u}, e_g (σ symmetry). The symmetry orbital constructed from the a.o species K (either p_σ or p_π), and transforming as the m th component of the irreducible representation Γ_g^1 of the point group O_h may be written [14]

$$|K_{gm}\rangle = (1 + \mathcal{X}_{gk})^{-1/2} \sum_{K_B} C_{gm,K_B} |K_B\rangle$$

where

$$\mathcal{X}_{gk} = \sum_{K_B \neq K_{B'}} \sum C_{gm,K_B} C_{gm,K_{B'}} \langle K_B | K_{B'} \rangle$$

and

$$\sum_{K_B} C^2_{gm,K_B} = 1$$

$(1 + \mathcal{X}_{gK})^{-\frac{1}{2}}$ is a normalising factor which corrects for the overlap of orbitals on different oxide ions, B and B'. The required summetry orbitals for octahedral AB_6 have been tabulated by Ballhausen and Gray,[3] so it is expedient to use the same

coordinate systems as these authors. The overlap functions, χ_{gK}, are presented in Table A-1, and correct a mistake for Πt_{1g} given in the authors' tabulation.

Table A-1. Overlap functions for AB_6 system

$\lvert Kg \rangle$	χ_{gK}
σa_{1g}	$S_\sigma(2a) + 2S_\sigma(a\sqrt{2}) + 2S_\pi(a\sqrt{2})$
σe_g	$S_\sigma(2a) - S_\sigma(a\sqrt{2}) - S_\pi(a\sqrt{2})$
σt_{1u}	$-S_\sigma(2a)$
Πt_{1g}	$-S_\pi(2a) - S_\sigma(a\sqrt{2}) - S_\pi(a\sqrt{2})$
Πt_{2g}	$-S_\pi(2a) + S_\sigma(a\sqrt{2}) + S_\pi(a\sqrt{2})$
Πt_{1u}	$S_\pi(2a) + 2S_\pi(a\sqrt{2})$
Πt_{2u}	$S_\pi(2a) - 2S_\pi(a\sqrt{2})$

S_σ and S_π are the optimally directed overlap integrals, $\langle \sigma_B \mid \sigma_{B'} \rangle$ and $\langle \pi_B \mid \pi_{B'} \rangle$ respectively.

For the purpose of the calculation a metal-oxygen separation of $\underline{a}$ = 0.212 nm was used; this corresponds to that in MgO. The S_σ and S_π overlaps were then computed using the O^{2-} wavefunctions as given by Watson for a +1 well.[15] The appropriate values are $S_\sigma(a\sqrt{2}) = 0.12174$, $S_\pi(a\sqrt{2}) = 0.05155$, $S_\sigma(2a) = 0.04758$ and $S_\pi(2a) = 0.01314$.

The relative one-electron energies for the B_6 symmetry orbitals may be estimated using the following simple model. Let the diagonal Fock elements for the oxide a.o be written

$$F_{K_B K_B} = \alpha$$

and the off-diagonal elements approximated as

$$F_{K_B l_{B'}} = 2 \langle K_B | l_{B'} \rangle \alpha \qquad B \neq B'$$

where α is a parameter. The diagonal matrix element for the symmetry orbital $|Kg\rangle$ is then just

$$F_{KgKg} = (1 + \chi_{gK})^{-1}(1 + 2\chi_{gK})\alpha$$

The problem now is to find the energies of the symmetry m.o's. These are achieved by solving the matrix equation

$$\hat{F}\,\underline{C} = \hat{S}\,\underline{C}$$

where $\hat{F}$ is the Fock operator, $\underline{C}$ the respective eigenvector and $\hat{S}$ the overlap integral matrix. The eigenvalues of this equation are the roots of the secular determinant,

$$\det \left| \hat{F} - \epsilon \hat{S} \right| = 0$$

The only non-zero off-diagonal Fock matrix elements in this calculation are the ones between $|\sigma_{t_{1u}}\rangle$ and $|\pi_{t_{1u}}\rangle$ and thus only a 2 x 2 secular determinant must be solved. The relevant overlap $\langle \sigma_{t_{1u}} | \pi_{t_{1u}} \rangle$ is given by

$$\langle \sigma_{t_{1u}} | \pi_{t_{1u}} \rangle = [(1 + \chi_{\sigma_{t_{1u}}})(1 + \chi_{\pi_{t_{1u}}})]^{\frac{1}{2}} \times \sqrt{2}[S_\sigma(a/2) - S_\pi(a/2)]$$

Solution of this secular determinant yields the following orbital eigenvalues

Orbital	Symmetry type	Eigenvalue
t_{1g}	π	0.77085α
e_g	σ	0.85621α
t_{1u}	predominantly σ	0.88980α
t_{2u}	π	0.90115α
t_{2g}	π	1.13804α
t_{1u}	predominantly π	1.14378α
a_{1g}	σ	1.28272α

(ii) Tight binding band structure calculation

The tight binding (LCAO) method was employed to predict the band structure of an infinite face-centred cubic array of oxide anions. Such an oxygen framework is representative of oxides exhibiting the rock salt structure (e.g. MgO). The calculation thus neglects all metal-oxygen interactions.

The general approach is to construct Bloch sums for each atomic orbital on each atom in the primitive cell.[16, 17] For this calculation there is only one atom in the primitive cell, and only the three normalised functions P_x, P_y and P_z corresponding to the triply degenerate O 2p orbital were considered. Each Bloch sum can be written as

$$\Psi_{nk}(\underline{r}) = \left[N(1+\alpha_{nk})\right]^{-\frac{1}{2}} \sum_{\underline{R}} \exp(i\underline{k}.\underline{R})\, \phi_n(\underline{r}-\underline{R})$$

$\phi_n(\underline{r} - \underline{R})$ is an atomic orbital, located on an atom with position vector $\underline{R}$, and with subscript n referring to the type of orbital (i.e. x for Px etc.). N is the total number of primitive cells in the lattice and $(1+\alpha_{nK})^{-\frac{1}{2}}$ is a normalising factor which corrects for the overlap of orbitals on different oxide ions.

For the face-centred cubic structure the atoms are located at the points $\underline{R} = a\underline{l}$ where a is the metal-oxygen separation and l_x, ly and l_z are integers with the additional proviso that $l_x + ly + l_z$ is even. The Bloch sum can now be written as

$$\Psi_{nk}(\underline{r}) = \left[N(1+\alpha_{nk})\right]^{-\frac{1}{2}} \sum_{\underline{l}} \exp(ia\underline{k}.\underline{l})\, \phi_n(\underline{r}-a\underline{l})$$

The normalising factor α_{nK} may be readily evaluated from the requirement $\langle \Psi_{nK} \mid \Psi_{nK} \rangle = 1$. We thus have

$$1 = \left[N(1+\chi_{nk})\right]^{-1} \sum_{l'} \sum_{l} \exp\{ia\underline{k}.(\underline{l}-\underline{l}')\} \times \int \phi_n^*(\underline{r}-a\underline{l}')\,\phi_n(\underline{r}-a\underline{l})\,d\tau$$

The double summation l,l' is over all lattice points, and thus it should be apparent that the expression can now be simplified to provide

$$1 + \chi_{nk} = \sum_{l} \exp(-ia\underline{l}.\underline{k}) \int \phi_n^*(\underline{r}-a\underline{l})\,\phi_n(\underline{r})\,d\tau$$

If we only include interactions between a central oxygen and its 12 nearest neighbours then it is possible to derive the following expression

$$\chi_{xk} = 2(S_\pi - S_\sigma)(\cos\phi_x \cos\phi_y + \cos\phi_z \cos\phi_x) + 4S_\pi \cos\phi_y \cos\phi_z$$

$\phi_x = aK_x$ etc. and S_π and S_σ refer to the optimally directed $S_\pi(a\sqrt{2})$ and $S_\sigma(a\sqrt{2})$ respectively. For the purpose of the calculation $\underline{a}$ was again chosen to be 0.212 nm (the M-O separation in MgO) and the overlaps are thus the same as those presented in section (i). The corresponding expressions for χ_{yK} and χ_{zK} may be obtained by cyclic permutation of the subscripts ($x \longrightarrow y \longrightarrow x \longrightarrow x$).

For a given value of $\underline{K}$, a wavefunction can be constructed which will be a linear combination of all the Bloch sums. In general, except at special $\underline{K}$ values (e.g. $\underline{K} = 0$), there will be energy matrix elements between all these Bloch sums, and thus a 3 x 3 secular determinant of the form

$$\det \left| \hat{F} - \epsilon \hat{S} \right| = 0$$

must be solved. To evaluate the matrix elements, we make

exactly the same assumptions as in the cluster calculation. The diagonal Fock matrix elements are given by

$$\langle \Psi_{nk} | \hat{F} | \Psi_{nk} \rangle = (1 + \chi_{nk})^{-1}(1 + 2\chi_{nk})\alpha$$

α being the diagonal Fock matrix element for the oxide a.o's. The off-diagonal matrix element between Bloch sums is then

$$\langle \Psi_{nk} | \hat{F} | \Psi_{mk} \rangle = 2\alpha S_{nk,mk}$$

where $S_{nK,mK}$ is the overlap between the Bloch sums. The overlap $S_{xK,yK}$ is given by

$$S_{xk,yK} = 2\{S_\sigma + S_\pi\} \sin\phi_x \sin\phi_y$$

the other overlaps being obtained by cyclic permutation ($x \longrightarrow y \longrightarrow z \longrightarrow x$). Hence for each value of $\underline{K}$ we can set up and solve the secular determinant.

The calculation was performed by randomly sampling 10000 such points in the irreducible wedge of the first Brillouin zone. The reciprocal lattice of a face-centred cubic lattice is a body-centred cubic (bcc) lattice; consequently the first Brillouin zone is the centred primitive all of the bcc lattice.[18] This is depicted in Figure A1, the edge of the cube being equal to $2\Pi a^{-1}$.

APPENDIX 4

The Special Theory of Relativity

The special theory of relativity is based on two assumptions[19-20]; (i) the laws of physics are the same in all coordinate systems which move uniformly relative to one another; and (ii) the velocity of light in empty space is the same in all reference frames and is independent of the motion of the emitting body. The implication of these two postulates is that one must consider coordinates of a point, referred to two reference frames which move with relative velocity $\underline{v}$, as being related by the Lorentz transformation rather than the Galilean transformation.[20] Hence, in addition to the usual three space-like components, a fourth time-like component is required. The four-component position vector $\underline{x}$ is represented by x_1, x_2, x_3 (the usual spatial coordinates) and $x_4 = ict$ (the time-like component).

Consideration of the energy-momentum four-vector leads to the Einstein equation

$$E^2 = p^2c^2 + m_o{}^2c^4 \qquad \text{(A4-1)}$$

E is the total energy of the system and is given by

$$E = \frac{m_o c^2}{\sqrt{\left(1 - \frac{u^2}{c^2}\right)}} \qquad \text{(A4-2)}$$

If we apply the binomial expansion to this equation and consider the non-relativistic limit ($u \longrightarrow 0$) then

$$E \simeq m_o c^2 + \tfrac{1}{2} m_o u^2 \qquad \text{(A4-3)}$$

that is E consists of the classical kinetic energy, $\frac{1}{2}m_o u^2$, plus the rest mass energy, $m_o c^2$. The quantity $\underline{p}$ in equation (A4-1) is the three-dimensional momentum,

$$\underline{p} = m\underline{u} = \frac{m_o \underline{u}}{\sqrt{(1 - \frac{u^2}{c^2})}} \qquad (A4-4)$$

Thus the momentum contains an effective mass

$$m = \frac{m_o}{\sqrt{(1 - \frac{u^2}{c^2})}} \qquad (A4-5)$$

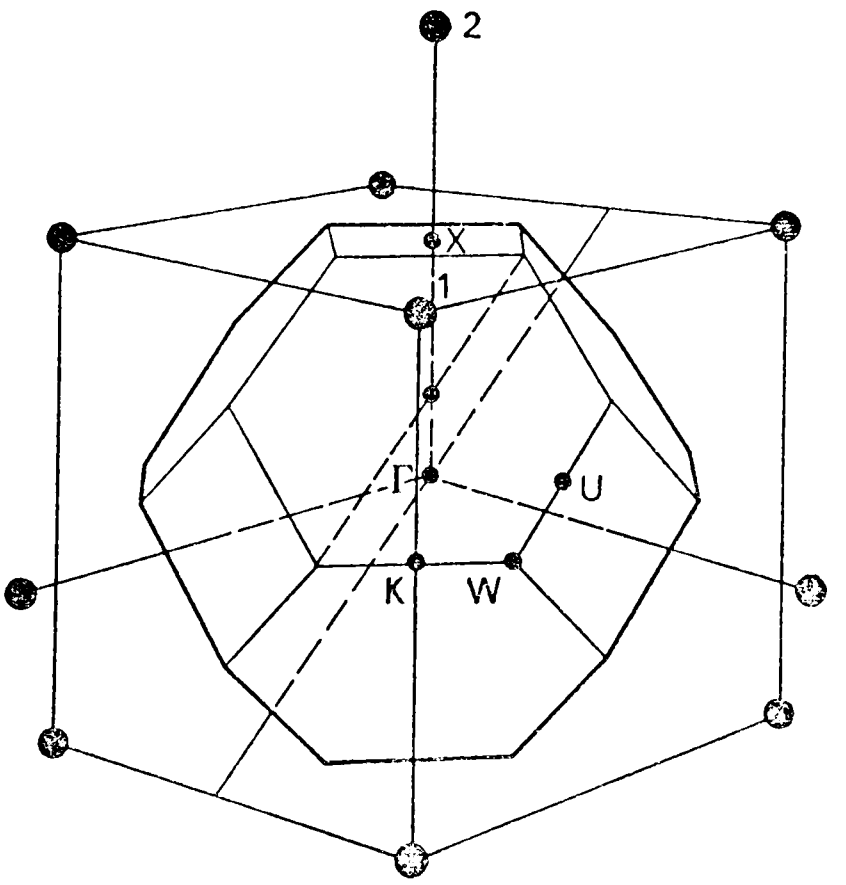


Fig. A.1. The first Brillouin zone for the face centred cubic lattice. The edge of the cube is equal to $2\pi a^{-1}$.

REFERENCES FOR APPENDICES

1. D. R. Hartree, Proc. Camb. Phil. Soc. 24 (1926) 89.
2. D. R. Brink, G. R. Satchler, "Angular Momentum" (1968), Oxford University Press, 2nd edition.
3. C. J. Ballhausen, H. B. Gray, "Molecular Orbital Theory", (1964) Benjamin, New York.
4. N. Beatham, Chemistry Part II thesis, Oxford (1975).
5. N. Beatham, A. F. Orchard, J. Elect. Spec. 9 (1976) 129.
6. I. P. Grant, D. F. Mayers, N. C. Pyper, J. Phys. B9 (1976) 2777.
7. I. P. Grant, Comput. Phys. Commun. 11 (1976) 397.
8. J. P. Desclaux, D. F. Mayers, F. O'Brien, J. Phys. B4 (1971) 631.
9. J. G. F. Francis, Comput. J. 4 (1961) 265 and 332.
10. J. H. Wilkinson, "The Algebraic Eigenvalue Problem" (1965), Oxford: Clarendon Press.
11. C. Froese Fischer, "The Hartree-Fock method for atoms. A numerical approach" (1977) Wiley-Interscience.
12. I. P. Grant, Comput. Phys. Commun. 4 (1972) 377 and 14 (1978) 311.
13. K. A. Berrington, P. G. Burke, J. J. Chang, A. T. Chivers, W. D. Robb, K. T. Taylor, Comput. Phys. Commun. 8 (1974) 151.
14. J. C. Green, M. L. H. Green, P. J. Joachim, A. F. Orchard, D. W. Tumer, Phil. Trans. Roy. Soc. London A268 (1970) 111.
15. R. E. Watson, Phys. Rev. 111 (1958) 1108.

16. J. C. Slater, G. F. Koster, Phys. Rev. 94 (1954) 1448.

17. T. F. Soules, E. J. Kelly, D. M. Vaught, J. W. Richardson, Phys. Rev. B6 (1972) 1519.

18. S. L. Altmann, "Band Theory of Metals" (1970) Pergamon Press.

19. A. Einstein, Ann. Physik 17 (1905) 132.

20. H. Muirhead, "The Special Theory of Relativity" (1973), MacMillan.